optima

IMAGING OF BREAST CANCER USING SERS AND SESORS

Anastasia Kapara

OPTIMA CDT
EPSRC and MRC Centre for Doctoral Training in Optical Medical Imaging

2019

EPSRC Pioneering research and skills

THE UNIVERSITY OF EDINBURGH

University of Strathclyde

MRC Medical Research Council

Signed: Date:

"The limit is the imagination."

Acknowledgements

I would like to start by thanking my supervisors Professor Karen Faulds, Professor Duncan Graham and Professor Val Brunton for all their guidance, patience and positivity. I had some amazing opportunities throughout my PhD, and I would not have the ability to explore them without your help. Thank you for everything!

This PhD could not have been possible without the precious help from all the PhD, and Postdoc members. Especially Sian Sloan-Dennison and William Tipping. You are two fantastic post-docs and the group is lucky to have you. Many thanks to all the group for the cakes, laughs and the "non-biased" Ramie award that I got as the "best Greek person in the final year". I will miss you all. I would like to especially thank my friend Kirsty Callan for being next to me all this time. Kirsty you have been more than amazing, and I could not have done it without you. Also, to Daniel Macdonald, Kirsty Milligan, Jenny Gracie and Amy Morison. We have all started this PhD together and I cannot believe that we managed to survive through this period! Time flies! I would also like to thank all OPTIMA members and students, especially Gillian Craig, Hazel Steward and Rachael Cameron for keeping my mind healthy through this PhD trip. The board game nights would not have been the same without you! Finally, thanks to my beautiful friend Maria Zachari for being next to me while I was writing this thesis and supporting me when I was ready to break.

Most importantly, I would like to thank my best friend, flatmate, soulmate, boyfriend and the kindest person that I have met in my life, Apostolos Paschalidis (also known as "Psit"). You have been next to me for the last ten years and you encourage me with everything I do. You push me forward every day Psit and I really do not know how you do it. I would have killed me! You and Aros (woof) kept me sane through this journey with lots of support, hugs, chocolates, walks and kisses. Can't wait for the coming psitonomoments! Ψιτονάκια ενωμένα ποτέ νικημένα!

Finally, to my beautiful parents Katerina and Alexandros for supporting me with closed eyes and keeping up with all my crazy and difficult life decisions all these years. I know that you miss me a lot all this time that I am away. I hope I will be half as open-minded and encouraging with my children as you are with me. This thesis is for you!

Ευχαριστώ μαμά και μπαμπά!

Abstract

Breast cancer is one of the leading causes of oncologic mortality and morbidity among women worldwide. It is estimated that every 10 minutes one person is diagnosed with the disease in the UK, while 1 in 8 women will develop breast cancer at some point in their lives. Although different techniques, for the characterisation of cancer phenotype, exist there are still limitations as these approaches are destructive, require processed/fixed samples and are not suitable for 3D tumour samples and *in vivo* models. Surface enhanced Raman spectroscopy (SERS) overcomes these limitations as a non-destructive bioanalytical method that offers high specificity, selectivity and multiplex capacities, in comparison to conventional imaging techniques.

The main aim of this research is to create a platform for targeting, detecting and tracking the intracellular distribution of estrogen receptor alpha (ERα) biomarker in breast cancer, using SERS combined with antibody functionalised gold nanoparticles (AuNPs). Specifically, the anti-ERα antibody functionalised AuNPs (ERα-AuNPs) were conjugated with 1,2-bis(4-pyridyl)ethylene (BPE) Raman reporter that enabled the spatial and temporal understanding of where ERα was located at a single cell level. The nanotags showed excellent biocompatibility with no cellular toxicity. 3D SERS cell mapping, under different endocytosis inhibition conditions, confirmed that ERα-AuNPs were using a temperature-dependent way for their uptake. Additionally, dynamin and membrane ERα were shown to be responsible, at least in a part, for the nanotags' uptake in MCF-7 cells. Therefore, SERS provided an excellent biological insight of ERα-AuNPs uptake by generating 3D images of the entire cell volume, without the need for destructive, time consuming and expensive imaging methods such as transition electron microscopy (TEM).

2D and 3D SERS also confirmed the strong targeting effect of ERα-AuNPs against ERα since a higher SERS signal and nanotag accumulation were observed in MCF-7 cells ($ER\alpha^{+}$) compared to SKBR-3 ($ER\alpha^{-}$) breast cancer cells. SERS was also used for investigating the efficacy of fulvestrant, the first-in-class approved selective estrogen receptor degrader (SERD). The results confirmed that ERα-AuNPs can be used as a tool for identifying and characterising different breast cancer cells, based on ERα expression, and informing about SERDs activity in breast cancer.

SERS also provided an excellent bioanalytical tool for the characterisation of breast cancer phenotype and the assessment of fulvestrant activity in a 3D environment using live MCF-7 spheroids formed in a microfluidic device. The results confirmed the great penetration capabilities and strong targeting effect of ERα-AuNPs towards ERα, compared to nonspecific anti-HER2 antibody functionalised AuNPs (HER2-AuNPs). Additionally, fulvestrant activity was found to have a lower therapeutic effect the 3D MCF-7 spheroids in comparison to the 2D cell cultures demonstrating that 2D and 3D tumour models had different biological and architectural behaviours that affected their sensitivity to fulvestrant. Therefore, SERS and microfluidics were used as a powerful analytical tool, that effectively bridged the gap between the 2D monolayer cultures and animal models, for breast cancer cells characterisation and investigation of fulvestrant efficacy.

Finally, this thesis investigated the potentials for detection of ERα *ex vivo* and *in vivo* using a handheld SORS instrument with back scattering optics. SESORS allowed the detection of ERα-AuNP nanotags through tissue barriers of up to 15 mm thickness. Most importantly, it was possible to detect and track *ex vivo* the ERα-AuNPs incubated in live breast tumour spheroids buried at 10 mm porcine tissue. The *in vivo* work indicated that SESORS was detecting scattered photon from areas deeper than the breast cancer tumour, mainly due to the fixed optical arrangements of the spectrometer. Nevertheless, a higher signal was detected *ex vivo* in breast tumours in comparison to the liver after their removal from sacrificed animals, suggesting the strong targeting effect of ERα-AuNP nanotags to the tumour site.

This thesis highlights the performance and capabilities of SERS, microfluidics and SESORS on detecting, targeting and tracking ERα and opens up exciting opportunities for using these techniques as non-destructive and sensitive tools for improved biomedical imaging in a clinical environment.

Abbreviations

Ab	antibody
Akt	protein kinase B
AuNPs	gold nanoparticles
BPE	1, 2-bis(4-pyridyl)ethylene
DCLS	direct classical least squares
dH_2O	distilled water
DLS	dynamic light scattering
EDC	1-ethyl-3-(3-dimethylaminopropyl) carbodiimide
EDTA	ethylenediaminetetraacetic acid
ELISA	enzyme linked immunosorbent assay
ER	estrogen receptor
ERα	estrogen receptor alpha
ERβ	estrogen receptor beta
FBS	foetal bovine serum
HEPES	4-(2-hydroxyethyl)-1-piperazineethancesulfonic acid
HER2	human epidermal growth factor receptor 2
IgG	immunoglobulin
LSPR	localised surface plasmon resonance
LUT	look up table
mAb	monoclonal antibody
MAPK	mitogen-activated protein kinase
MES	2-(N-morpholino) ethanesulfonic acid
MTS	multicellular tumour spheroids
NaCl	sodium chloride
NPs	nanoparticles
PBS	phosphate buffered saline
PCA	principal component analysis
PEG	polyethylene glycol
PI3K	phosphoinositide 3 kinase
PPY	4-(1H-pyrazol-4-yl)pyridine
RPMI	Rosewell park memorial institute medium
RRS	resonance Raman spectroscopy
SEM	scanning electron microscopy
SERS	surface enhanced Raman spectroscopy
SERRS	surface enhanced resonance Raman spectroscopy
SESORS	surface enhanced spatially offset Raman spectroscopy
SORS	spatially offset Raman spectroscopy
TBE	tris-borate-EDTA
TBS	tris buffered saline
TEM	transmission electron microscopy
UV-vis	ultraviolet- visible

Contents

1. Introduction

1.1 Breast Cancer

Breast cancer is the leading cancer diagnosed in women and a major health problem worldwide.[1,2] It has been shown that breast cancer contributes 11% of all diagnosed cancers annually.[3] The highest incidence rates appear to be in Europe, North America and Australia (Figure 1).[4] In the UK, one person is diagnosed with breast cancer every 10 minutes.[5] Specifically, over 55,000 women are diagnosed with breast cancer each year in the UK, of which 4,500 cases are in Scotland.[5] Current statistics also suggest than one in eight women will develop breast cancer at some point in their lifetime, while more than 71,000 new cases are expected to be diagnosed by 2035, in the UK.[5]

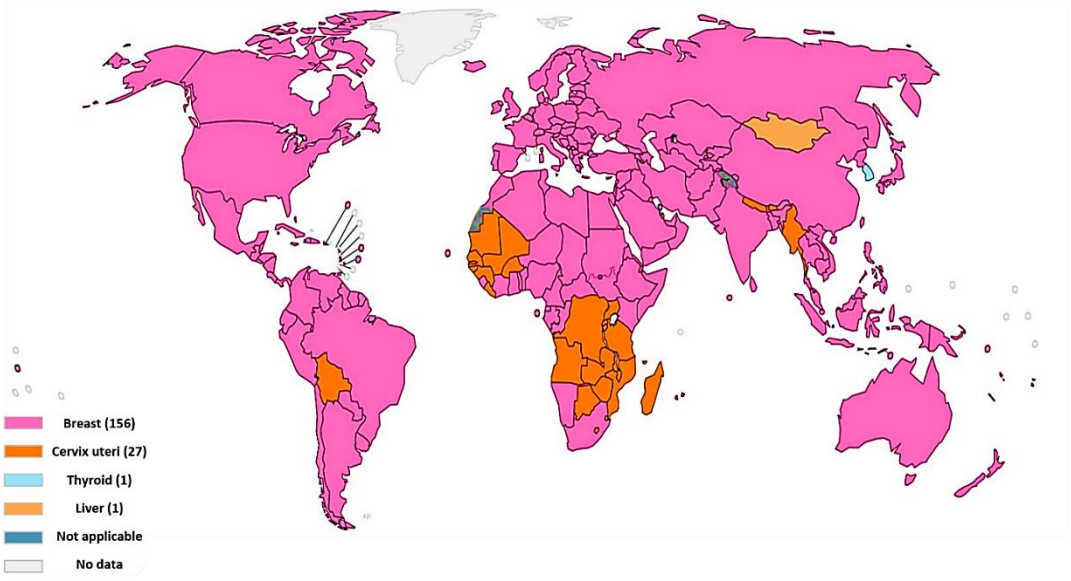

Figure 1: Worldwide map shows top cancer per country in females of all ages in 2018. The image was reproduced with permission from GLOBOCAN 2018 database Copyright 2018, Global Cancer Observatory.

The worldwide incidence patterns are influenced by the availability of screening programs[6] and the presence of breast cancer risk factors[2]. The main risk factors include: age, sex, family history, gene variations, prior medical radiation therapies, breast density, exo- and endogenous hormonal exposures and lifestyle factors such as alcohol consumption, obesity and sedentary lifestyle[7].

1.1.1 Breast Cancer Challenges

Breast cancer patients face complex challenges relating to diagnosis and treatment.[8] The main challenge of breast cancer is that, although the prognosis of cancer may be good in the early stages, recurrence can occur at any time, even decades after treatment, and it can vary by molecular subtype.[9] It is estimated that almost half of women with advanced stage breast cancer will relapse during the initial 5 years after diagnosis.[10] Additionally, the tumour microenvironment, known as a niche, plays an important role in the spread and metastatic profile of cancer. Specifically, the extracellular matrix, vasculature and inflammatory cells can fuel interactions of tumour cells with their surroundings that promote tumour progression.[11] Other breast cancer challenges are related to tumour resistance, lack of validated predictive biomarkers and absence of drugs that target new molecular pathways (Figure 2).[12] Most importantly though, breast cancer is a heterogeneous disease, which means that there is a high degree of diversity within and between the tumours among different patients.[13] The heterogeneity in primary breast tumour, and corresponding metastases affects significantly the cancer diagnosis and treatment.[14,15] These challenges can result in physical, psychological and emotional stress to the patients during their journey from disease screening and diagnosis to treatment.

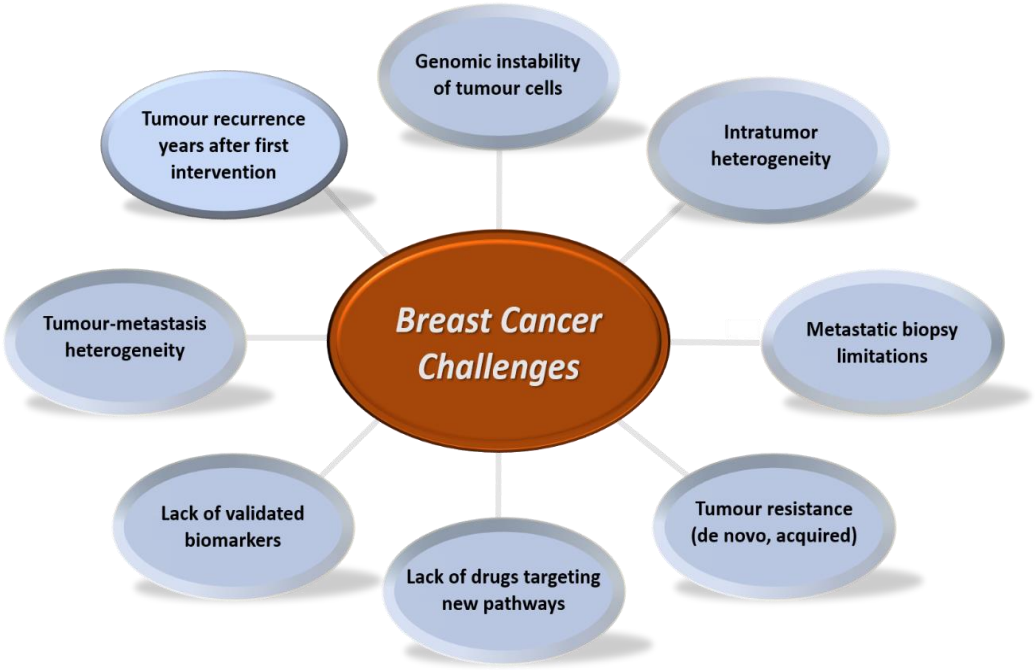

Figure 2: Schematic representation of some of the challenges in breast cancer.

1.1.2 Breast Cancer Screening

Breast cancer screening is used to detect cancerous and precancerous lesions at the earliest stage, before the symptoms and signs of breast cancer become apparent.[16] The early diagnosis of breast cancer plays a vital role in the success of the treatment and disease survival rates. For instance, stage I tumours, that are around 2 cm in size, have a 10-year survival of 85%.[17] On the other hand, delayed diagnosis of tumours at stage III have a 10-year survival of less than 60%.[17]

Mammography, clinical examination, digital breast tomosynthesis, breast ultrasound and magnetic resonance imaging (MRI) are some of the used methods for breast cancer screening.[18] Mammography and clinical examination are the most common approaches for detecting tumours larger than 1 cm.[19] However, the mammography sensitivity is around 24% lower in women with dense breast tissue compared to women with lower breast density.[20] Therefore, concerns about the accuracy of mammography screening and whether it should be combined with other supplemental screening methods, have arisen. On the other hand, breast examination requires an understanding of what the breast cancer looks like, which may lead to late diagnosis[21] and consequently to increase in the financial costs.[22] Digital breast tomosynthesis can reveal hidden changes in the breast tissue, however, it used ionising radiation and it is a new technology that has not yet become a standard screening method.[18] Breast ultrasound has also some limitations since it is highly operator dependent and it is affected by different factors, such as glandular tissue density and breast size[23] that may lead to increased false-positive results.[24] MRI is a sensitive breast cancer screening method; however, it is expensive and logistically complicated equipment that is not widely available. Additionally, MRI requires intravenous gadolinium injection, a contrast agent that allows higher MRI resolution, which is related to various side effects, such as nephrogenic systemic fibrosis and allergic reactions.[25] Moreover, MRI has overall lower specificity, in comparison to mammography, (85.9% vs 96.8%)[26] that may lead to increased false-positive and false negative results.[27] Based on the characteristics of the current breast cancer screening approaches, the main challenges are the false positive and false negative results as well as overdiagnosis that may result to late and non-efficacious treatment (Table 1).[28]

MAMMOGRAPHY RISKS	AVERAGE RISK BY AGE GROUP			
	40-49 Years	50-59 Years	60-69 Years	> 70 Years
FALSE NEGATIVE	1 in 3	1 in 4	2 in 9	2 in 11
FALSE POSITIVE (% screened) - Additional imaging (false positives) - Biopsy (false positives)	10 9 in 10 1 in 10	9 9 in 10 1 in 8	8 9 in 10 1 in 7	7 9 in 10 1 in 6
OVERDIAGNOSIS/ OVERTREATMENT	10-50% overdiagnosis rate means that 1/10 to 1/3 of all diagnosed breast cancers are pseudo-disease, which would never develop into symptomatic malignancy			

Table 1: Table shows a summary of the risks associated with screening mammography. The image was adapted with permission from[28] Copyright 2009, American College of Physicians.

Specifically, false negative results are the cases where the screening is not able to detect cancer.[29] On the other hand, false positive results is the identification of an abnormality that is found to be non-cancerous after additional screening methods.[29] False-positive results are one of the most common limitations of breast cancer screening, mainly due to a greater mammographic density, postmenopausal hormone therapy and the differences in performance and training of the interpreting radiologists.[30] Interestingly, the rate of false-positive diagnosis increases after 10 yearly mammograms, where the chance of having a false-positive result is about 50% (Figure 3).[31]

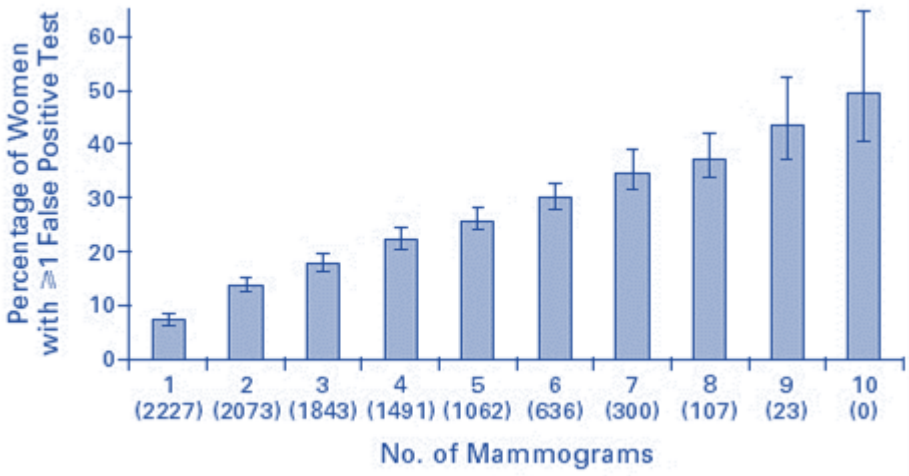

Figure 3: Estimated risk of having at least one false-positive screening mammogram according to the total number of screening mammograms performed. The numbers in parentheses are the numbers of women with at least that many mammograms. The image was reproduced with permission from[31] Copyright 1998, Massachusetts Medical Society.

Overdiagnosis is the diagnosis of asymptomatic cancer, that would have never been screened or have had any symptoms of the disease.[29] Overdiagnosis, therefore, leads to overtreatment and additional screening which can be costly and time consuming for the individuals. In the literature, the reports of overdiagnosis have a wide range from 0% to 60%.[32]

Breast cancer screening can be costly and challenging to be organised since major logistic issues exist. Hence, an innovative and effective screening method can be combined with current approaches to bring additional advantages in digital pathology for early diagnosis and treatment of breast cancer.

1.1.3 Breast Cancer Biomarkers: Potential Uses and Analytical Limitations

According to the National Cancer Institute (NCI), a biomarker is a biological molecule that is found in bodily fluids, or tissues, and indicates normal or abnormal processes of a disease.[33] Cancer biomarkers provide a powerful tool for disease screening, diagnosis and treatment. The major applications of biomarkers in clinical investigations are shown in Table 2.

Potential uses for biomarkers in oncology	Screen of disease
	Distinguish benign versus malignant processes (including staging)
	Predict response to therapy
	Determine prognosis independently from therapy
	Monitor disease status before and after therapy
	Assess risk of developing disease

Table 2: Potential uses for biomarkers in oncology.

Because of the critical role of biomarkers at all cancer stages, it is vital to evaluate each biomarker by utilising analytical tools.[34] Molecular biomarkers can be detected from their gene expression (e.g. microarrays), gene amplification (e.g. fluorescent *in situ* hybridization (FISH) and quantitative reverse transcription-polymerase chain reaction (RT-PCR)), gene sequence (e.g. DNA sequencing) and protein expression (e.g. immunohistochemistry (IHC), western blot and enzyme-linked immunosorbent assay (ELISA)). Although these methods can be useful for

measuring biomarker expression, there are still technical drawbacks that lead to false sampling errors.[35] The main observed limitations are the high background signal from fluorescence the time-consuming experimental steps, and, sometimes, the inability for direct detection in living cells or tissues.[36] RT-PCR and western blot are also destructive techniques that require cell lysis and cellular subfractionation.[37,38] On the other hand, IHC requires tissue fixation immediately after its collection to avoid sample degradation and false staining results.[39] The warm/cold ischemic time[40], the method for antigen retrieval and staff training also play an important role in IHC success.[41] Moreover, IHC limits any signal enhancement and the quality of the results rely on the natural visual yield after the staining that may uncover the presence, or absence, of proteins.[42] Additionally, sometimes it is challenging to classify the samples due to the complex cellular structures. Specifically, the segmentation of nuclei can be troublesome, since the nuclei structure may look dissimilar due to various factors such as type of nuclei, nuclei life cycle and severity of the disease.[43] To resolve these challenges, computer aided algorithms are used for the histopathological analysis of breast cancer. However, there is high computational complexity[44] and requirement of optimisation[45] for images containing high noise and excessive overlapping nuclei.[46] Techniques such as FISH are also used, however, FISH is nine times more time consuming and approximately three times more expensive compared to IHC.[47] Hence, FISH is not suitable for routine diagnosis since it requires expensive fluorescence equipment equipped with high-magnification oil immersion objectives and multiband filters for signal detection.[47]

1.1.3.1 Role of Estrogen Receptor Alpha in Breast Cancer

Breast cancer is divided into sub-classifications depending on the biomarker expression pattern. Estrogen receptor (ER), along with progesterone receptor (PR) and human epidermal growth factor receptor 2 (HER2), are the most common breast cancer biomarkers that play an important role in diagnosis and treatment.[48] Approximately 75% of primary breast tumours in women are positive for a hormone receptor, which can be either ER or PR.[15] In the UK, around three-quarters of all breast cancers are characterised by the presence of ERα[5], that is generally associated with poor prognosis and high rate of disease recurrence.[49] Therefore, ERα is a key receptor biomarker whose status plays a pivotal role in the classification of breast cancer subtypes.[50]

ER was first cloned in 1986 from human breast cancer cells and it is a ligand-activated transcription factor that regulates the expression of specific hormone response elements and other

non-coding RNAs.[51] Although many of these genes are only now being identified, it seems that they are responsible for different body functions of reproductive organs[52], immune system[53], bones[54] and brain.[55] In total there are two forms of ER: the estrogen receptor alpha (ERα) (66 kDa) and the estrogen receptor beta (ERβ) (54 kDa).[56] Although ERα and ERβ are widely expressed throughout the body, they exhibit distinct downstream transcriptional activities that lead to tissue-specific biological actions. Therefore, depending on the balance between these two forms, the estrogen receptor signalling pathway is selectively stimulated or inhibited in the target organs.[52] ERα is expressed primarily in the mammary gland, ovary, uterus, bone, liver and reproductive organs.[57] In contrast, ERβ is highly expressed in the prostate, colon, bladder, and central nervous system.[58] ERα consists of five structural domains based on the putative functions (Figure 4).[59] E/F or ligand binding domain (LBD), C or DNA binding domain (DBD), A/B domain and D or hinge domain. The LBD is located at the C-terminus of the receptor and is responsible for most functions activated by ligand binding. ERα and ERβ share only 56% similarity in their LBD.[60] The distinction of the residues lining the binding pocket influences the affinity of the receptor for its ligands.[61] LBD also contains a dimerisation surface and a second transactivation domain (AF-2), that has ligand-dependent transcriptional activity.[62] The DBD is located into the N-terminal of the receptor and it is responsible for its binding into specific DNA sequences, known as estrogen response elements (ERE), that are located in the major groove of the DNA helix.[63] The A/B domain is involved in N-terminal ligand-independent transcription activation (AF-1), which is constitutively active and contributes to the transcriptional activity and nuclear localisation of ER.[64] AF-1 is the least conserved region with only 30% similarity between ERα and ERβ, which leads to different recruitment of co-factors and observed variations in the downstream gene networks.[65] Studies have shown that AF-1 and AF-2 domains are in a synergistic interaction with one another which leads to transcriptional activation.[62] The hinge domain gets unmasked after the binding of the ligand and acts as a flexible domain which connects the LBD and DBD.[64]

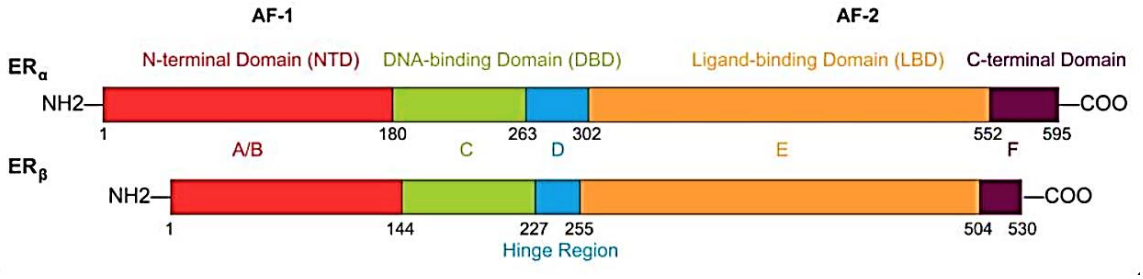

Figure 4: Structure of ERa (top) and ERβ (bottom). The sequence of the 5 domains is illustrated in different colours with the amino acid numbers. DBD: DNA-binding domain, LBD: ligand-binding domain, NTD: N-terminal transactivation domain. The image was reproduced with permission from[59] Copyright 2017, SAGE.

The main ligand for ERα activation is the primary natural female sex hormone, 17β-estradiol (E2). E2 is a small, carbon-rich estrogen that controls a plethora of biological functions, such as cell proliferation and differentiation.[66] E2 diffuses through the cell membrane and binds to the ERα with high affinity.[67] The information regarding E2-ERα relationship has been determined in different breast cancer cell lines.[68] Studies have shown that there are more than one possible E2-ERα pathways that provide plasticity and control different cellular responses. Overall, the molecular ER pathways are divided into genomic and non-genomic based on which proteins are activated into the signalling cascade (Figure).[69] The genomic mechanism is the most well-studied pathway and involves the binding of E2 to cytoplasmic ERα. The non-genomic mechanism involves the binding of E2 to membrane ERα or other membrane receptors, such as GRP30 (Figure 5).[69] Therefore, the E2-induced proliferative signalling involves both the nuclear and the membrane ERα.[70]

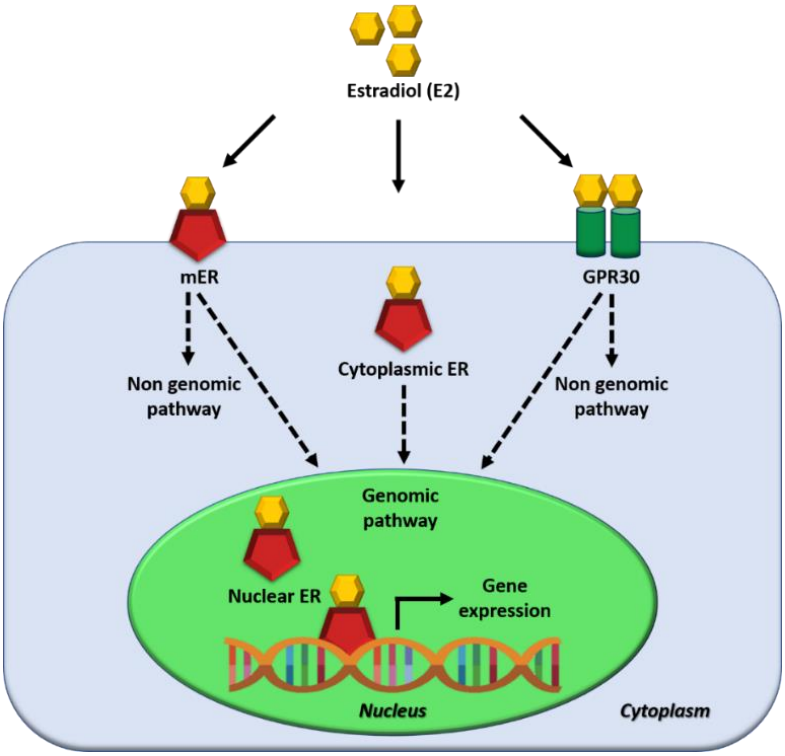

Figure 5: Schematic illustration of genomic and non-genomic ERα signalling pathways. Genomic pathway initiates when estradiol (E2) binds to ERα in the cytoplasm. The E2/ERα complex is transferred to the nucleus and leads to gene expression (within hours or days). In the non-genomic pathway, the ER2 binds to membrane proteins. Then, the membrane receptors activate other cellular secondary messenger proteins, that can lead to rapid cellular responses (within seconds or minutes). The image was adapted with permission from[69], Creative Commons CC-BY-NC-SA licence.

In the genomic pathway, after the binding of E2 to cytoplasmic ERα, there are conformation changes that lead to ERα dimerisation. The ERα is then transferred inside the nucleus (Figure 6).[55]

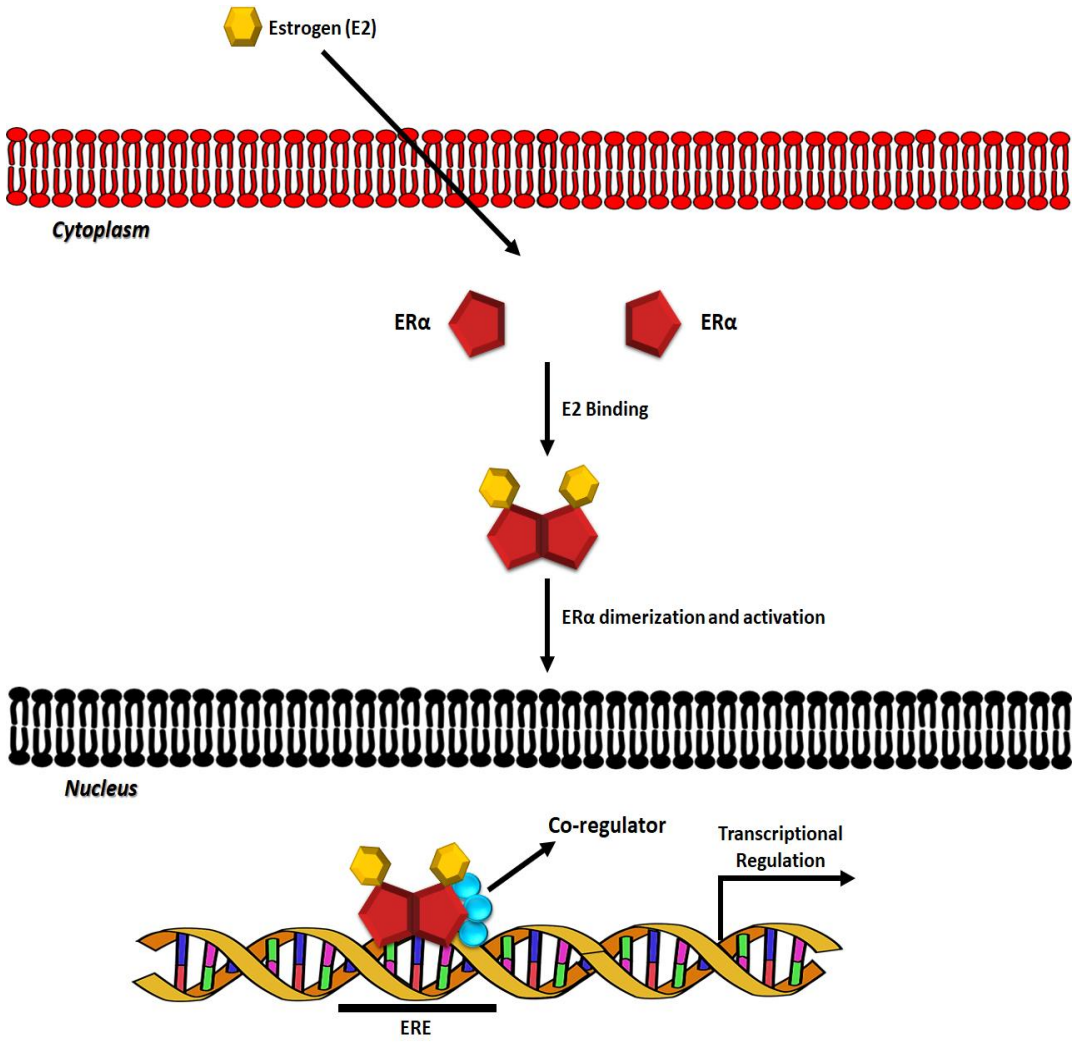

Figure 6: Schematic illustration of ERα genomic signalling pathway. Estradiol (E2) binds to ERα allowing its dimerisation. The ERα dimer is transferred inside the nucleus and mediates gene transcription by its binding to the estrogen-response element (ERE) of gene promoters. ERα binding also recruits transcription coactivators and RNA polymerase for transcriptional regulation. The image was adapted with permission from[55] Copyright 2014, SAGE.

Then the receptor can either bind to EREs on the DNA and work as a transcription factor (classical genomic mechanism)[71] or it can activate other factors downstream of the signalling pathway, such as Fos and Jun proteins, that bind to the DNA regulatory regions (non-classical genomic mechanism) (Figure 7).[72] In any case, the activated ERα recruits coregulator proteins and components that stimulate a cascade of events related to cell growth and proliferation.[73]

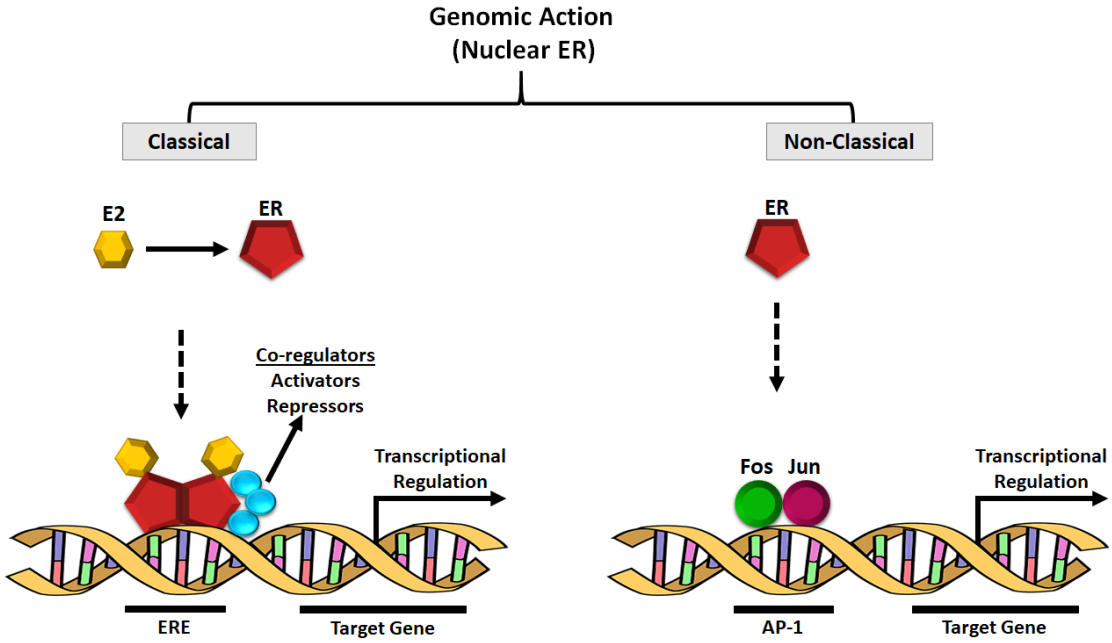

Figure 7: Schematic illustration of ERα genomic action. After the binding of E2, nuclear ERα activated the transcription of genes either by direct DNA binding to its response elements (ERE) in targeted gene promoters (classical action) or by tethering to other transcription factors, such as Fos/Jun activating protein-1 (AP-1) complex (non-classical action). The image was adapted with permission from[72] Copyright 2003, American Association for Cancer Research.

Recently, it has become clear that ERα also works as a plasma membrane-localised receptor.[74] The first investigation came from Pietras et. al. who reported the presence of high-affinity binding sites for ligands associated with the plasma membranes of MCF-7 breast cancer cells.[75] In the last two decades, it became apparent that there is a subpopulation of ERs (10-15%) that are membrane-associated estrogen receptors (mERs) which are also activated by estrogenic compounds.[76] There are two structurally different mER types. The palmitoylated membrane-bounds forms (or splice

variants) of the classical nuclear receptors and the G-protein coupled estrogen receptor (GPER), also known as GPR30, that is activated upon binding with a ligand.[77,78]

The membrane receptors seem to play a major role in the non-genomic pathway. Specifically, mERα and GPR30 can rapidly trigger the rapid activation and phosphorylation of second messenger systems.[79,80] including important growth regulatory kinases, such as mitogen-activated protein kinase (MAPK) and phosphoinositide 3-kinase (PI3K) (Figure 8).[72] This phosphorylation activates a cascade of cellular functions that are related to the regulation and transcription of different genes for proliferation and cell migration.[81] The trafficking of plasma ERα has been challenging to study and the mechanisms regulating membrane ERα levels have remained elusive.[82] However, there is compelling evidence that activated membrane ERα can be internalised from the plasma membrane into the cells.[83]

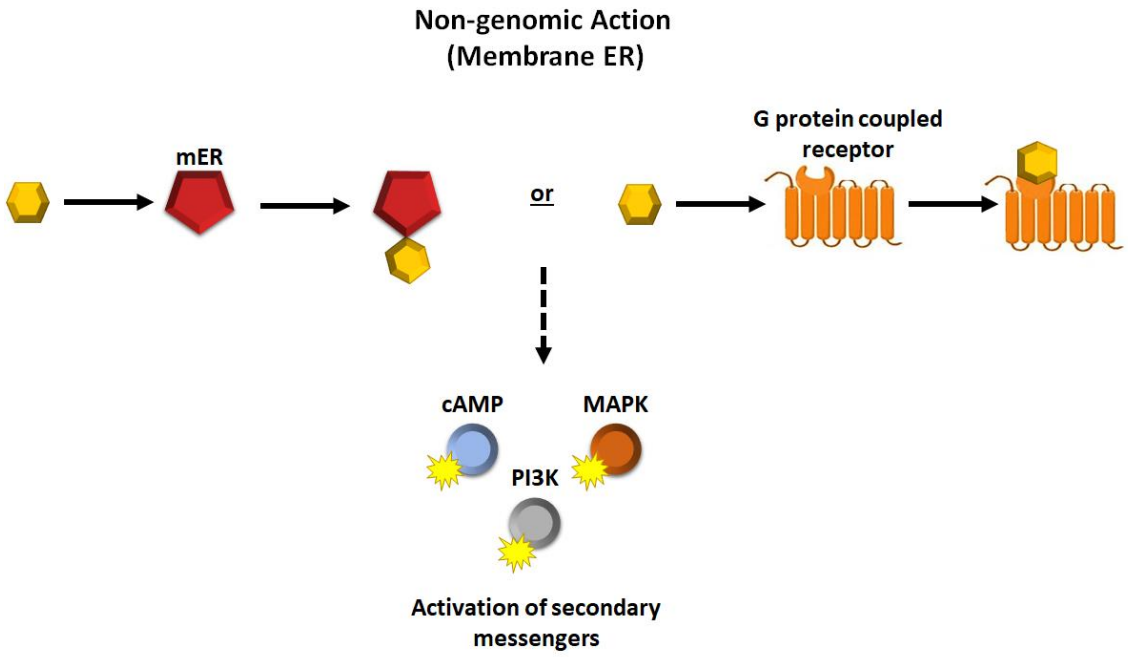

Figure 8: Schematic illustration of ERα non-genomic action. After the binding of E2 to mERα, or to G protein-coupled receptor, there is a rapid activation of secondary messenger proteins, such as MAPK and PI3K that regulate the transcription of different genes related to cell proliferation and growth. The image was adapted with permission from[72] Copyright 2003, American Association for Cancer Research.

ERα is an important marker for prediction of the likelihood of a patient developing metastatic disease.[84] The ERα positive breast cancers also tend to metastasize to the bones and the metastasis is in late stages.[85] Specifically, up to 75% of breast cancer patients with metastatic disease will have metastasis to the bones due to the secretion of cytokines that stimulate the osteoclastic activity and proliferation in bones.[86] Taking these characteristics into consideration, it is possible to predict the likelihood of a patient developing the metastatic disease at an earlier time from the diagnosis of breast cancer.[84] Therefore, the accurate assessment of ERα status is essential in diagnosis and treatment decision making for breast cancer, including metastatic disease.

1.1.3.2 Role of Human Epidermal Growth Factor Receptor 2 in Breast Cancer

The classification of breast cancer subtypes based on biomarkers is performed to predict the prognosis and determine the appropriate treatment regime for ERα negative patients.[87] After ERα, human epidermal growth factor receptor 2 (HER2) is the second most important biomarker for molecular diagnosis and targeted treatment of breast cancer. Specifically, HER2 acts as a prognostic and predictive breast cancer biomarker for approximately 20- 30% of breast cancer cases.[88]

HER2 is a receptor tyrosine-protein kinase and a part of the epidermal growth factor (EGF) family along with another three receptors: HER1 (erbB1), HER3 (erbB3) and HER4 (erbB4). It is a 185 kDa transmembrane glycoprotein that is encoded by the erbb2 gene on the long arm of chromosome 17.[89] HER2 comprises a cysteine-rich extracellular ligand binding site, a transmembrane lipophilic segment and an intracellular domain with tyrosine kinase catalytic activity.[90] HER2 exists as a monomer on the cell surface and its extracellular domain has no identifiable ligand.[91] It can be activated by different growth factors and undergo dimerisation with itself or with the other EGF receptors.[92] Dimerisation induces the phosphorylation of intracellular tyrosine residues within the cytoplasmic domain of the receptor (Figure 9).[93] This phosphorylation is an important process since it activates the intracellular signalling pathways of MAPK and PI3K which are related to cell cycle proliferation, survival, differentiation, migration and angiogenesis.[94]

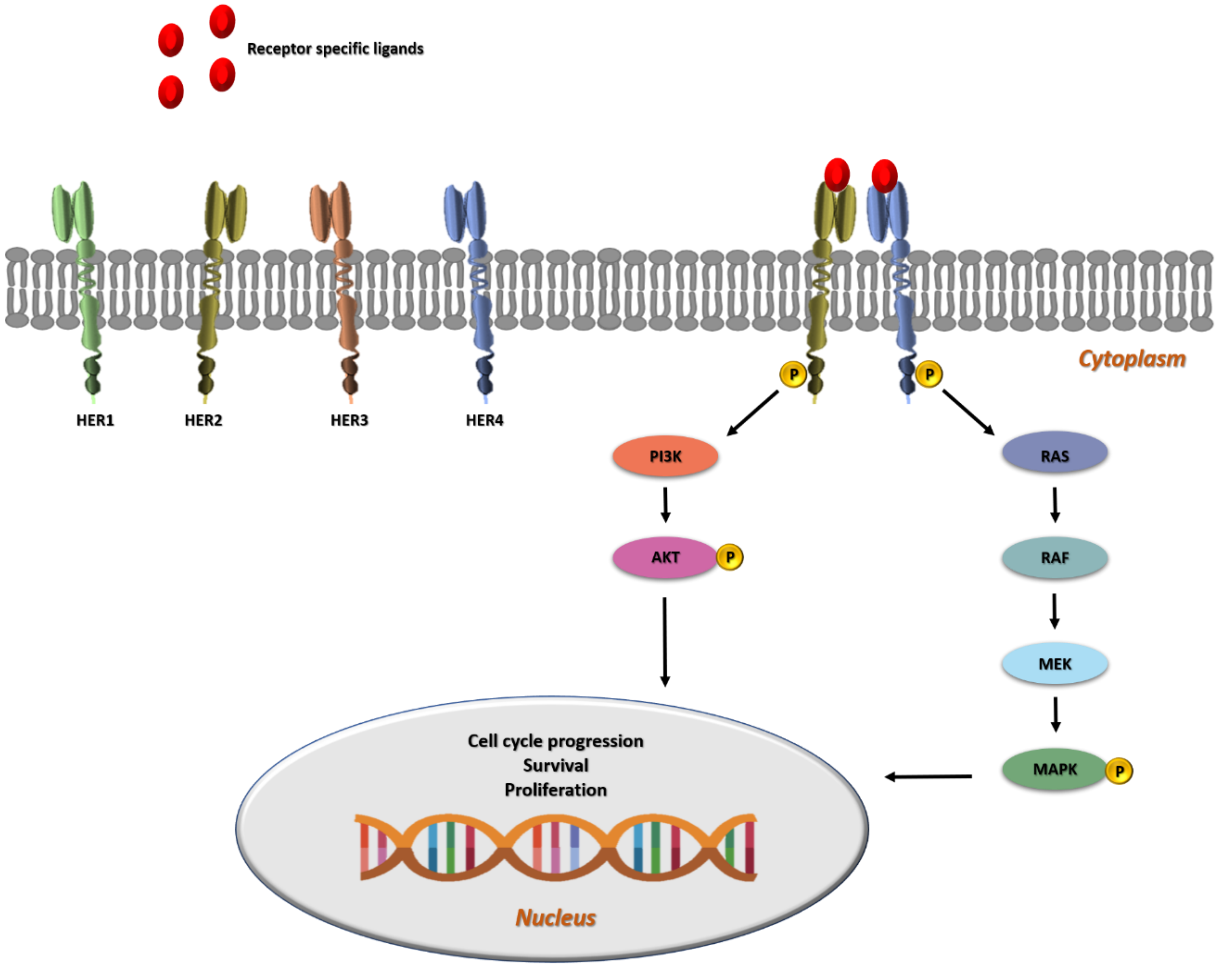

Figure 9: HER2 signalling pathway in breast cancer. HER2, as well as the other members of the EGFR family (HER1, HER3, HER4), are cell membrane receptor tyrosine kinases that respond to several receptor-specific ligands. The ligand-binding induces conformational changes in the receptor allowing homo and heterodimerisation and phosphorylation of the tyrosine kinase domain in the cytoplasm. Phosphorylation initiates downstream oncogenic signalling cascades, such as the PI3K/AKT pathway and RAS/MAPK pathway. The image was adapted with permission from[93], Creative Commons CC-BY-NC-SA licence.

In general, HER2 positive breast cancers tend to be more aggressive than other types of breast cancer.[95] Specifically, when HER2 is overexpressed, it contributes to high recurrence rate, poor prognosis[96], cancer progression and a higher rate of metastasis.[97] There is a high number of HER2-positive breast cancers that have the propensity to metastasise to the brain.[98,99] The overexpression

of HER2 present on the surface of breast cancer cells is around 100 times greater than in normal breast cells, resulting in approximately 2 million receptors at the cell surface.[100] Therefore, HER2 amplification has prognostic and predictive implications for the growth rate, metastasis and overall survival from breast cancer.[101]

1.1.4 Breast Cancer Treatment Options

The key decisions for breast cancer treatment are based on the data received from the screening and diagnosis approaches. The tumour-specific properties, including its size and localisation, as well as the tumour histology, are used to determine the treatment options. Therefore, clinicians need to propose treatment regimens according to the patient's molecular characteristics for increased drug efficacy, reduced side effects and longest life expectancy.[9] Currently, therapeutic strategies include local treatment, such as surgery and/or local radiotherapy and systemic therapy. The clinicians also need to agree if chemotherapy is needed before (neoadjuvant treatment) or after the surgery (adjuvant treatment) or if the breast needs to be removed (mastectomy).[102] Earlier diagnosis results in a lower percentage of mastectomy surgeries.[103] Studies have shown that many breast cancer patients do not respond to specific therapies from the beginning of the treatment (*de novo* drug resistance), while several breast cancer patients develop acquired resistance.[104] All these mechanisms involve complex interactions and signalling between the tumour cells and their environment.[105] Many studies have shown that a personalised approach to breast cancer treatment, in which therapy is based on the individual characteristics of each patient, will lead to better results. Therefore, data from translational studies that consider these aspects will be fundamental for future therapeutic approaches.

1.1.4.1 Anti-ERα Treatment

Most patients with ERα positive breast cancer will benefit from targeted therapeutic approaches that inhibit ERα pathway. However, different factors, including the ERα status, the tumour size and tumour grade may affect treatment success. Studies have shown that women that have been diagnosed with early ERα positive breast cancer and receive endocrine therapy for 5 years have a high risk of distant recurrence for up to 20 years after the treatment discontinuation.[106] Therefore, treatment failures can range from 5% up to 50% over 5-10 years from initial treatment.[6] Understanding the mechanisms of drug resistance is a challenging process, however, it is known

that during this process, the tumour continues to grow and metastasizes to secondary organs, particularly the bone, lung, brain and liver where survival is compromised.[107] Therefore, it is common that an extended endocrine therapy (more than 5 years) is usually considered for higher-risk patients who have responded well to the therapy in the first 5 years.[108]

Endocrine therapy, that targets the estradiol-ERα pathways, is recommended over chemotherapy due to higher efficacy and lower side effects.[109] The different classes of anticancer drugs inhibit the ERα function by acting on distinct areas. Consequently, a patient resistant to one type of drug can be treated with a different agent. Currently, different endocrine agents are used for ERα positive breast cancer treatment including aromatase inhibitors (AIs) that block estrogen synthesis[110], selective estrogen receptor modulators (SERMs) that inhibit estrogen-like action[111] and selective estrogen receptor down-regulators (SERDs) that cause ERα degradation (Figure 10).[111]

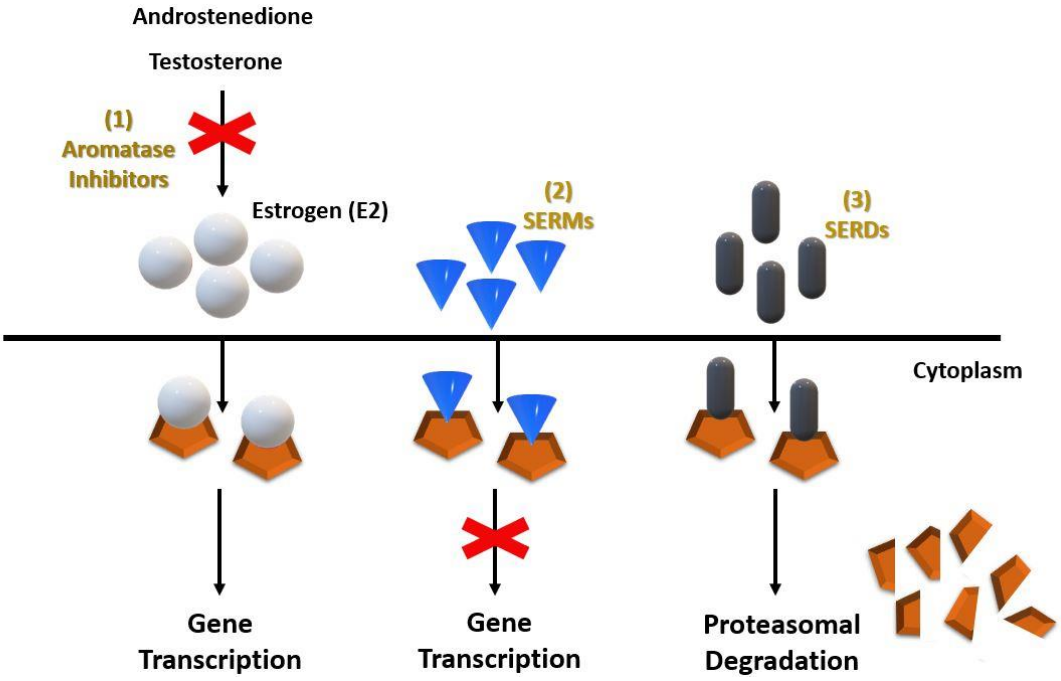

Figure 10: Schematic explaining the mechanisms of the main anti- ERα treatment categories: (1) AIs, (2) SERMs and (3) SERDs.

AIs are usually used for the treatment of early-stage breast cancer in postmenopausal women, since they are more effective with fewer serious side effects, compared to SERMs.[112] AIs work by blocking aromatase, an enzyme that metabolises oestrogens from androstenedione and testosterone chemical precursors.[113] Therefore, there is less estrogen available to stimulate the ERα pathway. Three common examples of AIs are anastrozole, exemestane and letrozole.

SERMs mimic estrogen by binding to the LBD pocket of the ERα, altering the structure and function of ERα. Therefore, they make ERα unable to function as a transcription factor and regulate gene expression.[114] Tamoxifen[115], raloxifene[116] and toremifene[117] are the three commercially available SERMs active against breast cancer (Figure 11). Tamoxifen is the most commonly used treatment,[112] however many patients develop endocrine resistance and tamoxifen subsequently fails.[118]

SERDs are drugs that bind to ERα resulting its degradation and downregulation. This unique characteristic of SERDs provides pure antagonism of *in vitro* and *in vivo* effects.[119] Like endogenous estradiol, SERDs have a steroid based structure, that provides a high ERα-binding affinity. Currently, the only SERD approved treatment is fulvestrant for ERα positive and HER2 negative metastatic breast cancer (Figure 11).[120]

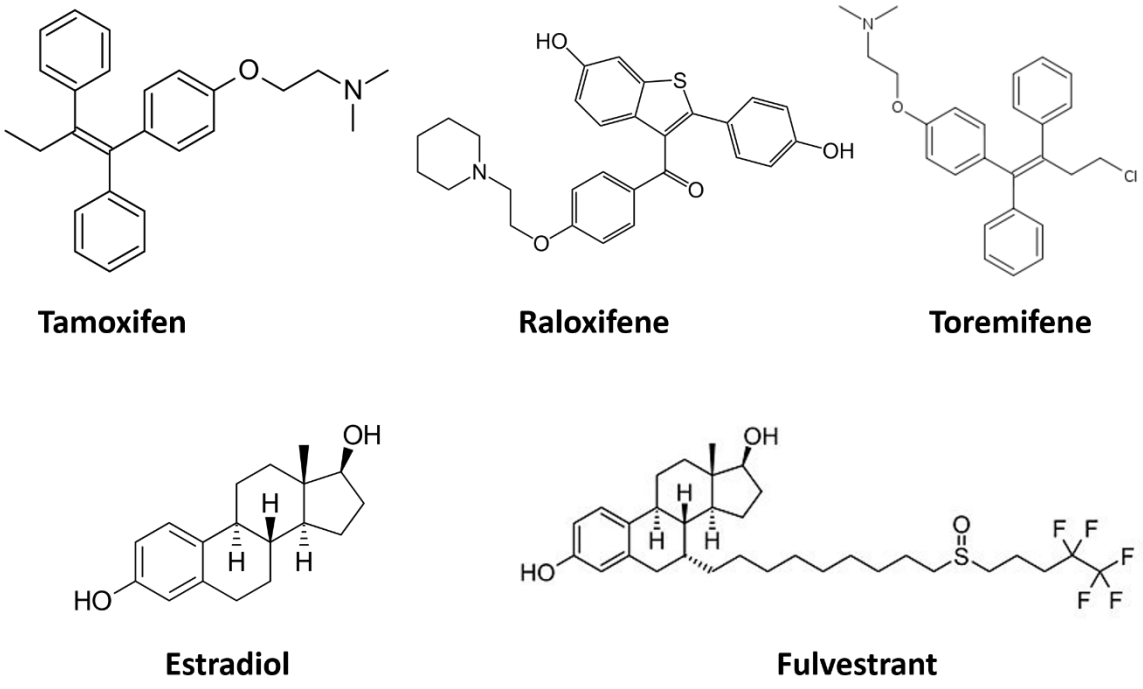

Figure 11: Structure of tamoxifen, raloxifene, toremifene, estradiol and fulvestant.

In general, fulvestrant blocks ERα dimerisation promotes ERα degradation through an accelerated loss of ERα protein. Therefore, due to the reduction of ERα, the whole ERα-mediated signalling pathway, from the cytoplasm to the nucleus, is disrupted and ERα -dependent genes are not expressed (Figure 12).[93]

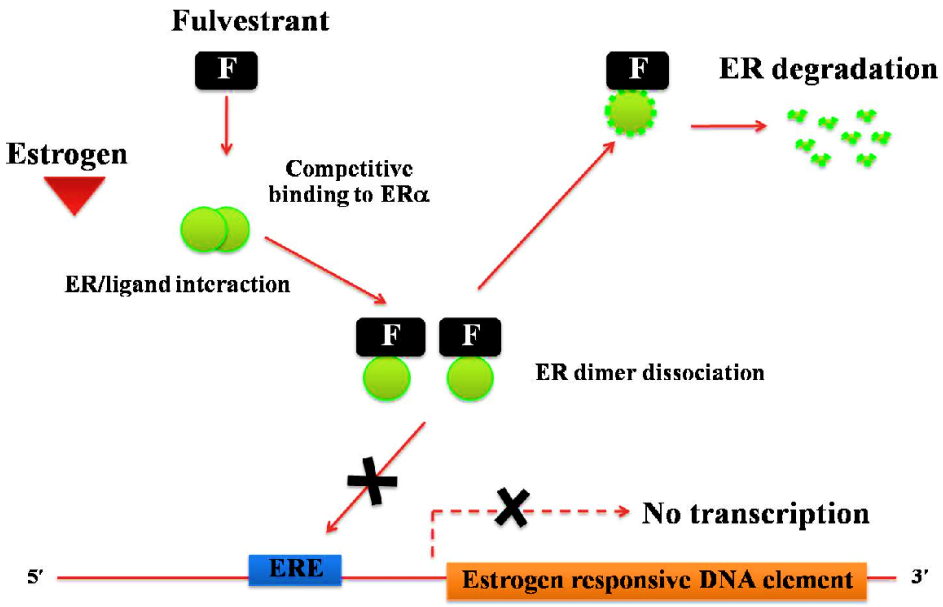

Figure 12: Mechanism of action of fulvestrant (F). Fulvestrant binds competitively to ERα with high affinity. It then acts as an antiestrogen agent by reducing the amount of ERα, resulting in a decrease in the receptor expression. Formation of fulvestrant-receptor complex leads to stabilization of the receptor, which is degraded by a ubiquitin-proteasome complex. The image was adapted with permission from[93], Creative Commons CC-BY-NC-SA 3.0 licence.

It has been shown that fulvestrant may not be sufficient to fully reduce the amount of ERα in some breast cancer patients due to its poor bioavailability.[121] Therefore, the mechanism of action of fulvestrant is currently being studied to inform the development of a new generation of SERDs with higher affinity. The discovery and development of SERDs provide the opportunity to combine anti-ERα treatment for ERα degradation in advanced metastatic breast cancers that are resistant to tamoxifen.[122] Studies have shown that almost 75% of ERα positive breast cancers respond to fulvestrant, tamoxifen, aromatase inhibitors and other hormonal therapies.[123]

1.1.4.2 Anti-HER2 Treatment

Different treatments that target HER2, such as monoclonal antibodies and small oral molecules are currently available.[124] The most used therapeutic agent is trastuzumab, a recombinant humanised monoclonal antibody that inhibits HER2 and blocks the PI3K/Akt and MAPK signal cascades (Figure 13).

Specifically, trastuzumab binds to domain IV of the extracellular segment of the receptor and induces antibody-dependent cell-mediated cytotoxicity (ADCC), including apoptosis, cell cycle arrest, inhibition of angiogenesis and DNA repair.[125] Although trastuzumab has modest activity as monotherapy, its combination with chemotherapy for one year reduces the disease progression and improves patients overall survival.[126] Data from randomised clinical trials have shown that the addition of trastuzumab to chemotherapy regimens improves the symptoms in women with metastatic breast cancer.[127] Clinical trials have demonstrated that one year of trastuzumab treatment provides 50% improvement in disease-free survival and 30% improvement in overall survival.[128] Despite the beneficial effects of trastuzumab on HER2 positive breast cancer patients, trastuzumab resistance is an important issue that causes therapeutic failure.[129] Specifically, more than 35% of patients do not respond to the treatment (primary resistance) while almost 70% are trastuzumab-resistant in the first year of treatment (secondary resistance).[130] Currently, novel versions of trastuzumab are being designed,[131] such as trastuzumab emtansine (T-DM1) an antibody-drug conjugate (ADC) in which trastuzumab is linked to a potent microtubule inhibitor that interrupts microtubules and thereby inhibits cell division.[132] T-DM1 is used in advanced and metastatic HER2 positive breast cancer patients.[133]

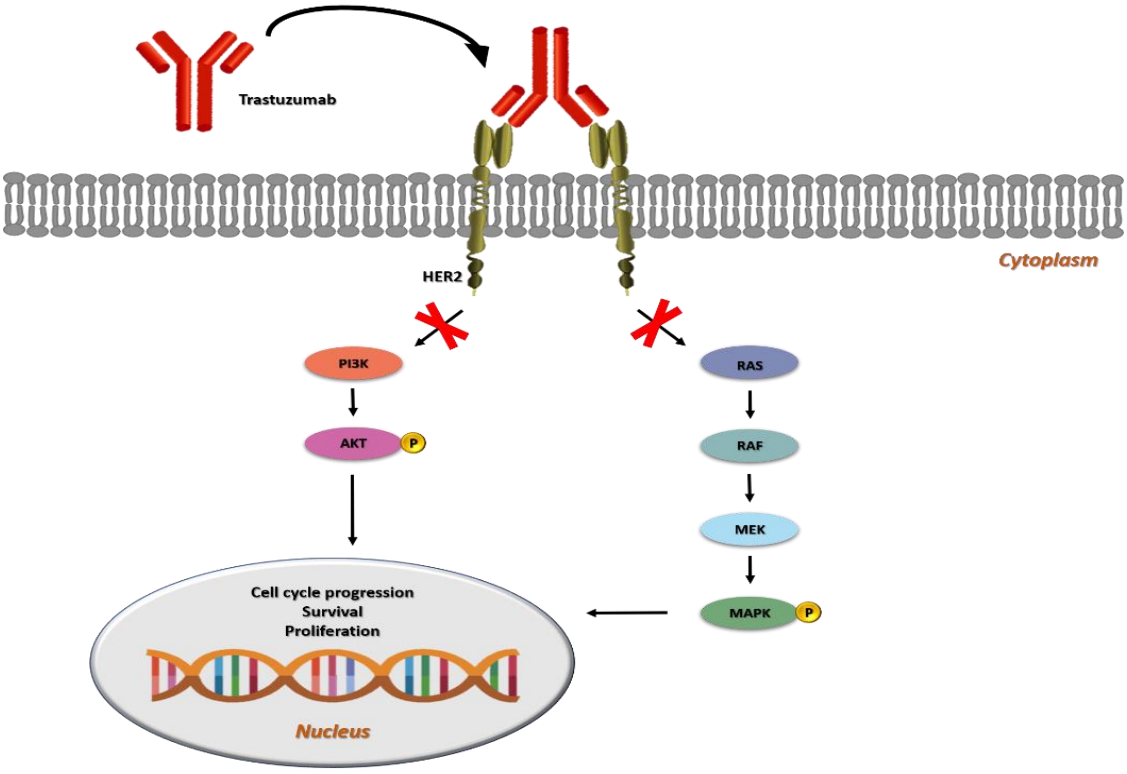

Figure 13: Mechanism of action of trastuzumab. Trastuzumab targets and binds to the extracellular domain of HER2 and prevents the receptor dimerisation and phosphorylation. The blocking of HER2 dimerisation further inhibits the PI3K/Akt and MAPK signalling pathways in the cell. The image was adapted with permission from[276] Copyright 2007, Massachusetts Medical Society.

Pertuzumab is another humanised monoclonal antibody that has been approved by the FDA for use in combination with trastuzumab in HER2 positive metastatic breast cancer. Like trastuzumab, pertuzumab inhibits HER2 activation by blocking its dimerisation, however, it uses a different ligand binding site to trastuzumab.[134] Clinical trials have shown that there is an increase in overall survival of more than 6 months in patients receiving pertuzumab with trastuzumab.[132]

In addition to the HER2 antibodies, HER2 treatment includes the oral tyrosine kinase inhibitors (TKIs), such as lapatinib, afatinib and neratinib. These small molecules compete for the adenosine triphosphate binding domain of the receptor within the cytoplasm preventing its phosphorylation and thereby the downstream pathways. Therefore, they reduce cell proliferation and promote apoptosis. Small molecules, such as lapatinib, that inhibit HER2 have shown promising results

after the relapse of trastuzumab-based treatment.[135] Clinical outcomes have shown that the addition of lapatinib, in combination with chemotherapy or trastuzumab, prolonged the overall survival and reduced the disease progression.[136]

Overall, innovative optical medical imaging approaches should be used to overcome the challenges and limitations of breast cancer diagnosis and treatment. This thesis will introduce the use of nanotechnology as a promising and sensitive analytical tool in biomedical imaging.

1.2 Nanoparticles

Particles that have at least one dimension in the range of 1-100 nm are defined as nanoparticles (NPs).[137] Nanoparticles can have different properties, which are dependent on their size, shape and surface composition.[138] Common shapes include spherical[139], stars[140], rods[141] and hollow[142] nanoparticles. The most commonly synthesised metal nanoparticles include gold (AuNPs)[137], silver (AgNPs)[143] and copper (CuNPs).[144] Each exhibits different physical and chemical characteristics compared to that of their bulk metal. Nanoparticles are attractive candidates for optical imaging due to their small size and large surface to volume ratio, structural robustness, target binding properties and chemically tailorable physical properties.[137]

1.2.1 Localised Surface Plasmon Resonance

The localised surface plasmon resonance (LSPR) of spherical nanoparticles is an optical phenomenon that occurs due to the collective oscillation of electrons at the surface of a nanoparticle that is coupled with the electromagnetic field of incoming light.[145] These oscillations are induced when the light interacts with nanoparticles that are much smaller than the wavelength of the light. Therefore, nanoparticles that are smaller than the wavelength of light fully interact with this incident light and the electron cloud of the nanoparticles is completely displaced by the electric field. Figure 14 shows how free electrons become polarised by the incident light. LSPR is strongly dependant on the size, shape, composition, interparticle distance and the nature of the capping agent of nanoparticles.[146,147]

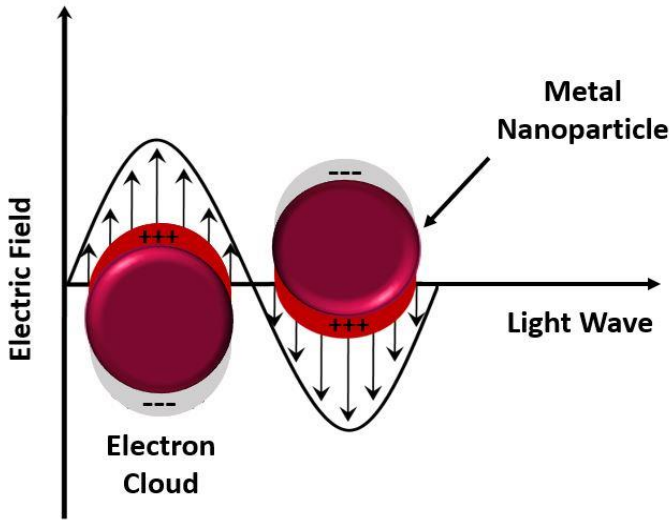

Figure 14: Schematic illustrating LSPR induced by an electromagnetic field interacting with a spherical metal nanoparticle. Coherent collective oscillations of free electrons of metal nanoparticles in response to light are present when the diameter of the nanoparticle is smaller than the wavelength of light.

Spherical AuNPs with a size in the region of 40 nm have a characteristic ruby red colour. As the size of AuNPs increases, the position of the LSPR band changes to a longer wavelength. This process is also known as "red shift".[148] Hence, LSPR change is responsible for the colour change from red to dark purple as AuNPs increase in size. The AuNPs shape, functionalisation with biomolecules and the use of specific solvents can also influence LSPR position. Therefore, any change can affect the colorimetric properties of the AuNPs, since it is dependent on the spectral position of the LSPR.[138]

1.3 Spectroscopy

Spectroscopy is a measure of the interaction of electromagnetic radiation with matter. It is used to determine the structure, functional groups and properties of different compounds. The interaction with the light may give rise to electronic excitations (UV-Vis spectroscopy), nuclear spin orientations (NMR spectroscopy), or molecular vibrations (Raman and IR spectroscopy). Only Raman and IR spectroscopy permit the structural resolution of a compound as the produced spectra are characteristic of the molecular components. Raman spectroscopy is complementary to IR since it measures the scattering rather than absorption of light.

1.3.1 Raman Spectroscopy

When a photon interacts with a molecule, it can distort and polarise the cloud of electrons surrounding the nuclei resulting in the formation of a short-lived, unstable "virtual state". Most of the time, the distortion of the electron cloud does not affect the nucleus and when the molecules relax to the ground state the scattered photons have the same energy as the incident light. This elastically scattered light is known as Rayleigh Scattering[149] However, approximately one in every 10^6–10^8 of the scattered photons will have an energy higher or lower than the incident light.[150] This is due to the photons interacting with the electron cloud of the bonds in the molecule. This weak scattering is described as Raman (or inelastic) scattering and was first experimentally observed by Raman and Krishnan in 1928.[151]

Once the molecule is excited from the ground state to a virtual energy state it can relax into a vibrational excited state. This is called Stokes Raman scattering and the molecule loses energy.[150] At room temperature, most molecules are in the ground state before laser excitation, hence, the majority of Raman scattering observed is Stokes. However, at higher temperatures, a molecule can be already in an excited vibrational energy state and it can return to the ground state with increased energy. This scattering is known as anti-Stokes. The intensity of Stokes Raman scattering is greater than that of anti-Stokes and thus it is employed more commonly in Raman spectroscopy for acquiring spectra (Figure 15).[150]

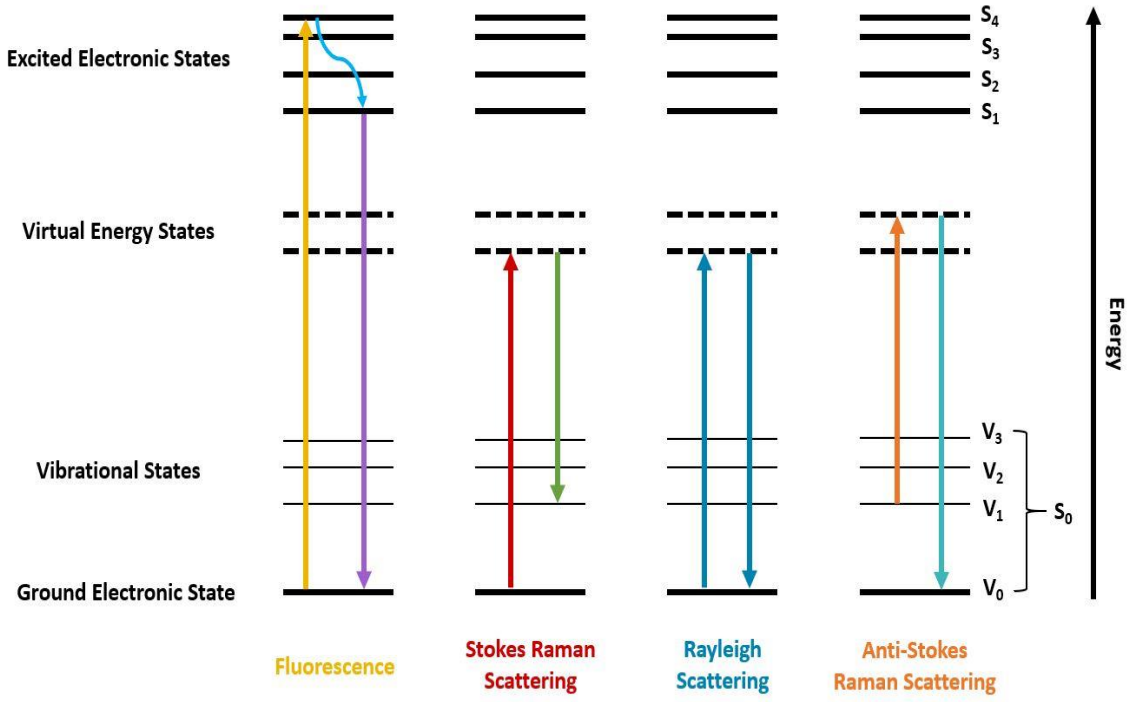

Figure 15: Jablonski diagram depicting typical vibrational and electronic energy levels of a molecule and the interaction with light during the Rayleigh and Raman scattering processes. Upward arrows represent excitation by a light source (laser) while downward arrows represent the resulting emitted photons that can be detected. The length of the arrow is proportional to the photon energy. The competing process of fluorescence is also shown in the diagram.

The Raman shift (cm^{-1}) is the difference between the initial and final vibrational energy levels (v) (Equation 1). The result of this calculation is what is plotted on a spectrum and is termed the Raman shift.

Equation 1: $$v = \frac{1}{\lambda\, incident} - \frac{1}{\lambda\, scattered}$$

Equation 1: Equation for calculation of energy difference between the initial and final vibrational levels (v). In the calculations, λ represents the wavelength of the incident and scattered photons respectively.

The proportion of photons that will be Stokes or anti-Stokes scattered is dependent on the population of the initial vibrational state. The Boltzmann equation (Equation 2) can be used to determine the number of molecules that are in their ground or excited vibrational state. The Boltzmann equation dictates that at room temperature most molecules are in the ground vibrational state before laser excitation. As a result, the majority of Raman scattering observed is Stokes scattering. Anti-stokes occurs at higher temperatures as there is an increase in the number of molecules which are in a vibrationally excited state resulting in increased anti-Stokes scattering.[152,150]

Equation 2: $$\frac{N_n}{N_m} = \frac{g_n}{g_m} \exp\left[\frac{-(E_n - E_m)}{kT}\right]$$

Equation 2: Boltzmann equation. Nn is the number of molecules in the excited vibrational energy levels, Nm is the molecules in the ground vibrational levels, g is the degeneracy of the energy levels, En-Em is the energy difference between the vibrational energy levels, En and Em, k is the Boltzmann constant (1.3807 x 10^{-23}) and (T) is the temperature.

As mentioned before, only 1 in every 10^{6-8} photons is Raman scattered. The Raman scattering intensity (I) is described in Equation 3.

Equation 3: $$I = KI_L\alpha^2 v^4$$

Equation 3: Equation for calculation of Raman intensity (I). K is a constant, I_L is the power of the laser, α is the polarizability and v the frequency.

In Raman, individual chemical bonds give rise to unique vibrations that result in molecularly specific spectra.[151] Therefore, Raman is a structural characterisation technique since it can generate a unique spectra fingerprint for each molecule analysed.[150] This characteristic Raman fingerprint of each chemical structure allows single molecule identification in a sample mixture.[153] Raman spectroscopy is a quick, non-destructive technique that requires minimal sample preparation and it can be carried out in water and in a very small volume.[154] However, Raman spectroscopy provides a relatively low signal intensity. Equation 3 shows that Raman intensity is proportional to the frequency of the laser to the power of four. Therefore, Raman intensity can be

improved by using a shorter excitation wavelength, that has higher frequency/energy.[150] Nevertheless, higher energy may result in sample degradation. Therefore, several approaches can be used to improve the signal intensity of Raman, including resonance Raman scattering (RRS) and surface enhanced Raman scattering (SERS).[150]

1.3.2 Resonance Raman Scattering

Resonance Raman scattering (RRS) signal enhancement is observed when the laser excitation wavelength is tuned to the electronic maxima of a particular molecule.[150] This provides enough energy to excite the electrons to a higher electronic state resulting in the enhancement of Raman signal by a factor of 10^3-10^4. Figure 16 provides a visual depiction of what non-resonance and resonance Raman scattering looks like in terms of energy levels. In contrast to Raman, where the molecule is excited to a virtual energy level, in RRS, excitation by a photon from the laser leads to the molecule being promoted to an excited state within the first excited vibrational electronic state. RRS can be used to obtain both electronic and vibrational information from a chromophore molecule at the same time.[150]

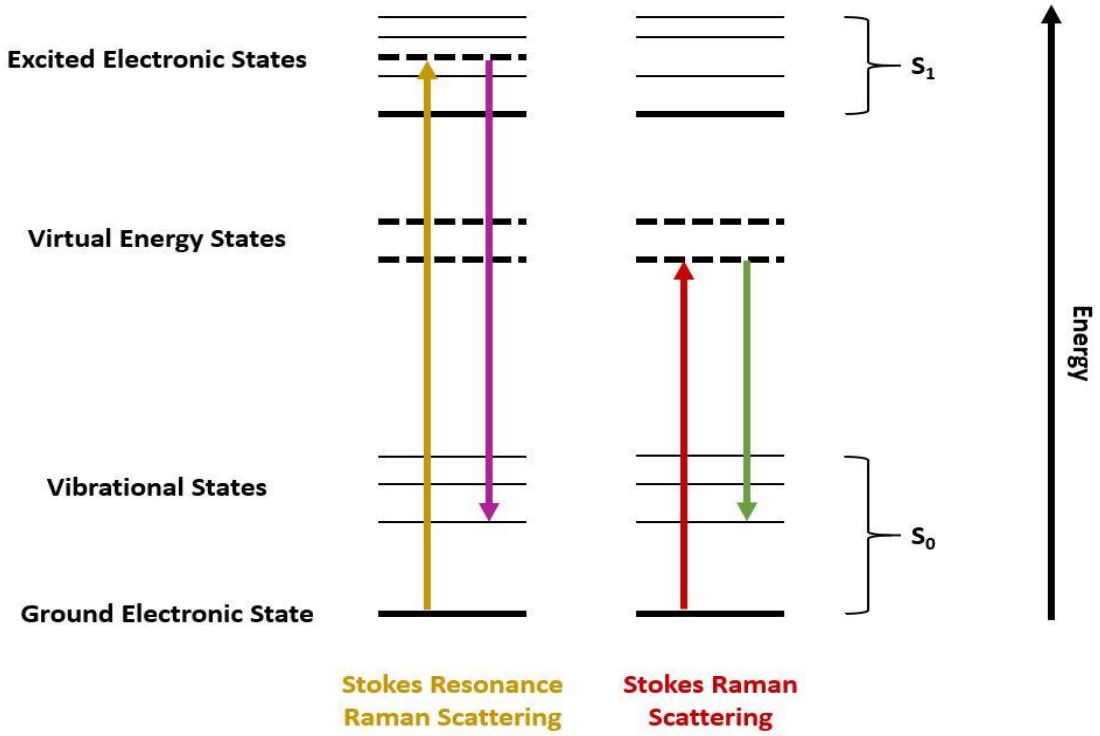

Figure 16: Energy transitions of resonance Raman scattering.

Therefore, RRS is a more sensitive technique than Raman as it allows the selective enhancement of specific bands resulting in simplified spectra that are easier to process.[150] The main limitation of RRS is fluorescence, a competing phenomenon that will obscure Raman peaks due to the unavoidable absorption process that can occur alongside RRS. Sample degradation is also a concern.[150] However, the use of pulsed lasers can minimise the fluorescence occurrence, since fluorescence typical requires more than a nanosecond to be completed while Raman is completed in picoseconds or less.[150]

1.3.3 Surface Enhanced Raman Scattering

Raman signal intensity can be further enhanced when a molecule is adsorbed onto or near a metal surface, leading to an interaction between the surface plasmons and the analyte.[155,156] This phenomenon is known as surface enhanced Raman spectroscopy (SERS). SERS was originally observed by Fleischmann *et al*., in 1974 when an enhancement in Raman signal form pyridine was observed in the presence of a silver electrode[155]. The enhancement factors of SERS are between 10^4 and 10^8 compared to conventional Raman spectra.[157]

Raman signal enhancement can be achieved due to electromagnetic and chemical enhancement, with electromagnetic enhancement playing a much more significant role in the overall signal enhancement. Specifically, when an analyte is adsorbed onto (or in proximity to) a metal surface there is an interaction between the surface plasmon and the molecule. For maximum signal enhancement, the incident laser light is tuned to be in resonance with the metallic nanoparticle surface plasmon. This tuning leads to surface plasmon oscillation, which increases the electromagnetic field surrounding the analyte and causes greater polarisation around the molecule.[150] On roughened metal surfaces, the plasmons oscillate in the perpendicular direction and a greater enhancement is observed.[150] This in turn results in an increase in the scattering from the analyte, resulting in SERS.

The chemical enhancement mechanism does not involve surface plasmons, but it relies on a charge transfer effect. Specifically, after the functionalisation of an analyte to the roughened metal, a charge transfer complex is formed.[150,158] Under these conditions, a series of charge transfer reactions can occur where the charge is transferred from the metal surface to the analyte and then back again before scattering occurs from the metal-analyte complex.[158] The signal intensity is,

therefore, increased via the creation of new electronic states, which arise from bond formation between the analyte and metal surface.[159] Analytes with loosely bound electrons, such as aromatic compounds, have greater sensitivity to charge-transfer interactions.[150] The signal enhancement is dependent on the degree of roughening of the metal surface, for colloidal suspensions of nanoparticles the enhancement is dependent on the chosen metal, the size of the nanoparticles and the surface area. The plasmon resonance of the metal colloids can be adjusted based on the size and shape of the nanoparticle and tuned to the laser excitation wavelength for high enhancement.[160]

Gold[146], silver[161], copper[144] and other metal colloidal suspensions[162] are found to be effective for Raman signal enhancement. The surface enhancement is higher in areas where the nanoparticles are clustered. Therefore, aggregating agents are often added decrease the repulsion energy between the nanoparticles and bring them close together. The clustering creates "hot spots" where a high electric field is generated between the particles which leads to a strong SERS signal.[163]

SERS is an excellent analytical technique for biological applications as spectra can be collected directly from aqueous environments as water exhibits very limited Raman scattering. SERS is a technique that provides sensitivity, selectivity and molecular specificity with reduced sample degradation. Most importantly, SERS spectra are characterised by multiple sharp distinguishing peaks which provide multivariate data and offer multiplex capacities. Therefore, it is possible to simultaneously detect analytes in a sample mixture, without separation steps.[164,165]

1.3.4 Surface Enhanced Resonance Raman Spectroscopy

Surface enhanced resonance Raman spectroscopy (SERRS) was first demonstrated in 1983[166] and it is the result of the combination of surface enhancement (SERS) and chromophore resonance (RRS). SERRS contributes to an enhanced Raman signal of up to 10^{13}-10^{14} over normal Raman scattering.[167,168]

In SERRS, a chromophore (Raman reporter) is adsorbed onto a roughened metal surface and a laser excitation wavelength is used which coincides with an electronic transition in the chromophore (Figure 17). The Raman signal is also maximised when the laser frequency coincides

with the resonant frequency of the surface plasmons on the metal surface. Therefore, the enhancement is an outcome of both surface plasmon resonance and molecular resonance. [150,162]

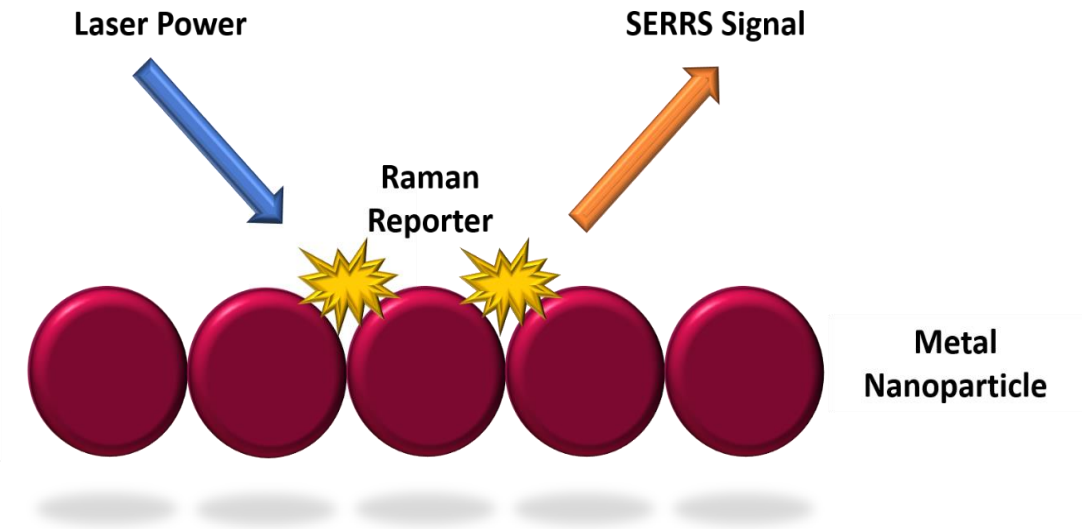

Figure 17: Conceptual illustration of SERRS.

SERRS uses different excitation wavelengths to perform measurements in a single sample, depending on the selected nanoparticle surface and the chromophore. Therefore, SERRS allows greater enhancement and as a result, lower detection limits of the analyte.[169] Additionally, the metal surface helps to quench the fluorescence background from the biomolecule leading to improved spectra and sensitivity.[162,170] Also, SERRS provides a sharp fingerprint spectrum, making it an extremely useful technique for multiplexed applications, compared to fluorescence and chemiluminescence that provide limited structural information and broad emission spectra.[171,172,173] The multiplexing capabilities are achieved when a broader range of chromophores, with different resonant frequencies, are introduced.[174,175] SERRS measurements have also been performed using lasers tuned close to near-IR where increased limits of detection of individual reporters have been observed at picomolar levels.[176,177]

1.3.5 Spatial Offset Raman Spectroscopy

Raman spectroscopy and SERS are two important analytical techniques that generate unique chemical fingerprints of molecules. However, they are often limited to cellular and tissue samples making them unable to detect analytes at depth. In both Raman spectroscopy and SERS, the laser illumination and collection point of the light are coincident. Spatially offset Raman spectroscopy (SORS) is a technique that collects the Raman scattered light at a laterally offset position from the point of the excitation laser spot on sample (Figure 18).[178]

An example of SORS is transmission Raman spectroscopy (TRS) which relies on an extreme spatial offset, where the laser beam and the collection point are on opposite sides of the sample (Figure 18). TRS scattering generates volumetric information and gives specific signals at an unknown location in the whole sample, rather than from different layers within a sample.[179]

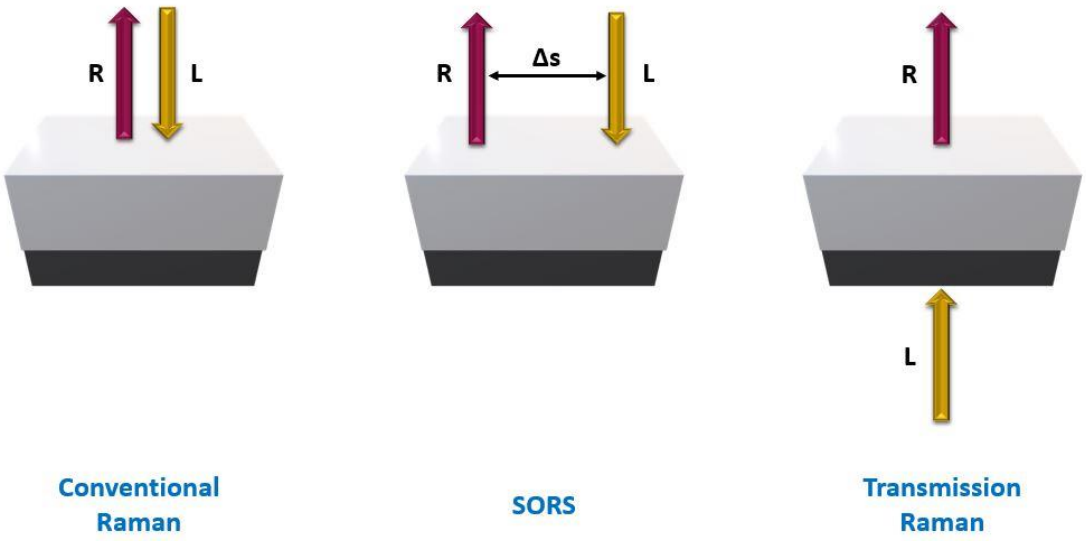

Figure 18: Schematic diagrams of basic Raman spectroscopy modalities: conventional backscattering Raman, SORS and transmission Raman. R- Raman light, L- Laser beam, Δs- spatial offset. The image was adapted with permission from[178] Copyright 2018, Elsevier.

The spectra that are collected in this way exhibit a variation in relative intensities between the contribution from the surface and layers at depth. Such a set of spectra can be numerically

processed to yield the pure Raman spectra of individual sub-layers. Increasing the spatial offset increases the signal contribution from deeper layers such that they gradually outweigh the signal from the top surface material, thereby enhancing the internal signal while attenuating the surface signal. [180,181,179] Therefore, SORS detects deeper photons that are more likely to migrate laterally before they finally reach their point of collection, and diffuse in different directions in comparison to the photons at the surface (Figure 19).[178]

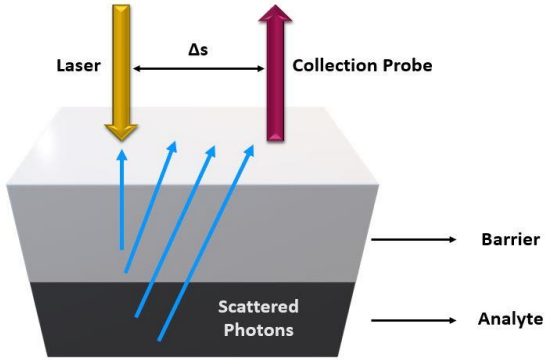

Figure 19: Principal of SORS using a backscattering geometry. As the collection point is moved away from the laser excitation point (Δs) scattered photons from deeper layers start to dominate the acquired spectra. The image was adapted with permission from[178] Copyright 2018, Elsevier.

Based on its characteristics, SORS provides a non-invasive screening tool to obtain Raman spectra and full chemical characterisation of samples at differing depth and thickness.[181] Currently, SORS continues to be developed and has been applied in a multitude of applications in biomedical area including the assessment of bone composition[182] and the analysis of cancerous tissues in breast cancer.[183] SORS spectra can be retrieved through many millimetres which can be used for detection of cancerous tumours[183,184] and disease diagnostics.[179,185] In 2016, Matousek and Stone reported that SORS provides depth penetration of two orders of magnitude higher than conventional Raman.[179] However, a further increase in penetration depth is required to match with the current screening programs, since mammograms can image through approximately 50 mm of tissue.[186] To further enhance the quality of the detected Raman signal intensity, the incident laser power can be increased, however, the safe illumination levels are restricted for application in human studies.[187] Therefore, other methods have been investigated to further increase the depth penetration, such as enhancement of the data processing methods and the combination of SORS with SERS to yield surface enhanced spatially offset Raman spectroscopy (SESORS).

1.3.6 Surface Enhanced Spatial Offset Raman Spectroscopy

SESORS combines the deep penetration capabilities of SORS with the signal enhancing, sensitivity and specificity of SERS.[188] SESORS was first introduced by Stone et. al., who demonstrated that this technique can achieve a greater sample interrogation at significant depth.[188] Although SESORS requires the introduction of SERS nanoparticles or substrates, the sample's readout can be completely non-invasive. The functionalisation of nanoparticles with Raman reporter molecules and/or biomolecules, such as antibodies, allows SESORS signal to be detected at higher depths in comparison to traditional Raman and SERS techniques.[189] SESORS has the potential to provide a multiplexed readout of functionalised SERS nanoparticles with specific molecules that are deeply buried within mammalian tissues. For instance, Stone *et al*., functionalised AgNPs with a NIR active dye and inserted into a tissue sample with 25 mm thickness.[189] A year later, after optimisation of both instrumentation and the choice of the SESORS nanoparticles, a further depth penetration of 45-50 mm in tissue was achieved.[188] This opened up opportunities to use SESORS for imaging and targeting small tumours *in vivo* using functionalised nanoparticles.[168,190] For instance, Nicolson *et al*., reported the detection of 3D breast tumour model buried at depths of 15 mm using SERRS active gold nanoparticles for the first time. The measurements were carried out using a handheld SORS instrument, which shows potential for use in a clinical environment (Figure 20).[191]

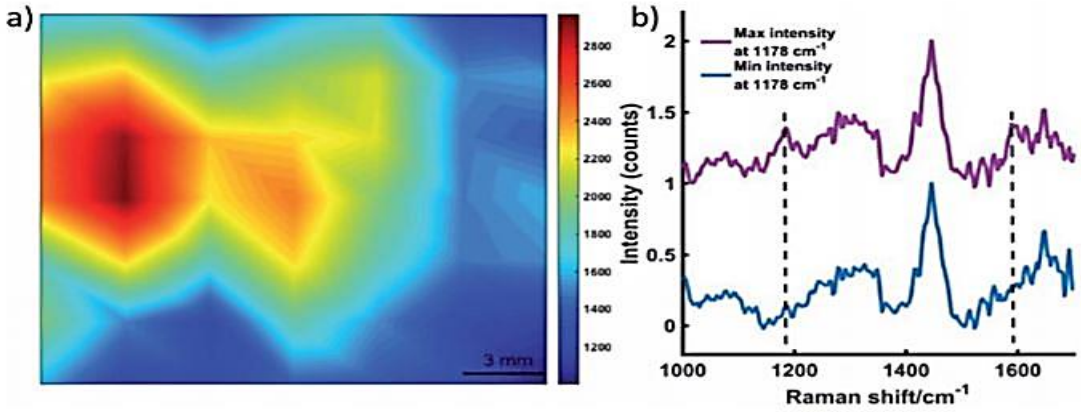

Figure 20: (a) A false colour xy-2D heat SESORRS map of 3D breast tumour model buried at depths of 15 mm in tissue. The map was constructed using the peak intensity at 1178 cm^{-1} (highest peak of the dye used). Measurements were carried out using a xy translational stage at step sizes of 3 mm to create an image of 77 pixels. A combination surface/contour false colour was used to generate a 2D heat map and show the tracking of the 3D breast tumours through 15 mm of tissue. Clear discrimination was seen between spectra collected at the point of maximum intensity where the nanoparticles were uptaken into MTS models were spotted, and that collected where the MTS were not present. (b) The corresponding maximum and minimum collected 8 mm offset spectra. All measurements were carried out using a 2 s integration time, 5 accumulations, 830 nm laser excitation wavelength. The image was reproduced with permission from[191], Creative Commons Attribution-Non Commercial 3.0 Licence.

Additionally, Harmsen *et al*. functionalised AuNPs with chalcogenpyrylium based dyes and a targeting antibody against EGFR to successfully detect tumours using a mouse model *in vivo*.[167] Yuen *et al*. used SESORS for biosensing applications, where SERS nanoparticles were implanted into rats to monitor the glucose concentration in the interstitial fluid.[192] In this method, a SERS implant was first inserted under the skin and analysed using SORS through skin non-invasively. Sharma et.al. investigated the potential of using SESORS for the detection of low-level analytes in brain tissue through skull.[193] Currently, the group have performed SERS measurements to detect serotonin, melatonin and epinephrine neurotransmitters at different concentration followed by SESORS measurements in a brain tissue mimic through the skull.[194] Different studies have also shown that SESORS instruments can detect the nanoparticles at high depth of tissues and bones.[188,189,193]

All these biomedical applications expand the potential for SESORS to be used in future clinical applications. Due to the need of introduction of SERS nanoparticles *in vivo*, SESORS may have potential toxicity issues in the human body. Currently, there are not a lot of studies that have addressed these cytotoxicity effects, therefore, this key issue remains to be addressed.[179] However, SESORS holds notable potential for *in vivo* applications as it can be combined with targeted delivery of nanoparticles for diagnosis and/or treatment, using nanoparticles functionalised with specific biomolecules, such as antibody and drug agents.

1.4 Functionalisation of SERS Nanoparticles for Cellular Delivery

A gold nanoparticle surface can be functionalised with different Raman reporters and biomolecules resulting in the production of novel, selective, sensitive, chemical and biological sensing nanotags for molecular imaging. The Raman reporter functionalised to nanoparticles surface provides a spatial and temporal understanding of the target biomolecule localisation. The Raman reporter can be attached directly to the surface of the nanotags or it can be attached directly to the biomolecule.[195,196] Biorecognition molecules such as antibodies, DNA, proteins and cell penetrating peptides can be attached onto the surface of nanoparticles for biomarker targeting.[197] The reporter and the biomolecules can be attached electrostatically or covalently to the nanoparticle surface.[198] The most common biomolecules used for the nanotags functionalisation are summarised in Figure 21.

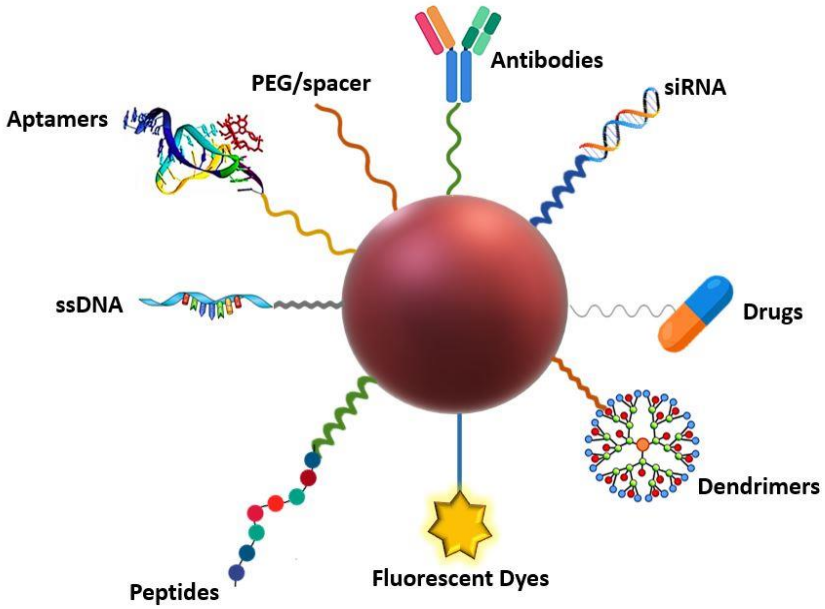

Figure 21: Schematic representation of the nanotags functionalisation with different biomolecules.

When biomolecules are attached to nanoparticles they can interact with overexpressed cell surface proteins potentially resulting in an increased cellular uptake of the nanotags.[199] These surface-bound proteins can activate other intracellular signalling pathways.[200] Antibody functionalised SERS nanotags have been widely used for the detection of specific biomarkers that are overexpressed in cancer cells. These approaches not only can be used as diagnostic tools, but they can also provide important information regarding the disease biochemical processes and progression. Additionally, nanotags can be used to investigate the drug efficacy and its therapeutic effects under different conditions. There is a multitude of SERS applications for biomolecule detection in different tumour environments that will be discussed in section 1.7.

Fundamental aspects, such as the nanotags functionalization, the instrumentation used, and the selection of the appropriate biological model should be taken into consideration when designing SERS nanotags. Poly-ethylene glycol (PEG) and silica can be added to the nanoparticle surface to avoid dissociation of the biomolecules, decrease toxic effects and further help the functionalisation process.[160] Specifically, PEGylation of the nanotags is important for the design of stable nanotags with reduced non-specific binding and longer circulation times in biological fluids.[201,202,203] The coating with PEG must be dense with long hydrophilic polymer chains (2-10 kDa) for a relatively good brush formation.[203]

1.5 Cellular Uptake of Nanoparticles and Delivery Strategies

AuNPs use various endocytic pathways for their cellular uptake. The different internalisation processes of the nanoparticles influence their intracellular fate. Although considerable achievements have been made to understand the cellular uptake of nanoparticles, these studies are mostly based on *in vitro* experiments. Therefore, there is a major need to further investigate the cellular mechanisms used for nanoparticles internalisation in a more *in vivo* representative.

1.5.1 Endocytosis Pathways for Nanoparticles Cellular Uptake

Traditionally, small molecules that are used as drugs enter cells mainly through passive diffusion or active transport. However, it has been shown that nanoparticles usually use the endocytosis pathway for their uptake into specific cell populations.[204] It has been shown that the cell type and the physicochemical properties of the nanoparticles affect the endocytosis pathways. However, there are still processes that have not been fully understood regarding the factors that affect the

uptake of nanoparticles, the role of specific proteins involved in their endocytosis pathways and their intracellular fate. The traditional classification of endocytosis is divided into two categories: phagocytosis and pinocytosis (Figure 22).[204]

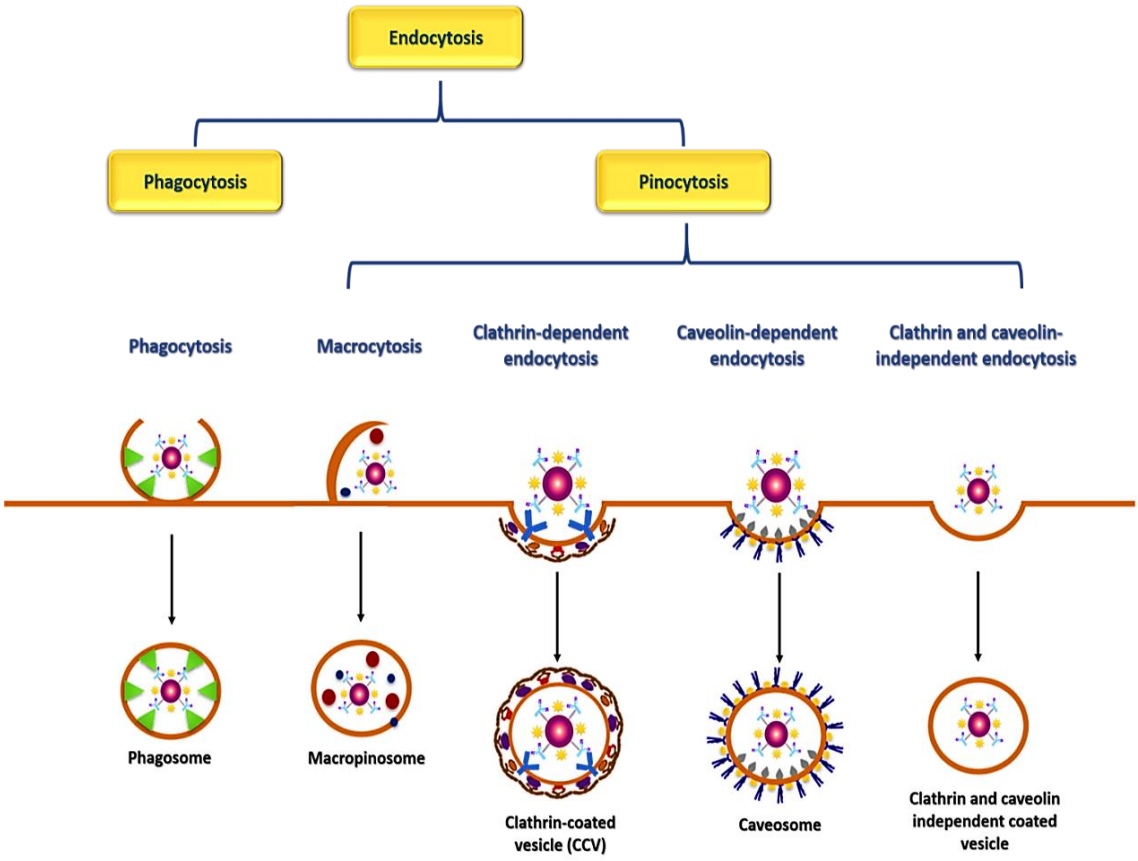

Figure 22: Main pathways for nanoparticle internalisation in mammalian cells. The figure briefly shows the classification of endocytic trafficking and different mechanisms of endocytosis. Larger particles can be taken up by phagocytosis, while fluid uptake occurs by macrocytosis. Most internalised particles are uptaken via clathrin- or caveolin-coated vesicles that are derived from the plasma membrane. The image was adapted with permission from[204] Copyright 2013, Elsevier.

Phagocytosis is associated with the uptake of larger molecules and it is predominantly occurred in phagocytes, such as macrophages, monocytes and neutrophils.[205] Phagocytosis is related to degradation of nanoparticles in the cells. Specifically, for the phagocytosis pathway to occur the nanoparticles bind to the cell surface and form the cup-shaped membrane extension. This

extension is responsible for nanoparticle's internalisation and the formation of phagosomes. (Figure).[204] The phagosomes are usually 0.5-10 μm and they are degraded in the lysosomes.[205]

Pinocytosis is classified into four different forms based on the proteins involved in the pathway: macrocytosis, clathrin-mediated, caveolin-mediated, and clathrin- and caveolae-independent endocytosis (Figure).[204] Macrocytosis is a process that assists in the internalisation of the surrounding fluid by the formation of waving sheet-like extension of the plasma membrane.[206] When these extensions close, they lead to the formation of large organelles called macropinosomes.[203] This is a nonspecific cargo absorption that is not directly driven by the receptor or the cargo associated with it. The macropinosomes are typically heterogeneous in size (from 0.5-10 μm) with an irregular shape when they cleaved off from the membrane.[203] The main difference between macropinosomes with phagosomes is their fate which is dependent on the cell type. That means that macropinosomes can move into the lysosomes for degradation or back to the cell membrane to release their contents outside of the cell.[207]

Clathrin-dependent endocytosis has been observed to be one of the most common pathways for nanoparticle internalisation in mammalian cells.[208] The internalisation is triggered upon the binding of nanoparticles with the transmembrane receptors. This binding leads to the formation of "coated pits" on the cytosolic side of the plasma membrane.[203] The cargo interacts with clathrin-1 which is present in the cytosol. Clathrin-1 is polymerised on the cytosolic side of the membrane when the nanoparticles are internalised.[209] The nanoparticles are then enclosed in the clathrin-coated vesicle (CCV) that is formed using GTPase activity. After its formation, CCV is detached from plasma membrane and it moved inside the cytoplasm (Figure 23).[210]

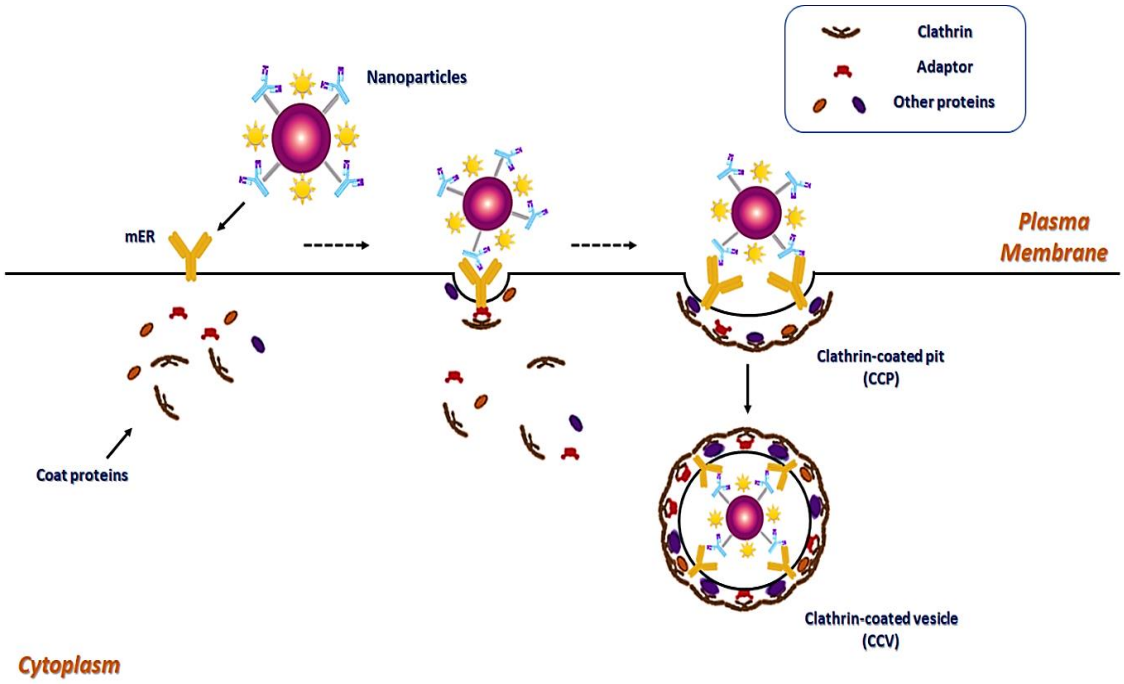

Figure 23: Schematic of clathrin-mediated endocytosis of nanoparticles in mammalian cells. The image was adapted with permission from[210] Copyright 2018, Elsevier.

Caveolae-dependent endocytosis bypasses lysosomes and avoids cargo degradation in contrast to other pathways. It is, therefore, preferred a pathway for bacteria and viruses.[211] Caveolin protein plays an important role for the internalisation as it helps in the formation of the caveolar vesicles, that are cut off from the membrane (Figure).[204] Caveolae-dependent endocytosis pathways take a longer time compared to clathrin-dependent endocytosis, and it usually involves smaller vesicles.[212] After the caveolae-mediated endocytosis, the vesicle, containing the nanoparticles, is delivered to the Golgi complex or endoplasmic reticulum or is extracellularly released.[213]

The clathrin- and caveolae-independent endocytosis is a distinct pathway that relies on specific lipid composition and cholesterol.[204] This endocytic system is GTPase-dependent, but there is still need for further research to deeply understand the later stages of the pathway.

1.5.2 Cellular Endocytosis Inhibitors

Most of the uptake mechanisms can operate simultaneously, therefore, it is challenging to identify a specific endocytosis pathway. To overcome this limitation, endocytic inhibitors, that block a specific part of endocytosis, can be utilised to confirm the pathways that nanoparticles are using for their cellular uptake.[214] Low temperature can also inhibit the nanoparticles' uptake since most of the endocytic pathways are energy dependent. With respect to specific endocytosis, dynasore, potassium depletion and chlorpromazine can be used as endocytosis inhibitors.[215] Dynasore is a cell-permeable inhibitor of dynamin, which is a 100 kDa membrane-remodelling GTPase that plays a crucial role during the clathrin-mediated endocytosis (Figure 24).[216] Specifically, dynamin is essential for the invagination of the cell membrane to form clathrin-coated pits since it assembles into a helical polymer around the phospholipid neck formed by the invagination of the cell membrane. Thus, it is polymerised to form helical structures around the neck of budding vesicles of the plasma membrane and induces membrane scission and the production of free clathrin-coated vesicles.[217]

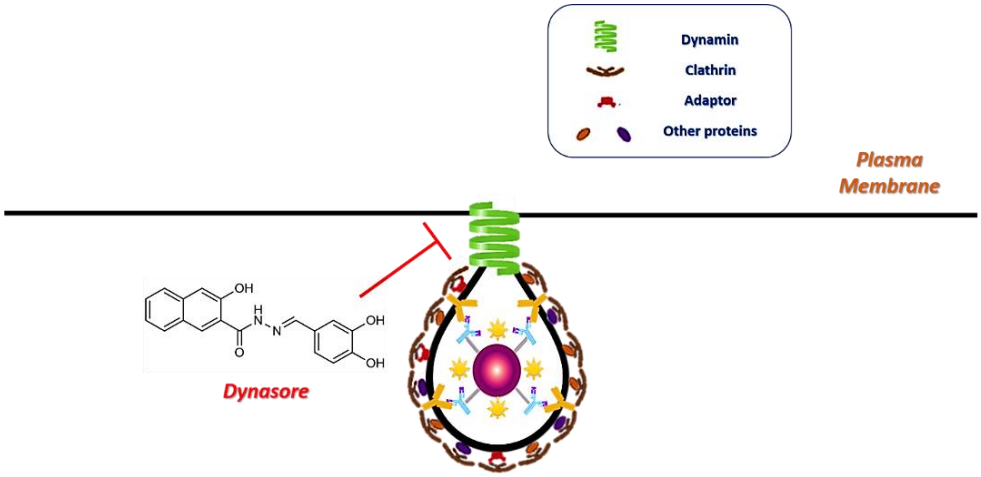

Figure 24: Mechanism of action of dynasore. Dynasore inhibits the GTPase of dynamin, which prevents clathrin-coated endocytosis, including the internalisation of nanoparticles into the cells. The image was adapted with permission from[216], Creative Commons CC-BY-NC-SA licence.

In total there are three isoforms of dynamin with similar functions, dynamin 1, dynamin 2 and dynamin 3. Studies have shown that dynamin 2 plays an important role in the regulation of the ERα-based pathway in breast cancer, such as signalling and degradation.[218] Dynasore is a dynamin 2 inhibitor that rapidly and reversibly blocks dynamin GTPase activity and, therefore,

endocytosis.[219] Specifically, it inhibits the formation of endocytic clathrin-coated pits and vesicles while it does not affect the dynamin-independent functions.[216] This effect can be reversed in approximately 30 minutes after the removal of the inhibitor.[219]

1.5.3 Factors Affecting Endocytosis Pathway Fate of Nanoparticles

The physicochemical characteristic of nanoparticles (size, charge, hydrophobicity, shape), the extracellular matrix environment (ion concentration, pH, temperature) and the cell type determine the endocytic pathway fate of the nanoparticles.[220] The nanoparticle size is a considerable factor that affects their endocytosis pathways.[221] Studies have shown that nanoparticles around 60-100 nm enter the cells using clathrin and caveolae-mediated endocytosis.[222] Additionally, nanoparticles larger than 5 μm are most likely to be engulfed via macrocytosis. The membrane stretching, and its bending energy, may also be involved in why the size of the nanoparticles plays such a critical role in the cellular uptake.

The surface charge of nanoparticles also affects their cellular uptake since cationic nanoparticles show a strong electrostatic interaction with the negatively charged cell membrane resulting in rapid cellular uptake.[223] On the other hand, anionic nanoparticles may interact with the positively charged membrane proteins but they have lower internalisation rate compared to the cationic nanoparticles, due to their repulsive interaction with the cell membrane.[224] Neutral nanoparticles may interact with cells using hydrophobic and hydrogen bonding interactions at physiological pH[225], however, they show no specific preference for their endocytosis fate.[204]

The shape of the nanoparticle also influences their cellular uptake since spherical nanoparticles have a significant advantage over nanorods due to their characteristic dimension that interact more efficiently to the surface receptors.[226,227] Finally, the cell type will affect the endocytic fate due to the presence of specific proteins on their surface that result in preference of selected pathway. For example, HepG2 cells have no endogenous caveolin, therefore, they are not able to use caveolae mediate endocytosis for nanoparticle uptake.[228] The overexpression of proteins and hormones in cancer cells brings distinct differences in the endocytic pathways between normal and cancerous cells.[229]

1.6 Nanoparticles and Cell Toxicity

There is a strong interest in exploiting nanoparticles for medical purposes, therefore, there is an increased the number of studies investigating their possible cytotoxicity effects.[230,231] In general, the cellular uptake of nanoparticles can cause a wide range of biological responses such as the formation of reactive oxygen species (ROS)[232], increased production of specific cytokines[233] and appearance of apoptotic and inflammatory markers.[234] AuNPs are noble metal particles, and are recognized as nonbiodegradable and inert.[235] Although AuNPs safety is dependent on many factors, such as their physicochemical properties, the coating agent, the cell incubation conditions and the cell type, it has been shown that functionalised AuNPs show lower toxicity in biological systems compared to other metal nanoparticles.[236,237] For this reason, functionalised AuNPs are preferred for *in vitro* and *in vivo* applications. Currently, AuNPs have been approved to be used by clinicians as a drug-delivery system.[238] Additionally, it has been shown that the functionalisation of AuNPs can further decrease their toxicity since there is a reduced interaction between the metal surface of the nanoparticles with the surrounding biological environment.[239] Specifically, the addition of PEG is widely used as a nanoparticle surface coating since it is a very biocompatible polymer that inhibits intracellular degradation, and thereby reduces cell toxicity.[240] Xie *et al*. found that PEGylated gold nanoparticles showed no aggregation in cell culture which decreased the potential of cellular toxicity from the nanoparticles.[241] Connor *et al*. showed that citrate coated AuNPs uptaken by human leukaemia cells did not cause any acute cytotoxicity.[242] Qu *et al*. investigated 20 nm spherical citrate coated AuNPs and showed they were non-toxic, even at 300 μM, in a human dermal fibroblast fetal cell line.[243] Additionally, no induction of oxidative stress markers and inflammatory cytokines were observed in human alveolar epithelial-like cells incubated with 15 nm AuNPs using RT-PCR and ELISA analysis.[244]

1.7 SERS Applications in Healthcare

The numerous advantages of SERS have been utilised for sensing, targeting, delivery and imaging biomolecules.[245,246] In contrast to fluorescence, SERS offers sharp molecularly specific spectra, that allow multiplexed detection opportunities with high sensitivity and selectivity.[247] Additionally, using SERS, it is possible to gain information regarding a biomolecule distribution and cellular localisation using two-dimension (2D) and three-dimension (3D) SERS cell

mapping.[248,249] Therefore, SERS has become an invaluable analytical tool that is widely used for *in vitro*, *ex vivo* and *in vivo* applications.

1.7.1 SERS and *In Vitro* Applications

In vitro analysis using SERS is vital for understanding the molecular pathways before moving towards the *in vivo* applications. There are different experimental approaches that highlight the vast capabilities of SERS *in vitro*. Most of the researches involve the detection of DNA or protein that are disease related for characterising healthy and non-healthy cells.[164] Specifically, there are many *in vitro* cell culture studies that use SERS nanotags for the detection of cancer biomarkers allowing cancer phenotyping.[250,251,252] Lee *et al*. performed optical imaging of human embryonic kidney cells (HEK293) expressing the PLCγ1 biomarker using bimetallic gold-silver nanoparticles and SERS. The functionalisation was achieved by coating silver layers over Raman reporter (R6G) labelled gold nanoparticles and the bimetallic nanoparticles were then labelled with secondary antibodies and used for biomedical SERS imaging. SERS imaging was found to be more sensitive compared to fluorescence (Figure 25).[250]

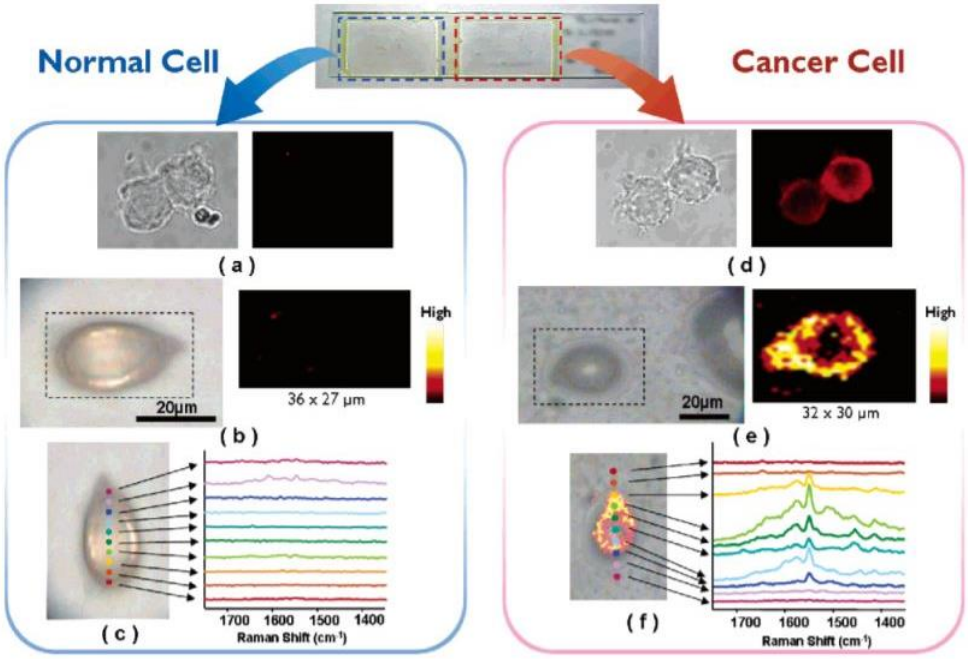

Figure 25: Fluorescence and SERS images of normal HEK293 cells and PLCγ1-expressing HEK293 cells. **(a)** Fluorescence images of normal cells: (left) brightfield image, (right) fluorescence image. **(b)** SERS images of single normal cell: (left) brightfield image, (right) Raman mapping image of a single normal cell based on the 1650-cm^{-1} (R6G highest peak). **(c)** Overlay image of brightfield and Raman mapping for a single normal cell. Colourful spots indicate the laser spots across the middle of the cell along the y-axis. **(d)** Fluorescence images of cancer cells: (left) brightfield image, (right) fluorescence image. **(e)** SERS images of a single cancer cell: (left) brightfield image, (right) Raman mapping image of a single cancer cell based on the 1650-cm^{-1}. **(f)** Overlay image of brightfield and Raman mapping for single cancer cell. Colourful spots indicate the laser spots across the middle of the cell along the y-axis. The image was reproduced with permission from[250] Copyright 2007, American Chemical Society.

A few years later, Lee *et al*. investigated the use of antibody conjugated hollow gold nanospheres, as imaging agents, for the detection of HER2 biomarker in cancer using SERS. The nanospheres were observed in modified MCF-7 cells using a crystal violet Raman reporter.[251] Furthermore, three dimensional (3D) *in vitro* cell cultures have recently be used for SERS imaging.[253,254] These 3D cell models provide a more realistic *in vivo* environment without the ethical considerations required for using animal models and *ex vivo* samples. These applications demonstrate the potentials of using SERS for highly sensitive imaging of cancer biomarkers *in vitro*.

1.7.2 SERS and *Ex Vivo* Applications

SERS can be used *ex vivo* as an excellent tool for the detection of biomolecules in body fluids and tissue samples with high sensitivity. For the *ex vivo* biofluids, whole blood, serum and isolated red blood cells are usually analysed. Most SERS assays detect the signal from Raman reporter attached on the nanoparticles. The nanoparticles have also been functionalised with specific biomolecules that target proteins and oligonucleotide sequences.[197,255] The detection of viral and bacterial DNA sequences are important tools in molecular biology for disease diagnosis. In 1998, it was reported for the first time the use of PCR, in combination with SERS, for detecting the human immunodeficiency virus *gag* gene (HIV detection).[256] Additionally, Graham *et al.* conducted a multiplexed detection of two different DNA sequences in a single assay with SERRS.[257] Faulds *et al.* managed to detect five different oligonucleotide sequences in a mixture of all species using dye labelled DNA nanoparticles and two excitation wavelengths.[171] Finally, Gracie *et al*. demonstrated the first approach of detection and quantification of three meningitis pathogens within a single multiplex assay.[172]

SERS nanoparticles have been used in place of fluorescent dyes to increase the multiplexing and sensitivity capabilities. The first SERS based immunoassay was reported in 1989.[258] Since then, there have been many approaches for the detection of antigens. Wang *et al.* demonstrated a SERS method to detect and quantify four target antigens while Dou *et al*. established an ELISA approach, using SERS for enzyme detection and measurement.[259,260] *Ex vivo* tissue bioanalysis is a new method that involves the use of SERS nanoparticles, as diagnostics, for the recognition of disease biomarkers in tissue sections and excised tissue samples.[261,262] In 2008, Lutz *et al*. demonstrated a method of imaging formalin fixed paraffin embedded tissue sections using SERS for the detection of two cytokeratin-18 and prostate specific antigen (CK-18 and PSA).[263]

1.7.3 SERS and *In Vivo* Applications

Recently, many *in vivo* scientific approaches have been developed using functionalised SERS nanoparticles with biomolecules that bind to disease biomarkers. Similar to *in vitro* and *ex vivo* applications, *in vivo* SERS permits multiplexed detection of biomarkers by using nanoparticles with different bio-recognition molecules and Raman reporters. One of the first *in vivo* applications

was carried out in 2008 where Qian *et al.* functionalised nanoparticles with single-chain variable fragment (ScFv) antibodies to target EGFR in different cancers (Figure 26).[168]

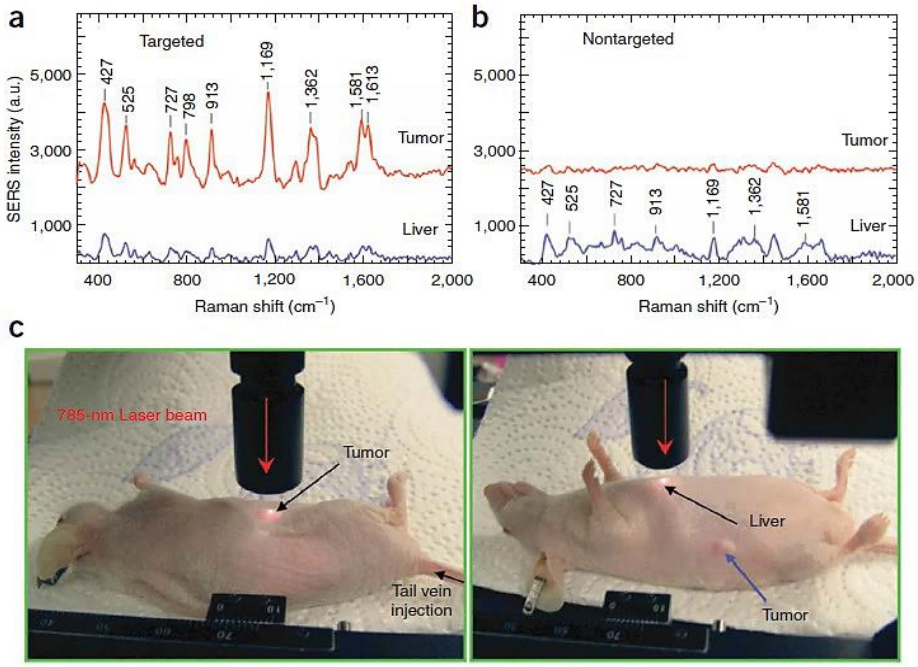

Figure 26: *In vivo* cancer targeting using SERS with ScFv-antibody conjugated gold nanoparticles that target EGFR tumour biomarker. (a,b) SERS spectra obtained from the tumour (red) and the liver (blue) areas by using targeted (a) and non-targeted (b) to EGFR conjugates. Two nude mice bearing human head-and-neck squamous cell carcinoma (Tu686) xenograft tumour (3-mm diameter) received 90 μL of ScFv EGFR-conjugated SERS tags or pegylated SERS tags (460 ρM). The particles were administered via tail vein single injection. SERS spectra were taken 5 h after injection. (c) Images showing a laser beam focusing on the tumour site or the anatomical location of the liver. *In vivo* SERS spectra were obtained from the tumour site (red) and the liver site (blue) with 2-s signal integration and at 785 nm excitation. The spectra were background subtracted and shifted for better visualisation. The Raman reporter molecule is malachite green, with distinct spectral signatures as labelled in a and b. Laser power, 20 mW. The image was reproduced with permission from[168] Copyright 2007, Springer Nature.

Another study verified that functionalised nanoparticles showed greater affinity for the tumour after injection into the tail of xenograft tumour-bearing mice models in comparison to the non-functionalised ones.[264] Wang *et al*. worked on the functionalisation of nanoparticles with three

different antibodies: anti-HER2, anti-EGFR and an isotype control. The nanotags were tested *in vivo* into two different tumour types with a varied expression of HER2 and EGFR. After the topical administration of the nanoparticles, the tumours were implanted and were analysed using SERS. The results showed the potential of simultaneous detection and ratiometric quantification of the targeted nanoparticles for the assessment of the molecular expression of cancer.[265]

Nanoparticles have also been used for the diagnosis of other diseases *in vivo*, such as the indication of atherosclerosis and inflammation.[266] Recently, Noonan *et al*. reported the targeted *in vivo* imaging of different vascular inflammatory biomarkers, using SERS and antibody-functionalised nanoparticles to assess localised vascular inflammation. Specifically, the team designed a series of antibody-functionalised gold nanoparticles (BFNP) for the detection of vascular cell adhesion molecule 1 (VCAM-1), intercellular adhesion molecule 1 (ICAM-1) and P-selectin. SERS showed that VCAM-1, ICAM-1 and P-selectin were detected, discriminated and quantified both *in vitro* in human endothelial cells and *in vivo* in humanised mouse models, demonstrating the capabilities of SERS as a potential clinical imaging technique.[267]

1.7.4 SERS Applications in Breast Cancer

Different experimental approaches have been carried out, using SERS nanoparticles for breast cancer detection. Moisoiu *et al*. used SERS as a diagnostic tool for breast cancer detection by testing 53 people with, and 22 people without, breast cancer. The SERS spectra were acquired using silver nanoparticles on a urine sample from the subjects. The nanotags were then activated by adding $Ca(NO_3)^2$ to promote the specific adsorption to the silver surface of the anionic purine metabolites such as uric acid, xanthine and hypoxanthine. A droplet of the sample was analysed by Raman spectroscopy in liquid form. The results showed that the SERS spectra of urine from breast cancer patients could be distinguished from the healthy subjects with 81% sensitivity, 95% specificity and 88% overall accuracy.[268] Cervo *et al*. used SERS spectroscopy of serum to detect breast cancer at different stages from a group of 60 participants. The subjects were separated into three groups based on their clinical condition: healthy women, women with localised small breast cancer and women with breast cancer that also had lymph node involvement. Using linear discriminant analysis (LDA) and principal component analysis (PCA), the group managed to distinguish the healthy from the breast cancer subjects with 92% sensitivity and 85% specificity. Additionally, participants with different breast cancer stage were separated with 84% overall

accuracy making this approach a promising diagnostic tool.[269] Allain and Vo-Dinh exploited SERS to screen DNA hybridisation of fragments of BRCA1, a gene that its mutation is related to breast cancer development, this a potential breast cancer screening test.[270]

Additional studies have been carried out where SERS nanoparticles were functionalised with antibodies to characterise breast cancer. Specifically, Davis *et al*. synthesised CD47 antibody labelled SERS nanoparticles against CD47, a cell surface receptor overexpressed in several cancers. Fluorescence assisted cell sorting (FACS) was used to assess the binding potential of conjugates on different human breast cancer cell lines. The results from the mouse xenograft model of human breast cancer showed that the SERS nanoparticles actively bound to CD47 on breast cancer cells (Figure 27).[271] These findings further open the potentials of topically applying SERS nanotags to breast cancer for detection of CD47 marker during lumpectomy.[271]

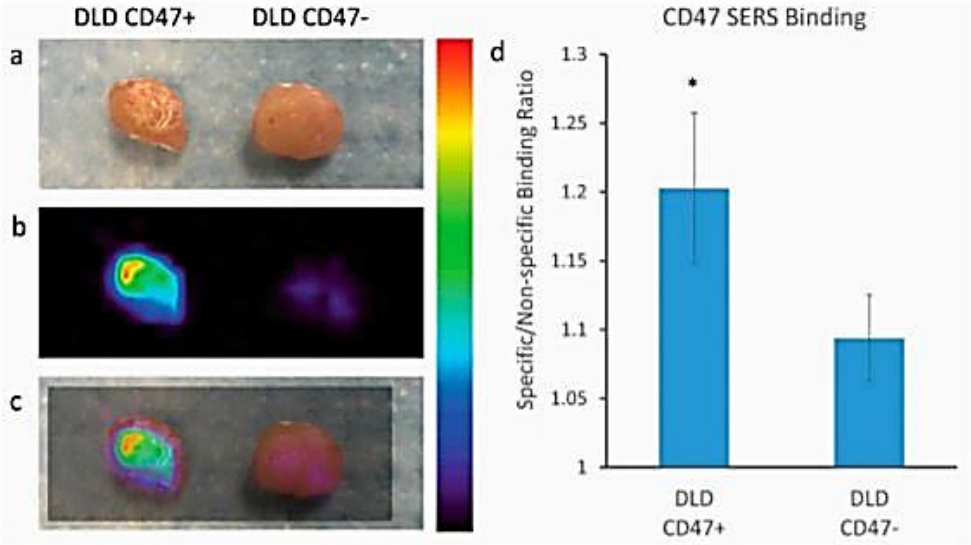

Figure 27: Raman imaging of positive and negative CD47 expressing tissues harvested from mouse xenograft. (a) Digital photo of tissue after nanoparticles administration; (b) Raman imaging of tissues; (c) overlay of Raman imaging with tissue sample; (d) quantitative ratiometric analysis of specific CD47 SERS nanoparticles binding to non-specific isotype IgG SERS nanoparticles binding on the tissue sample. The image was reproduced with permission from[271], Creative Commons CC-BY 4.0 licence.

Wang *et al*. demonstrated that the topical application and quantification of differently functionalised SERS nanoparticles enables the rapid quantitative molecular phenotyping of the surface of breast cancer tissue to determine the presence of malignant cells. The SERS results were achieved in less than 15 minutes and they agreed with the immunohistochemistry and flow cytometry data which open up the potential use of this approach in guiding breast-conserving surgeries.[272] Lee *et al*., used SERS to test breast cancer phenotype by identifying the epidermal growth factor (EGF) and insulin-like growth factor-1 (IGF-1) proteins in the KPL4, MDA-MB-468 and SKBR-3 human breast cancer cell lines. This experimental approach additionally confirmed that SERS may be used for earlier breast cancer diagnosis and for the guidance of the treatment.[252] Dinish *et al*. have also shown the *in vivo* detection of EGFR, TGF beta II (TGFβII) and CD44 biomarkers using antibody functionalised nanoparticles. The functionalised nanoparticles were shown to remain in the body of mice for up to 48 h before clearing after 72 h. On the other hand, the non-functionalised nanoparticles were cleared within 6 h and no signal from their reporters was observed after 24 h.[273] Qian *et al*., used PEGylated gold nanoparticles, with ScFv antibodies, a ligand that binds to epidermal growth factor receptor (EGFR) with high specificity and affinity, for *in vitro* and *in vivo* tumour targeting. The group proposed that the SERS nanotags were able to detect deep tumours with specificity, selectivity and low toxicity.[168] Xia *et al*. used SERS to image EGFR on single breast cancer cells. The researchers incubated the SERS nanoparticles, that were functionalised with an anti-EGFR antibody, in the EGFR over-expressing A431 breast cancer cell line. SERS results confirmed the immunoblot data regarding the EGFR levels and revealed that the SERS nanotags were located primarily at the cell surface, which adds new insights regarding EGFR localisation in cells which is not possible using the immunoblot method.[274] These experimental approaches contribute to the translation of SERS in the clinical setting and highlighted the potential use of SERS as a novel tool for screening of breast cancer.

SERS has also been used for targeted photothermal therapy in breast cancer. Feng *et al.* developed a theranostic SERS probe for early diagnosis and treatment of breast cancer. The team synthesised gold bipyramidal-shaped nanoparticles to specifically detect and kill MCF-7 breast cancer cells using SERS and the photothermal properties of metal nanoparticles. The sharp tips of the nanotags provided sensitivity for *in vitro* detection of MCF-7 cells and *in vivo* SERS imaging of MCF-7 tumour. This is another experimental verification that SERS nanotags can be promising candidates for the detection and photothermal enhancement of chemotherapy for breast cancer.[275]

1.8 Introductory Conclusions and Project Aims

The characterisation of biomarkers using antibody functionalised gold nanoparticles (AuNPs) is an area of intense interest in the biomedical spectroscopy community. SERS can provide an advanced imaging tool for the investigation of the presence of different biomarkers *in vitro*, *ex vivo* and *in vivo*. To date, few reports have investigated the full potentials of SERS nanotags in different biological environments. Therefore, the main aim of this thesis is to explore the capabilities of anti-ERα antibody functionalised AuNPs (ERα-AuNPs) for the detection of ERα using 2D and 3D breast cancer tumour models.

Specifically, non-destructive 2D and 3D SERS mapping will be used to track the cellular uptake and localisation of ERα-AuNP nanotags in MCF-7 breast cancer cells under different endocytosis inhibition conditions. This study will address the role of nanotag functionalisation in biological environments and will highlight the benefits of using 3D SERS for the investigation of the cellular uptake of nanotags compared to other destructive, time-consuming and expensive techniques such as immunofluorescence. This thesis also aims to investigate how ERα-AuNP nanotags can be utilised to phenotypically characterise and classify breast cancer cells with different ERα expression status. It will also investigate the benefits of using SERS for investigating efficacy of the drug fulvestrant, the first-in-class approved selective estrogen receptor degrader (SERD), compared to other techniques.

Moreover, this work will explore the combination of SERS with microfluidic devices for the detection of ERα in live 3D breast cancer tumour spheroids. In parallel, it will highlight the benefits of using live 3D breast tumour models as a more representative *in vivo* model for breast cancer characterisation and understanding of fulvestrant efficacy.

Finally, this thesis will investigate the detection of ERα *ex vivo* and *in vivo* at high depths, by combing SERS with SORS (SESORS). Specifically, live 3D breast cancer spheroids and live mice will be used to detect and track targeted nanotags at high tissue thicknesses using SERS and SESORS. This work will address the suitability of handheld Raman and SORS spectrometers for imaging tumour models and will highlight the potentials of using SERS and SESORS as powerful techniques in the field of biomedical imaging and disease detection.

2. Investigation of Cellular Uptake Mechanism of Functionalised Gold Nanoparticles into Breast Cancer Cells Using SERS

Contributing authors:

Anastasia Kapara[1,2], Valerie Brunton[2], Duncan Graham[1], Karen Faulds[1]

1. Centre for Molecular Nanometrology, Department of Pure and Applied Chemistry, Technology and Innovation Centre, University of Strathclyde, 99 George Street, Glasgow G1 1RD, UK.

2. MRC Institute of Genetics and Molecular Medicine, Edinburgh Cancer Research UK Centre, University of Edinburgh, Western General Hospital, Crewe Road South, Edinburgh, EH4 2XU, UK

2.1 Abstract

Gold nanoparticles (AuNPs) have been widely used in different applications such as in cancer imaging, drug delivery and photothermal therapy. The functionalisation of AuNPs has been shown to affect their cellular internalisation, accumulation and targeting efficiency. The mechanism of cellular uptake of functionalised AuNPs by different cancer cells is not well understood. Therefore, a detailed understanding of the molecular processes is necessary to improve AuNPs for their selective uptake and fate in specific cellular systems. This knowledge can greatly help in designing nanotags with higher cellular uptake for more selective and specific targeting capabilities with less off-target effects. Here, we demonstrate for the first time a straightforward and non-destructive 3D surface enhanced Raman spectroscopy (SERS) imaging approach to track the cellular uptake and localisation of AuNPs functionalised with an anti-ERα antibody and a Raman reporter, 1,2-bis(4-pyridyl) ethylene (BPE), in MCF-7 ERα-positive human breast cancer cells under different cellular endocytosis inhibition conditions. 3D SERS enabled information rich monitoring of the intracellular internalisation of SERS nanotags. It was found that the ERα-AuNPs were internalised by MCF-7 cells in a temperature-dependent manner suggesting an active endocytosis-dependent mechanism, rather than passive pathway diffusion. The 3D SERS cell mapping experiments suggested that the nanotags entered the cells using dynamin dependent endocytosis, as incubation with dynasore, a dynamin inhibitor, resulted in a SERS signal being obtained close to the cell surface rather than inside the cells indicating that the nanotags accumulated in the plasma membrane. Finally, a lower number of ERα-AuNPs were found to enter the cells after pre-blocking with an anti-ERα antibody. Therefore, this study indicates that the nanotags were internalised into MCF-7 cells using an ERα receptor-mediated endocytosis process. This study addresses the importance of SERS nanotags' functionalisation in biological environments and highlights the benefits of using 3D SERS for the investigation of cellular uptake processes.

2.2 Introduction

Gold nanoparticles (AuNPs) have been extensively investigated as tools for sensing and tracking of biomedically important cellular markers in a broad range of applications including *in vitro*[1] and *in vivo*[2,3] imaging. The effective design of AuNPs, for dynamic cell imaging and biocompatibility, requires careful consideration of their fundamental cellular uptake interactions within living systems. In general, these investigations include different studies to determine the amount and location of internalised nanotags and they are usually conducted in conjunction with viability and inhibition studies that block individual cellular uptake mechanisms.[4]

The intracellular uptake and fate of AuNPs are dependent on different factors, such as their physicochemical characteristics[5,6,7] and the experimental procedures, including incubation time and Au NP concentration.[8,9] The functionalisation of AuNPs with targeting biomolecules greatly affects their trafficking behaviour and their cellular localisation.[10] The binding of biomolecule functionalised AuNPs to their cellular targets increases the accumulation of the AuNPs in the cell and minimises exocytosis processes.[9,11,12] Antibody-conjugated nanoparticles have been shown to have increased cellular uptake[13] due to the presence of the antibodies on the nanoparticle surface affecting the nanoparticle-cell interactions, leading to enhanced signals and long-term tracking of antigen expression in the cell.[14]

Different uptake mechanisms exist for the cellular internalisation of AuNPs including phagocytosis, micropinocytosis, clathrin- and caveolae-dependent and clathrin- and caveolae-independent endocytosis.[15] Endocytosis involves the formation of new intracellular membrane-enclosed vesicles from the cell membrane with a concomitant internalisation of the cargo along with other proteins, lipids and extracellular fluids.[15] It has been shown that the energy-dependent endocytosis pathways, rather than passive diffusion, are the main mechanisms that cell lines use for nanoparticle uptake.[16,17] Specifically, receptor-mediated endocytosis (RME) is known to be one of the main uptake pathways for AuNPs. For RME, the biomolecules attached to the AuNP surface bind to the extracellular surface of the plasma membrane receptor and membrane fusion is induced. This membrane enfolding leads to the formation of an endosome, which allows the cell to carry the cargo into the cytosolic region.[18,19] RME involves the participation of other proteins, such as clathrin or caveolae, for the cellular internalisation mechanisms.[20,21]

Traditionally, transmission electron microscopy (TEM)[22] and fluorescence microscopy[23,24] have been used for investigating cellular uptake and localisation of nanoparticles in cells. However, TEM is a destructive and expensive technique that requires microtoming of the cells with long and complicated sample preparation. Also, the fluorophores that are required to stain cells for fluorescence imaging are prone to photobleaching making 3D imaging challenging since bleaching can compromise the definition of 3D structures leading to false results.[25] Additionally, fluorescence generates broad emission bands that makes the detection of multiple components within the same sample challenging.[26]

Therefore, high-resolution optical imaging has gained increasing importance, providing clear evidence of nanotag cellular uptake and localisation in a non-destructive fashion. Surface enhanced Raman spectroscopy (SERS) is a non-destructive method that can study the interactions of nanotags with biological environments with various advantages, such as high sensitivity, selectivity and multiplexing capacities, without the need for fluorogenic staining.[1,27] Recently, nanoparticle-based SERS approaches have been conducted to map the intracellular distribution of different molecules in fixed[28,29,30,31] and live cells[32,33,34] to monitor different cellular functions and compartments. The addition of a Raman reporter to the surface of AuNPs gives a characteristic signal that is distinctive from the intrinsic Raman signal from the cell components. This allows visualisation of the AuNPs localisation with high multiplexing capabilities and photostability.

In this study, we introduce for the first time the use of non-destructive 3D SERS imaging for the investigation of the cellular uptake mechanisms of AuNPs functionalised with an anti-ERα antibody and 1,2-Bis(4-pyridyl) ethylene (BPE) Raman reporter (ERα-AuNPs) in breast cancer cells under different endocytosis pathway inhibition conditions. Additionally, the novelty of this work comes from the ability to investigate the cellular uptake and localisation of SERS nanotags in the entire volume of the cell. The collected data were processed and analysed as one data set making SERS a quick and affordable technique, in contrast to TEM that requires laborious sample preparation with potential artefacts. The ability to investigate the cellular uptake and cellular accumulation of SERS nanotags using a sensitive and non-destructive technique is of crucial importance for the validation of AuNPs as an important tool in optical medical imaging.

2.3 Experimental

2.3.1 Materials

Anti-estrogen receptor alpha antibody (ab16660) was purchased from Abcam (330 Cambridge Science Park, Cambridge, CB4 0FL, UK). Anti-mouse IgG HRP-linked antibody (7076S) and anti-rabbit IgG HRP-linked antibody (7074S) were purchased from Cell Signalling Technology (Hamilton House, Mabledon Place, London, WC1H 9BB, UK). Sodium tetrachloroaurate dihydrate, (N-(3-Dimethylaminopropyl)-N'-ethylcarbodiimide hydrochloride) (EDC), N-hydroxysulfosuccinimide sodium salt (NHS), poly (ethylene glycol) 2-mercaptoethyl ether acetic acid (HS-PEG5000-COOH), dynasore hydrate, 1,2-Bis(4-pyridyl) ethylene (BPE), 4-(2-hydroxyethyl)-1-piperazineethancesulfonic acid (HEPES), and 2-(N-morpholino) ethanesulfonic acid (MES) were obtained from Sigma-Aldrich Ltd (The Old Brickyard, New Road, Gillingham, Dorset, SP8 4XT, UK). LIVE/DEAD Viability/Cytotoxicity Assay Kit was purchased from ThermoFisher Scientific (3 Fountain Dr, Inchinnan, Renfrew PA4 9RF, UK). All glassware was cleaned in aqua regia (3 HCl: 1 HNO_3).

2.3.2 Nanoparticle Synthesis and Functionalisation of ERα-AuNPs

Citrate reduced gold (Au) nanoparticles were synthesised according to the Turkevich, Stevenson and Hillier method [35]. Briefly, sodium tetrachloroaurate dihydrate solution (10 mL, 15 mM) in 490 mL deionised water was boiled under continuous stirring. Sodium citrate tribasic dihydrate solution (7.5 mL, 26 mM) was then added. The mixture was boiled with stirring for about 1 h. The average diameter of the gold nanoparticles was measured to be approximately 40 nm by scanning electron microscopy. For the carbodiimide crosslinking functionalisation, 74 µL of EDC solution (1 mg/mL in 10 mM MES, pH 6.0) was mixed with 40 µL of HS-PEG5000-COOH (12.5 µM in dH_20) followed by the addition of 217 µL of NHS (1 mg/mL in 10 mM MES, pH 6.0) and 20 µL of Anti-ERα antibody (2.5 mg/mL in dH_20). The final solution was incubated in 669 µL of 10 mM HEPES buffer pH 7.0 on a shaker plate for 18 h at room temperature. 10 µL of 1,2-bis(4-pyridyl) ethylene (BPE) (0.1 µM) was added to bare AuNPs (990 µL) and the solution was incubated on the shaker plate for 30 min followed by centrifugation at 6,000 rpm for 20 min. The solution of EDC-NHS-PEG5000-mAb was added dropwise to the pelleted BPE-AuNPs. The nanotags were incubated on a shaker plate for 3 h. Excess of free antibody was removed by

centrifugation at 6,000 rpm for 10 min and was used for protein concentration estimation analysis. The schematic of the carbodiimide crosslinking functionalisation is shown in Figure 1.

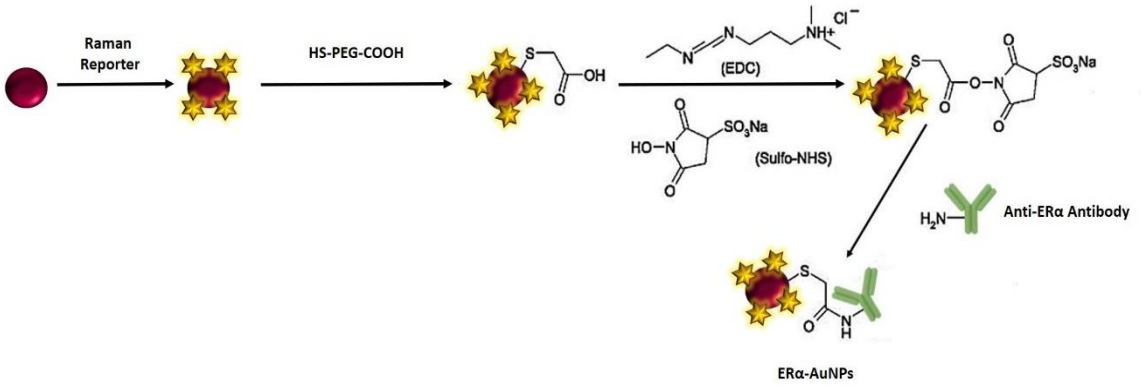

Figure 1: Schematic of ERα-AuNPs conjugation. AuNPs are first functionalised with BPE Raman reporter to create a monolayer. BPE has been used routinely as a Raman reporter in SERS bioanalysis since it is a non-resonant molecule, with low fluorescent background, resulting in high Raman signal.[57] Carbodiimide crosslinking chemistry creates an amide bond between the HS-PEG5000-COOH and the amine of an antibody via the addition of EDC and sulfo-NHS.

2.3.3 Nanotags Characterisation

Extinction spectra were measured using an Agilent Cary 60 UV-Visible (UV-vis) spectrophotometer with Win UV scan V.2.00 software. The instrument was allowed to equilibrate to RT before using poly(methyl methacrylate) (PMMA) disposable plastic micro cuvettes with 500 µL sample volumes to scan wavelengths from 300-800 nm. Where required, samples were diluted to give extinction values of less than one to adhere to the Beer-Lambert law, to allow calculation of the concentration of AuNPs. Dynamic light scattering (DLS) and z-potential were measured using a Malvern Zetasizer Nano ZS with 800 µL of the sample in a PMMA disposable micro cuvette with Zetasizer µV and APS v.6.20 software. Polystyrene latex beads (40 nm) were used as a standard to validate the calibration of the system before running samples. Measurements were taken in triplicate. A scanning electron microscope (SEM) FEI Quanta 250 FEG-ESEM was used to image at an accelerating voltage of 30 kV and typically a spot size of 4 was selected, and an Everhart-Thornley detector collected secondary electrons. For the solution measurements of nanotags, SERS analysis was carried out on a Snowy Range CBEx 2.0 handheld Raman spectrometer (Snowy Range Instruments, Laramie WY USA) equipped with a 638 nm laser with

a maximum laser power of 40 mW. Samples were deposited in glass vials for interrogation. The sample volumes were 600 µL and spectra were collected using 100% laser power at the sample with a 0.05 s accumulation time. The software used to acquire spectra was Peak 1.1.112. Resulting spectra were baseline corrected in Matlab 2014b.[36]

2.3.4 Cell Culture and ERα-AuNP Nanotags Incubation

MCF-7 (ATCC® HTB-22™) and SKBR-3 (ATCC® HTB-30™) human breast cancer cells were obtained from American Type Culture Collection (ATCC) (Queens Road, Teddington, Middlesex, TW11 0LY, UK). The cells were cultured in Rosewell Park Memorial Institute medium (RPMI 1640) supplemented with 1% penicillin/streptomycin (10000 units per mL), 1% fungizone, and 10% heat-inactivated fetal bovine serum (FBS). Cells were incubated at 37 °C and 5% CO_2 in a humidified incubator. Cells at a confluence of ca. 90% growing in a T175 flask were trypsinised and re-suspended in medium to give a concentration of ca. 1×10^6 cells per mL. For fixed cell microscopy, the cells ($1x10^6$ cells per mL) were seeded onto sterile 22-mm square glass coverslips with culture medium containing the ERα-AuNP SERS nanotags at 37 °C, 5% CO_2 in a humidified incubator. Based on the experimental requirements, different concentrations of ERα-AuNP SERS nanotags (3 pM to 60 pM) and different incubation times (5 min to 120 min) were used. The coverslips were washed with PBS three times and fixed in 4% paraformaldehyde for 15 min. The fixed cells were washed with PBS and dH_20 and left to air dry before mounting on a standard glass microscope slide for data collection. For temperature-dependent inhibition studies, MCF-7 cells ($1x\ 10^6$ cells per mL) were cultured in a 6-well dish for 24 h. The cells were then exposed to ERα-AuNPs for 2 h either at low temperature (4 °C) or normal temperature (37 °C), washed with PBS three times and fixed with 4% paraformaldehyde for SERS imaging.

2.3.5 Cell Viability Studies

2.3.5.1 Live/ Dead Cell Staining Assay

The assessment of cell toxicity was carried out with LIVE/DEAD® Viability/Cytotoxicity Assay Kit for mammalian cells using green-fluorescent calcein-AM to indicate intracellular esterase activity and red-fluorescent ethidium homodimer-1 (EthD-1) to indicate loss of plasma membrane integrity (#L3224, ThermoFisher Scientific). Briefly, the cells were plated at a density of 0.5 ×

10^6 cells per 35 mm Ibidi chamber and left to adhere overnight. The cells were exposed to PEG5000-AuNPs and ERα-AuNPs (60 pM) nanotags for 48 h at 37 °C. Before the assay, the cells were washed three times with PBS. A solution of Calcein AM (10 µL, 4 mM) and EthD-1 (20 µL, 2 mM) were diluted in 10 mL of PBS. The fluorescent staining solution (750 µL) was then added to the cells at 37 °C for 15 min before removing for imaging using a Leica Microsystems TCS SP8 with continuous wave visible lasers and a Leica DMi8 inverted microscope and DFC 7000T and TL LED cameras. The Leica Application Suite X V.3.1.5.16308 software was used to carry out live/dead studies using a Leica 20× magnification HC PL APO water objective with a 1.2 NA. Intensity and area of fluorescence was measured using Fiji image processing software.[37]

2.3.5.2 Trypan Blue Cell Viability Counts

MCF-7 cells were seeded in a 6-well plate ($5x10^5$ cells per mL). After 24 h the cells were treated with BPE-AuNPs, PEG5000-AuNPs and ERα-AuNPs at a concentration of 60 pM for 48 h before counting. After 48 h the media was removed, cells were rinsed with PBS three times and 1 mL of trypsin was added to detach cells. Finally, 1 mL of complete RPMI medium was added to recover the cells for counting. The cells were diluted (1/5 dilution) before counting on a haemocytometer slide following the addition of trypan blue viability dye. Each condition was conducted in triplicate. The number of viable (non-blue) cells were recorded.

2.3.6 Dynamic Dependent Endocytosis

MCF-7 cells ($1x10^6$ cells per mL) were cultured in a 6-well dish for 24 h. The cells were then treated with 80 µM dynasore for 30 min at 37 °C before the addition of ERα-AuNPs (60 pM, 2 h). Cells were washed with PBS three times and fixed with 4% paraformaldehyde for 15 min. The fixed cells were washed with PBS and dH_20 and left to be air dried and mounted to a standard glass microscope slide for SERS imaging.

2.3.7 Estrogen Receptor Mediated Endocytosis

MCF-7 cells ($1x10^6$ cells per mL) were cultured in a 6-well dish for 24 h. The cells were then exposed to free ERα (10 µg/mL) for 1 h before the addition of ERα-AuNPs (60 pM, 2 h). The coverslips were washed with PBS three times and fixed in 4% paraformaldehyde for 15 min. The

fixed cells were washed with PBS and dH_20 and left to be air dried and mounted to a standard glass microscope slide for SERS imaging.

2.3.8 Western Blot Experiments

Cells ($1x10^6$ per mL) were plated in 10 cm diameter dishes with 10 mL RPMI and left for 24 h. The cells were washed with 1X ice cold PBS twice and were lysed with 200 µL ice cold RIPA buffer (#10017003, Thermo Fisher) containing protease and phosphatase inhibitors (# A32959, Pierce). Cell lysates (20 µL, 1 mg/mL) were diluted with 5X SDS loading buffer, heated to 95 ºC for 5 mins and 20 µL of the denatured cell lysate loaded into a 12% gel (Mini Protean TGX stain free Pre-cast gels, #456-8085, Bio-Rad) and run at 140 V for 40 min. The gel was electrotransferred to a 0.2 µm nitrocellulose membrane (#170-4159, Bio-Rad) with the BioRad TransBlot Turbo Transfer System using the Midi gel 10 mins transfer setting. The membrane was blocked with 5% BSA blocking buffer for 1 hr at room temperature. After blocking, the membrane was incubated at 4 ºC overnight whilst rocking with the appropriate primary antibody diluted in 5 mL 5% w/v BSA, 1X TBS, 0.1% Tween 20. The next day the membrane was washed three times for 5 min each with 15 mL of TBST buffer (1.5% Tween 20 in 1x TBS). The membrane was incubated with the appropriate secondary antibody in 10 ml of 5% BSA blocking buffer with gentle agitation for 1 hr at room temperature and was washed three times for 5 mins each with 15 mL of TBST buffer afterwards. Finally, for the detection of the proteins, the membrane was incubated with 1:1 of Pierce™ ECL western blotting substrate (# 32106, Thermo Fisher) for 1 min. A Bio-Rad ChemiDoc MP Imaging System- Universal Hood III with Image Lab V.4.1 software was used to image and quantify the protein levels on the membrane.

2.3.9 Raman Cell Mapping

The intracellular uptake of the nanotags was examined using Raman cell mapping. A Renishaw InVia Raman confocal microscope was used to create initial depth profiles, to establish the focal plane of the fixed cells in correlation with the white light images. Subsequently, 3D SERS maps were collected in edge Streamline HR high confocality mode at 1 µm resolution in the X and Y directions and 3 µm between Z-stacks. A 50× magnification NIR APO Nikon water immersion objective with a 1.0 NA was used on the samples at a laser power of 1.2 mW (10% power) at the sample, from a HeNe 633 nm excitation source with a 0.1 s acquisition time per point, and a 1200

l/mm grating in high confocality mode. Windows-based Raman Environment (WiRE™ - Renishaw plc) 4.4 software package was used to pre-process the data for cosmic ray removal and baseline subtraction. The image was generated using direct classical least square analysis (DCLS) based on Raman reporter reference spectrum. Therefore, the false colour was generated only when there was a good spectral fit between the reference and the collected spectra. All SERS experiments contained n = 10 biological replicates and experiments were in triplicate.

2.3.10 Calculation of Relative SERS Response Value in MCF-7 Cells

The SERS response in cells was evaluated using Fiji image processing package[37] by taking into consideration the pixel numbers of the nanotags and cell area after the Raman mapping. This was an estimation of the SERS response per cell and not a quantification of the total number of nanotags in the cells. Using this approach, we were able to estimate the SERS signal per cell area, quantify the pixels that corresponded this signal, identify the localisation of the nanotags, and allowing comparison between different samples. Before the analysis of the nanotag uptake, all the cells were scanned using three-dimensional (3D) SERS to verify their intracellular distribution. Briefly, the spectra from the SERS cell mapping analysis were baselined and cosmic rays were removed using the WiRE™ - Renishaw plc 4.4 software package. The images were generated using direct classical least square analysis (DCLS) based on the Raman reporter reference spectrum. DCLS fitted the unknown data (collected during cell mapping) to a linear combination of the specified component spectrum (Raman reporter reference spectrum). If there was a good spectral fit between the Raman reporter reference and the collected spectra a gradient red false colour was assigned. Associated with each false colour image was a look up table (LUT). The minimum and maximum values of the LUT indicates the degree of spectral fit. The minimum value of LUT was set to 0.4, which showed a good overlapping of the BPE reference spectrum with the collecting spectra. The gradient red false colour was then converted to monochromatic red colour, without affecting the intracellular SERS signal, using the Windows-based Raman Environment (WiRE™ - Renishaw plc) 4.4 software package. The cellular area was selected by masking everything outside of it using Fiji image processing. The image was then colour split to the monochromatic red channel, where only the red pixels were present. A 200-threshold was set to count only the pixels that correspond to the nanotags and not to any cellular component. Finally, the percentage of the red pixel area (corresponding to SERS response) versus the full cell area was calculated (Figure 2).

(A)

Gradient red color images representing ERα-AuNP nanotags, were generated using DCLS in WiRE software

Conversion to monochromatic red color

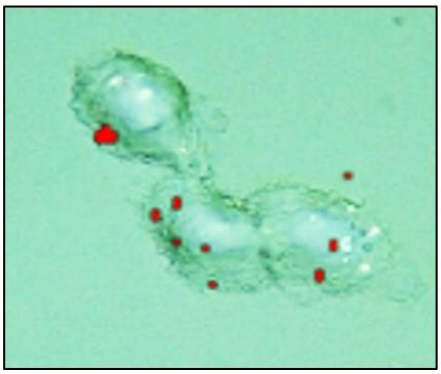

(B) **(C)**

Images with monochromatic red color SERS signal

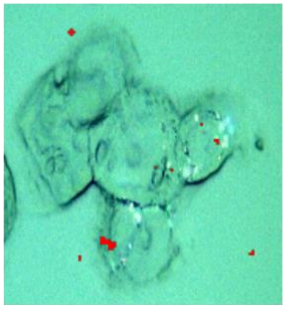

Creation of a mask based on the selected area

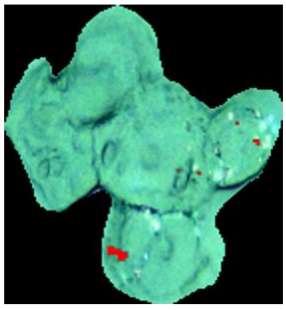

Split image to monochromatic red channel

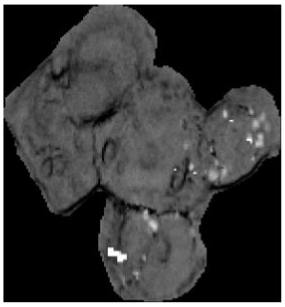

(D) **(E)**

Threshold adjustment= 200

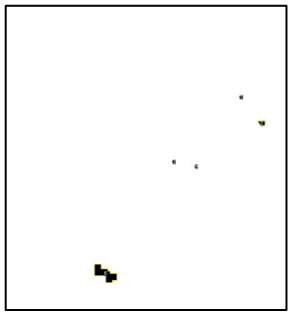

Calculation of % Area of Red Pixels from the selected area

Count	Total Area	Average Size	%Area
5	49	9.800	0.197

Figure 2: Schematic representing the step carried out for the calculation of relative SERS response in MCF-7 cells using WiRE™ - Renishaw plc 4.4 and Fiji image processing package. **(A)** After the generation of false colour images using DCLS from WiRE™ - Renishaw plc 4.4 software, the gradient red false colour was converted to monochromatic red colour, without affecting the intracellular SERS signal. The images with the monochromatic red signal were then analysed using Fiji. **(B)** The cellular area was then selected by masking everything outside it. **(C)** Afterwards, the image was colour split to the monochromatic red channel where only the red pixels were represented as bright white spots. **(D)** Only the red pixels that were above 200-threshold were extracted for the calculations. **(E)** Finally, the percentage of the red pixel area (corresponding to SERS response) versus the full cell area was calculated. 10 cells per sample group were analysed. The percentage of SERS response was plotted and analysed statistically using one-way analysis of variance (ANOVA).

2.3.11 Statistical Analysis

Statistical analysis was carried out on GraphPad Prism 8.1.2 (GraphPad Software, Inc., San Diego, CA). The Student's t-test was used for comparison of two variables and one-way analysis of variance (ANOVA) test for comparison of three or more groups. Differences between groups were considered to be significant at a P value of < 0.05.

2.4 Results and Discussion

2.4.1 Nanoparticle Synthesis and Characterisation of ERα-AuNPs

Bare AuNPs were synthesised by standard citrate reduction [35] and were characterised by UV, DLS and SEM analysis. The results revealed that the AuNPs had a spherical shape and were 40-50 nm in diameter (Figure 3).

(A)

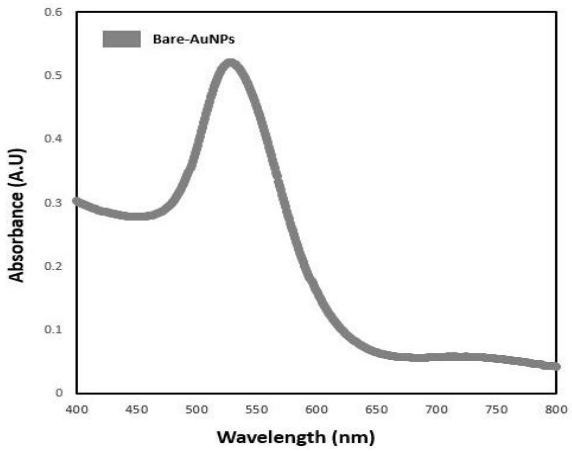

(B)

	Peak 1 Mean (d.nm)	Peak 2 Mean (d.nm)	Peak 1 %	Peak 2 %	Mean z-average	PdI
	53.35	4.38	88.4	11.6	32.57	0.367
	52.30	4.58	88.3	11.7	30.25	0.482
	51.81	4.67	84.6	15.4	31.75	0.366
Average	52.49	4.54	87.1	12.9	31.52	0.405
STDEV	0.79	0.15	2.2	2.17	1.18	0.067

(C)

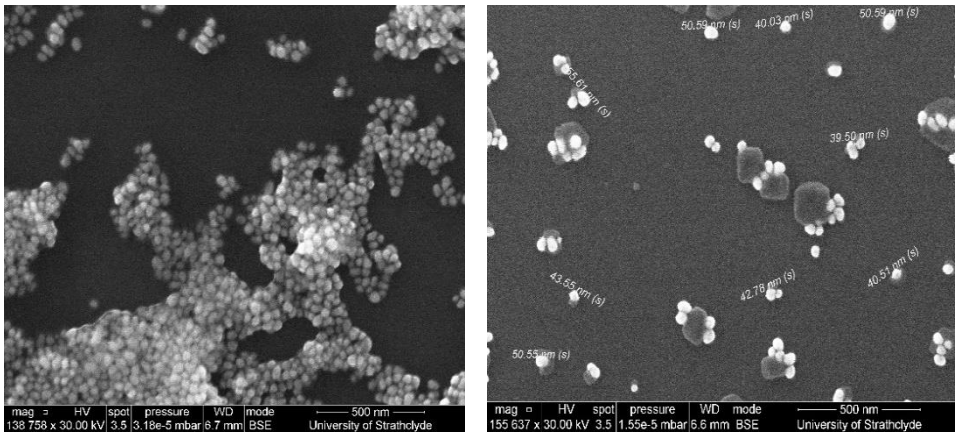

Figure 3: Characterisation of bare 40 nm citrate reduced AuNPs in dH20. **(A)** Extinction spectra of AuNPs revealed a sharp and narrow plasmon band at 529 nm indicating colloid monodispersity. **(B)** Differential light scanning analysis (DLS) of AuNPs showing that the average size of AuNPs was 52.5 ± 0.79 nm with a narrow size distribution. **(C)** Scanning electron microscopy (SEM) of AuNPs agreed with the DLS measurements and confirmed that AuNPs had a spherical shape with a diameter distribution ranging from 40 to 50 nm.

Anti-ERα antibodies were attached to the gold surface via carbodiimide crosslinking chemistry, which created an amide bond between the carboxylic acid of a PEG molecule (HS-PEG5000-COOH) and an amine group on the antibody. The HS-PEG5000-COOH was also used to prevent nonspecific interactions between the functionalised nanotags and other cellular components. The coupling chemistry was achieved after the attachment of the Raman reporter, 1,2-bis(4-pyridyl) ethylene (BPE), to the AuNP surface (Figure 4).

(A)

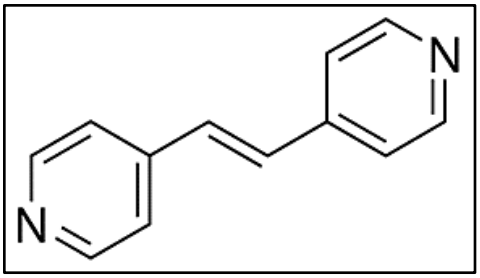

(B)

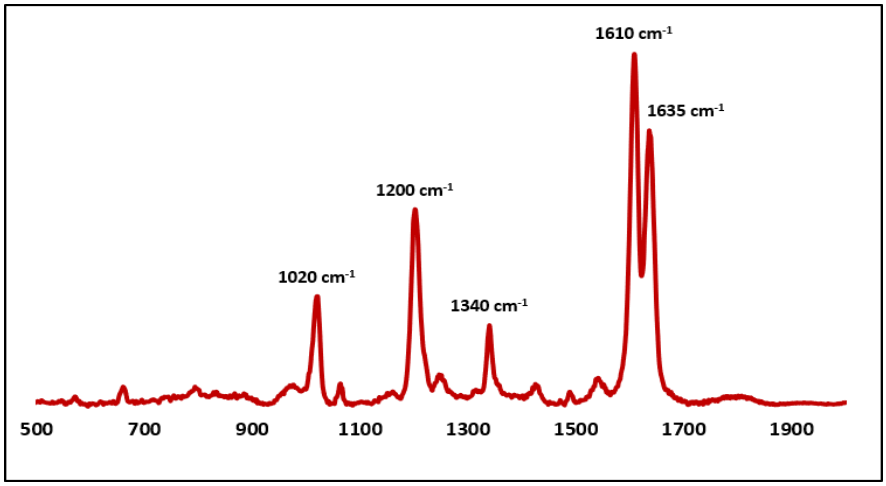

Figure 4: **(A)** Structure of BPE Raman Reporter. **(B)** SERS spectrum of BPE Raman reporters adsorbed on 40 nm AuNPs in an aqueous solution at 10^{-7} M concentration. The SERS analysis was carried out using a Snowy Range CBEx 2.0 handheld Raman spectrometer equipped with a 638 nm laser with a maximum laser power of 40 mW. The spectrum was collected using 100% laser power with 0.05 s accumulation time. The software used to acquire spectra was Peak 1.1.112.

The successful bioconjugation of ERα-AuNP nanotags was characterised using extinction spectroscopy, DLS, agarose electrophoresis and a lateral flow immunosorbent assay. Extinction spectroscopy showed that ERα-AuNPs did not show any aggregation indicating that they were

stable after their functionalisation (Figure 5A). DLS confirmed the successful antibody functionalisation since the hydrodynamic diameter of the nanotags increased from 73.31 ± 0.96 d.nm to 80.34 ± 1.59 d.nm at pH 7.0 after the bioconjugation (Figure 5B). Z-potential of PEG5000-AuNPs (grey) and ERα-AuNPs (orange) nanotags showing the increase of the zeta potential values (from -54.54 ± 0.69 mV to -51.62 ± 1.13 mV). This was a further verification of the anti-ERα antibody attachment to the AuNPs surface since the antibody carried a slightly positive charge at pH 7.0 (isoelectric point of anti-ERα antibody: 8.3) that increased the charge of the AuNPs. (Figure 5C). Additionally, the agarose electrophoresis verified that PEG5000-AuNPs travelled further than the ERα-AuNPs suggesting that ERα-AuNP nanotags were of a bigger size (Figure 5D). Finally, the lateral flow immunosorbent assay showed that ERα antibodies on the gold surface were active since a spot from ERα-AuNPs was present when the matching secondary IgG antibody for ERα applied on the strip (Figure 5E).

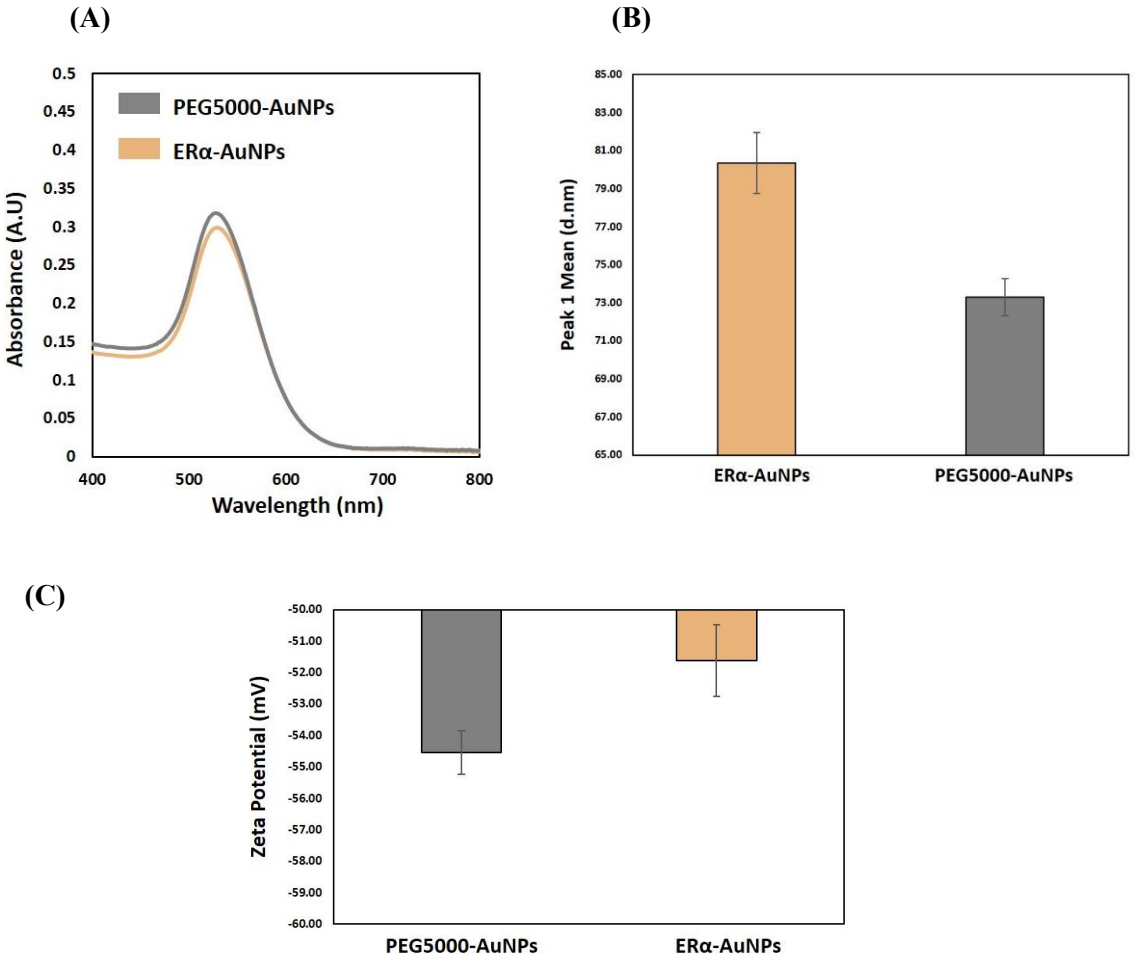

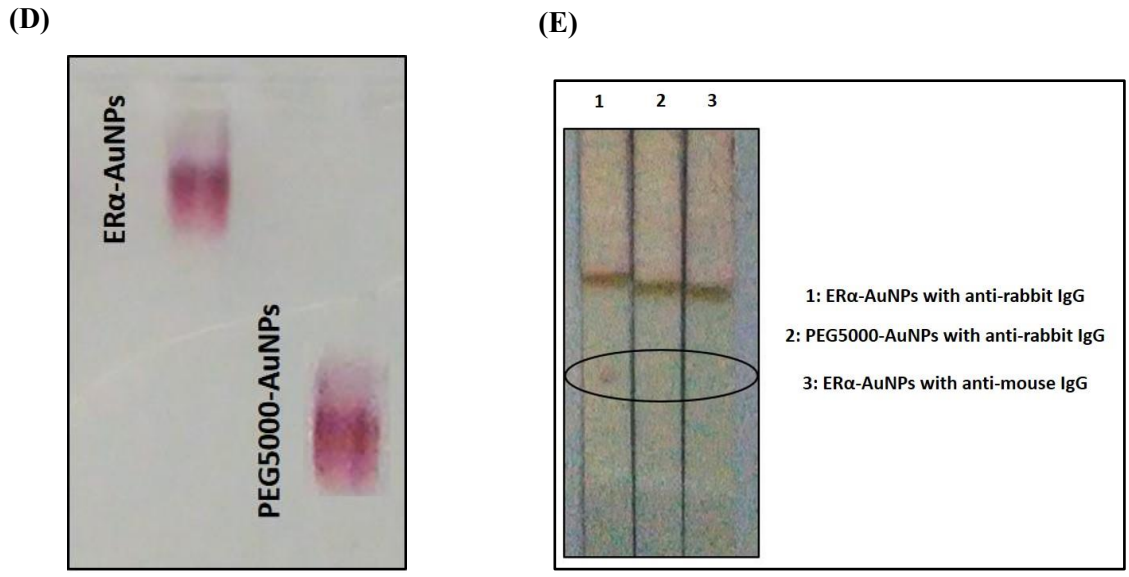

Figure 5: Characterisation of ERα-AuNPs after their functionalisation **(A)** Extinction spectra of PEG5000-AuNPs (grey) and ERα-AuNPs (orange) nanotags showing that there was a shift in the wavelength when the antibody was added to the surface of AuNPs (from 529 to 533 nm). **(B)** Differential light scanning analysis (DLS) of PEG5000-AuNPs (grey) and ERα-AuNPs (orange) nanotags confirmed the successful functionalisation of the anti-ERα antibody as the hydrodynamic diameter of AuNPs increased and became more positive as each layer was added. The ERα-AuNPs were 80.34 ± 1.59 d.nm in comparison to the PEG5000-AuNPs (73.31 ± 0.96 d.nm) at pH 7.0. **(C)** Z-potential of PEG5000-AuNPs (grey) and ERα-AuNPs (orange) nanotags showing the increase of the zeta potential values (from -54.54 ± 0.69 mV to -51.62 ± 1.13 mV). This was a further verification of the anti-ERα antibody attachment to the AuNPs surface since the antibody carried a slightly positive charge at pH 7.0 (isoelectric point of anti-ERα antibody: 8.3) that increased the charge of the AuNPs. **(D)** Agarose gel after electrophoresis showing the distance travelled by PEG5000-AuNPs and ERα-AuNP nanotags. Gel electrophoresis is a method of separation and analysis, based on the size and charge of the samples being analysed. Here, gel electrophoresis confirmed the PEG5000-AuNPs travelled further than the ERα-AuNPs suggesting that the nanotags were of different size and/or charge and successful antibody functionalisation. **(E)** Lateral flow immunosorbent assay strips showing the spot from ERα-AuNPs onto the detection zone of the nitrocellulose strip. The spot was present only for samples with the matching secondary IgG antibody for ERα applied (anti-rabbit). There was no detected spot when the nanotags were applied to a lateral flow that contained a non-specific secondary IgG antibody (anti-mouse) or when PEG5000-AuNPs was tested with the anti-rabbit IgG confirming the successful binding of the anti-ERα antibody on the AuNPs surface.

The quantification of the bound ERα antibody to AuNPs surface was estimated using BCA assay. The results showed that the average number of the ERα antibody molecules adsorbed per AuNP was 63.81± 5.88 (Figure 6).

Sample	Absorbance	Concentration (mg/mL)	Concentration (µg/mL)
Std 1	0.1128	0.25	250
Std 2	0.1316	0.5	500
Std 3	0.1648	1	1000
Std 4	0.1950	1.5	1500
Std 5	0.2144	2	2000
Std 6	0.2540	3	3000
Std 7	0.3254	4	4000
Sample 1	0.1079	0.0196	19.6
Sample 2	0.1071	0.0233	23.3
Average	0.1070	0.0214	21.4
STDEV	0.0001	0.0026	2.6

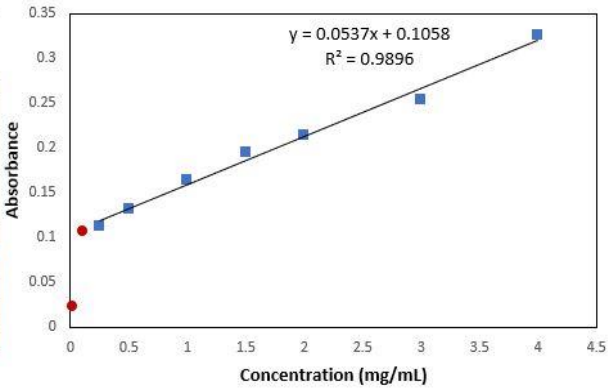

Added Antibody Concentration (µg/mL)	Supernatant Concentration (µg/mL)*	Adsorbed Antibody Concentration (µg/mL)**	Antibody Molecules per AuNPs (Ab/AuNPs)***
50	21.41 ± 2.63	28.58 ± 2.63	63.81 ± 5.88

Figure 6: Raw Data and calculations to determine the ERα antibody loading onto AuNPs using the bicinchoninic acid assay (BCA). *Concentration of remaining antibody in the supernatant calculated from the calibration curve. Absorbance was corrected by subtracting the absorbance of the PEG5000-AuNPs control sample (0 µg/mL antibody) per Bio-Rad protocol. **Amount of antibody absorbed onto AuNPs presented as the concentration and calculated as the difference in the antibody added and antibody remaining in the supernatant. *** The average number of antibody molecules adsorbed onto each AuNPs was calculated by dividing the concentration of adsorbed antibody (converted to 178.65 nM using antibody MW of 160,000 g/mL) by the concentration of AuNPs (Initial concentration was 0.028 nM and AuNPs were centrifuged and concentrated to 2.8 nM).

ERα-AuNPs were also analysed using SERS on a Snowy Range CBEx 2.0 handheld Raman spectrometer equipped with a 638 nm laser with 40 mW maximum laser power. The results showed that ERα-AuNPs gave a strong and characteristic SERS signal from BPE Raman reporter (attached on ERα-AuNPs surface) Therefore, the AuNPs were successfully functionalised and could be further used in cell studies.

2.4.2 Characterisation of Breast Cancer Cells

MCF-7 breast cancer cell line is known to overexpress the estrogen receptor alpha (ERα) biomarker. To confirm ERα expression, a western blot was performed which showed that ERα was detectable in the MCF-7 cells (Figure 7). Therefore, the MCF-7 cells were used to study the uptake of the ERα-AuNP nanotags.

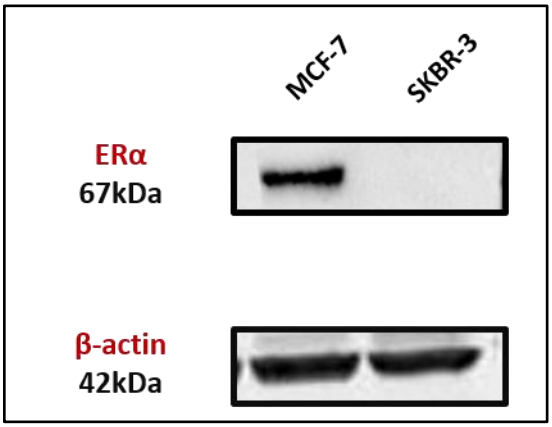

Figure 7: ERα expression in breast cancer cell lines. Cell lysates were prepared from breast cancer lines and western blot analysis carried out using an antibody to ERα, b-actin was used as a loading control.

2.4.3 Cytotoxicity Evaluation of ERα-AuNP Nanotags in MCF-7 Cells

SERS was utilised first to investigate the accumulation of ERα-AuNP nanotags in MCF-7 breast cancer cells under different cellular incubation conditions. Specifically, MCF-7 cells were incubated with the nanotags at different concentrations, incubation times and temperatures. The results showed that the MCF-7 cells had high nanotag accumulation and strong SERS signal after 2 h incubation with the ERα-AuNP nanotags (Figure 8A). Therefore, 2h incubation time was used in subsequent experiments. The bright-field images showed that the cells treated with 60 pM ERα-AuNPs were adherent with no changes to morphology in comparison to untreated MCF-7 cells (data not shown). To further test the effect of ERα-AuNPs on the viability of MCF-7 cells, live/dead staining with green-fluorescent calcein-AM and red-fluorescent ethidium homodimer-1 was performed after incubation of ERα-AuNPs in MCF-7 cells for 48 h. The viability studies verified that ERα-AuNPs showed good biocompatibility without any toxic effect on MCF-7 cells

over the culture period since a significant green colour corresponding to viable cells (Calcein AM) was present in contrast to the red colour corresponding to non-viable cells (EthD Br-1) (Figure 8B). Further cell viability studies were carried out using trypan blue cell viability assay. The results showed that MCF-7 cells treated with AuNPs, coated with only the BPE Raman reporter, exhibited approximately 85% viability in contrast to the PEGylated BPE-AuNPs (96% cell viability). MCF-7 cells had the highest cell viability (97% cell viability) when they were incubated with ERα-AuNP nanotags (Figure 8C). These results indicated that 60 pM of ERα-AuNPs incubated in MCF-7 for 48 h did not cause any cell toxicity indicating good biocompatibility of the nanotags.

(A)

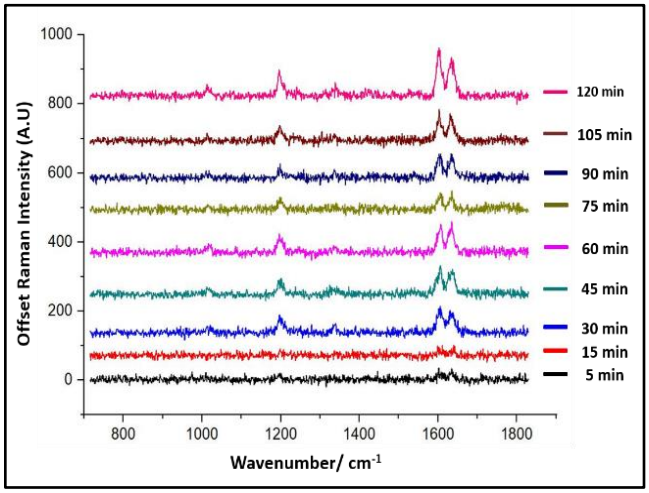

(B)

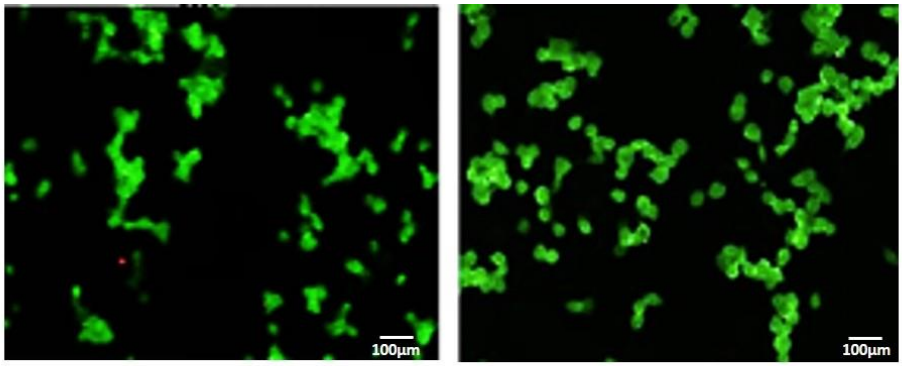

(C)

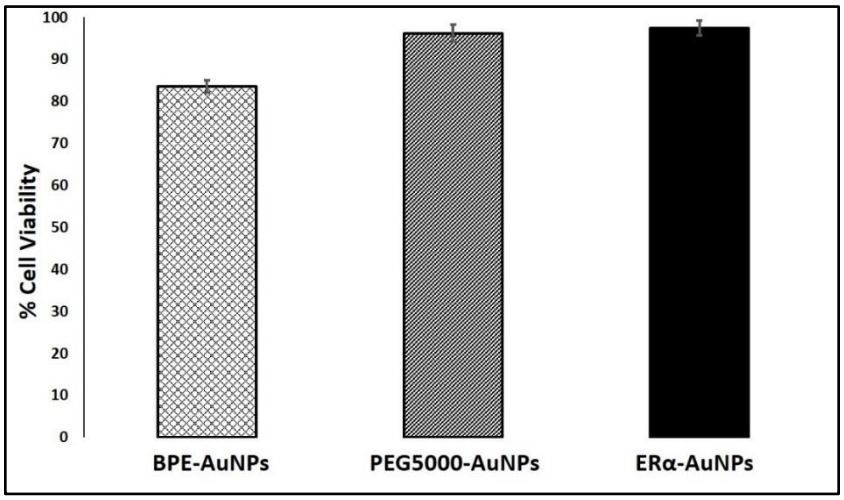

Figure 8: ERα-AuNPs incubated in MCF-7 cells showed strong SERS signal with no detectable cell toxicity. **(A)** Average SERS signal from ERα-AuNPs in MCF-7 cells under different nanotags incubation times ranging from 5 min to 120 min. **(B)** Cell viability assay of MCF-7 cells treated with 60 pM ERα-AuNPs (left) and 60 pM PEG5000-AuNPs (nanotags without ERα antibody functionalisation) (right) for 48 h using live/dead staining with Calcein AM and EthD Br-1 assay. Viable cells appear as green (Calcein AM), while non-viable cells appear as red (EthD Br-1). Scale bar 100 µm. **(C)** Cell viability using trypan blue assay for MCF-7 cells treated with 60 pM BPE-AuNPs, 60 pM PEG5000-AuNPs or 60 pM ERα-AuNPs for 48 h. The average of ten samples from three independent biological replicates is shown. Error bars presented as mean ± S.D.

2.4.4 Calculation of Relative SERS Response Value in MCF-7 Cells

The quantitative estimation of the number of SERS nanotags inside cells is a very challenging process since the exact number of AuNPs in each aggregate cannot be simply identified from the SERS signal obtained for each image. Therefore, here, we developed a method to calculate the number of pixels that corresponded to ERα-AuNPs in MCF-7 cells, based on the location of SERS response, versus the total cell area mapped. Before the evaluation of SERS response, all cells were analysed by three-dimensional (3D) SERS imaging to verify that ERα-AuNPs signal was generated within the cell. After the 2D SERS mapping, all spectra were baselined, and any cosmic rays were removed. False colour images were then generated using direct classical least square analysis (DCLS) based on the BPE reference spectrum (Raman reporter attached on ERα-AuNPs). Specifically, when there was a good spectral fit between BPE spectrum and the collected spectra of the cells, a gradient red false colour was assigned. The gradient red false colours were then

converted to monochromatic red colour, without affecting the intracellular SERS signal, using the Windows-based Raman Environment (WiRE™ - Renishaw plc) 4.4 software package as shown in SI, Figure S2A. A 200-threshold was then set, using Fiji image processing package, to exclude any red pixels that did not correspond SERS response. The percentage of the red pixel area versus the full cell area was then calculated.

This approach gives an estimation of the percentage of SERS responsive pixels per cell and provides an indication of the relative value for the uptake of nanotags per condition as the SERS signal will increase with the number of nanotags uptaken. It should be noted that this is not a direct quantification of the total number of nanotags in the cells. In this way, we can obtain a relative assessment of nanotags uptake using a direct, rapid and non-destructive optical approach averaged across multiple cells (10 per condition investigated). This is of huge advantage compared to other techniques used for the analysis of nanotags in cells such as TEM which is highly destructive, time consuming and expensive and it would be very challenging to measure enough cells to get a meaningful average statistical value per condition. Here, the exposure of MCF-7 cells to different ERα-AuNPs concentrations (3-60 pM) for 2 h showed that 60 pM is an effective concentration for providing high SERS response per cell (Figure 9) without affecting the viability of MCF-7 cells. Therefore, 60 pM ERα-AuNPs was used in subsequent experiments.

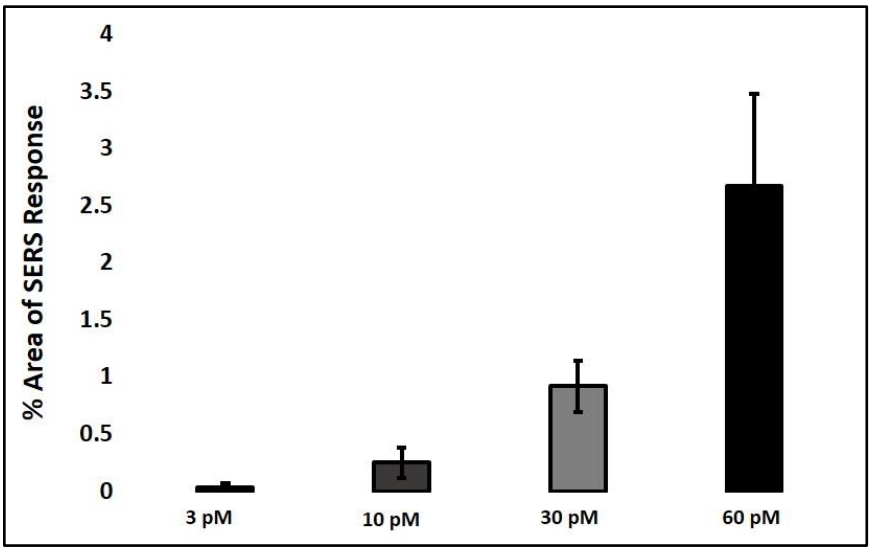

Figure 9: Calculation of relative SERS response value under different ERα-AuNPs concentrations. 60 pM ERα-AuNPs led to a higher percentage of SERS response in MCF-7 cells. The calculations were carried out using WiRE™ - Renishaw plc 4.4 and Fiji image processing package. The average of ten samples from three independent biological replicates is shown. Error bars presented as mean ± S.D.

2.4.5 ERα-AuNPs Enter MCF-7 Cells Using A Temperature Dependent Process

For the evaluation of ERα-AuNPs uptake mechanisms from MCF-7 cells, a low-temperature assay was performed to investigate whether the nanotags were using an energy-dependent mechanism to enter the cells. In this experimental approach, MCF-7 cells were incubated with ERα-AuNPs (60 pM) at either low temperature (4 ºC) or at normal incubation temperature (37 ºC) for 2 h. Previous studies have shown that if the nanoparticles enter cells via endocytosis, then a decrease in their cell uptake is observed when the temperature is lower.[15,38] Here, it was observed that there was a lower level of ERα-AuNP nanotag accumulation into MCF-7 cells at 4 ºC, compared to the cells treated with the nanotags at 37 ºC (Figure 10A). Specifically, there was around a threefold decrease in the percentage of SERS response in MCF-7 cells treated with ERα-AuNPs at 4 ºC in comparison to 37 ºC (Figure 10B). Additionally, there was a lower and noisy average SERS signal in the MCF-7 cells treated with ERα-AuNPs at 4 ºC compared to 37 ºC (Figure 10C). The decreased internalisation of ERα-AuNPs at 4 ºC demonstrated that their cellular uptake is an energy- and temperature-dependent process. This implies that the ERα-AuNPs interacted with the MCF-7 cells by non-passive diffusion transport since they require energy for their internalisation.

(A)

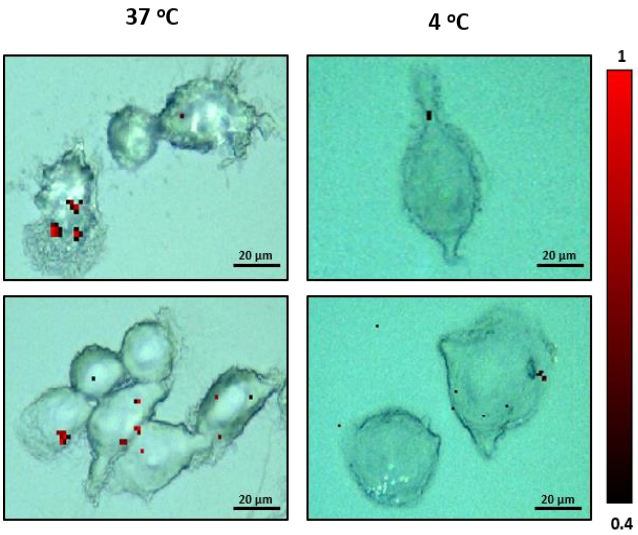

(B) **(C)**

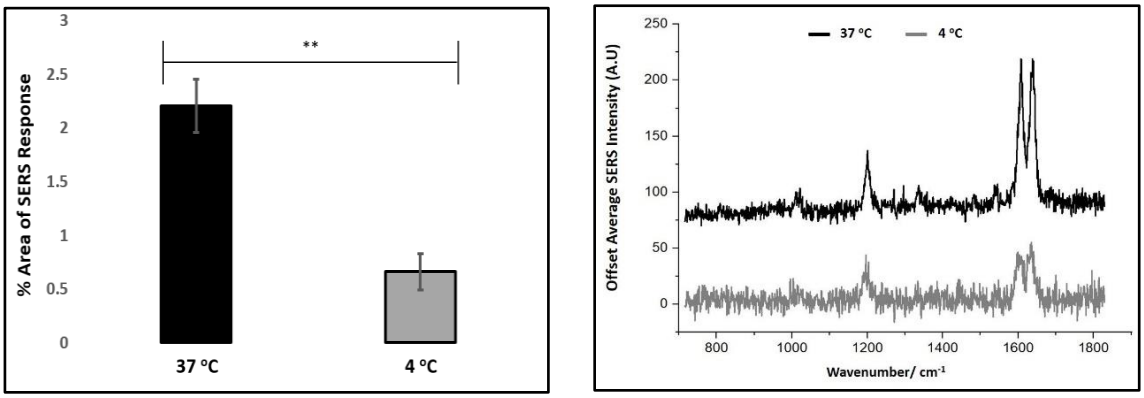

Figure 10: ERα-AuNPs enter MCF-7 cells in a temperature dependent manner **(A)** SERS map of MCF-7 cells treated with ERα-AuNPs (60 pM) for 2 h at 37 ºC (left) and 4 ºC (right). The images were generating using a Renishaw InVia Raman microscope with 50× magnification NIR APO Nikon water immersion objective with a 1.0 NA and 1.2 mW laser power (10% power) from a HeNe 633 nm excitation source with step size y,x 1.0 µm, 0.1s acquisition time and a 1200 l/mm grating in high confocality mode. The red false colour images, representing ERα-AuNPs, were generated using WiRE™ - Renishaw plc 4.4 software and direct classical least square analysis (DCLS) based on a BPE Raman reporter spectrum. DCLS fitted the unknown data (collected during cell mapping) to a linear combination of BPE reference spectrum. The minimum look up table (LUT) thresholds were set to exclude any poorly correlating or noisy spectra (min= 0.4). Results are representative of 3 independent experiments (SERS mapping of 10 cells in each experiment). Scale bars= 20 µm. **(B)** Percentage of relative SERS response value in MCF-7 cells incubated with ERα-AuNPs (60 pM for 2 h) at 37 ºC (black) and 4 ºC (grey). The area was calculated using the Fiji image processing package by calculating the red pixel number, corresponding to ERα-AuNPs, and the mapped cell area. The average of ten samples from three independent biological replicates is shown. Error bars presented as mean ± S.D. * Significant difference ($p < 0.05$) in a Student's *t*-test. **(C)** Representative average SERS spectra of MCF-7 cells incubated with ERα-AuNPs (60 pM for 2 h) at 37 ºC (black) and 4 ºC (grey) calculated from 10 cells of 3 independent experiments.

2.4.6 ERα-AuNPs Enter MCF-7 Cells Using Dynamin Dependent Endocytosis

Nanotags functionalised with biomolecules can be internalised by cells using different pathways such as micropinocytosis, clathrin- or caveolin-mediated endocytosis. Typically, most of the nanotags are uptaken into cells by endocytosis after binding to membrane proteins.[39,40] Clathrin is one of the main proteins that play a major role in the endocytosis pathway. Specifically, clathrin molecules self-assemble together to form a spherical coated vesicle, known as clathrin coated vesicle (CCV). CCVs mediate the transport of cargo from the cell membrane inside the cell and between organelles.[41,42] The formed CCV detaches from the membrane using dynamin, an intracellular GTPase protein that cleaves the neck of the vesicles being formed during endocytosis.[43,44] Marczell et. al. have shown that the ERα pathway is linked to dynamin-dependent receptor endocytosis in MCF-7 cells.[45] Specifically, immunoelectron microscopy imaging showed that membrane bound ERα undergoes ligand-mediated receptor internalisation via a dynamin-dependent pathway. [45] To demonstrate whether dynamin plays a role in ERα-AuNPs cellular uptake, MCF-7 cells were treated with dynasore, a GTPase inhibitor of dynamin.[46] The use of dynasore aimed to informed whether the inhibition of dynamin would corrupt the internalization of ERα-AuNPs. Therefore, MCF-7 cells were pre-treated with dynasore (80 μM for 30 min), then media was removed, and fresh media was added to the cells before ERα-AuNPs (60 pM for 2 h) incubation. The 2D SERS mapping suggested the untreated cells seemed to have higher SERS signal from the interior of the cells in contrast to dynasore treated cells where the highest signal generated from the cell surface (Figure 11A). Additionally, the inhibition of the dynamin-dependent pathway significantly reduced the uptake of ERα-AuNPs into MCF-7 cells and led to lower accumulation of the nanotags (Figure 11B). To further investigate the localisation of the nanotags, 3D SERS cell mapping was performed using a 0.1 s accumulation time per spectrum and 1.2 mW laser power with a 633 nm excitation source. Each cell map was obtained with a 1 μm lateral resolution in x and y directions and 3 μm in the z-direction (30 μm overall depth). The average SERS spectra per z-slice of the map confirmed that dynamin inhibition led to a significant reduction in SERS signal throughout MCF-7 cells while SERS signal seemed to be generated from the cell surface (Figure 3D, 3F). In contrast, a strong SERS signal was observed within the cell in the untreated MCF-7 cells (Figure 11E, 11G). The exact points in the cells that were used for the generation of SERS spectra throughout the z-axis are shown in Figure 12. 3D SERS imaging

suggested that dynasore disrupted the formation of endocytic vesicles which led to ERα-AuNPs being trapped on the cell surface and not being internalised.

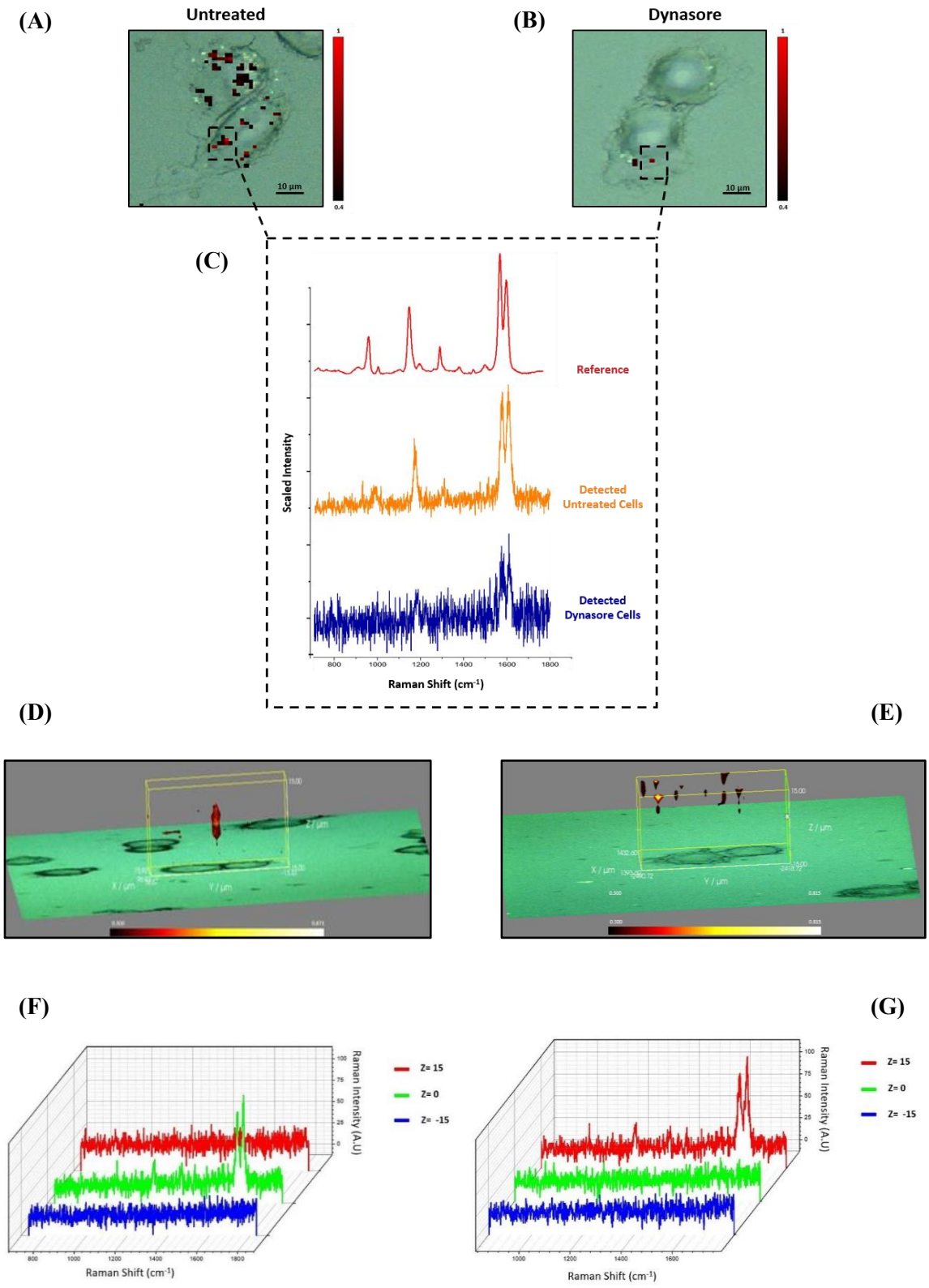

Figure 11: ERα-AuNPs use dynamin for their cellular uptake in MCF-7 cells. **(A)** False colour SERS map images for MCF-7 cells incubated with only ERα-AuNP nanotags (60 pM, 2 h) or **(B)** with dynasore (80 µM, 30 min). and ERα-AuNP nanotags (60 pM, 2 h). The images were generating using a Renishaw InVia Raman microscope with 50× magnification NIR APO Nikon water immersion objective with a 1.0 NA and 1.2 mW laser power (10% power) from a HeNe 633 nm excitation source with step size y,x 1.0 µm, 0.1s acquisition time and a 1200 l/mm grating in high confocality mode. The minimum and maximum look up table thresholds were set to exclude any poorly correlating or noisy spectra (min= 0.4). Scale bar= 10 µm. **(C)** Average SERS spectra from untreated (orange) and dynasore treated (blue) cells stacked with BPE Raman reporter reference spectrum (attached on ERα-AuNPs) (red). **(D)** 3D SERS map from MCF-7 treated with only ERα-AuNPs (60 pM, 2h) or **(E)** with dynasore (80 µM, 30 min) and ERα-AuNP nanotags (60 pM, 2 h). 3D SERS images were generating using a Renishaw InVia Raman microscope with 50× magnification NIR APO Nikon water immersion objective with a 1.0 NA and 1.2 mW laser power (10% power) from a HeNe 633 nm excitation source with step size y,x=1.0 µm and z= 3.0 µm, 0.1 s acquisition time and a 1200 l/mm grating in high confocality mode. **(F)** 3D Raman mapping waterfall plot of average SERS spectra at different z-axis points, z= 15 µm (red), z= 0 µm (green) and z= -15 µm (blue) from MCF-7 treated with only ERα-AuNPs (60 pM, 2 h) or **(G)** with dynasore (80 µM, 30 min) and ERα-AuNP nanotags (60 pM, 2 h).

(A) **(B)**

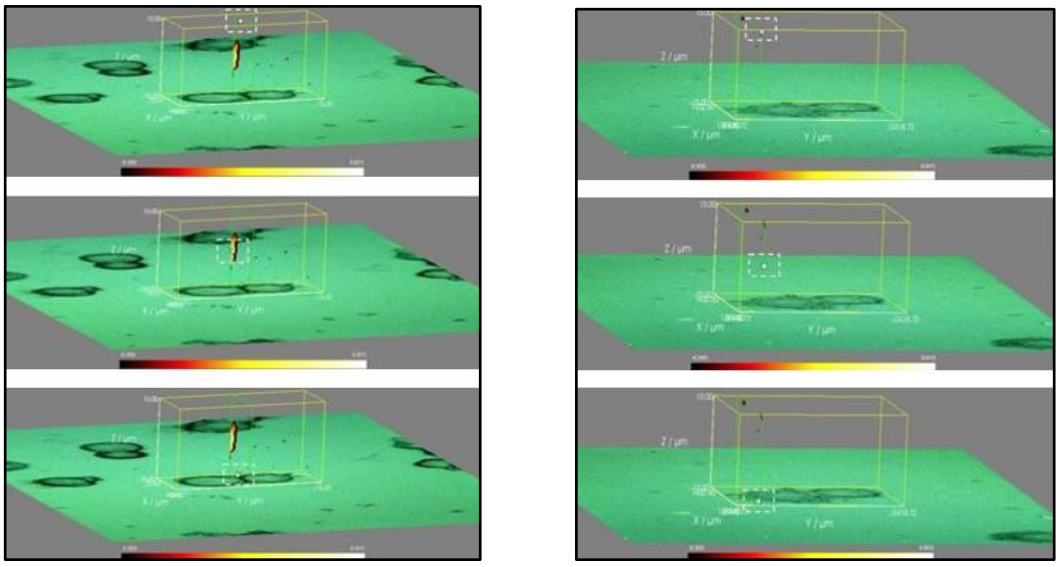

Figure 12: 3D Raman mapping results and SERS spectra detected into different z-axis points (dashed white box). **(A)** Untreated MCF-7 cells: as the z-axis moves from top to bottom of the cell, the BPE labelled ERα-AuNPs signal appeared throughout the MCF-7 cell. **(B)** When the cells were treated with 3D SERS images were generating using a Renishaw InVia Raman microscope with 50× magnification NIR APO Nikon water immersion objective with a 1.0 NA and 1.2 mW laser power (10% power) from a HeNe 633 nm excitation source with step size y,x=1.0 µm and z= 3.0 µm, 0.1 s acquisition time and a 1200 l/mm grating in high confocality mode. The minimum and maximum look up table thresholds were set to exclude any poorly correlating or noisy spectra (min= 0.4). Coupling the data with the 2D Raman mapping, there is an indication that ERα-AuNPs did not enter the MCF-7 cells when dynasore was present.

2.4.7 ERα-AuNPs Enter MCF-7 Cells Using Membrane ERα

Since the results showed that ERα-AuNPs appeared to use dynamin for their internalisation in MCF-7 cells, another study was conducted to investigate if the nanotag uptake was dependent on specific receptor-mediated endocytosis (RME). RME is a process of specific recognition in which the nanotags are internalised in cells after their binding with cell membrane proteins that are specific to biomolecules attached on the nanotags surface.[47] The binding of the membrane receptor with its ligand leads to its activation.[48] The cell membrane region, that contains the receptor-nanotag complex, then undergoes endocytosis using a transport vesicle. The rate at which the

cargo is internalised is related to the amount of its corresponding receptor on the cell surface. Although ERα was long considered to be located in the cytoplasm, it is now clear that it also works as a plasma membrane-localised receptor.[49,50,51] The trafficking of membrane ERa (mERα) has been challenging and the mechanisms regulating mERα levels have remained elusive.[52] However, there is compelling evidence that activated mERα can be internalised from the plasma membrane into cells.[53] The mERα activation and internalisation play an important role in proliferation and other cellular functions.[54] To investigate the role of mERα on ERα-AuNPs internalisation, MCF-7 cells were pre-blocked with anti-ERα antibody (10 μg/mL, 1 h), which has been designed to bind to the ligand-binding site of ERα. Therefore, the free anti-ERα antibodies will compete with the anti-ERα antibodies functionalised on the nanotags. The results demonstrate that a suppression effect was observed in MCF-7 cells pre-blocked with free anti-ERα antibody since there was a much lower ERα-AuNPs accumulation in the pre-treated with free ERα antibody MCF-7 cells (Figure 13A). Specifically, the 2D SERS maps showed that the signal was produced around the cell indicating the presence of the nanotags in the cell membrane and the absence of SERS signal in the interior of the cell (Figure 13B). To further confirm this statement, 3D SERS mapping was performed in the untreated and pre-blocked with free anti-ERα antibody MCF-7 cells using a Renishaw InVia Raman microscope with 633 nm wavelength excitation at step size y,x=1.0 μm and z= 3.0 μm. The 3D SERS images showed that SERS signal was observed throughout the cell only in the untreated samples (Figure 13D, 13F). However, when the cells were pre-blocked with anti-ERα antibody, there was a significant reduction in the SERS signal though the z-plane (Figure 13E, 13G). Specifically, the SERS signal generated mostly from areas closer to the cell membrane than intracellularly, suggesting that ERα-AuNPs were adhered to the cell surface and not internalised. The exact points in the cells that were used for the generation of SERS spectra throughout the z-axis are shown in Figure 14. Coupling these 3D SERS results with the 2D Raman mapping, there is a clear indication that mERα appeared to interact with the ERα-AuNPs and, therefore, the nanotags were using ERα receptor-mediated endocytosis for their uptake. These data agreed on the low temperature experiments, as low temperature slowed down the ligand-receptor binding rate which led to decreased internalisation of ERα-AuNPs. Therefore, there was a clear indication that ERα-AuNP SERS nanotags enter MCF-7 cells through a receptor-mediated endocytosis mechanism. Studies have also shown that there are other ER-like membrane receptors such as ER-X and GPR30 that can be activated upon ligand binding.[55,56] Therefore, future studies should be performed to investigate if the presence of these receptors has any possible contribution to the cellular uptake of the ERα-AuNP nanotags.

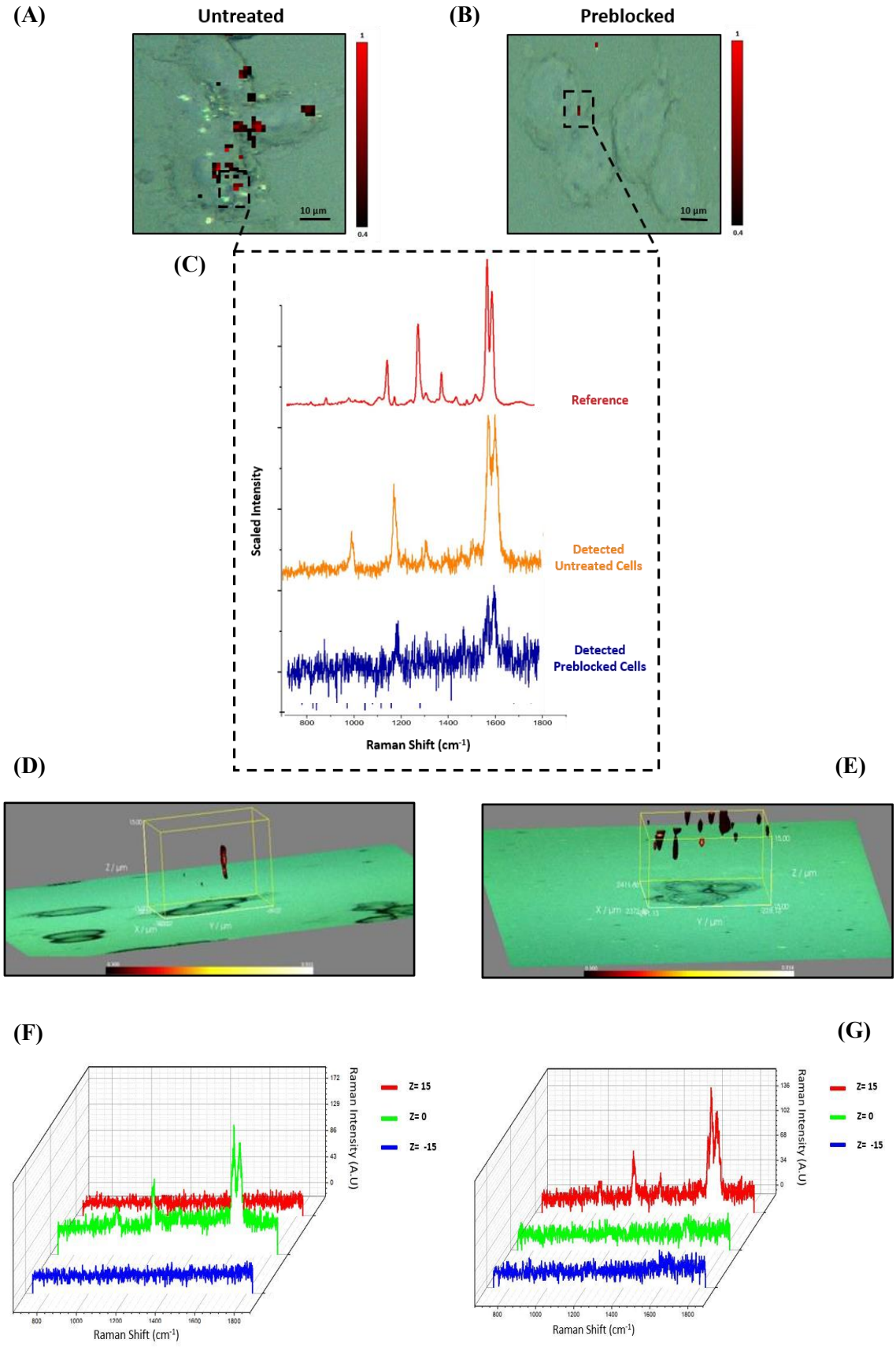
(A)
Untreated
(B)
Preblocked
10 µm
10 µm
(C)
Reference
Detected Untreated Cells
Detected Preblocked Cells
Scaled Intensity
Raman Shift (cm-1)
(D)
(E)
(F)
(G)
Z= 15
Z= 0
Z= -15
Raman Intensity (A.U)
Raman Shift (cm-1)

Figure 13: ERα-AuNPs use mERα for their cellular uptake in MCF-7 cells. **(A)** False colour SERS map images for MCF-7 cells incubated with only ERα-AuNP nanotags (60 pM, 2 h) or **(B)** pre-blocked with free anti-ERα antibody (10 µg/ mL, 1 h) and then treated with ERα-AuNP nanotags (60 pM, 2 h). The images were generating using a Renishaw InVia Raman microscope with 50× magnification NIR APO Nikon water immersion objective with a 1.0 NA and 1.2 mW laser power (10% power) from a HeNe 633 nm excitation source with step size y,x 1.0 µm, 0.1s acquisition time and a 1200 l/mm grating in high confocality mode. The minimum and maximum look up table thresholds were set to exclude any poorly correlating or noisy spectra (min= 0.4). Scale bar= 10 µm **(C)** Average SERS spectra from untreated (orange) and pre-blocked with free anti-ERα antibody (blue) cells stacked with reference spectrum from nanotags (red). **(D)** 3D SERS map from MCF-7 cells treated with only ERα-AuNPs (60 pM, 2h) and **(E)** MCF-7 cells pre-blocked with free anti-ERα antibody (10 µg/ mL, 1 h) and then treated with ERα-AuNP nanotags (60 pM, 2 h). 3D SERS images were generating using a Renishaw InVia Raman microscope with 50× magnification NIR APO Nikon water immersion objective with a 1.0 NA and 1.2 mW laser power (10% power) from a HeNe 633 nm excitation source with step size y,x=1.0 µm and z= 3.0 µm, 0.1 s acquisition time and a 1200 l/mm grating in high confocality mode. **(F)** 3D Raman mapping waterfall plot of average SERS spectra into different z-axis points, z= 15 µm (red), z= 0 µm (green) and z= -15 µm (blue) from MCF-7 cells treated with only ERα-AuNPs (60 pM, 2 h) or **(G)** with free anti-ERα antibody (10 µg/ mL, 1 h) and then treated with ERα-AuNP nanotags (60 pM, 2 h).

(A) **(B)**

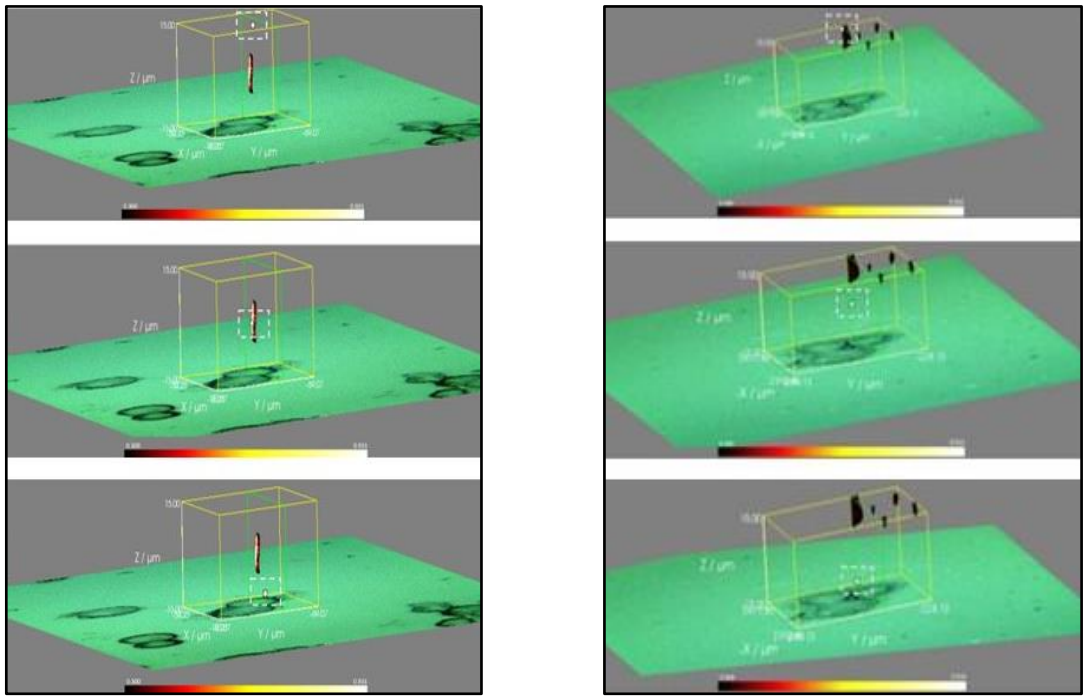

Figure 14: 3D Raman mapping results and SERS spectra detected from different z-axis points. The white dashed box depicting the z-axis of the image from where the SERS signal was extracted. (A) Untreated MCF-7 cells: as the z-axis moves from top to bottom of the cell, the BPE labelled ERα -PEG5000-AuNPs signal appeared throughout the MCF-7 cell. (B) When the cells were preblocked with free anti-ERα antibody (10 µg/mL, 1 h) there was a significant reduction in the SERS signal throughout the z-axis. 3D SERS images were generating using a Renishaw InVia Raman microscope with 50× magnification NIR APO Nikon water immersion objective with a 1.0 NA and 1.2 mW laser power (10% power) from a HeNe 633 nm excitation source with step size y,x=1.0 µm and z= 3.0 µm, 0.1 s acquisition time and a 1200 l/mm grating in high confocality mode. The minimum and maximum look up table thresholds were set to exclude any poorly correlating or noisy spectra (min= 0.4). Coupling the data with the 2D Raman mapping, there is an indication that ERα-AuNPs did not enter the MCF-7 cells when they were preblocked with the anti-ERα antibody.

2.5 Conclusion

In this study, we investigated the cellular uptake of gold nanoparticles functionalised with an anti-ERα antibody and BPE Raman reporter (ERα-AuNPs) using non-destructive 2D and 3D SERS imaging approaches. 3D SERS cell mapping confirmed that ERα-AuNPs cellular uptake was temperature-dependent, excluding the scenario of the passive transport way for their internalisation. 3D SERS images also confirmed that dynamin was responsible, at least in a part, for the intracellular delivery of ERα-AuNPs in MCF-7 cells. Specifically, the 3D SERS suggested that ERα-AuNPs adhered to plasma membrane due to the blocking of constriction and fission of the forming endocytic vesicles (Figure 15A). This mechanism suggests that ERα-AuNPs are internalised in an endocytosis vesicle that is expected to release its cargo (ERα-AuNPs) inside the cell. Additionally, 3D SERS images showed that ERα-AuNPs entered MCF-7 cells using receptor-mediated endocytosis after their binding to ERα located in the plasma membrane of the cells (Figure 15B). Hence, this study has provided an important biological insight into the intracellular uptake of nanotags by generating 3D SERS images of the entire cell volume, whilst maintaining the integrity of the cell. The novelty of this work also relied on the development of an accurate way for calculating the relative SERS response value in MCF-7 cells to obtain a qualitative indication for the nanotags uptake per condition. In this way it was possible to acquire a relative assessment of ERα-AuNPs internalisation without the need for destructive, time consuming and expensive imaging, such as TEM. The study gives important insights into the uptake of functionalised SERS nanotags where a crucial fundamental understanding is required for their application in diagnostics and targeted drug delivery systems. Therefore, it is highlighted that SERS can be used as an excellent tool for investigating nanotags cellular uptake mechanisms for their potential use in cell imaging applications.

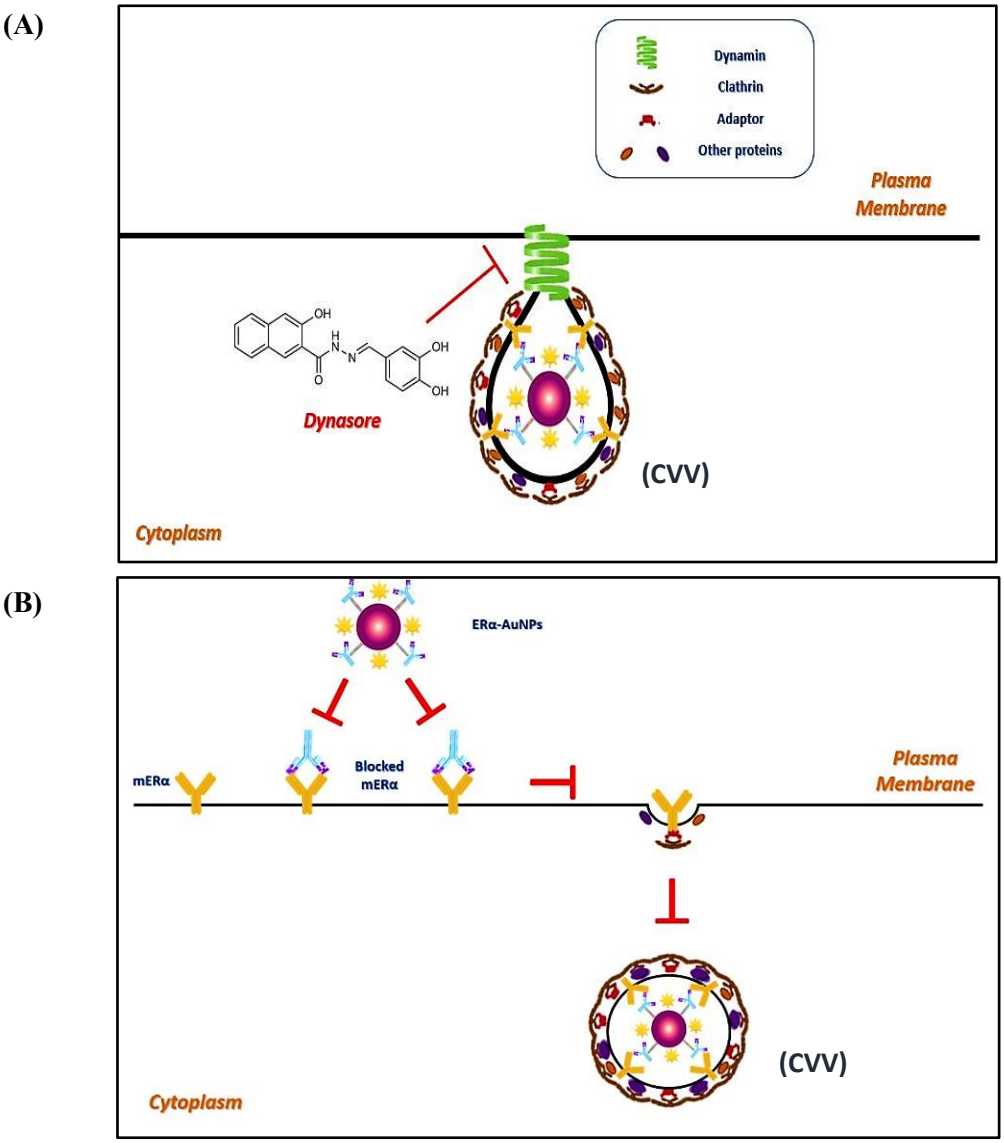

Figure 15: ERα-AuNPs are using dynamin and mERα for their internalisation in MCF-7 cells. **(A)** Schematic representing the action of dynasore in mammalian cells. Clathrin coated vesicle (CCV) is formed, and cargo-specific adaptors are selected after the incubation of ERα-AuNP nanotags. Dynamin is recruited to the neck of the forming vesicle to induce plasma membrane scission. Dynasore inhibits the GTPase activity of dynamin, blocking constriction and fission and, therefore, nanotags are trapped into the submembrane regions. **(B)** Schematic diagram of blocking mERα in MCF-7 cells with the free anti-ERα antibody. Free anti-ERα antibodies compete with anti-ERα antibodies attached on nanotags, resulting in blocking of ERα-AuNPs internalization via mERα-mediated endocytosis. CCV is, therefore, not formed. In normal conditions, for their internalisation, ERα-AuNPs first bind to mERα, forming a mERα-ERα-AuNPs complex. The complex binds the coat proteins, and CCV assembly begins. The CCV either grows to form a vesicle and the ERα-AuNP is then internalized.

2.6 References

1. Laing, S., Gracie, K. & Faulds, K. Multiplex in vitro detection using SERS. *Chemical Society Reviews* (2016). doi:10.1039/c5cs00644a
2. Noonan, J. *et al.* In vivo multiplex molecular imaging of vascular inflammation using surface-enhanced Raman spectroscopy. *Theranostics* (2018). doi:10.7150/thno.28665
3. Smith, B. R. & Gambhir, S. S. Nanomaterials for in Vivo Imaging. *Chemical Reviews* (2017). doi:10.1021/acs.chemrev.6b00073
4. Dutta, D. & Donaldson, J. G. Search for inhibitors of endocytosis Intended specificity and unintended consequences. *Cellular Logistics* (2012). doi:http://dx.doi.org/10.4161/cl.23967
5. Shang, L., Nienhaus, K. & Nienhaus, G. U. Engineered nanoparticles interacting with cells: Size matters. *Journal of Nanobiotechnology* (2014). doi:10.1186/1477-3155-12-5
6. Huang, X., Teng, X., Chen, D., Tang, F. & He, J. The effect of the shape of mesoporous silica nanoparticles on cellular uptake and cell function. *Biomaterials* (2010). doi:10.1016/j.biomaterials.2009.09.060
7. Lesniak, A. *et al.* Effects of the presence or absence of a protein corona on silica nanoparticle uptake and impact on cells. *ACS Nano* (2012). doi:10.1021/nn300223w
8. Mironava, T., Hadjiargyrou, M., Simon, M., Jurukovski, V. & Rafailovich, M. H. Gold nanoparticles cellular toxicity and recovery: Effect of size, concentration and exposure time. *Nanotoxicology* (2010). doi:10.3109/17435390903471463
9. Albanese, A., Tang, P. S. & Chan, W. C. W. The Effect of Nanoparticle Size, Shape, and Surface Chemistry on Biological Systems. *Annual Review of Biomedical Engineering* (2012). doi:10.1146/annurev-bioeng-071811-150124
10. Pannico, M., Calarco, A., Peluso, G. & Musto, P. Functionalized Gold Nanoparticles as Biosensors for Monitoring Cellular Uptake and Localization in Normal and Tumor Prostatic Cells. *Biosensors* (2018). doi:10.3390/bios8040087
11. Escudero-Francos, M. A. *et al.* Cellular uptake and tissue biodistribution of functionalized gold nanoparticles and nanoclusters. *Journal of Biomedical Nanotechnology* (2017). doi:10.1166/jbn.2017.2344
12. Chaudhuri, A., Battaglia, G. & Golestanian, R. The effect of interactions on the cellular uptake of nanoparticles. *Physical Biology* (2011). doi:10.1088/1478-3975/8/4/046002
13. Gao, H. *et al.* Ligand modified nanoparticles increases cell uptake, alters endocytosis and

elevates glioma distribution and internalization. *Scientific Reports* (2013). doi:10.1038/srep02534

14. Taylor, A., Wilson, K. M., Murray, P., Fernig, D. G. & Lévy, R. Long-term tracking of cells using inorganic nanoparticles as contrast agents: Are we there yet? *Chemical Society Reviews* (2012). doi:10.1039/c2cs35031a
15. Yameen, B. *et al.* Insight into nanoparticle cellular uptake and intracellular targeting. *Journal of Controlled Release* (2014). doi:10.1016/j.jconrel.2014.06.038
16. Tang, H., Zhang, H., Ye, H. & Zheng, Y. Receptor-Mediated Endocytosis of Nanoparticles: Roles of Shapes, Orientations, and Rotations of Nanoparticles. *Journal of Physical Chemistry B* (2018). doi:10.1021/acs.jpcb.7b09619
17. Cho, E. C., Zhang, Q. & Xia, Y. The effect of sedimentation and diffusion on cellular uptake of gold nanoparticles. *Nature Nanotechnology* (2011). doi:10.1038/nnano.2011.58
18. Chithrani, D. B. Intracellular uptake, transport, and processing of gold nanostructures. *Molecular Membrane Biology* (2010). doi:10.3109/09687688.2010.507787
19. Jin, H., Heller, D. A., Sharma, R. & Strano, M. S. Size-dependent cellular uptake and expulsion of single-walled carbon nanotubes: Single particle tracking and a generic uptake model for nanoparticles. *ACS Nano* (2009). doi:10.1021/nn800532m
20. Shen, Z., Ye, H. & Li, Y. Understanding receptor-mediated endocytosis of elastic nanoparticles through coarse grained molecular dynamic simulation. *Physical Chemistry Chemical Physics* (2018). doi:10.1039/c7cp08644j
21. Rejman, J., Oberle, V., Zuhorn, I. S. & Hoekstra, D. Size-dependent internalization of particles via the pathways of clathrin- and caveolae-mediated endocytosis. *The Biochemical journal* (2004). doi:10.1042/BJ20031253
22. Brown, A. P., Brydson, R. M. D. & Hondow, N. S. Measuring in vitro cellular uptake of nanoparticles by transmission electron microscopy. in *Journal of Physics: Conference Series* (2014). doi:10.1088/1742-6596/522/1/012058
23. Basuki, J. S. *et al.* Using fluorescence lifetime imaging microscopy to monitor theranostic nanoparticle uptake and intracellular doxorubicin release. *ACS Nano* (2013). doi:10.1021/nn404407g
24. Torrano, A. A. *et al.* A fast analysis method to quantify nanoparticle uptake on a single cell level. *Nanomedicine* (2013). doi:10.2217/nnm.12.178
25. Michalet, X. *et al.* Quantum dots for live cells, in vivo imaging, and diagnostics. *Science* (2005). doi:10.1126/science.1104274

26. Dougan, J. A. & Faulds, K. Surface enhanced Raman scattering for multiplexed detection. *Analyst* (2012). doi:10.1039/c2an15979a
27. Harper, M. M., McKeating, K. S. & Faulds, K. Recent developments and future directions in SERS for bioanalysis. *Physical Chemistry Chemical Physics* (2013). doi:10.1039/c2cp43859c
28. Lee, S. *et al.* Rapid and sensitive phenotypic marker detection on breast cancer cells using surface-enhanced Raman scattering (SERS) imaging. *Biosensors and Bioelectronics* (2014). doi:10.1016/j.bios.2013.07.063
29. McAughtrie, S., Lau, K., Faulds, K. & Graham, D. 3D optical imaging of multiple SERS nanotags in cells. *Chemical Science* (2013). doi:10.1039/c3sc51437d
30. Craig, D. *et al.* Confocal SERS mapping of glycan expression for the identification of cancerous cells. *Analytical Chemistry* (2014). doi:10.1021/ac4038762
31. Stevenson, R. *et al.* Analysis of intracellular enzyme activity by surface enhanced Raman scattering. *Analyst* (2013). doi:10.1039/c3an00729d
32. Xiao, L., Harihar, S., Welch, D. R. & Zhou, A. Imaging of epidermal growth factor receptor on single breast cancer cells using surface-enhanced Raman spectroscopy. *Analytica Chimica Acta* (2014). doi:10.1016/j.aca.2014.06.036
33. Jamieson, L. E. *et al.* Simultaneous intracellular redox potential and pH measurements in live cells using SERS nanosensors. *Analyst* (2015). doi:10.1039/c4an02365j
34. Zhang, G. *et al.* Controlling carbon encapsulation of gold nano-aggregates as highly sensitive and spectrally stable SERS tags for live cell imaging. *Journal of Materials Chemistry B* (2013). doi:10.1039/c3tb20801j
35. J. Turkevich; P.C. Stevenson; J. Hiller. Synthesis of Gold Nanoparticles Turkevich method. *Faraday Discuss.* (1951). doi:10.13140/RG.2.2.15238.37449
36. Guide, M. U. The MathWorks Inc. *Natick, MA* (2014).
37. Schindelin, J. *et al.* Fiji: An open-source platform for biological-image analysis. *Nature Methods* (2012). doi:10.1038/nmeth.2019
38. Yang, J. *et al.* Distinguishing breast cancer cells using surface-enhanced Raman scattering. *Analytical and Bioanalytical Chemistry* (2012). doi:10.1007/s00216-011-5577-z
39. Albertazzi, L., Fernandez-Villamarin, M., Riguera, R. & Fernandez-Megia, E. Peripheral functionalization of dendrimers regulates internalization and intracellular trafficking in living cells. *Bioconjugate Chemistry* (2012). doi:10.1021/bc300079h

40. Zhou, F. *et al.* New insights of transmembranal mechanism and subcellular localization of noncovalently modified single-walled carbon nanotubes. *Nano Letters* (2010). doi:10.1021/nl100004m
41. Lacy, M. M., Ma, R., Ravindra, N. G. & Berro, J. Molecular mechanisms of force production in clathrin-mediated endocytosis. *FEBS Letters* (2018). doi:10.1002/1873-3468.13192
42. Wang, C. *et al.* Differential Regulation of Clathrin and Its Adaptor Proteins during Membrane Recruitment for Endocytosis. *Plant Physiology* (2016). doi:10.1104/pp.15.01716
43. Cocucci, E., Gaudin, R. & Kirchhausen, T. Dynamin recruitment and membrane scission at the neck of a clathrin-coated pit. *Molecular Biology of the Cell* (2014). doi:10.1091/mbc.e14-07-1240
44. Antonny, B. *et al.* Membrane fission by dynamin: what we know and what we need to know. *The EMBO Journal* (2016). doi:10.15252/embj.201694613
45. Marczell, I. *et al.* Membrane-bound estrogen receptor alpha initiated signaling is dynamin dependent in breast cancer cells. *European Journal of Medical Research* (2018). doi:10.1186/s40001-018-0328-7
46. Macia, E. *et al.* Dynasore, a Cell-Permeable Inhibitor of Dynamin. *Developmental Cell* (2006). doi:10.1016/j.devcel.2006.04.002
47. Irannejad, R., Tsvetanova, N. G., Lobingier, B. T. & von Zastrow, M. Effects of endocytosis on receptor-mediated signaling. *Current Opinion in Cell Biology* (2015). doi:10.1016/j.ceb.2015.05.005
48. Mellman, I. ENDOCYTOSIS AND MOLECULAR SORTING. *Annual Review of Cell and Developmental Biology* (2002). doi:10.1146/annurev.cellbio.12.1.575
49. Pedram, A., Razandi, M., Lewis, M., Hammes, S. & Levin, E. R. Membrane-localized estrogen receptor α is required for normal organ development and function. *Developmental Cell* (2014). doi:10.1016/j.devcel.2014.04.016
50. Adlanmerini, M. *et al.* Mutation of the palmitoylation site of estrogen receptor in vivo reveals tissue-specific roles for membrane versus nuclear actions. *Proceedings of the National Academy of Sciences* (2014). doi:10.1073/pnas.1322057111
51. La Rosa, P., Pesiri, V., Leclercq, G., Marino, M. & Acconcia, F. Palmitoylation Regulates 17β-Estradiol-Induced Estrogen Receptor-α Degradation and Transcriptional Activity. *Molecular Endocrinology* (2012). doi:10.1210/me.2011-1208

52. Levin, E. R. Rapid signaling by steroid receptors. *AJP: Regulatory, Integrative and Comparative Physiology* (2008). doi:10.1152/ajpregu.90605.2008

53. Bondar, G., Kuo, J., Hamid, N. & Micevych, P. Estradiol-Induced Estrogen Receptor-Trafficking. *Journal of Neuroscience* (2009). doi:10.1523/JNEUROSCI.2107-09.2009

54. Zivadinovic, D., Gametchu, B. & Watson, C. S. Membrane estrogen receptor-α levels in MCF-7 breast cancer cells predict cAMP and proliferation responses. *Breast Cancer Research* (2004). doi:10.1186/bcr958

55. Micevych, P. E. & Kelly, M. J. Membrane estrogen receptor regulation of hypothalamic function. *Neuroendocrinology* (2012). doi:10.1080/02664763.2014.999030

56. Dominguez, R., Dewing, P., Kuo, J. & Micevych, P. Membrane-initiated estradiol signaling in immortalized hypothalamic N-38 neurons. in *Steroids* (2013). doi:10.1016/j.steroids.2012.12.008

57. Nicolson, F. *et al.* Through barrier detection of ethanol using handheld Raman spectroscopy—Conventional Raman versus spatially offset Raman spectroscopy (SORS). *Journal of Raman Spectroscopy* (2017). doi:10.1002/jrs.5258

3. Characterisation of Estrogen Receptor Alpha (ERα) Positive Breast Cancer Cells and Understanding of Fulvestrant Activity Using SERS

Contributing authors:

Anastasia Kapara[1,2], Valerie Brunton[2], Duncan Graham[1], Karen Faulds[1]

1. Centre for Molecular Nanometrology, Department of Pure and Applied Chemistry, Technology and Innovation Centre, University of Strathclyde, 99 George Street, Glasgow G1 1RD, UK.

2. MRC Institute of Genetics and Molecular Medicine, Edinburgh Cancer Research UK Centre, University of Edinburgh, Western General Hospital, Crewe Road South, Edinburgh, EH4 2XU, UK

3.1 Abstract

Estrogen receptor alpha (ERα) is one of the main breast cancer biomarkers, which plays a pivotal role in therapeutic decision making and in determining breast cancer's clinical outcome. Therefore, the detection and identification of ERα in breast cancer cells are crucial for the clinical diagnosis and therapy of the disease. Here, we aim to use a non-destructive approach for detecting and localising ERα at the single cell level using surface enhanced Raman spectroscopy (SERS) combined with functionalised gold nanoparticles (AuNPs). Specifically, anti-ERα antibody functionalised AuNPs (ERα-AuNPs) were synthesised to enable the spatial and temporal understanding of where ERα was located in cell lines with different ERα expression status. To investigate the ability of ERα-AuNP nanotags to discriminate breast cancer phenotype, MCF-7 ($ERα^+$) and SKBR-3 ($ERα^-$) breast cancer cells were chosen as cell models. The experimental results indicated that ERα-AuNPs showed excellent biocompatibility since breast cancer cells had high viability after their incubation with ERα-AuNPs. Additionally, SERS cell imaging showed that MCF-7 cells exhibited a much stronger SERS signal and higher nanotag accumulation in comparison to SKBR-3. This result verified the strong labelling specificity of the nanotags for the ERα positive cells and suggested that ERα-AuNPs could potentially be used as a tool for identifying and characterising different breast cancer cell lines. ERα-AuNPs were also used for investigating the efficacy of fulvestrant, the first-in-class approved selective estrogen receptor degrader (SERD). SERS mapping confirmed the ERα degradation occurred after fulvestrant treatment since a weaker SERS signal, and hence nanotags accumulation was observed in MCF-7 cells treated with fulvestrant. These results further confirmed that ERα-AuNP nanotags can be used as a tool for the classification of breast cancer cells, based on the ERα expression, and the understanding of SERDs efficacy in breast cancer.

Keywords: Surface-enhanced Raman scattering, ERα, cancer targeting, drug efficacy, fulvestrant, MCF-7, SKBR-3

3.2 Introduction

Breast cancer is a major disease and the leading cause of oncologic mortality and morbidity among women worldwide.[1,2] In the UK, one person is diagnosed with breast cancer every 10 minutes, which makes the disease the most common cancer and one of the leading causes of death in women.[3] Current statistics also suggest than one in eight women will develop breast cancer at some point in their lifetime and more than 71,000 new cases are expected to be diagnosed by 2035 in the UK.[3] Approximately 75% of primary breast tumours are diagnosed as being positive for a hormone receptor, which can either be progesterone (PR) or the estrogen receptor alpha (ERα).[4] ERα is a ligand-activated transcription factor, which regulates the expression of sequences containing specific hormone response elements responsible for body functions in the reproductive system[5], immune system[6], bones[7] and brain[8]. In the UK, the phenotype of around three-quarters of all breast cancers is characterised by the presence of ERα[3,9,10] Therefore, ERα is a key receptor biomarker whose status plays a pivotal role in the classification of breast cancer subtypes, since its overexpression is related with increased proliferation and metastasis in breast cancer[11] which makes it an important marker for prediction of the likelihood of a patient developing metastatic disease.[12] Hence, the accurate assessment of ERα status is essential for diagnosis and treatment decision making for breast cancer patients.

Currently, the most commonly used methods for assessing and characterising ERα in human breast cancer cell lines are immunofluorescence[13,14], western blotting[15] and reverse transcription polymerase chain reaction (RT-PCR).[16] Although these methods can be useful for measuring ERα expression, there are still technical limitations as these approaches are destructive, require processed/fixed samples[17,18] and are not always suitable for *in viv*o use. Immunofluorescence uses fluorescent dyes which usually have high background signals[19] and limited multiplexing capabilities. Additionally, western blot and RT-PCR involve time-consuming experimental steps which require cell lysis and cellular subfractionation.[20,21]

Surface-enhanced Raman spectroscopy (SERS) has attracted considerable interest as a non-invasive optical technique with unique advantages, such as narrow spectral bands that increase the multiplexing capabilities, high sensitivity, selectivity and specificity.[22,23,24] Most importantly, SERS allows the detection of single nanotags and enables the spatial and temporal understanding of where a molecule is located at a single cell level.

SERS nanotags have been successfully synthesised for various bioanalytical characterisation of cancers[25,26] including breast cancer.[27,28,29] The design of SERS nanotags usually involves attaching Raman reporters to the surface of gold (Au) or silver (Ag) nanoparticles (NPs) and functionalising with a specific targeting biomolecule, such as monoclonal antibodies, drugs or DNA sequences.[30] Poly-ethylene glycol (PEG) can also be attached to the nanoparticles to decrease the toxic effects[31], reduce non-specific cellular internalisation[32], facilitate longer circulation time in biological fluids[33] and reduce aggregation of nanotags in biological solutions.[34] These nanotags can be introduced to unprocessed samples in a range of *in vitro*, *ex vivo* and *in vivo* applications making SERS a powerful bioanalytical tool for early tumour identification and characterisation.

Here, anti-ERα antibody functionalised AuNPs (ERα-AuNPs) were developed for characterising and distinguishing breast cancer cells with different ERα statuses using SERS. In parallel, we were able to investigate the efficacy of fulvestrant, a commercially available ERα degrader. To our knowledge, this is the first study where the assessment of SERS response per cell has been utilised to characterise ERα cancer phenotype at a single cell level and inform about fulvestrant drug activity. This is a novel first step towards using SERS for both diagnosis and investigation of the efficacy of SERDs drugs in breast cancer. This research opens up potential future personalised clinical approaches where patient derived samples could be screened for assessing the receptor status and the treatment efficacy for overcoming late diagnosis and drug resistance outcomes.

3.3 Experimental

3.3.1 Materials

As previously described in 2.3.1.

3.3.2 Nanoparticle Synthesis and Functionalisation of ERα-AuNPs

As previously described in 2.3.2.

3.3.3 Nanotags Characterisation

As previously described in 2.3.3.

3.3.4 Cell Culture Conditions

MCF-7 cells (ATCC® HTB-22™) and SKBR-3 (ATCC® HTB-30™) were obtained from American Type Culture Collection (ATCC) (Queens Road, Teddington, Middlesex, TW11 0LY, UK). Cells were maintained between passage number 5 and 30. The human breast cancer cells were cultured in Rosewell Park Memorial Institute medium (RPMI 1640) supplemented with 1% penicillin/streptomycin (10000 units per mL), 1% fungizone, and 10% heat-inactivated fetal bovine serum (FBS). Cells were incubated under humidified 37 °C and 5% CO_2 in a humidified incubator. Cells at a confluence of ca. 90% growing in a T175 flask were trypsinised and re-suspended in medium to give a concentration of ca. 1×10^6 cells per mL.

3.3.5 ERα-AuNPs and Fulvestrant Treatment

MCF-7 cells ($1x10^6$ cells per mL) were seeded onto sterile 22-mm square glass coverslips with culture medium. ERα-AuNP nanotags (60 pM, 2h) were incubated with the cells at 37 °C, 5% CO_2 in a humidified incubator. The coverslips were washed in PBS three times and fixed in 4% paraformaldehyde for 15 min. For assessing fulvestrant activity, MCF-7 cells ($1x10^6$ cells per mL) seeded onto sterile 22-mm square glass coverslips and treated with 1% DMSO (control) or with fulvestrant (500 nM and 1 µM) for 24 h. ERα-AuNPs (60 pM) were then added to cells for 2 h. The coverslips were washed in PBS three times and fixed in 4% paraformaldehyde for 15 min. All fixed cells were washed in PBS and dH_20 and left to air dry before mounting on a standard glass microscope slide for SERS imaging.

3.3.6 Western Blot Experiments After Fulvestrant Treatment

Cells ($1x10^6$ per mL) were plated in 10 cm diameter dishes with 10 mL RPMI and left for 24 h before fulvestrant treatment (0.01 µM to 1 µM, 24 h). The next day the media was aspirated from the culture. The treatments were washed in ice cold PBS twice and were lysed with 200 µL of ice cold RIPA buffer (#10017003, Thermo Fisher), containing protease and phosphatase inhibitors (# A32959, Pierce). The cells were immediately scraped off the plate and their extracts were transferred to a microcentrifuge tube. The samples were kept on ice for 15 min and were centrifuged at 14,000 rpm for 15 min at 4 ºC. The cell lysate supernatant was then used for protein quantification using the BCA assay. The cell lysate samples (20 µL, 1 mg/mL) were diluted with

5X SDS loading buffer, heated to 95 ºC for 5 mins and microcentrifuged for 5 min at RT. 20 µL of the denatured cell lysate was loaded into a 12% gel (Mini Protean TGX stain free Pre-cast gels, #456-8085, Bio-Rad) and run at 140 V for 40 min. A prestained molecular weight marker (5 µL) was also loaded into the gel to determine the molecular weights of the proteins. The gel was electrotransferred to a 0.2 µm nitrocellulose membrane (#170-4159, Bio-Rad) with the BioRad TransBlot Turbo Transfer System using the Midi gel 10 mins transfer setting. The membrane was blocked with 5% BSA blocking buffer for 1 hr at room temperature. After blocking, the membrane was incubated at 4 ºC overnight whilst rocking with the appropriate primary antibody diluted in 5 mL 5% w/v BSA, 1X TBS, 0.1% Tween 20. The next day the membrane was washed three times for 5 min each with 15 mL of TBST buffer (1.5% Tween 20 in 1x TBS). The membrane was incubated with the appropriate secondary antibody in 10 ml of 5% BSA blocking buffer with gentle agitation for 1hr at room temperature and was washed three times for 5 mins each with 15 mL of TBST buffer afterwards. Finally, for the detection of the proteins, the membrane was incubated with 1:1 of Pierce™ ECL western blotting substrate (# 32106, Thermo Fisher) for 1 min. Finally, a Bio-Rad ChemiDoc MP Imaging System- Universal Hood III with Image Lab V.4.1 software was used to image and quantify the protein levels on the membrane.

3.3.7 Fluorescence Microscopy

MCF-7 cells were seeded onto a 6-well plate ($1x10^6$ cells per mL) and incubated at 37 °C and 5% CO_2 for 24 h. After 24 h the cells were washed in PBS three times and fixed in 4% paraformaldehyde for 15 min at room temperature. The fixed cells were permeabilised with 0.1% Triton X-100 in PBS for 10 min. The cells were then washed in PBS three times for 5 min. Then, the cells were blocked with 1% BSA, 22.52 mg/mL glycine in 0.1% PBS-Tween for 1 h. The cells were then incubated with the diluted antibody (ab16660) (1/200 dilution in 1% BSA in PBS-Tween) overnight at 4 ºC. The cells were then washed in PBS three times for 5 min. Finally, the cells were incubated with the secondary antibody (Alexa Fluor® 647) (1/200 dilution in 1% BSA) for 1 h at room temperature in the dark. The cells were then washed in PBS three times for 5 min and 1 µg/mL of DAPI (DNA stain) was added for 10 min. The images were generated using a Leica Microsystems TCS SP8 with continuous wave visible lasers and Leica DMi8 inverted microscope and DFC 7000T and TL LED cameras. The software was Leica Application Suite X V.3.1.5.16308 to carry out live/dead studies a 63× magnification HC PL APO water objective with

a 1.2 NA was used. Intensity and area of fluorescence were measured using Image J (National Institute of Health (NIH)) software with Fiji plug-in to measure the area of the fluorescent stain.[35]

3.3.8 Raman Cell Mapping

As previously described in 2.3.9.

3.3.9 Calculation of Relative SERS Response Value in MCF-7 Cells

As previously described in 2.3.10.

3.3.10 Statistical Analysis

As previously described in 2.3.11.

3.4 Results and Discussion

3.4.1 Effects of ERα-AuNPs on Cell Viability

The nanoparticle synthesis and characterisation of ERα-AuNPs have been previously discussed in section 2.4.1. Here, to validate the ability of SERS nanotags to identify and distinguish breast cancer cells with different ERα statuses, two breast cancer cell lines, ERα-positive MCF-7 cells and ERα-negative SKBR-3 cells were chosen.[36] Previous western blot experiments showed that ERα protein was detectable only in MCF-7 cells but not in the SKBR-3 cells (as previously shown in 2.4.2). Immunofluorescence experiments also confirmed that ERα was highly expressed in MCF-7 cells, in contrast to SKBR-3 where there was no detectable ERα (Figure 1).

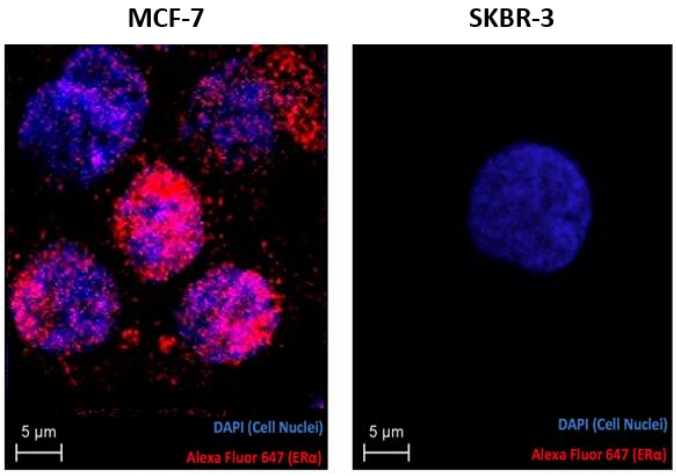

Figure 1: Immunofluorescence analysis for ERα distribution in MCF-7 and SKBR-3 cells. ERα expression was detected in MCF-7 cells in contrast to SKBR-3 cells. ERα was stained with Alexa Fluor® 647 (red) and nuclei stained with DAPI (blue). Scale bar= 5µm.

Before introducing the ERα-AuNPs in cells, their cytotoxicity was assessed in MCF-7 and SKBR-3 cells. 60 pM of nanotags, with and without anti-ERα antibody functionalisation, were incubated with cells for 2 h before cell viability experiments. As described in 2.4.3, the viability in MCF-7 cells treated with ERα-AuNPs was over 97%. Similarly, SKBR-3 cells treated with ERα-AuNP nanotags exhibited 99% viability in contrast to PEG5000-AuNPs (94% cell viability) and BPE-AuNPs (81% cell viability) (Figure 2). These results indicated that the ERα-AuNPs showed good biocompatibility and did not cause any detectable cell toxicity.

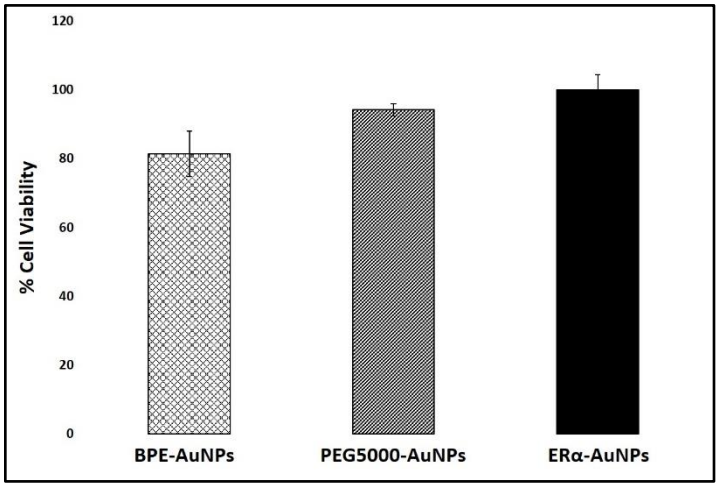

Figure 2: Cell viability carried out using trypan blue cell viability assay for SKBR-3 cells following treatment with 60 pM BPE-AuNPs, 60 pM PEG5000-AuNPs or 60 pM ERα-AuNPs for 48 h Data are expressed as the mean ± standard deviation of experiments performed in three biological repeats.

3.4.2 Characterisation of Breast Cancer Cells Using SERS

To characterise the breast cancer cell phenotype based on the ERα expression, MCF-7 cells and SKBR-3 cells were incubated with the ERα-AuNP nanotags under the same conditions (60 pM, 2 h). SERS imaging showed that ERα-AuNPs were more accumulated in MCF-7 cells rather than SKBR-3 cells (Figure 3A). Additionally, the average SERS signal, calculated from ten cells in three independent biological replicates, showed that MCF-7 cells had a higher and less noisy SERS spectrum compared to SKBR-3 cells (Figure 3B). Specifically, the SERS intensity of BPE Raman reporter (attached on ERα-AuNPs) at 1610 cm^{-1} (highest peak intensity) was statistically significant higher in MCF-7 in comparison to SKBR-3 cells (4.5-times higher) (Figure 3C). Therefore, 2D SERS showed that ERα-AuNP nanotags were specifically associated with the ERα positive cells.

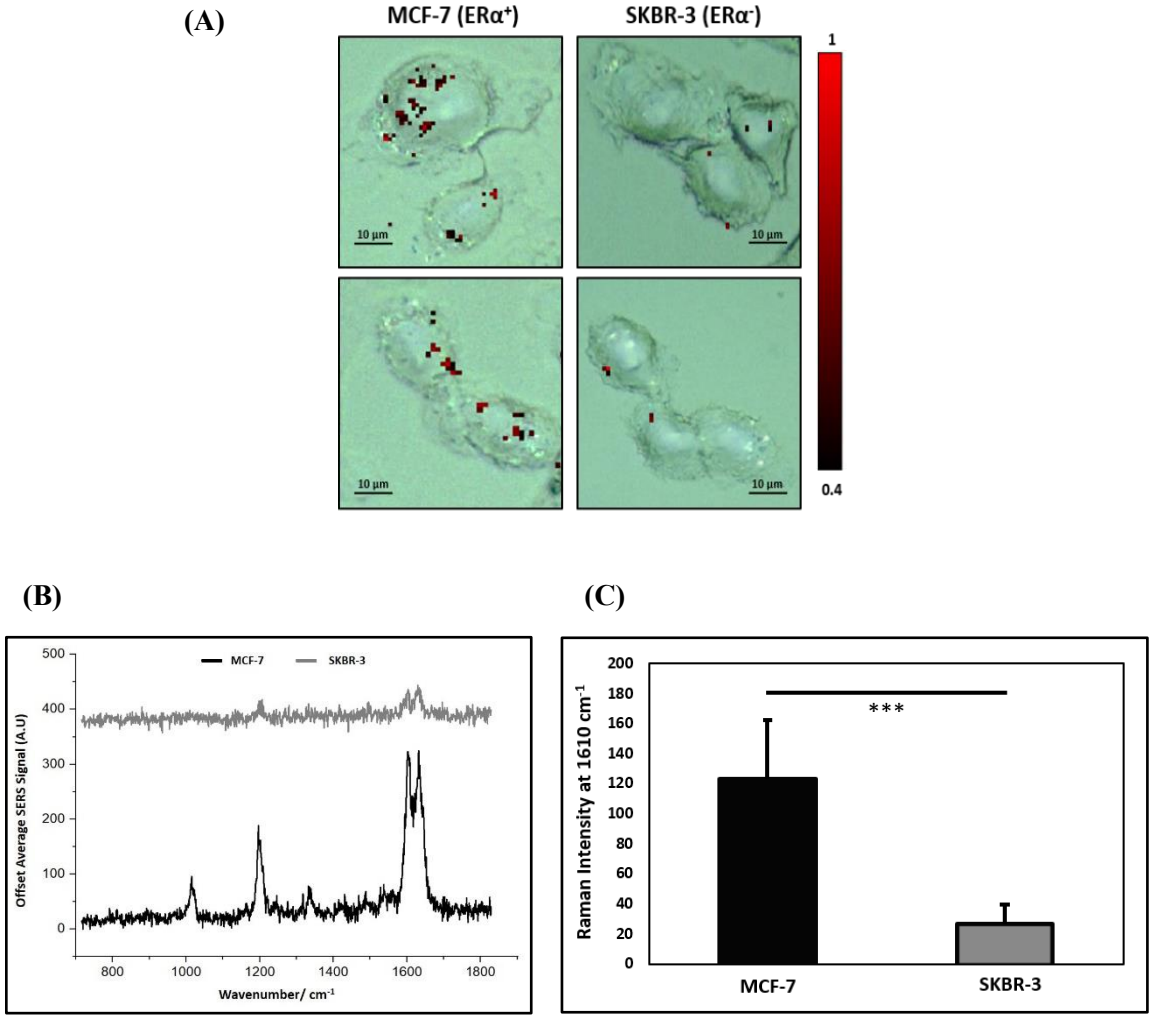

Figure 3: ERα-AuNPs were more accumulated in MCF-7 compared to SKBR-3 cells **(A)** SERS map of MCF-7 and SKBR-3 cells incubated with ERα-AuNPs (60 pM, 2 h) at 37 ºC. The images were generating using a Renishaw InVia Raman microscope with 50× magnification NIR APO Nikon water immersion objective with a 1.0 NA and 1.2 mW laser power (10% power) from a HeNe 633 nm excitation source with step size y,x 1.0 μm, 0.1s acquisition time and a 1200 l/mm grating in high confocality mode. The red false colour images, representing ERα-AuNPs, were generated using WiRE™ - Renishaw plc 4.4 software and direct classical least square analysis (DCLS) based on a BPE Raman reporter spectrum. DCLS fitted the unknown data (collected during cell mapping) to a linear combination of BPE reference spectrum. The minimum look up table (LUT) thresholds were set to exclude any poorly correlating or noisy spectra (min= 0.4). Results are representative of 3 independent experiments (SERS mapping of 10 cells in each experiment). Scale bars= 10 μm. **(B)** Average SERS spectra of MCF-7 (black) and SKBR-3 (grey) cells incubated with ERα-AuNPs (60 pM for 2 h) calculated from 10 cells in 3 independent experiments. **(C)** Average SERS intensity at 1610 cm^{-1} (highest peak of BPE Raman reporter). The average of 10 samples from 3 independent biological replicates is shown. Error bars presented as mean ± S.D. * Significant difference ($p < 0.05$) in a Student's *t*-test.

To further investigate ERα-AuNPs location within MCF-7 cells, 3D SERS mapping experiments were performed throughout the whole cell depth (30 μm in total). The 3D images confirmed that the SERS signal was generated within the cells rather than the surface (Figure 4A). 3D SERS images confirmed that the nanotags were concentrated in certain intracellular locations, suggesting the presence of ERα within the cells. The exact points in MCF-7 cells that were used for the generation of SERS spectra throughout the z-axis are shown in Figure 4B. The images were generated by creating a false colour image using WiRE™ - Renishaw plc 4.4 software package on a Renishaw InVia microspectrometer. Direct classical least square analysis (DCLS) was used to match the cell spectra with the reference spectrum of BPE Raman reporter, which corresponded to ERα-AuNP nanotags. The minimum and maximum look up table (LUT) thresholds were set to exclude any poorly correlating or noisy spectra, (min= 0.4).

(A) **(B)**

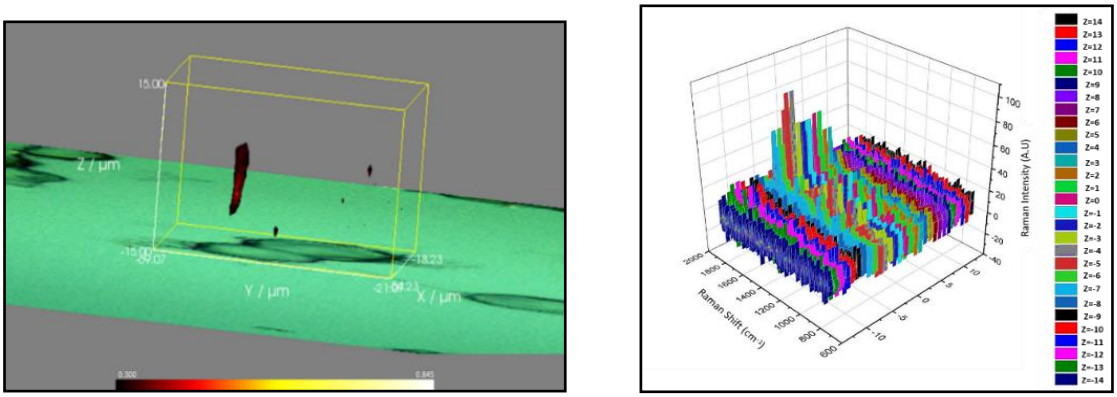

Figure 4: SERS signal in MCF-7 came from within the cells rather than the surface **(A)** 3D SERS map from MCF-7 treated with ERα-AuNPs (60 pM, 2h). **(B)** 3D Raman mapping waterfall plot of average SERS spectra at different z-axis points treated with ERα-AuNPs (60 pM, 2 h). 3D SERS images were generating using a Renishaw InVia Raman microscope with 50× magnification NIR APO Nikon water immersion objective with a 1.0 NA and 1.2 mW laser power (10% power) from a HeNe 633 nm excitation source with step size y,x=1.0 µm and z= 3.0 µm, 0.1 s acquisition time and a 1200 l/mm grating in high confocality mode.

SERS was found to be more effective for investigating ERα expression and localisation compared to immunofluorescence. Specifically, the immunofluorescence experiments that were carried out in MCF-7 cells gave high background signal in comparison to SERS experiments (Figure 1). Additionally, immunofluorescence was a laborious experiment that involved fixation, permeabilization and blocking of the cells before the incubation of primary and secondary antibodies. SERS avoids all these steps by being a quick, non-destructive technique that requires only one primary antibody for the characterisation of MCF-7 cells. This clearly demonstrates that SERS and ERα-AuNPs can be utilised to investigate ERα status in different breast cancer cells with high sensitivity and specificity.

3.4.3 Calculation of Relative SERS Response Value in Breast Cancer Cells

As previously described in 2.4.4 the calculation of relative SERS response value can be performed using WiRE™ - Renishaw plc 4.4 and Fiji image processing software. This calculation gives an estimation of the percentage of SERS responsive pixels per cell and indicates SERS relative value per condition. It should be noted that this is not a direct quantification of the total number of nanotags in cells. However, it is a way to obtain a relative assessment of nanotags uptake using a direct, rapid and non-destructive optical approach averaged across multiple cells (10 per condition investigated). Here, MCF-7 and SKBR-3 cells were treated with ERα-AuNPs (60 nM, 2h) or PEG5000-AuNPs (60 nM, 2h) to evaluate their SERS response value. The results showed that there was a statistically significant higher percentage area of SERS response in MCF-7 compared to SKBR-3 cells (4.2-times higher) (Figure 5). Additionally, it was observed that the SERS response from ERα-AuNPs was 3.8-times higher in comparison to PEG5000-AuNPs (no anti-ERα antibody functionalisation) in MCF-7 cells (1.68% and 0.44% respectively). In contrast, there was no statistically significant difference between the ERα-AuNPs and PEG5000-AuNPs (0.4% and 0.6% respectively) in SKBR-3 cells (Figure 5). These results further confirmed the strong targeting effect of ERα-AuNPs for ERα positive cells compared to the negative ones, while the nanotags with no anti-ERα antibody functionalisation had no targeting effect in both cell lines.

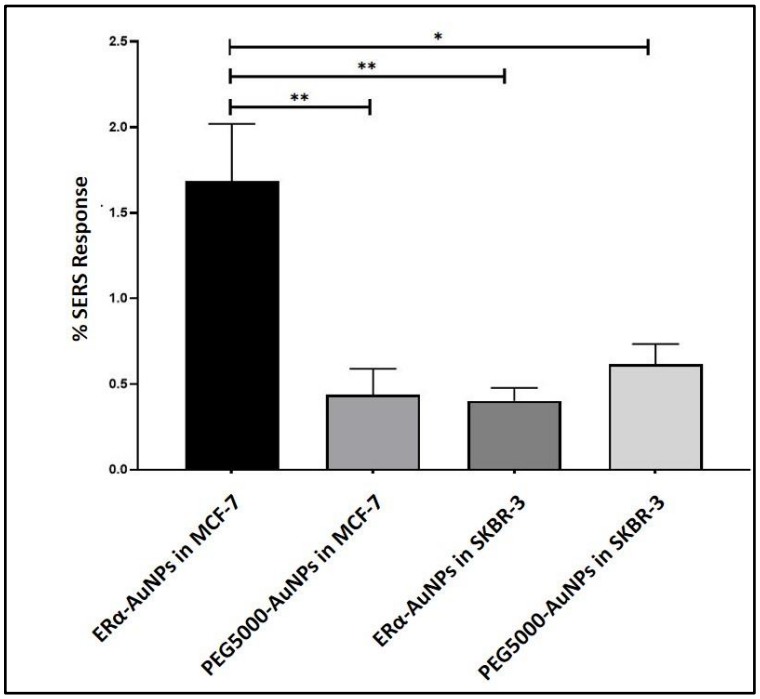

Figure 5: Calculation of relative SERS response value in MCF-7 and SKBR-3 cells treated with ERα-AuNPs (60 nM, 2h) or PEG5000-AuNPs (60 nM, 2h). A statistically significant higher SERS response was observed in MCF-7 incubated with ERα-AuNPs compared to SKBR-3 cells. The average of 10 samples from 3 independent biological replicates is shown. Error bars presented as mean ± S.D. *Significant difference ($p < 0.05$) in a one-way analysis of variance (ANOVA) test.

3.4.4 Assessment of Fulvestrant Efficacy Using SERS in Breast Cancer

Approximately 75% of primary breast tumours in women are positive to hormone receptor which can either be progesterone (PR) and/or estrogen receptor alpha (ERα).[4] In the UK, the phenotype of around three-quarters of all breast cancers is characterised by the presence of ERα.[3,9] Currently, both ERα and PR positive patient are treated with the same hormonal therapy.[37] Therefore, the assessment of anti-ERα treatment efficacy will also be beneficial for patients with PR positive breast cancer. Fulvestrant is the first commercially available selective estrogen receptor degrader (SERD).[38,39] SERD is a category of drugs that binds to ERα and causes its degradation and, thus, its downregulation.[40] However, like other hormonal drugs, fulvestrant is related to side effects, such as decreased white blood cells, abnormal liver functions and infections.[39,41] The ability to understand fulvestrant efficacy is important for improving the way that drug is used clinically. Here, we used SERS to assess fulvestrant activity in MCF-7 cells. Firstly, MCF-7 cells were treated with increasing concentrations of fulvestrant (0.01 μM to 1 μM) for 24 h before their lysing and western blot analysis. The results showed that higher fulvestrant concentration led to a higher decrease of ERα expression in MCF-7 cells compared to DMSO (vehicle control) treated cells (Figure 6A, 6B). Since 500 nM and 1 μM fulvestrant resulted in the lowest ERα expression, these concentrations were used for SERS imaging. Specifically, MCF-7 cells were treated with 500 nM and 1 μM fulvestrant for 24 h before the addition of ERα-AuNPs nanotags (60 pM) for 2h.

SERS clearly correlated with western blot experiment and showed that SERS provided a relative quantification of ERα expression levels since a decreased nanotags accumulation was observed after 500 nM and 1 μM fulvestrant treatment compared to DMSO (vehicle control) (Figure 3C). Specifically, a higher reduction in ERα-AuNPs accumulation was observed at 1 μM fulvestrant in comparison to 500 nM fulvestrant treatment (Figure 6C). The calculation of SERS response value in MCF-7 cells showed that there was a statistically significant decrease (5.4-times reduction) between the MCF-7 cells treated with 1% DMSO (vehicle control) and the ones treated with 1 μM

fulvestrant (Figure 6D). Moreover, 500 nM fulvestrant treatment led to 2.3 times decrease in the area of SERS response compared to 1% DMSO. These results proved that that SERS can be used as a powerful method for understanding the activity of commercially available drugs by providing real time measurements of activity at the single cell level. Additionally, new potentials are opened for correlating SERS response with the quantification data from western blot to estimate ERα expression levels using SERS without the need of time consuming and destructive western blot analysis.

(A)

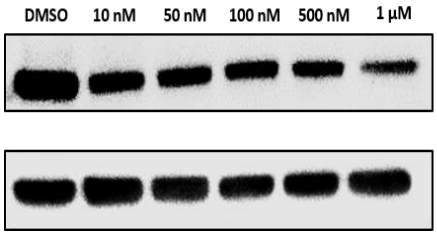

(B)

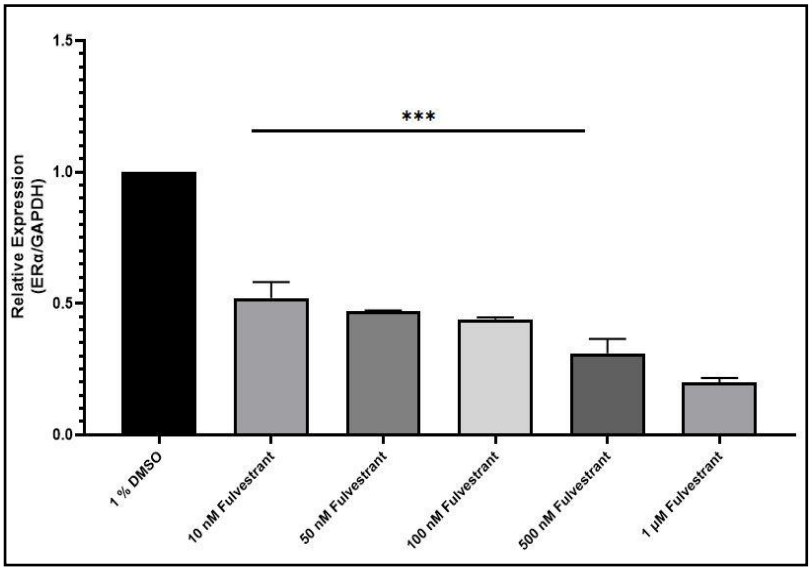

(C)

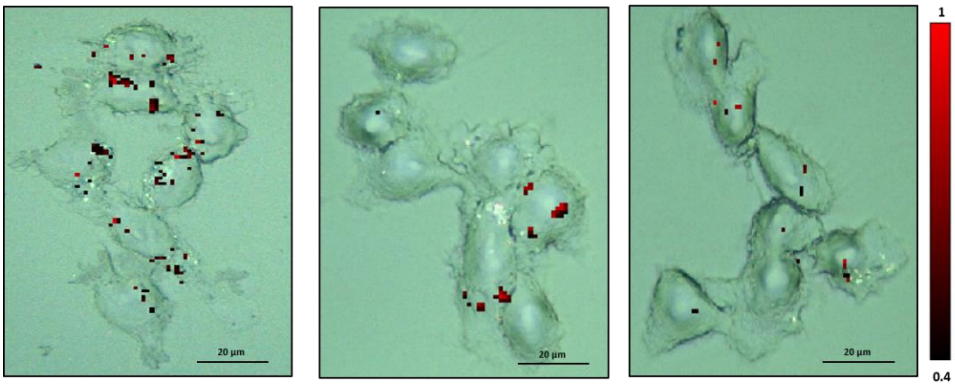

(D)

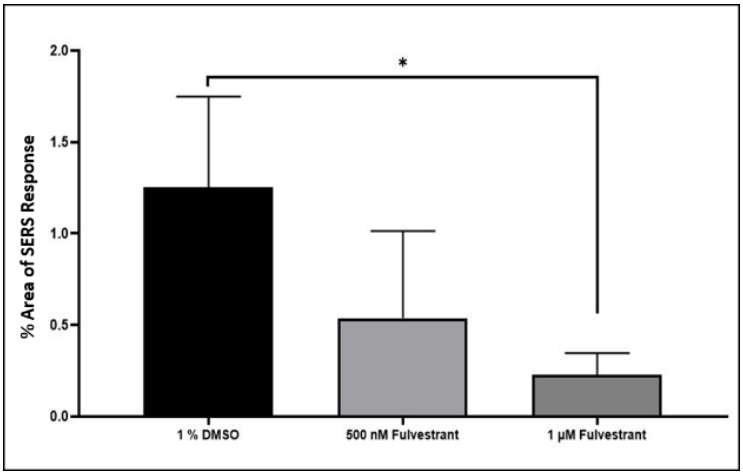

Figure 6: ERα-AuNPs used to assess fulvestrant activity in MCF-7 cells. **(A)** ERα expression in MCF-7 cells treated with different concentrations of fulvestrant (0.01 µM to 1 µM) for 24 h. Cell lysates were prepared from breast cancer lines and western blot analysis carried out using a secondary antibody to ERα, b-actin was used as a loading control. **(B)** Quantitative analysis of the relative expression of ERα and GAPDH (housekeeping protein). The results are expressed as means ± SD of triplicate determinations. $P < 0.001$ versus 1% DMSO (vesicle control). **(C)** Images were generating using a Renishaw InVia Raman microscope with 50× magnification NIR APO Nikon water immersion objective with a 1.0 NA and 1.2 mW laser power (10% power) from a HeNe 633 nm excitation source with step size y,x 1.0 µm, 0.1s acquisition time and a 1200 l/mm grating in high confocality mode. The red false colour images, representing ERα-AuNPs, were generated using WiRE™ - Renishaw plc 4.4 software and direct classical least square analysis (DCLS) based on a BPE Raman reporter spectrum. The minimum look up table (LUT) thresholds were set to exclude any poorly correlating or noisy spectra (min= 0.4). Scale bar= 20 µM **(D)** Percentage area of SERS response in MCF-7 treated with fulvestrant (500 nM and 1 µM) for 24 h and then with ERα-AuNP nanotags (60 pM, 2 h). The average of ten samples from three independent biological replicates is shown. Error bars presented as mean ± S.D. *Significant difference ($p < 0.05$) in a one-way analysis of variance (ANOVA).

3.5 Conclusion

ERα-AuNP nanotags and SERS imaging were successfully demonstrated for characterising ERα-positive breast cancer cells and informing about the efficacy of fulvestrant, a commercial ERα degrader. SERS was used as a non-destructive method that allowed the spatial and temporal understanding of ERα location at a single cell level. Specifically, SERS imaging showed a higher nanotag accumulation in ERα-positive (MCF-7) cells compared to ERα-negative cells (SKBR-3) confirming the specificity and strong targeting effect of ERα-AuNPs against ERα. Most importantly, SERS was found to be more effective to identify ERα in breast cancer cells compared to immunofluorescence experiments performed since it was a less time-consuming process that led to low background signals. The novelty of our work also relies on the fact that relative SERS response had an excellent correlation with western blot experiments carried out after fulvestrant treatment. Therefore, SERS can be used to get a qualitative idea of ERα expression levels, before and after fulvestrant treatment, and inform about drug's efficacy. It is, therefore, highlighted that SERS imaging could be of great importance for diagnostic accuracy, involving molecular characterisation and intracellular imaging, and understanding of drug activity in different cell types. Future prospective studies may involve using SERS as a complementary approach for monitoring patient derived breast cancer cells for diagnosis and evaluation of drug treatment.

3.6 References

1. Ferlay, J., Soerjomataram, I., Dikshit, R. & All, E. Cancer incidence and mortality worldwide: Sources, methods and major patterns in GLOBOCAN 2012. *Int J Cancer* (2015). doi:10.1002/ijc.29210
2. Torre, L. A., Siegel, R. L., Ward, E. M. & Jemal, A. Global cancer incidence and mortality rates and trends - An update. *Cancer Epidemiology Biomarkers and Prevention* (2016). doi:10.1158/1055-9965.EPI-15-0578
3. UK, C. R. Breast cancer incidence (invasive) statistics: Breast cancer incidence (invasive) statistics. *Online Source* (2016).
4. Giordano, S. B. & Gradishar, W. Breast cancer: Updates and advances in 2016. *Current Opinion in Obstetrics and Gynecology* (2017). doi:10.1097/GCO.0000000000000343
5. Lee, H.-R., Kim, T.-H. & Choi, K.-C. Functions and physiological roles of two types of estrogen receptors, ERα and ERβ, identified by estrogen receptor knockout mouse.

Laboratory Animal Research (2012). doi:10.5625/lar.2012.28.2.71

6. Kovats, S. Estrogen receptors regulate innate immune cells and signaling pathways. *Cellular Immunology* (2015). doi:10.1016/j.cellimm.2015.01.018
7. Khalid, A. B. & Krum, S. A. Estrogen receptors alpha and beta in bone. *Bone* (2016). doi:10.1016/j.bone.2016.03.016
8. Bean, L. A., Ianov, L. & Foster, T. C. Estrogen receptors, the hippocampus, and memory. *Neuroscientist* (2014). doi:10.1177/1073858413519865
9. Richman, J. & Dowsett, M. Beyond 5 years: enduring risk of recurrence in oestrogen receptor-positive breast cancer. *Nature Reviews Clinical Oncology* (2018). doi:10.1038/s41571-018-0145-5
10. Jensen, E. V. *et al.* Estrogen receptors and proliferation markers in primary and recurrent breast cancer. *Proceedings of the National Academy of Sciences* (2001). doi:10.1073/pnas.211556298
11. Louie, M. C. & Sevigny, M. B. Steroid hormone receptors as prognostic markers in breast cancer. *American Journal of Cancer Research* (2017).
12. Cabioglu, N. *et al.* Expression of growth factor and chemokine receptors: New insights in the biology of inflammatory breast cancer. *Annals of Oncology* (2007). doi:10.1093/annonc/mdm060
13. Meng, P. *et al.* Propagation of functional estrogen receptor positive normal human breast cells in 3D cultures. *Breast Cancer Research and Treatment* (2019). doi:10.1007/s10549-019-05229-5
14. Lee, J. K. *et al.* Age and the means of bypassing stasis influence the intrinsic subtype of immortalized human mammary epithelial cells. *Frontiers in Cell and Developmental Biology* (2015). doi:10.3389/fcell.2015.00013
15. Ford, C. H. J., Maie, A. L. B., Bushra, A. L. A. & Issam, F. Reassessment of estrogen receptor expression in human breast cancer cell lines. *Anticancer Research* (2011).
16. Al-Bader, M., Al-Saji, S., Ford, C. H. J., Francis, I. & Al-Ayadhy, B. Real-time PCR: Detection of oestrogen receptor-alpha and -beta isoforms and variants in breast cancer. *Anticancer Research* **30**, 4147–4156 (2010).
17. Thompson, A. *et al.* Evaluation of the current knowledge limitations in breast cancer research: A gap analysis. *Breast Cancer Research* (2008). doi:10.1186/bcr1983
18. Pusztai, L. Molecular Classification of Breast Cancer: Limitations and Potential. *The Oncologist* (2006). doi:10.1634/theoncologist.11-8-868

19. Schlücker, S. SERS microscopy: Nanoparticle probes and biomedical applications. *ChemPhysChem* (2009). doi:10.1002/cphc.200900119
20. Bass, J. J. *et al.* An overview of technical considerations for Western blotting applications to physiological research. *Scandinavian Journal of Medicine and Science in Sports* (2017). doi:10.1111/sms.12702
21. Smith, C. J. & Osborn, A. M. Advantages and limitations of quantitative PCR (Q-PCR)-based approaches in microbial ecology. *FEMS Microbiology Ecology* (2009). doi:10.1111/j.1574-6941.2008.00629.x
22. Dougan, J. A. & Faulds, K. Surface enhanced Raman scattering for multiplexed detection. *Analyst* (2012). doi:10.1039/c2an15979a
23. Laing, S., Gracie, K. & Faulds, K. Multiplex in vitro detection using SERS. *Chemical Society Reviews* (2016). doi:10.1039/c5cs00644a
24. McAughtrie, S., Faulds, K. & Graham, D. Surface enhanced Raman spectroscopy (SERS): Potential applications for disease detection and treatment. *Journal of Photochemistry and Photobiology C: Photochemistry Reviews* (2014). doi:10.1016/j.jphotochemrev.2014.09.002
25. Sun, C., Gao, M. & Zhang, X. Surface-enhanced Raman scattering (SERS) imaging-guided real-time photothermal ablation of target cancer cells using polydopamine-encapsulated gold nanorods as multifunctional agents. *Analytical and Bioanalytical Chemistry* (2017). doi:10.1007/s00216-017-0435-2
26. Li, L., Liao, M., Chen, Y., Shan, B. & Li, M. Surface-enhanced Raman spectroscopy (SERS) nanoprobes for ratiometric detection of cancer cells. *Journal of Materials Chemistry B* **7**, 815–822 (2019).
27. Davis, R. *et al.* A Raman Imaging Approach Using CD47 Antibody-Labeled SERS Nanoparticles for Identifying Breast Cancer and Its Potential to Guide Surgical Resection. *Nanomaterials* (2018). doi:10.3390/nano8110953
28. Yu, M. K., Park, J. & Jon, S. Targeting strategies for multifunctional nanoparticles in cancer imaging and therapy. *Theranostics* (2012). doi:10.7150/thno.3463
29. Lee, S. *et al.* Rapid and sensitive phenotypic marker detection on breast cancer cells using surface-enhanced Raman scattering (SERS) imaging. *Biosensors and Bioelectronics* (2014). doi:10.1016/j.bios.2013.07.063
30. Thiruppathi, R., Mishra, S., Ganapathy, M., Padmanabhan, P. & Gulyás, B. Nanoparticle functionalization and its potentials for molecular imaging. *Advanced Science* (2017).

doi:10.1002/advs.201600279

31. Jokerst, J. V., Lobovkina, T., Zare, R. N. & Gambhir, S. S. Nanoparticle PEGylation for imaging and therapy. *Nanomedicine* (2011). doi:10.2217/nnm.11.19
32. Canton, I. & Battaglia, G. Endocytosis at the nanoscale. *Chemical Society Reviews* (2012). doi:10.1039/c2cs15309b
33. Suh, J. *et al.* PEGylation of nanoparticles improves their cytoplasmic transport. *International journal of nanomedicine* (2007).
34. Gillich, T. *et al.* PEG-stabilized core-shell nanoparticles: Impact of linear versus dendritic polymer shell architecture on colloidal properties and the reversibility of temperature-induced aggregation. *ACS Nano* (2013). doi:10.1021/nn304045q
35. Schindelin, J. *et al.* Fiji: An open-source platform for biological-image analysis. *Nature Methods* (2012). doi:10.1038/nmeth.2019
36. Karimpour, M. *et al.* Development of curcumin-loaded gemini surfactant nanoparticles: Synthesis, characterization and evaluation of anticancer activity against human breast cancer cell lines. *Phytomedicine* (2019). doi:10.1016/j.phymed.2018.11.017
37. Mohammed, H. *et al.* Progesterone receptor modulates ERα action in breast cancer. *Nature* (2015). doi:10.1038/nature14583
38. Croxtall, J. D. & McKeage, K. Fulvestrant: A review of its use in the management of hormone receptor-positive metastatic breast cancer in postmenopausal women. in *Drugs* (2011). doi:10.2165/11204810-000000000-00000
39. Nathan, M. R. & Schmid, P. A Review of Fulvestrant in Breast Cancer. *Oncology and Therapy* (2017). doi:10.1007/s40487-017-0046-2
40. Patel, H. K. & Bihani, T. Selective estrogen receptor modulators (SERMs) and selective estrogen receptor degraders (SERDs) in cancer treatment. *Pharmacology and Therapeutics* (2018). doi:10.1016/j.pharmthera.2017.12.012
41. O'Sullivan, C. C. & Ruddy, K. J. Management of Potential Long-Term Toxicities in Breast Cancer Patients. *Current Breast Cancer Reports* (2016). doi:10.1007/s12609-016-0229-0

4. Detection of Estrogen Receptor Alpha (ERα) and Assessment of Fulvestrant Efficacy in Live MCF-7 Tumour Spheroids Using Microfluidic Devices and SERS

Contributing authors:

Anastasia Kapara[1,2], Karla Anna Findlay Paterson[3], Valerie Brunton[2], Duncan Graham[1], Michele Zagnoni[3], Karen Faulds[1]

1. Centre for Molecular Nanometrology, Department of Pure and Applied Chemistry, Technology and Innovation Centre, University of Strathclyde, 99 George Street, Glasgow G1 1RD, UK.

2. MRC Institute of Genetics and Molecular Medicine, Edinburgh Cancer Research UK Centre, University of Edinburgh, Western General Hospital, Crewe Road South, Edinburgh, EH4 2XU, UK

3. Centre for Microsystems and Photonics, Department of Electronic and Electrical Engineering, Technology and Innovation Centre, University of Strathclyde, 99 George Street, Glasgow G1 1RD, UK.

4.1 Abstract

Breast cancer is an increasing public health problem as it is the most commonly diagnosed cancer and the leading cancer death cause among women. The characterisation of cancer phenotype is usually performed in 2D monolayered *in vitro* tumour models that are unable to recapitulate the complexity of tumour microenvironment. Thus, it is important to develop three-dimensional (3D) breast tumour models that are better *in vivo* mimics for understanding the tumour growth mechanisms and its response to therapeutics. The combination of surface enhanced Raman scattering (SERS) with microfluidic devices can provide a biological characterisation of cancer phenotype and understanding of drug activity in an animal-free 3D environment with high selectivity, specificity and multiplex capacity. Here, we present the first application of SERS with microfluidic devices for the detection of estrogen receptor alpha (ERα) in 3D live breast cancer spheroids. The *ex vivo* spheroid model was formed in a microfluidic device using the ERα positive MCF-7 human breast cancer cells. The anti-ERα antibody-functionalised gold nanoparticles (ERα-AuNPs) and the anti-HER2 antibody-functionalised gold nanoparticles (HER2-AuNPs) were incubated with MCF-7 spheroids in the microfluidic devices and spectroscopically analysed using SERS. 2D SERS mapping confirmed the strong targeting effect of the specific ERα-AuNP nanotags toward ERα in contrast to the non-specific HER2-AuNPs. Moreover, 3D SERS confirmed the great penetration capabilities of the nanotags into the tumour models as high SERS signals were generated within the spheroids. We also introduced the drug fulvestrant in the microfluidic devices, the first-in-class approved selective estrogen receptor degrader (SERD), to assess its efficacy in MCF-7 spheroids compared to 2D cultures. The results demonstrated that the 2D and 3D MCF-7 cells have different biological and architectural behaviours that affected their sensitivity to fulvestrant exposure. The importance of carrying out experiments using 3D tumour spheroids is, therefore, highlighted to further improve the understanding of the molecular actions of the drug. These results illustrate the potential of using SERS and microfluidic systems as a tool for cancer cells characterisation and SERD investigation in a more representative *in vivo* environment.

Keywords: Surface-enhanced spectroscopy (SERS), estrogen receptor alpha (ERα), microfluidic devices, MCF-7 spheroids, cancer targeting, fulvestrant efficacy

4.2 Introduction

Breast cancer is a major health issue among women worldwide.[1,2] In the UK, one person is diagnosed with breast cancer every 10 minutes and one in eight women will develop breast cancer at some point in their life.[3] Different studies have shown that breast cancer proliferation and metastasis are highly affected by the cancers cellular and physical microenvironment.[4,5,6] A limitation of cell-based studies for breast cancer is that the majority of the characterisation and development of new therapeutic agents are conducted in two-dimensional (2D) monolayer cell cultures.[7] Therefore, cellular processes, such as drug transport, cell-cell and/or cell-matrix interactions, are not taken into consideration.[8,9] Studies have shown that 2D breast cancer cell cultures have different behaviours, gene expressions and, usually, higher sensitivity to anti-cancer drugs than three-dimensional (3D) models.[10,11] Significantly, often drug compounds tested positive in 2D cultures fail in clinical trials.[12,13] These findings highlight the need for 3D *in vitro* tumour models that better recapitulate aspects of the *in vivo* breast cancer microenvironment.

Microfluidic technologies offer a powerful tool for the creation of 3D breast cancer tumour spheroids and the *in vitro* investigation of the physiological and biological properties of the tumour.[14,15] The technology is an excellent tool to bridge the gap between 2D monolayer cultures and animal models, offering excellent solutions for miniaturised yet large throughput spheroid assays with high accuracy, faster analysis and potential for automation.[16,17,18,19]

Importantly, microfluidics can be combined with analytical spectroscopic methods using fluorescence [20] [21] [22] or surface enhanced Raman spectroscopy (SERS)[23] for high-throughput detection of molecules and facilitating understanding of 3D biological systems. The combination of SERS with microfluidic devices has been carried out in a variety of experimental conditions, such as rapid analysis of food contaminants[24], multiplex recognition of interleukins from blood plasma[25] and detection of prostate cancer biomarkers[26]. SERS offers signal enhancement factors of 10^4-10^8 in comparison to conventional Raman by adsorbing a molecule of interest onto a roughened metal surface, such as colloidal suspensions of gold and silver nanoparticles [27,28,29]. SERS is a non- destructive analytical technique that offers high specificity, selectivity and multiplexed capabilities due to the sharp fingerprint spectra produced.[30,31] Recently, significant developments have been produced using SERS for cancer imaging[32,33,34] and drug screening.[35,36]

In this study, we developed a novel assay whereby 3D breast cancer spheroids, grown and cultured in microfluidic devices, were characterised with SERS using gold nanoparticles (AuNPs) functionalised with anti-ERα antibodies and BPE Raman reporter (ERα-AuNPs) or anti-HER2 antibody-functionalised nanotags and PPY Raman reporter (HER2-AuNPs). Also, we investigated the effects of Fulvestrant, a commercially available selective estrogen receptor degrader (SERD), on MCF-7 spheroids using SERS under different drug treatments. To our knowledge, this is the first time the combination of microfluidics and SERS has been used for tumour identification, phenotype characterisation and assessment of drug activity in a 3D breast cancer model.

4.3 Experimental

4.3.1 Materials

Anti-Erb2 antibody (ab16899) and anti-Erb2 antibody (ab16899) were purchased from Abcam (330 Cambridge Science Park, Cambridge, CB4 0FL, UK). LIVE/DEAD Viability/Cytotoxicity Assay Kit diacetate (FDA) -propidium iodide (PI) and Synperonic F108 were purchased from Sigma-Aldrich (The Old Brickyard, New Road, Gillingham, Dorset, SP8 4XT, UK). Hoechst33342 was purchased from Thermo Scientific (3 Fountain Dr, Inchinnan, Renfrew PA4 9RF, UK). All other materials are previously described in 2.3.1.

4.3.2 Device Design and Preparation

Multi-layered microfluidic devices were produced using standard soft lithography techniques and used for culturing spheroids, following established protocols.[37] Briefly, a 10:1 ratio of Polydimethylsiloxane (PDMS) prepolymer (Sylgard 184, Dow Corning) and curing agent were mixed and dispensed onto patterned silicon wafers. The wafers were degassed and subsequently incubated at 85°C for a minimum of 3 h to allow curing of the PDMS solution. PDMS layers were then cut from the wafers and wells were formed using a 4 mm surgical biopsy punch (Miltex). PDMS layers were cleaned and treated with oxygen plasma (Pico plasma cleaner, Diener electronic) to permanently bond the layers together, forming a microfluidic device. Devices were then stored overnight at 85°C and exposed a second time to oxygen plasma before injecting a 1% solution of Synperonic F108, creating ultra-low adhesion conditions. After storage of the devices for a 24 h in an incubator at 37°C and 5% CO_2, they were washed using phosphate buffered saline

(PBS) and Roswell Park Memorial Institute 1640 culture medium (RPMI). Devices were stored at 37 °C and 5% CO_2 in a humidified incubator before cell seeding. MCF-7 cells were seeded into devices at a concentration of 5×10^6 cells/mL to form spheroids, with each microfluidic channel containing at least 100 spheroids. Media was exchanged every 48 h.

4.3.3 Nanoparticle Synthesis and Functionalisation of ERα-AuNP and HER2-AuNP Nanotags

The nanoparticle synthesis and the functionalisation of ERα-AuNPs are described in 2.3.2. For anti-HER2 functionalisation, 74 µL of EDC solution (1 mg/mL in 10 mM MES, pH 6.0) was mixed with 40 µL of HS-PEG5000-COOH (12.5 µM in dH20) followed by the addition of 217 µL of NHS (1 mg/mL in 10 mM MES, pH 6.0) and 20 µL of anti-HER2 antibody (2.5 mg/mL in dH20). The final solution was incubated in 669 µL of 10 mM HEPES buffer pH 7.0 on a shaker plate for 18 h at room temperature. 10 µL of 4-(1H-pyrazol-4-yl)pyridine (PPY) (0.1 µM) was added to bare AuNPs (990 µL) and the solution was incubated on the shaker plate for 30 min followed by centrifugation at 6,000 rpm for 20 min. The solution of EDC-NHS-PEG5000-mAb was added dropwise to the pelleted PPY-AuNPs. The nanotags were incubated on a shaker plate for 3 h. The excess of free antibody was removed by centrifugation at 6,000 rpm for 10 min.

4.3.4 Nanotags Characterisation

As previously described in 2.3.3.

4.3.5 2D Breast Cancer Cell Culture

MCF-7 cells (ATCC® HTB-22™) were obtained from American Type Culture Collection (ATCC) (Queens Road, Teddington, Middlesex, TW11 0LY, UK). The cells were cultured in Rosewell Park Memorial Institute medium (RPMI 1640) supplemented with 1% penicillin/streptomycin (10000 units per mL), 1% fungizone, and 10% heat-inactivated fetal bovine serum (FBS) at 37 °C and 5% CO_2 in a humidified incubator. Cells at a confluence of ca. 90% growing in a T175 flask were trypsinised and re-suspended in RMPI medium. Solutions containing ca. 5×10^6 cells/ mL were used for microfluidic devices.

4.3.6 Nanotags Loading and Fulvestrant Treatment in Microfluidic Devices

Fulvestrant stock solution was dissolved in DMSO and stored at 4 °C. Immediately prior to injection into devices, fulvestrant solution was diluted in RPMI media to the desired concentration. Both concentrations had been modified from previously obtained 2D data to be suitable for 3D culture (as described in 3.4.4). Spheroids were exposed to fulvestrant solution (1 μM and 10 μM) on the third day of their culture in the microfluidic devices and incubated for 24 h at 37 °C and 5% CO_2. Fulvestrant was then removed from microfluidic devices and ERα-AuNPs (60 pM), HER2-AuNPs (60 pM) or a mixture of ERα/HER2-AuNPs (60 pM) nanotags were incubated into the devices for 2 h. Nanotags were gently pipetted prior to injection into devices, ensuring their flow through the entirety of the microfluidic channel. After 2 h, nanotags were removed, and the channels were washed twice with PBS to remove any unbound nanotags. Control experiments were performed for each set of experiments, where spheroids were cultured in the absence of nanotags or fulvestrant treatment.

4.3.7 Cell Viability Studies in Microfluidic Devices

Spheroids were observed via bright-field microscopy using an inverted microscope (Axio Observer Z1, Zeiss) connected to an Orca Flash 4.0 camera (Hamamatsu). Images were collected every second day, and, before and after nanotag or drug treatment. To determine spheroid viability throughout the culture period, live/dead staining of spheroids was performed at several time points: 2 h after nanotag exposure (day 4), 3 days after nanotag exposure (day 7) and 6 days after nanotag exposure (day 10). Spheroids were stained with 8 μg/mL fluorescein diacetate (FDA), 20 μg/mL propidium iodide (PI) and 5 μmol/L Hoechst33342. The staining solution was added to the devices for 30 min. PBS was then used to wash out excess staining solution. Epifluorescence microscopy was performed in accordance with the schedule for the spheroid's viability studies.

4.3.8 Quantification of Viability Studies

The viable fraction (V_f) of spheroids was calculated by calculating the ratio of FDA area on the day of staining ($Area_{FDA}$) over the brightfield area of the spheroid on the day before treatment ($Area_{BF}$), as seen in the following equation:

$$V_f = \frac{Area_{FDA}}{Area_{BF}}$$

Spheroids possessing a $V_f \geq 1$ were considered to have been unaltered by exposure to nanotags or fulvestrant treatment since they had either remained the same size or increased in size over the culture period. Brightfield and fluorescent spheroid areas were also used to extricate spheroid perimeters for shape factor and area growth analysis. The shape factor (S_f) of a spheroid was also used as an assessment of its health:

$$S_f = \frac{P^2}{4\pi A'}$$

P denotes the spheroid perimeter where P= 2πr. A represents the area of the spheroid, described as (A=πr2).

4.3.9 SERS Cell Mapping

A Renishaw InVia Raman confocal microscope (Renishaw, Wolton-under-Edge, U.K) was used to generate 2D and 3D SERS data. 2D SERS maps were collected using edge Streamline HR high confocality mode with 3 µm spatial resolution in the x and y directions. 3D SERS maps were collected using edge Streamline HR high confocality mode with a 3 µm step size resolution in the x and y directions and 4 µm between z-stacks. A 20× objective (N.A. 0.40), 1.2 mW laser power (10% power) from a HeNe 633 nm excitation source and a 1200 l/mm grating in high confocality mode were used. Windows-based Raman Environment (WiRE™ - Renishaw plc) 4.4 software package was used to pre-process the data using cosmic ray removal and baseline correction features. The image was generated using direct classical least square analysis (DCLS) based on a BPE or PPY Raman reference spectrum whereby a false colour was generated only when there was a good spectral fit between the reference and the collected spectra.

4.3.10 Statistical Analysis

As previously described in 2.3.11.

4.4 Results and Discussion

4.4.1 Synthesis and Characterisation of ERα-AuNPs and HER2-AuNPs

The nanoparticle synthesis and characterisation have been previously discussed in section 2.4.1. Briefly, gold nanoparticles (AuNPs) were functionalised with anti-ERα and anti-HER2 antibodies via carbodiimide crosslinking chemistry using carboxyl acid PEG polymer (HS-PEG5000-COOH). The coupling chemistry was achieved after the attachment of the Raman reporters 1,2-Bis(4-pyridyl) ethylene (BPE) (for anti-ERα functionalisation) or 4-(1H-pyrazol-4-yl) pyridine (PPY) (for anti-HER2 functionalisation) to the AuNPs surface. To confirm the successful functionalisation, the nanotags were characterised using extinction spectroscopy, agarose electrophoresis and a lateral flow immunosorbent assay. The extinction spectroscopy spectra showed that there was a shift in localised surface plasmon resonance when antibodies were added to AuNPs (Figure 1A, 1B), confirming the successful attachment of the antibody to the metal surface. The nanotags did not show any aggregation in the extinction spectra, indicating the AuNPs were stable after the addition of the antibodies on their surface. The successful antibody functionalisation was also confirmed with agarose gel electrophoresis, since the PEG5000-AuNPs travelled further than the ERα-AuNPs and HER2-AuNPs, suggesting that the nanotags were of different size and/or charge (Figure 1C). Lateral flow immunosorbent assay (LFA) also showed that the antibodies were on the AuNPs surface and that they remained active since a spot onto the detection zone of the nitrocellulose strip appeared when the nanotags bound to their matching secondary IgG antibodies (anti-rabbit IgG for ERα and anti-mouse IgG for HER2). The spot was present only in samples with the There was no detected spot when PEG5000-AuNPs was tested with the anti-mouse IgG and anti-rabbit IgG confirming the successful binding of the anti-ERα antibody and anti-HER2 to the AuNPs surface (Figure 1D). The functionalised AuNPs were analysed by Raman using a 638 nm laser excitation which showed that both ERα-AuNPs and HER2-AuNPs gave strong and characteristic SERS signal from their representative Raman reporter (BPE and PPY Raman reporter respectively) (Figure 2). Therefore, the nanotags characterisation confirmed that the AuNPs were successfully functionalised with ERα and HER2 antibodies along with BPE and PPY Raman reporters respectively.

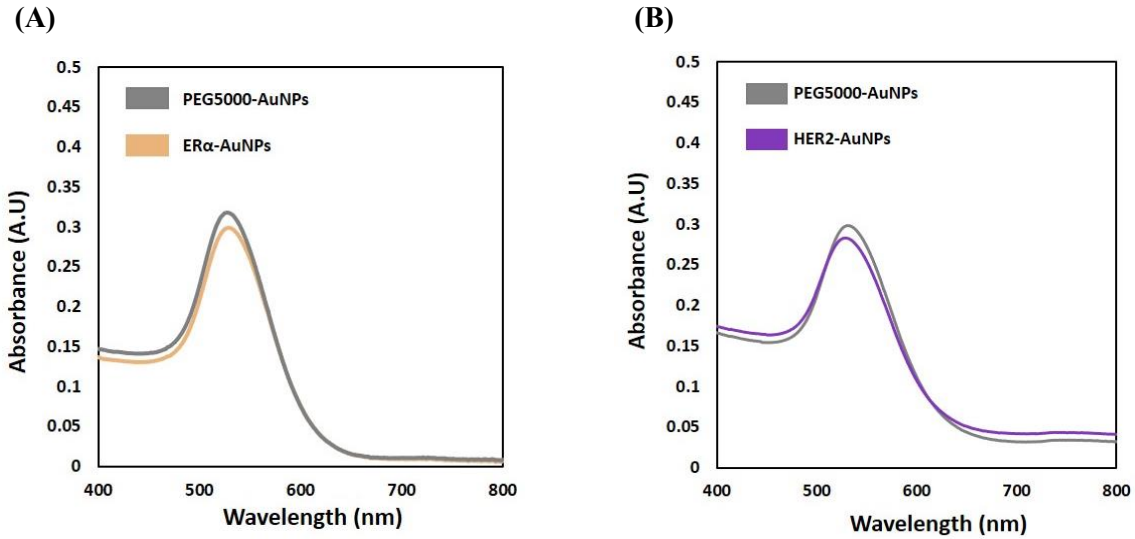
(A)
PEG5000-AuNPs
ERα-AuNPs
Absorbance (A.U)
Wavelength (nm)
(B)
PEG5000-AuNPs
HER2-AuNPs
Absorbance (A.U)
Wavelength (nm)

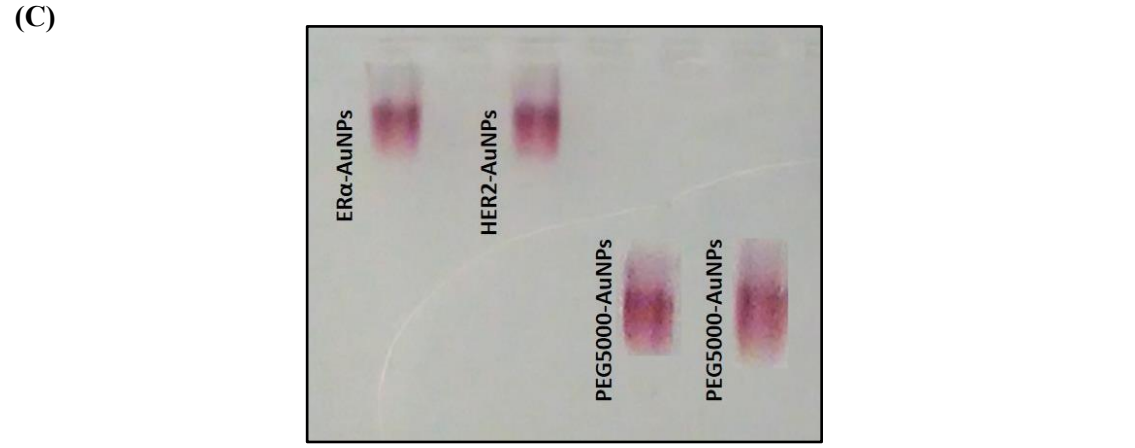
(C)
ERα-AuNPs
HER2-AuNPs
PEG5000-AuNPs
PEG5000-AuNPs

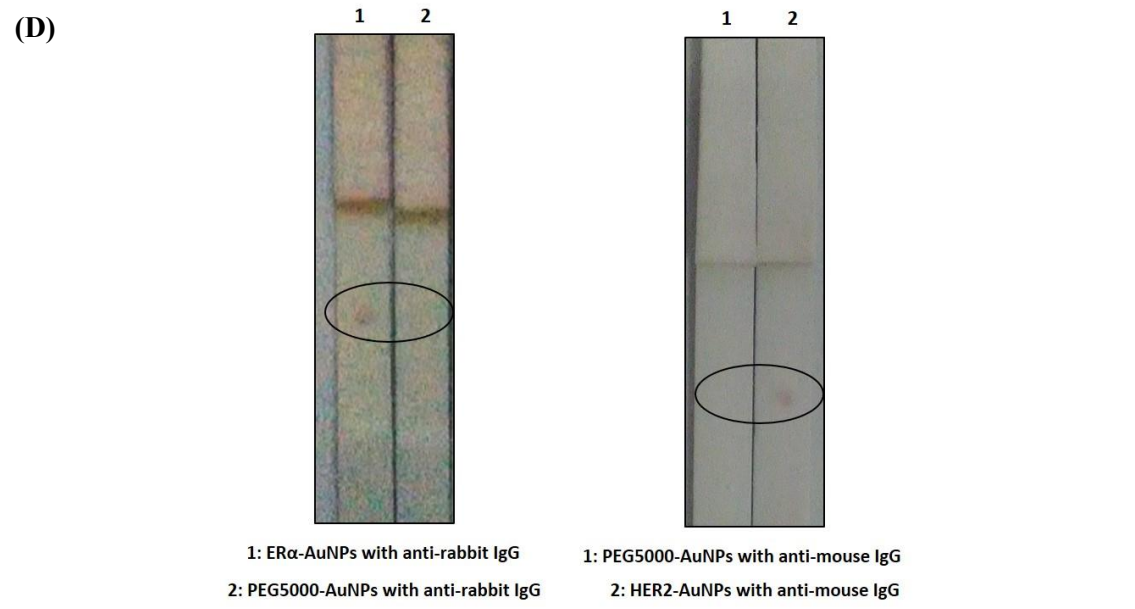
(D)
1
2
1
2
1: ERα-AuNPs with anti-rabbit IgG
2: PEG5000-AuNPs with anti-rabbit IgG
1: PEG5000-AuNPs with anti-mouse IgG
2: HER2-AuNPs with anti-mouse IgG

Figure 1: **(A)** Extinction spectra of PEG5000-AuNPs (grey) and ERα-AuNPs (orange) nanotags. **(B)** Extinction spectra of PEG5000-AuNPs (grey) and HER2-AuNPs (purple) nanotags. **(C)** Agarose gel after electrophoresis showing the distance travelled by PEG5000-AuNPs, ERα-AuNPs and HER2-AuNP nanotags. Gel electrophoresis is a method of separation and analysis, based on the size and charge of the samples being analysed. Samples travel through a gel matrix due to an electric charge being applied through the gel. Larger samples travel slower through the gel compared to smaller samples, which can travel faster through the porous matrix.[50] **(D)** Lateral flow immunosorbent assay strips showing the spot from ERα-AuNPs and HER2-AuNPs on the detection zone of the nitrocellulose strip. The spot was present only in samples with the matching secondary IgG antibody for ERα (anti-rabbit) or HER2 (anti-mouse) applied. There was no detected spot when PEG5000-AuNPs was tested with the anti-rabbit IgG and anti-mouse IgG confirming the successful binding of the anti-ERα antibody and anti-HER2 to the AuNPs surface. The HS-PEG5000-COOH was used for the functionalisation to prevent nonspecific interactions between the functionalised nanotags and other cellular components. Additionally, it provides the functional group for the covalent the attachment of the anti-ERα antibody or anti-HER2 antibody. The HS-PEG5000-COOH was able to bind to the gold surface due to the strong binding affinity of the thiol group to gold surface.[51]

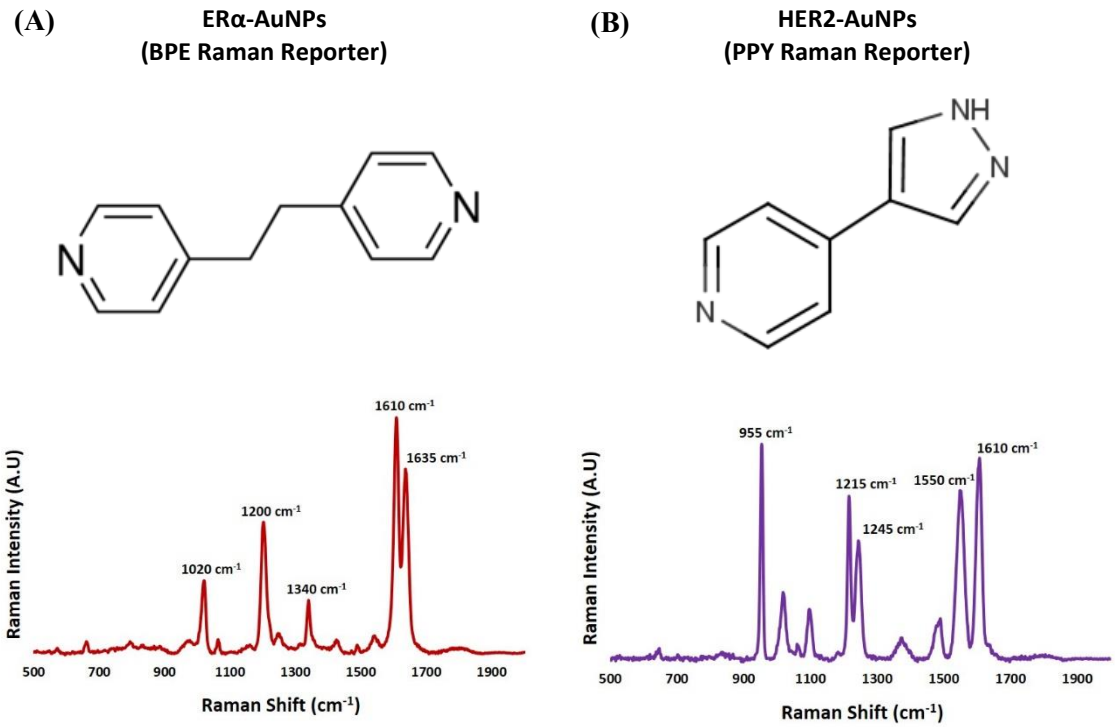

Figure 2: **(A)** Structure of BPE Raman Reporter and its SERS spectrum after its adsorbed on 40 nm AuNPs in an aqueous solution at 10^{-7} M concentration. **(B)** Structure of PPY Raman Reporter and its SERS spectrum after its adsorbed on 40 nm AuNPs in an aqueous solution at 10^{-7} M concentration. The SERS analysis was carried out using a Snowy Range CBEx 2.0 handheld Raman spectrometer equipped with a 638 nm laser with a maximum laser power of 40 mW. The spectra were collected using 100% laser power with 0.05 s accumulation time. The software used to acquire spectra was Peak 1.1.112.

4.4.2 Formation of Live MCF-7 Spheroids and Cell Viability Studies After Nanotags Incubation

The microfluidic device was developed with polydimethylsiloxane (PDMS) which has excellent optical transparency and biocompatibility. A suspension of MCF-7 cells was seeded into each open wells of a microfluidic device containing seven independent channels (Figure 3A), each of which had four arrays of 64 microwells (150 µm). Cells sedimented at the bottom of microwells (Figure 3B) and, due to low adhesion condition, formed compact spheroids within 24 h of culture (Figure 4A).

(A) **(B)**

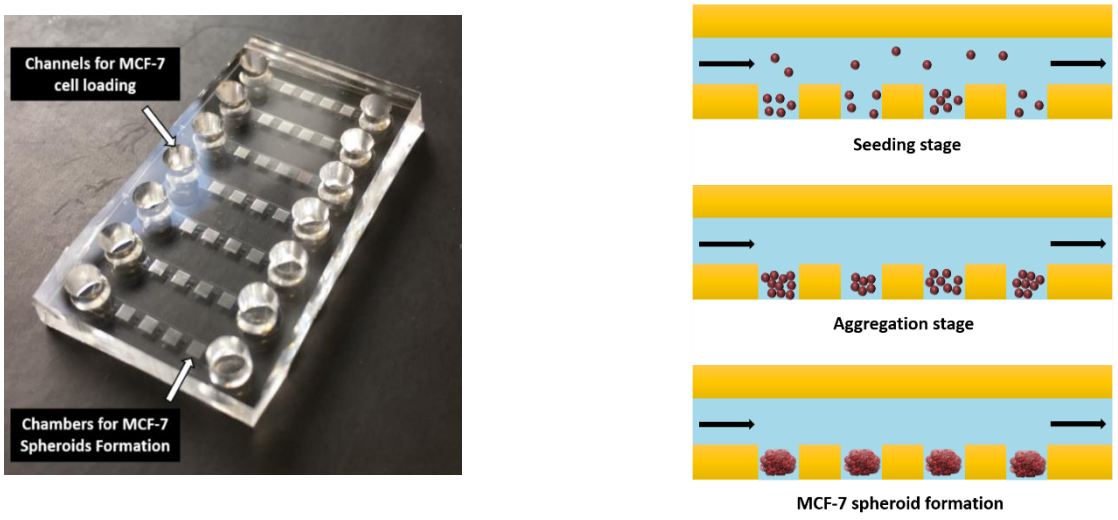

Figure 3: The MCF-7 spheroids were formed in PDMS microfluidic devices. **(A)** Photograph of the microfluidic device. Each device had seven channels, containing up to 256 spheroids. **(B)** Schematic diagram showing the principle of formation of MCF-7 spheroids in the low-adhesion microfluidic device.

To investigate the targeting effect of ERα-AuNP nanotags against ERα, MCF-7 spheroids were also treated on day 4 of culture with specific ERα-AuNPs, non-specific HER2-AuNPs or with a mixture of specific ERα-AuNP nanotags and non-specific HER2-AuNP nanotags (ERα/HER2-AuNPs). Western blot and immunofluorescence experiments confirmed that MCF-7 are positive for ERα, whilst they do not express any detectable levels of HER2 (as described in section 2.7 SI, Figure S9 and section 3.7 SI, Figure S1). ERα-AuNPs, HER2-AuNP or ERα/HER2-AuNPs mixture were incubated in the spheroids for 2 h. Spheroid viability was investigated on day 4 (after the addition of the nanotags), day 7 and day 10 after cell seeding in devices. The bright-field images showed that ERα-AuNPs and ERα/HER2-AuNPs incubation did not affect spheroids integrity (Figure 4B, 4C). Moreover, no significant difference in the area growth of spheroids was observed between controls and nanotag treated spheroids (Figure 4D), nor in the shape of the spheroids, throughout the 10-day culture period (Figure 4E). To further test the effect of ERα-AuNPs and ERα/HER2-AuNPs mixture on the viability of MCF-7 spheroids, live/dead staining with fluorescein diacetate (FDA) and propidium iodide (PI) was performed. Results showed that nanotags did not produce toxic effects on the spheroids over the culture period (Figure 4F, 4G).

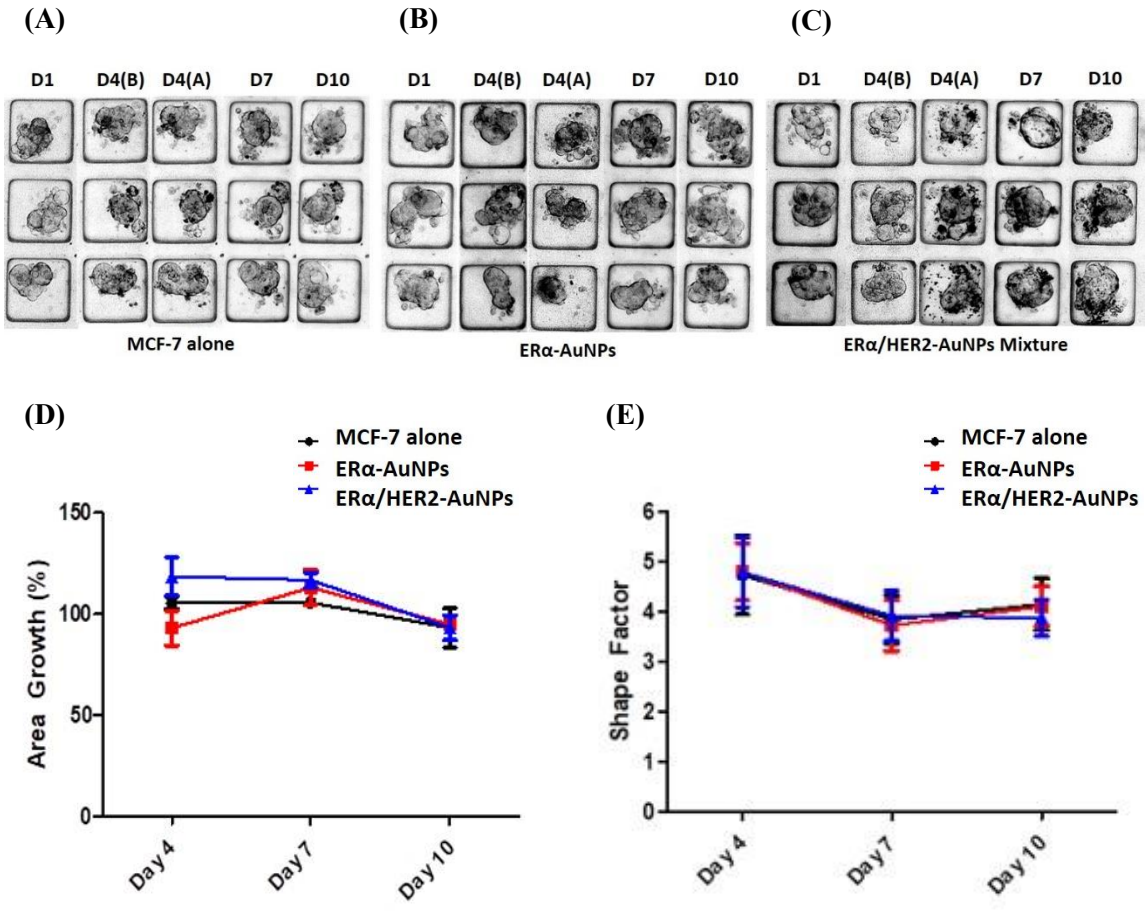

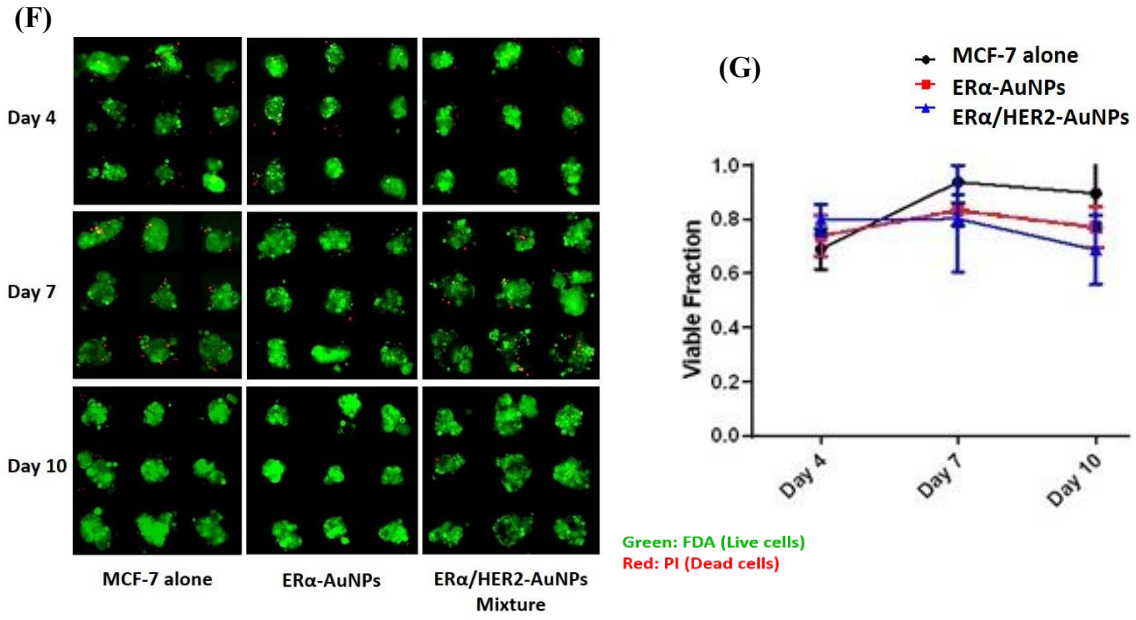

Figure 4: Effects of ERα-AuNPs and ERα/HER2-AuNPs mixture on the formation and viability of MCF-7 spheroids. **(A)** Brightfield images showing the temporal evolution of MCF-7 spheroids cultured in a microfluidic device over ten days without nanotags treatment, **(B)** with ERα-AuNPs treatment and **(C)** with ERα/HER2-AuNPs mixture treatment. D1 = day 1 of cell seeding, D4(B) = day 4 of cell seeding (before the addition of nanotags), D4(A) = day 4 of cell seeding (after the addition of nanotags), D7 = day 7 of cell seeding, D10 = day 10 of cell seeding. **(D) P**lot of the spheroid area growth (%) for untreated MCF-7 cells (black), MCF-7 cells treated with ERα-AuNP nanotags (red) and MCF-7 cells treated ERα/HER2-AuNPs mixture (blue). **(E)** Plot of spheroids shape factor in untreated cells (black), cells treated with ERα-AuNP nanotags (red) and cells treated with ERα/HER2-AuNPs mixture (blue). **(F)** Representative images of spheroid viability at different time points. Viable cells appeared as green (FDA staining), while non-viable MCF-7 cells appear as red (PI staining). **(G)** Plot of the viable fraction (Vf) of spheroids for untreated MCF-7 cells (black), MCF-7 cells treated with ERα-AuNP nanotags (red) and MCF-7 cells treated ERα-AuNPs and ERα/HER2-AuNPs mixture (blue). For all plots, each point was obtained from 32 spheroids. Error bars presented as mean ± S.D.

4.4.3 Targeting Effect of ERα-AuNP Nanotags in MCF-7 Spheroids: 2D SERS Imaging

To determine the targeting effect of ERα -AuNPs in ERα-positive MCF-7 breast cancer spheroids, the spheroids were incubated with either the specific ERα-AuNPs, which should bind to ERα on MCF-7 cells, or with the non-specific HER2-AuNP nanotags, serving as negative control As previously characterised in section 2.4.2, MCF-7 cells express high levels of ERα and no detectable levels of human epidermal growth factor receptor 2 (HER2). Therefore, HER2-AuNP nanotags provided an excellent negative control. First, an empty microfluidic device was characterised to identify potential unwanted SERS signal. The results showed that although PDMS gave a low intensity SERS at 1260 cm^{-1} and 1410 cm^{-1} these peaks did not overlap with the peaks from BPE and PPY Raman reporters on the nanotags (Figure 5).

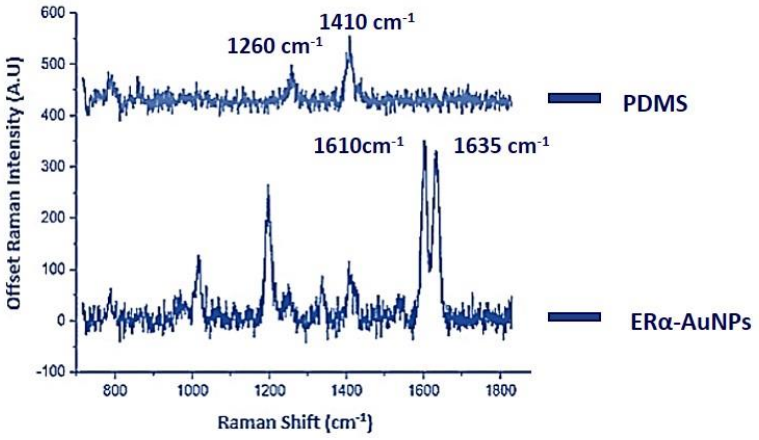

Figure 5: Stacked SERS spectra from PDMS and ERα-AuNPs in a microfluidic device. The peak from PDMS at 1410 cm^{-1} does not overlap with the Raman peak at 1610 cm^{-1} (representative peak for ERα-AuNP nanotags). Therefore, PDMS will not interfere with the SERS spheroids mapping results.

At day 4, ERα-AuNPs (60 pM, 2 h), HER2-AuNPs (60 pM, 2 h), or with ERα/HER2-AuNPs mixture (60 pM, 2 h) were introduced into the microfluidic device and incubated for 2 h before washing twice with PBS to remove any unbound nanotags. The spheroids were then Raman imaged using a laser excitation wavelength of 633 nm. Specifically, 2D SERS mapping was carried out by focussing the laser of a Renishaw InVia Raman confocal microscope through the microfluidic device which was mounted on a coverslip

2D SERS mapping from spheroids incubated with ERα-AuNPs demonstrated a high nanotag accumulation and a strong SERS signal in the spheroids, confirming the strong targeting effect of the ERα-AuNP nanotags to the MCF-7 spheroids (Figure 6A, 6B). In contrast, the spheroids treated with the HER2-AuNP nanotags appeared to have lower nanotag accumulation, demonstrated by the low SERS signal corresponding to PPY Raman reporter on HER2-AuNP nanotags (Figure 6C, 6D), probably due to low non-specific binding of HER2-AuNP nanotags in MCF-7 spheroids. Some non-specific binding was expected due to the enhanced permeability and retention (EPR) effect where tumours retain nanoparticles in their microenvironments.[38,39,40]

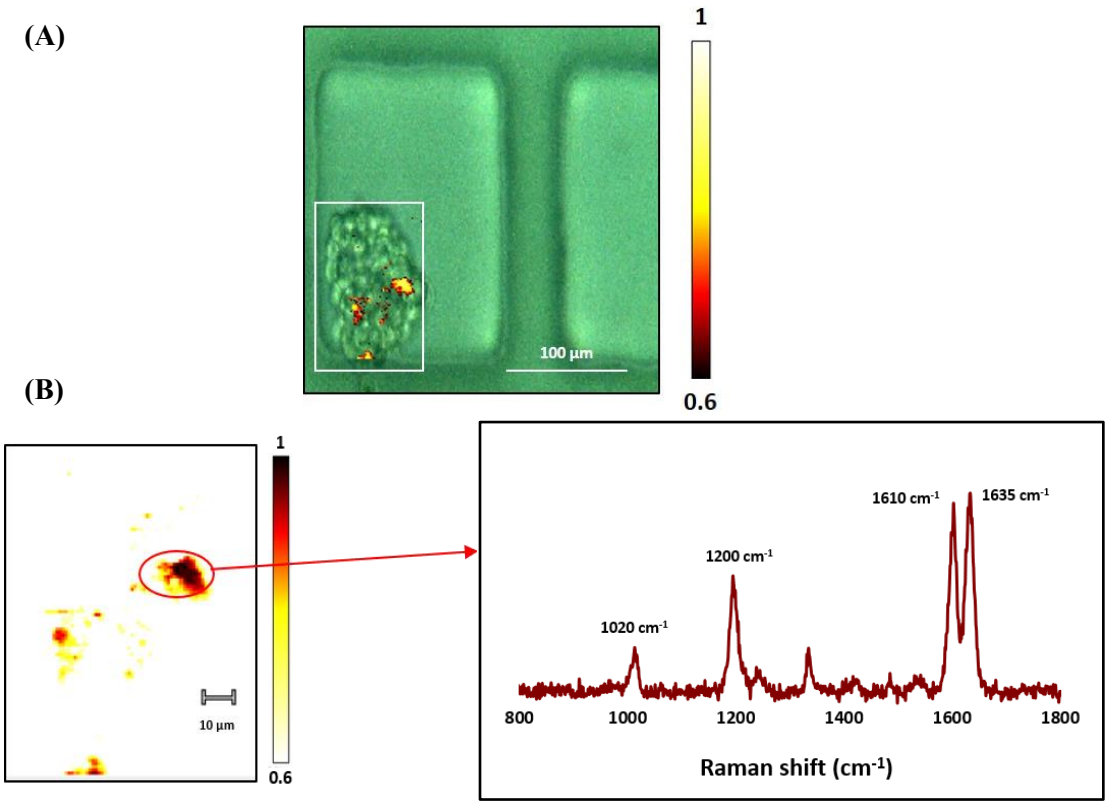

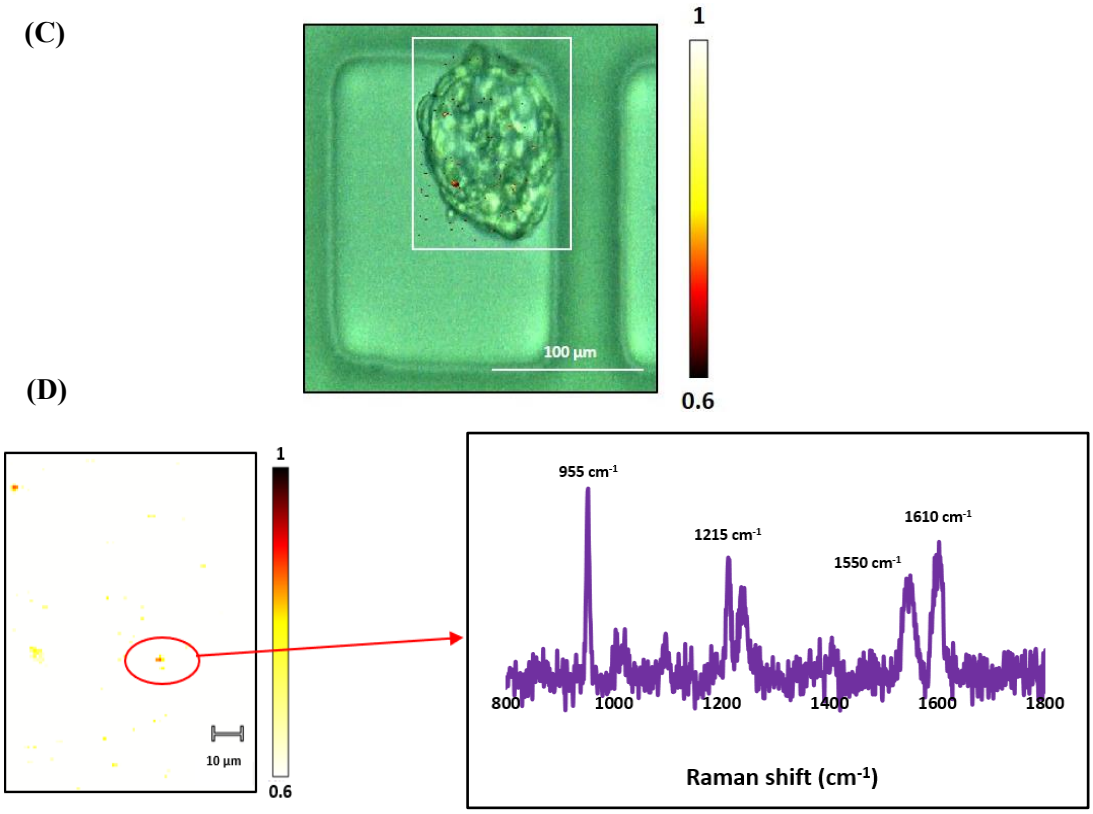

Figure 6: ERα-AuNP nanotags showed strong targeting effect towards MCF-7 spheroids, while low HER2-AuNP accumulation was observed in MCF-7 spheroids due to non-specific binding of the nanotags with the cells. **(A)** Brightfield image of an MCF-7 spheroid in a microfluidic channel merged with the corresponding SERS signal from ERα-AuNP nanotags. **(B)** SERS signal from ERα-AuNP nanotags and representative SERS spectrum from the highest signal point. **(C)** Brightfield image of an MCF-7 spheroid in a microfluidic channel merged with the corresponding SERS signal from HER2-AuNPs control nanotags. **(D)** SERS signal from HER2-AuNP nanotags and the representative SERS spectrum from the highest signal point. The images were generated with a 20× magnification NIR APO Nikon objective, laser power of 12 mW (100% power), from a HeNe 633 nm excitation source with a 0.1 s acquisition time per point, and 1200 l/mm grating in high confocality mode. The false coloured images that represent the ERα-AuNPs were generated using the WiRE™ - Renishaw plc 4.4 software package on a Renishaw InVia microspectrometer and direct classical least square analysis (DCLS) based on a BPE Raman reporter spectrum. The minimum and maximum look up table (LUT) thresholds were set to exclude any poorly correlating or noisy spectra (min= 0.6).

To further confirm the specificity of ERα-AuNP nanotags for the MCF-7 spheroids, a 1:1 mixture of both the ERα and HER2 targeted nanotags, ERα/HER2-AuNPs mixture, was co-incubated in MCF-7 spheroids. The results confirmed that ERα-AuNP nanotags had a stronger targeting effect towards MCF-7 spheroids compared to HER2-AuNPs. Specifically, the ERα-AuNPs showed greater accumulation than HER2-AuNPs within the same spheroid (Figure 7A). Additionally, the spheroids had statistically significant higher (2.7 times) Raman signal at 1610 cm^{-1} (representative peak of BPE Raman reporter on ERα-AuNPs) than at 955 cm^{-1} (representative peak of PPY Raman reporter on HER2-AuNPs) (Figure 7B). These results established the ability of ERα-AuNP nanotags to identify and characterise ERα positive breast cancer spheroids using SERS.

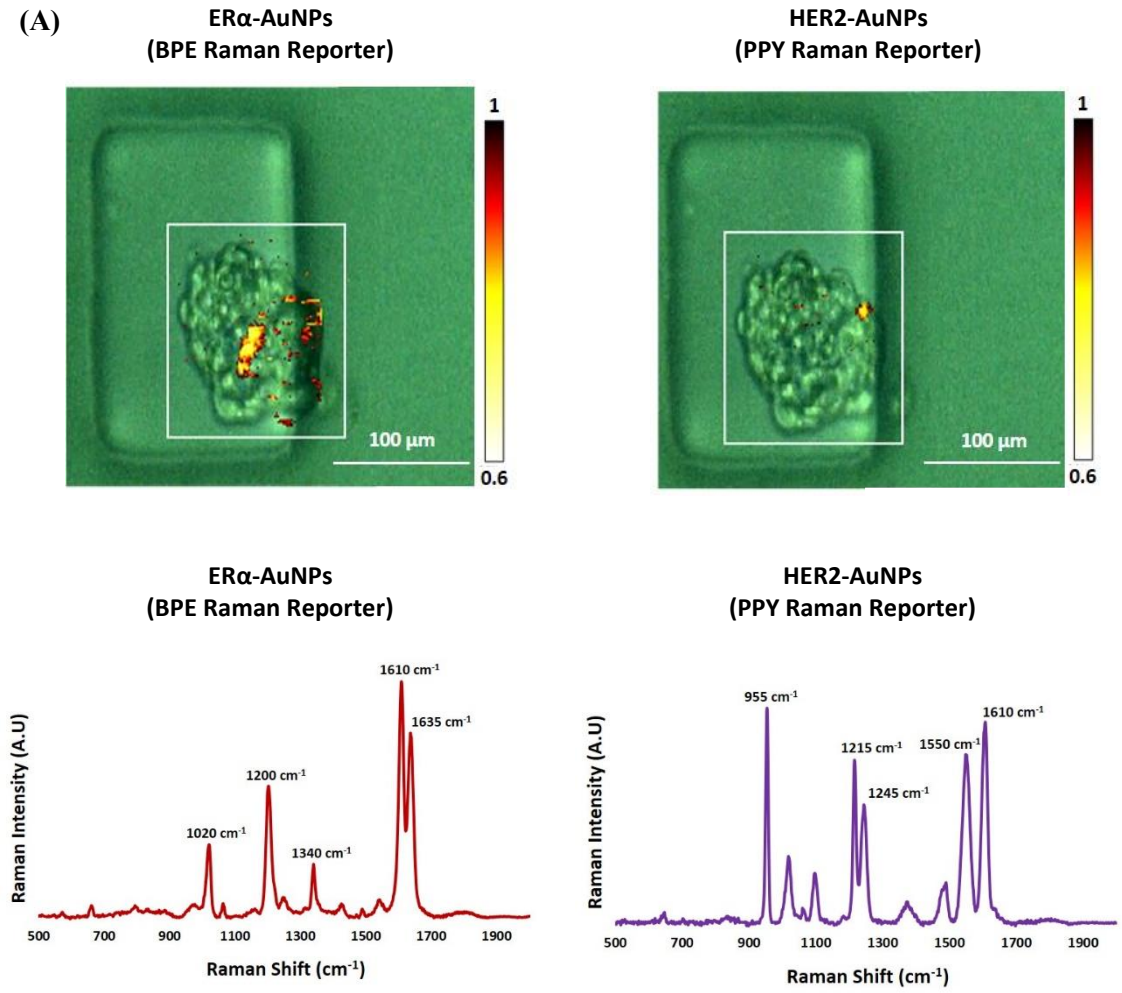

(B)

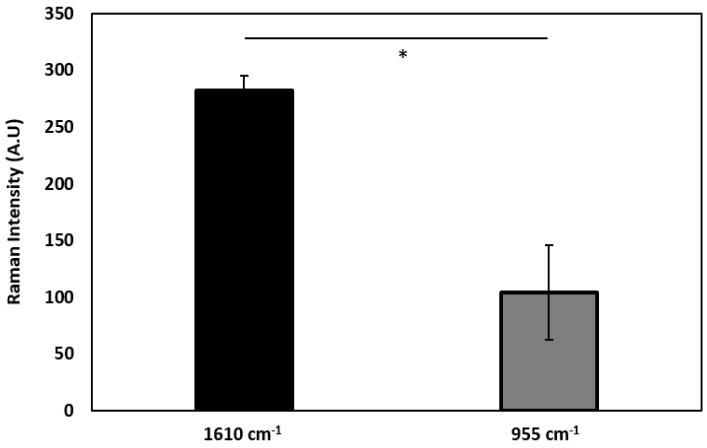

Figure 7: ERα-AuNPs showed great targeting effect and specificity for MCF-7 spheroids compared to HER2-AuNPs **(A)** MCF-7 spheroid incubated with ERα/HER2-AuNPs mixture (60 pM, 2h) in microfluidic devices. The false colour images correspond to the SERS signal from ERα-AuNPs (left) and HER2-AuNPs (right) within the same spheroid. The images were generated using the WiRE™ - Renishaw plc 4.4 software package on a Renishaw InVia microspectrometer and direct classical least square analysis (DCLS) based on a BPE and PPY Raman reporter reference spectrum for ERα-AuNPs and HER2-AuNPs respectively. The minimum and maximum look up table (LUT) thresholds were set to exclude any poorly correlating or noisy spectra (min= 0.6). SERS was performed with a 20× magnification NIR APO Nikon objective, laser power of 12 mW (100% power), from a HeNe 633 nm excitation source with a 0.1 s acquisition time per point, and 1200 lines/mm grating in high confocality mode. **(B)** Representative reference spectrum of ERα-AuNPs (BPE Raman reporter) (red) and HER2-AuNPs (PPY Raman reporter) (purple) in H_20 The SERS analysis was carried out on a Snowy Range CBEx 2.0 handheld Raman spectrometer equipped with a 638 nm laser with a maximum laser power of 40 mW. The spectrum was collected using 100% laser power with 1 s accumulation time. The software used to acquire spectra was Peak 1.1.112. **(C)** Average Raman intensity at 1610 cm^{-1} (representative peak for BPE Raman reporter attached on ERα-AuNPs) and 955 cm^{-1} (representative peak for PPY Raman reporter attached HER2-AuNPs). The average of three samples from three independent biological replicates is shown. Error bars presented as mean ± S.D. * Significant difference ($p< 0.05$) in a Student's *t*-test.

4.4.4 Targeting Effect of ERα-AuNP Nanotags in MCF-7 Spheroids: 3D SERS Imaging

Previous work from our group has shown that SERS signal in 2D MCF-7 cells was generated within the cells rather than the surface confirming that the nanotags were uptaken from MCF-7 cells and were located in certain intracellular areas (as described in 3.4.2) Here, 3D SERS was also used as a non-destructive imaging approach for investigating the uptake and penetration abilities of the AuNPs nanotags through the MCF-7 spheroids. Specifically, to validate whether the signal from ERα-AuNP nanotags came from the surface or from within the spheroids, 3D SERS mapping was carried out throughout the whole volume (200 µm in total) of MCF-7 spheroids treated with ERα-AuNPs (60 pM, 2 h) or HER2-AuNPs (60 pM, 2 h). The 3D SERS maps were collected using edge Streamline HR high confocality mode with a 3 µm step size resolution in the x and y directions and 4 µm between z-stacks. The representative average z-stacking results showed that SERS signal was detected from locations within the spheroids volume, rather than just the spheroid surface (Figure 8A, 8B). These results strongly suggested the nanotags were targeting ERα and penetrating the spheroids, giving a strong SERS signal depth. The spheroids incubated with HER2-AuNPs were also mapped using 3D SERS. The representative SERS z-stack signal from HER2-AuNPs showed that although SERS signal was detected within the spheroids, it was much lower compared to ERα-AuNPs (Figure 8C, 8D). These results suggest that the non-specific nanotags were also able to diffuse into the spheroids. However, their much lower accumulation indicated that their uptake was non-specific as there was no HER2 for them to target. The maximum SERS signal and the z-plane at different z-axis points from ERα-AuNPs are shown in Figure 9A, 9B. These results further established the great labelling ability of the ERα-AuNP nanotags to target ERα with great penetration capabilities. Therefore, microfluidics and SERS could potentially be utilised for identification and characterisation of breast cancer tumours *ex vivo* at high depth with sensitivity and specificity.

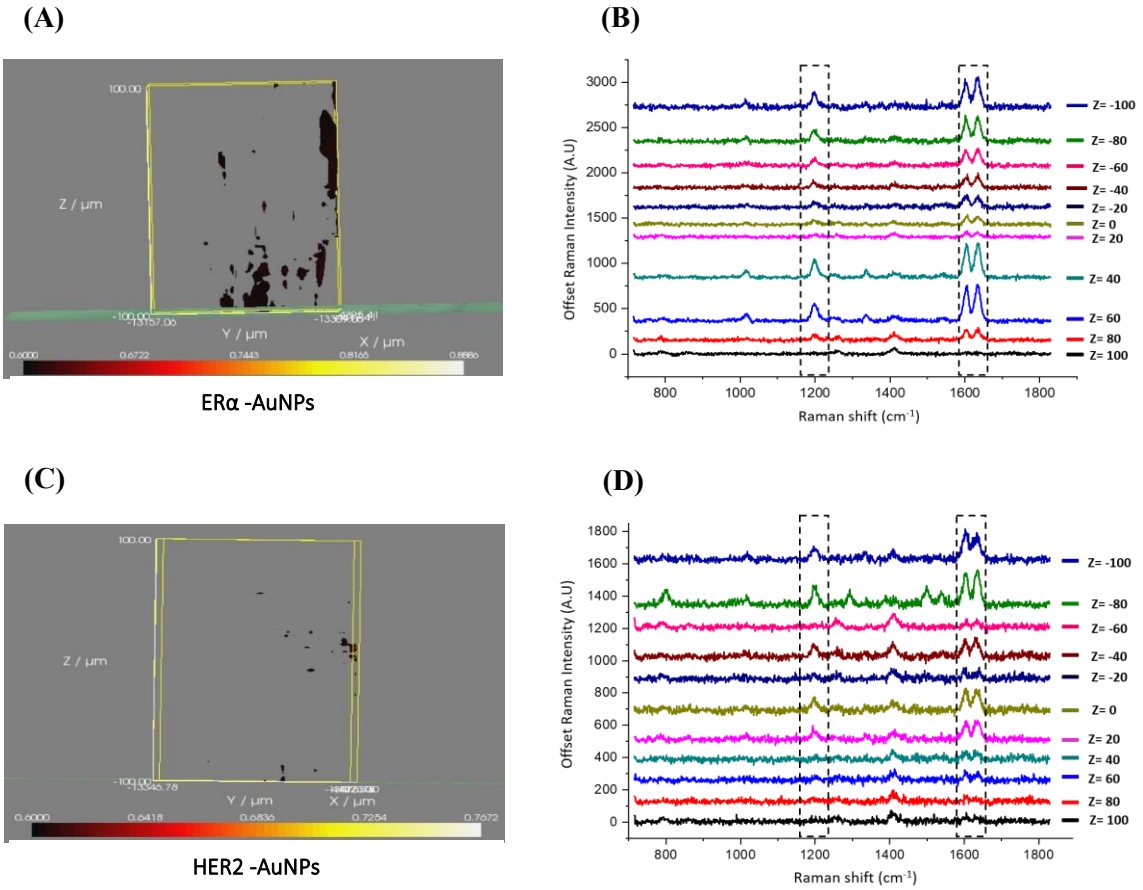

Figure 8: ERα-AuNP nanotags demonstrated greater accumulation within the MCF-7 spheroids in comparison to HER2-AuNPs. **(A)** 3D SERS map of an MCF-7 spheroid incubated with ERα-AuNP nanotags (60 pM, 2 h) in the microfluidic device. **(B)** Stacked 3D SERS spectra from ERα-AuNP nanotags generated at different z positions in the spheroid. **(C)** 3D SERS map of an MCF-7 spheroid incubated with HER2-AuNPs (60 pM, 2 h) in the microfluidic device. **(B)** Stacked 3D SERS spectra from HER2-AuNPs generated at different z positions in the spheroid. Spheroids were mapped with a total volume of 200 µm. False colour represents the areas where SERS signal from nanotags was present throughout the spheroids. The minimum look up table (LUT) threshold was set to exclude any poorly correlating or noisy spectra (min= 0.6). A 20× magnification NIR APO Nikon water immersion objective with a 1.0 NA was used on the samples at a laser power of 12 mW (100% power) at the sample, from a HeNe 633 nm excitation source with step size y,x: 3.0 µm, z: 4.0 µm, 0.1s acquisition time and a 1200 l/mm grating in high confocality mode.

(A)

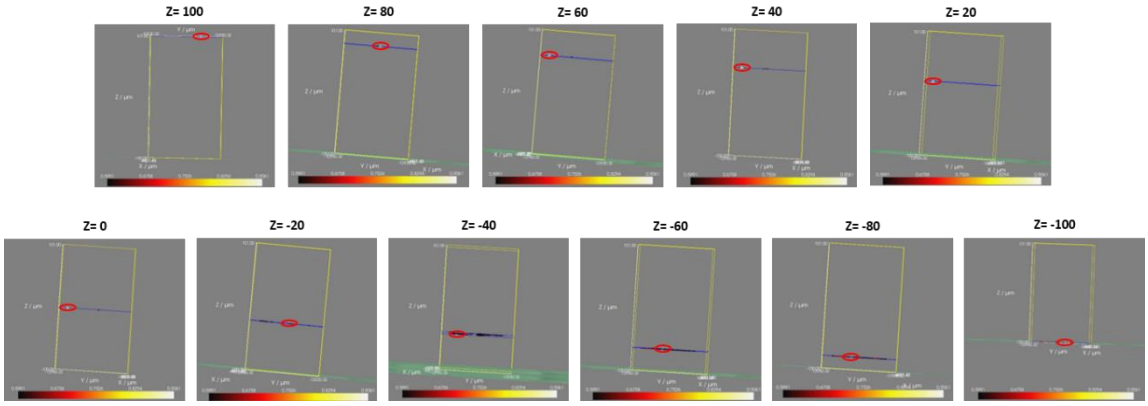

(B)

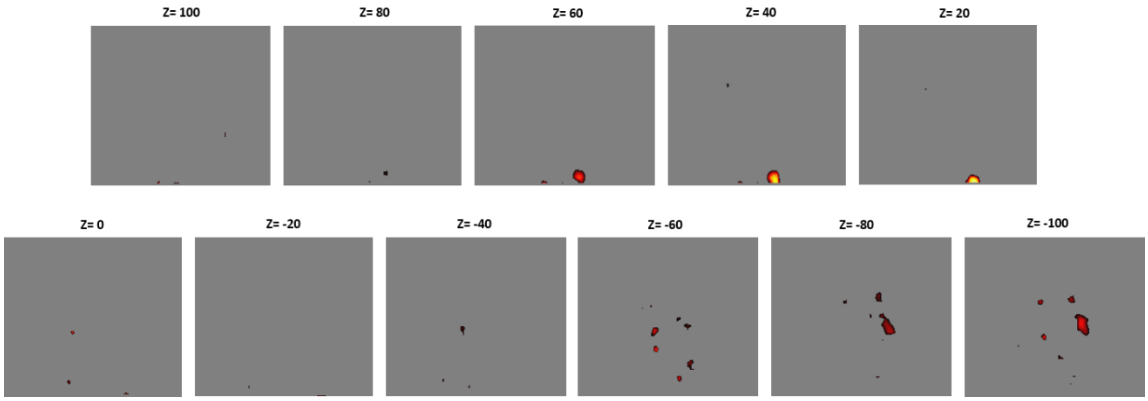

Figure 9: **(A)** 3D Raman mapping results and SERS spectra obtained at different z-axis points (red circle) through MCF-7 spheroids with ERα-AuNP nanotags (60 pM, 2h). The z-axis moves from top to bottom of the spheroids to get the SERS signal from the nanotags throughout the spheroid. **(B)** Z-plane representing the different z-axis points of MCF-7 spheroids SERS mapping. The plane shows that SERS signal from ERα-AuNPs is detected in different areas within the spheroids confirming the penetration of the nanotags into the spheroids. A 20× magnification NIR APO Nikon water immersion objective with a 0.4 NA was used on the samples at a laser power of 12 mW (100% power) at the sample, from a HeNe 633 nm excitation source with step size y,x: 3.0 µm, z: 4.0 µm, 0.1s acquisition time and a 1200 l/mm grating in high confocality mode. The minimum and maximum look up table thresholds were set to exclude any poorly correlating or noisy spectra (min= 0.6).

4.4.5 Assessment of Fulvestrant Activity in MCF-7 Tumour Spheroids

Most patients with ERα positive breast cancer benefit from endocrine therapy that targets the ERα pathway with higher efficacy and lower side effects.[41] Endocrine therapy involves a class of drugs called selective estrogen receptor down-regulators (SERDs) which bind to ERα resulting in its degradation and downregulation.[42] Fulvestrant is the first approved SERD for the treatment of ERα positive breast cancer.[43,44] Understanding the activity of fulvestrant using *in vitro* models can lead to improving the way the drug is used in the clinic. Previous work from our group, using SERS, has shown that 1 μM of fulvestrant decreased the relative expression levels of the ERα protein in 2D MCF-7 cell cultures (as shown in section 3.4.4). Here, SERS and microfluidics were used to assess the efficacy of fulvestrant in spheroids. On day 3 of culture, fulvestrant (1 μM and 10 μM) was added to the spheroids for 24 h. Bright-field imaging was performed after fulvestrant addition to investigate any induced toxicity and structural differences in the spheroids (Figure 10A). The results showed no significant difference at day 4 between the fulvestrant treated and the intreated spheroids. Viability staining showed that at day 4 there were no significant changes in the area of growth (Figure 10B) and the cell viability (Figure 10C) between the untreated and fulvestrant treated spheroids. Therefore, day 4 was considered optimal for the addition of the nanotags in the spheroids. However, a significant decrease in the area growth of the spheroids treated with 1 μM and 10 μM fulvestrant compared to the controls was observed on day 10 (Figure 10B). Additionally, the live/dead staining showed that both 1 μM of fulvestrant and 10 μM of fulvestrant had a toxic effect on the MCF-7 spheroids. (Figure 10C, 10D).

(A)

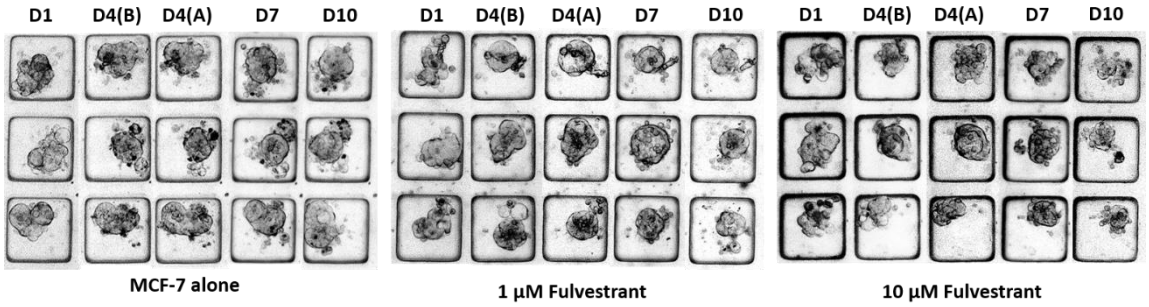

(B)

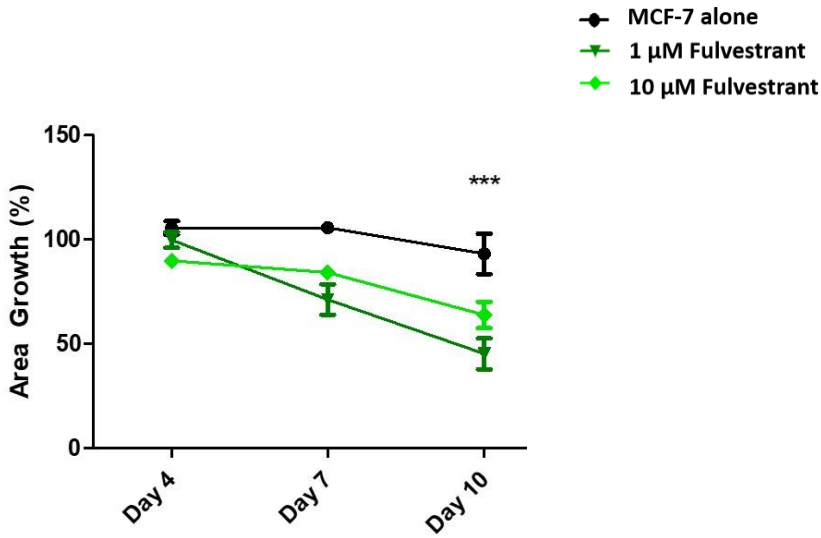

(C)

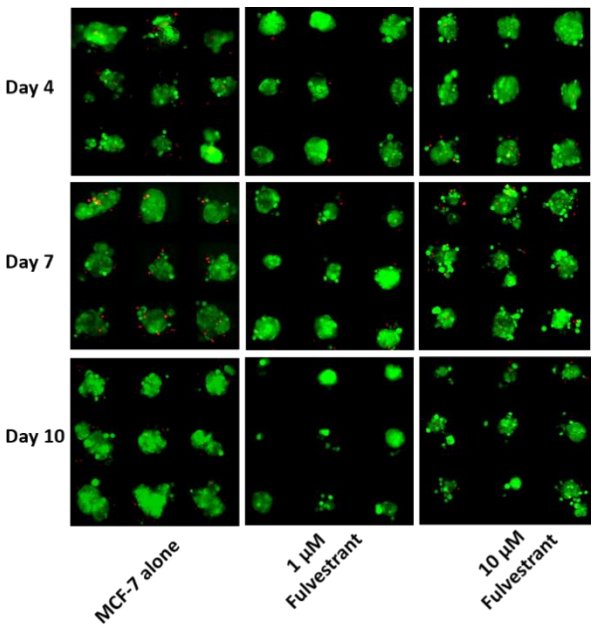

(D)

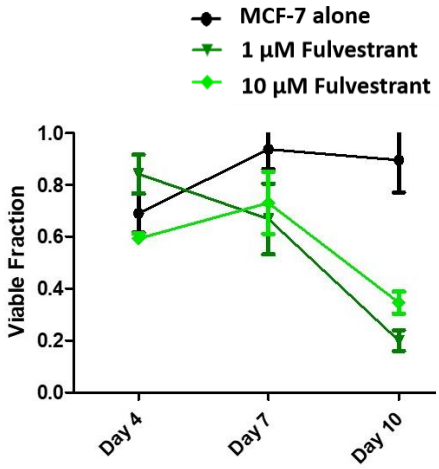

Green: FDA (Live cells)
Red: PI (Dead cells)

Figure 10: Fulvestrant treatment affected the growth and viability of MCF-7 spheroids in the microfluidic devices. **(A)** Brightfield imaging analysis was carried out on different days in spheroids without treatment (MCF-7 alone) and with 1 µM and 10 µM fulvestrant treatment. There was a significantly greater disaggregation with 10 µM (light green) fulvestrant treated spheroids in comparison to the untreated spheroids (black) by day 10. **(B)** Calculation of the percentage area growth of spheroids after 1 µM (dark green) and 10 µM (light green) fulvestrant treatment. Interestingly, it was shown that 1µM fulvestrant has a greater effect on the spheroids in terms of the area of grown compared to 10 µM fulvestrant. Although there was not a significant difference, this result was less expected. Hence, it was assumed that it may have been an anomaly with that particular channel in the device. Different devices should be used for each staining day to compare these results. **(C)** Cell viability assay of spheroid at different day points using live/dead staining with fluorescein diacetate (FDA) and propidium iodide (PI). Viable cells appear green, while non-viable cells appear red. **(D)** Calculation of viable fraction of untreated spheroids (black), spheroids treated with 1 µM fulvestrant (dark green) and 10 µM fulvestrant (light green). Similar to the area of growth, the viable fraction was slightly lower for 1 µM fulvestrant compared to 10 µM fulvestrant. Further live/dead staining should be performed to investigate these results. The viable fraction was estimated by calculating the ratio of FDA area on the day of staining over the brightfield area of the spheroid on the day prior to nanotags treatment. The average of 32 spheroids is shown. Error bars presented as mean ± S.D

To assess the nanotag targeting effect based on the SERS response after 24 h of fulvestrant treatment, the spheroids were incubated on day 4 with ERα-AuNPs (60 pM, 2h). After 2h incubation of ERα-AuNPs (60 pM), the spheroids were washed twice with PBS to remove any unbound nanotags and SERS imaging was carried out using a laser excitation wavelength of 633 nm. For the SERS mapping, similarly sized spheroids were chosen from both the untreated and fulvestrant treated samples. This step was carried out to increase the confidence that any eventual reduction of the SERS signal in the fulvestrant treated spheroids was due to the ERα degradation and not reduction of the spheroid size. 2D SERS mapping was carried out by focussing the laser of a Renishaw InVia Raman confocal microscope through the microfluidic device which was mounted on a coverslip. A 20× objective (N.A. 0.40) was used on the samples with a laser power of 12 mW (100% power) at the sample, from a HeNe 633 nm excitation source with a 0.1 s acquisition time per point, and a 1200 l/mm grating in high confocality mode. SERS mapping showed that there was lower nanotag accumulation in the spheroids treated with 10 µM fulvestrant

in comparison to 1 μM fulvestrant and the untreated spheroids (Figure 11A). Additionally, a statistically significant decrease (1.8 times) was observed in the SERS intensity at 1610 cm^{-1} (representative peak of BPE Raman reporter attached to the ERα-AuNPs) after treatment with 10 μM of fulvestrant compared to the untreated spheroids (Figure 11B). On the other hand, no significant difference was observed between the untreated spheroids and 1 μM fulvestrant treatment (Figure 11B). Therefore, this suggested that 10 μM of fulvestrant reduced the amount of ERα in the spheroids, while 1 μM fulvestrant seemed to not cause any ERα reduction. These results showed some differences with our previous SERS experiments that evaluated fulvestrant efficacy in 2D MCF-7 cell culture (as shown in section 3.4.4). Specifically, in the 2D environment, 1 μM fulvestrant was sufficient to statistically reduce the amount of ERα. However, in the MCF-7 spheroids, this concentration seemed to not cause any reduction. This data highlights that 2D and 3D MCF-7 cultures may have different biological behaviours and architectural phenotypes that contribute to how MCF-7 cells are exposed and react to drug, in this case fulvestrant, treatment. Therefore, the ERα association and localisation may be different in the spheroids compared to 2D monolayered MCF-7 cell cultures that have affected sensitivity to fulvestrant exposure. The requirement for higher fulvestrant concentration in the spheroids suggests that there was probably a lower drug penetration and distribution into the spheroids which may have reduced the therapeutic effect of the drug at the target site. Therefore, it is vital to identify these variabilities and perform the same experimental approach using various fulvestrant concentrations at different treatment times to investigate the drug efficacy and penetration performance in more representative *in vivo* environment.

(A)

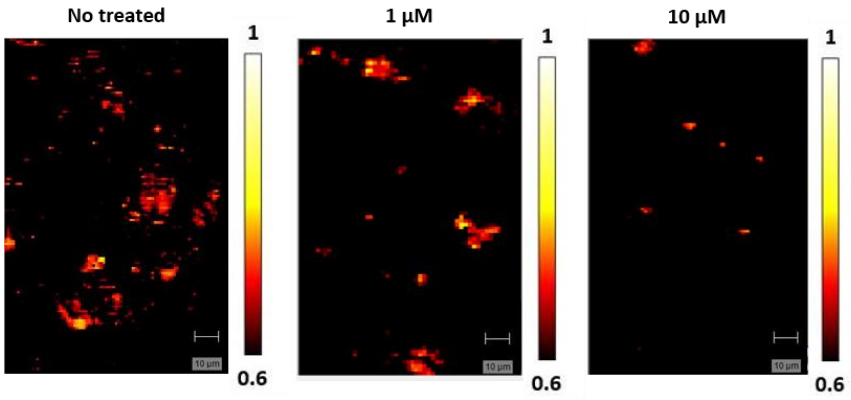

(B)

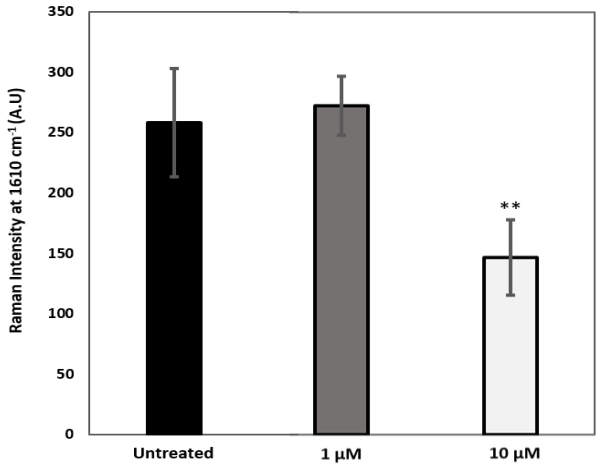

Figure 11: Spheroid treatment with 10 µM of fulvestrant led to lower ERα-AuNP accumulation suggesting ERα reduction in MCF-7 spheroids. **(A)** SERS map of untreated MCF-7 spheroids and spheroids treated with fulvestrant (1 µM and 10 µM) for 24 h and then with ERα-AuNP nanotags (60 pM, 2 h). The images were generated with a 20× magnification NIR APO Nikon objective, laser power of 12 mW (100% power), from a HeNe 633 nm excitation source with a 0.1 s acquisition time per point, and a 1200 l/mm grating in high confocality mode. The false coloured images representing the ERα-AuNPs were generated using the WiRE™ - Renishaw plc 4.4 software package on a Renishaw InVia microspectrometer and direct classical least square analysis (DCLS) based on a BPE Raman reporter reference spectrum. The minimum and maximum look up table (LUT) thresholds were set to exclude any poorly correlating or noisy spectra (min= 0.6). Scale bar= 10 µm **(B)** Average Raman intensity at 1610 cm^{-1} (representative peak for BPE Raman reporter). The average of three samples is shown. Error bars presented as mean ± S.D. * Significant difference ($p< 0.05$) in a one-way analysis of variance (ANOVA) test.

4.5 Conclusion

Many recent studies on high-throughput microfluidics are based on fluorescence. [22,45] Here, we demonstrate that the multiplexing capabilities of SERS combined with anti-ERα antibody functionalised (ERα-AuNPs) and anti-HER2 antibody functionalised (HER2-AuNPs) nanotags can be successfully applied to characterising tumour spheroids with the advantages of high sensitivity and specificity. The results showed that SERS can provide a high-throughput method without the use of fluorescence for analysis of 3D tumour models. This novel combination of microfluidics and SERS was successfully applied to identifying and classifying live ERα-positive MCF-7 breast cancer spheroids. Also, it allowed us to assess the activity of fulvestrant, the first commercially available ERα degrader in 3D models. The spheroids formed inside the microfluidic device maintained their integrity and viability after SERS nanotags treatment. Specifically, a strong targeting effect of ERα-AuNPs was observed in MCF-7 spheroids compared to HER2-AuNPs. Most importantly, 3D SERS mapping revealed that SERS signal was detected from areas within the inner part of the spheroid, confirming the uptake and penetration of the nanotags into the cells in a 3D environment. The reduction of ERα protein after fulvestrant treatment was also verified from the lower SERS signal generated in the fulvestrant treated spheroids. Different studies have reported similar drug behaviours[46,47,48,49] which support our evidence that the type of cell culture can substantially alter the effect of a drug on the cells. Therefore, this work highlights the importance of performing assay based on 3D cultures that may better reflect some aspects of the *in vivo* tumour environment. This paper emphasises the benefits of combining microfluidics and SERS as a fundamental non-destructive analytical tool alternative t fluorescence microscopy. Future opportunities may involve multiplex detection of different biomarkers and investigation of the drug efficacy in spheroids grown from patient derived cells for personalised therapeutic approaches by using a combination of nanotechnology and microfluidics for targeted, high throughput and high sensitivity methods.

4.6 References

1. Ferlay, J., Soerjomataram, I., Dikshit, R. & All, E. Cancer incidence and mortality worldwide: Sources, methods and major patterns in GLOBOCAN 2012. *Int J Cancer* (2015). doi:10.1002/ijc.29210
2. Torre, L. A., Siegel, R. L., Ward, E. M. & Jemal, A. Global cancer incidence and mortality rates and trends - An update. *Cancer Epidemiology Biomarkers and Prevention* (2016). doi:10.1158/1055-9965.EPI-15-0578
3. UK, C. R. Breast cancer incidence (invasive) statistics: Breast cancer incidence (invasive) statistics. *Online Source* (2016).
4. Korkaya, H., Liu, S. & Wicha, M. S. Breast cancer stem cells, cytokine networks, and the tumor microenvironment. *Journal of Clinical Investigation* (2011). doi:10.1172/JCI57099
5. Quail, D. F. & Joyce, J. A. Microenvironmental regulation of tumor progression and metastasis. *Nature Medicine* (2013). doi:10.1038/nm.3394
6. Mao, Y., Keller, E. T., Garfield, D. H., Shen, K. & Wang, J. Stromal cells in tumor microenvironment and breast cancer. *Cancer and Metastasis Reviews* (2013). doi:10.1007/s10555-012-9415-3
7. Jernström, S. *et al.* Drug-screening and genomic analyses of HER2-positive breast cancer cell lines reveal predictors for treatment response. *Breast Cancer: Targets and Therapy* (2017). doi:10.2147/BCTT.S115600
8. Imamura, Y. *et al.* Comparison of 2D- and 3D-culture models as drug-testing platforms in breast cancer. *Oncology Reports* (2015). doi:10.3892/or.2015.3767
9. Yamada, K. M. & Cukierman, E. Modeling Tissue Morphogenesis and Cancer in 3D. *Cell* (2007). doi:10.1016/j.cell.2007.08.006
10. DelNero, P. *et al.* 3D culture broadly regulates tumor cell hypoxia response and angiogenesis via pro-inflammatory pathways. *Biomaterials* (2015). doi:10.1016/j.biomaterials.2015.03.035
11. Faute, M. A. D. *et al.* Distinctive alterations of invasiveness, drug resistance and cell-cell organization in 3D-cultures of MCF-7, a human breast cancer cell line, and its multidrug resistant variant. *Clinical and Experimental Metastasis* (2002). doi:10.1023/A:1014594825502
12. Fang, Y. & Eglen, R. M. Three-Dimensional Cell Cultures in Drug Discovery and

Development. *SLAS Discovery* (2017). doi:10.1177/1087057117696795

13. Breslin, S. & O'Driscoll, L. Three-dimensional cell culture: The missing link in drug discovery. *Drug Discovery Today* (2013). doi:10.1016/j.drudis.2012.10.003
14. Jeon, J. S. *et al.* Human 3D vascularized organotypic microfluidic assays to study breast cancer cell extravasation. *Proceedings of the National Academy of Sciences* (2015). doi:10.1073/pnas.1417115112
15. Yang, Y. *et al.* Evaluation of photodynamic therapy efficiency using an in vitro three-dimensional microfluidic breast cancer tissue model. *Lab on a Chip* (2015). doi:10.1039/c4lc01065e
16. Sackmann, E. K., Fulton, A. L. & Beebe, D. J. The present and future role of microfluidics in biomedical research. *Nature* (2014). doi:10.1038/nature13118
17. Mehling, M. & Tay, S. Microfluidic cell culture. *Current Opinion in Biotechnology* (2014). doi:10.1016/j.copbio.2013.10.005
18. Du, G., Fang, Q. & den Toonder, J. M. J. Microfluidics for cell-based high throughput screening platforms-A review. *Analytica Chimica Acta* (2016). doi:10.1016/j.aca.2015.11.023
19. Salameh, T. S. *et al.* An ex vivo co-culture model system to evaluate stromal-epithelial interactions in breast cancer. *International Journal of Cancer* (2013). doi:10.1002/ijc.27672
20. MacKerron, C., Robertson, G., Zagnoni, M. & Bushell, T. J. A Microfluidic Platform for the Characterisation of CNS Active Compounds. *Scientific Reports* (2017). doi:10.1038/s41598-017-15950-0
21. Migliozzi, D., Nguyen, H. T. & Gijs, M. A. M. Combining fluorescence-based image segmentation and automated microfluidics for ultrafast cell-by-cell assessment of biomarkers for HER2-type breast carcinoma. *Journal of Biomedical Optics* (2018). doi:10.1117/1.jbo.24.2.021204
22. Lin, S. W., Chang, C. H. & Lin, C. H. High-throughput Fluorescence Detections in Microfluidic Systems. *Genomic Medicine, Biomarkers, and Health Sciences* (2011). doi:10.1016/S2211-4254(11)60005-8
23. Willner, M. R., McMillan, K. S., Graham, D., Vikesland, P. J. & Zagnoni, M. Surface-Enhanced Raman Scattering Based Microfluidics for Single-Cell Analysis. *Analytical Chemistry* (2018). doi:10.1021/acs.analchem.8b02636
24. Pu, H., Xiao, W. & Sun, D. W. SERS-microfluidic systems: A potential platform for

rapid analysis of food contaminants. *Trends in Food Science and Technology* (2017). doi:10.1016/j.tifs.2017.10.001

25. Kamińska, A. *et al.* SERS-based Immunoassay in a Microfluidic System for the Multiplexed Recognition of Interleukins from Blood Plasma: Towards Picogram Detection. *Scientific Reports* (2017). doi:10.1038/s41598-017-11152-w
26. Gao, R. *et al.* SERS-Based Pump-Free Microfluidic Chip for Highly Sensitive Immunoassay of Prostate-Specific Antigen Biomarkers. *ACS Sensors* (2019). doi:10.1021/acssensors.9b00039
27. Albrecht, M. G. & Creighton, J. A. Anomalously Intense Raman Spectra of Pyridine at a Silver Electrode. *Journal of the American Chemical Society* (1977). doi:10.1021/ja00457a071
28. Liao, P. F. & Wokaun, A. Lightning rod effect in surface enhanced Raman scattering. *The Journal of Chemical Physics* (1982). doi:10.1063/1.442690
29. Asiala, S. M. & Schultz, Z. D. Characterization of hotspots in a highly enhancing SERS substrate. *Analyst* (2011). doi:10.1039/c1an15432j
30. Faulds, K., McKenzie, F., Smith, W. E. & Graham, D. Quantitative simultaneous multianalyte detection of DNA by dual-wavelength surface-enhanced resonance raman scattering. *Angewandte Chemie - International Edition* (2007). doi:10.1002/anie.200604265
31. Gracie, K. *et al.* Simultaneous detection and quantification of three bacterial meningitis pathogens by SERS. *Chemical Science* (2014). doi:10.1039/c3sc52875h
32. Lee, S. *et al.* Rapid and sensitive phenotypic marker detection on breast cancer cells using surface-enhanced Raman scattering (SERS) imaging. *Biosensors and Bioelectronics* (2014). doi:10.1016/j.bios.2013.07.063
33. Davis, R. *et al.* A Raman Imaging Approach Using CD47 Antibody-Labeled SERS Nanoparticles for Identifying Breast Cancer and Its Potential to Guide Surgical Resection. *Nanomaterials* (2018). doi:10.3390/nano8110953
34. Harmsen, S., Wall, M. A., Huang, R. & Kircher, M. F. Cancer imaging using surface-enhanced resonance Raman scattering nanoparticles. *Nature Protocols* (2017). doi:10.1038/nprot.2017.031
35. El-Said, W. A., Yoon, J. & Choi, J. W. Nanostructured surfaces for analysis of anticancer drug and cell diagnosis based on electrochemical and SERS tools. *Nano Convergence* (2018). doi:10.1186/s40580-018-0143-4

36. Panikar, S. S. *et al.* Ultrasensitive SERS Substrate for Label-Free Therapeutic-Drug Monitoring of Paclitaxel and Cyclophosphamide in Blood Serum. *Analytical Chemistry* (2019). doi:10.1021/acs.analchem.8b04523
37. Mulholland, T. *et al.* Drug screening of biopsy-derived spheroids using a self-generated microfluidic concentration gradient. *Scientific Reports* (2018). doi:10.1038/s41598-018-33055-0
38. Kalyane, D. *et al.* Employment of enhanced permeability and retention effect (EPR): Nanoparticle-based precision tools for targeting of therapeutic and diagnostic agent in cancer. *Materials Science and Engineering C* (2019). doi:10.1016/j.msec.2019.01.066
39. Nel, A., Ruoslahti, E. & Meng, H. New Insights into 'permeability' as in the Enhanced Permeability and Retention Effect of Cancer Nanotherapeutics. *ACS Nano* (2017). doi:10.1021/acsnano.7b07214
40. Huynh, E. & Zheng, G. Cancer nanomedicine: Addressing the dark side of the enhanced permeability and retention effect. *Nanomedicine* (2015). doi:10.2217/nnm.15.86
41. Bonotto, M. *et al.* Chemotherapy versus endocrine therapy as first-line treatment in patients with luminal-like HER2-negative metastatic breast cancer: A propensity score analysis. *Breast* (2017). doi:10.1016/j.breast.2016.10.021
42. Patel, H. K. & Bihani, T. Selective estrogen receptor modulators (SERMs) and selective estrogen receptor degraders (SERDs) in cancer treatment. *Pharmacology and Therapeutics* (2018). doi:10.1016/j.pharmthera.2017.12.012
43. Croxtall, J. D. & McKeage, K. Fulvestrant: A review of its use in the management of hormone receptor-positive metastatic breast cancer in postmenopausal women. in *Drugs* (2011). doi:10.2165/11204810-000000000-00000
44. Nathan, M. R. & Schmid, P. A Review of Fulvestrant in Breast Cancer. *Oncology and Therapy* (2017). doi:10.1007/s40487-017-0046-2
45. Pedrol, E. *et al.* Microfluidic device with dual-channel fluorescence acquisition for quantification/identification of cancer cells. *Microfluidics and Nanofluidics* (2017). doi:10.1007/s10404-017-2015-3
46. Pickl, M. & Ries, C. H. Comparison of 3D and 2D tumor models reveals enhanced HER2 activation in 3D associated with an increased response to trastuzumab. *Oncogene* (2009). doi:10.1038/onc.2008.394
47. Lee, G. Y., Kenny, P. A., Lee, E. H. & Bissell, M. J. Three-dimensional culture models of normal and malignant breast epithelial cells. *Nature Methods* (2007).

doi:10.1038/nmeth1015

48. Shaw, K. R., Wrobel, C. N. & Brugge, J. S. Use of three-dimensional basement membrane cultures to model oncogene-induced changes in mammary epithelial morphogenesis. *Journal of Mammary Gland Biology and Neoplasia* (2004). doi:10.1007/s10911-004-1402-z
49. Gao, Y. *et al.* A versatile valve-enabled microfluidic cell co-culture platform and demonstration of its applications to neurobiology and cancer biology. *Biomedical Microdevices* (2011). doi:10.1007/s10544-011-9523-9
50. Hanauer, M., Pierrat, S., Zins, I., Lotz, A. & Sönnichsen, C. Separation of nanoparticles by gel electrophoresis according to size and shape. *Nano Letters* (2007). doi:10.1021/nl071615y
51. Rahme, K. *et al.* PEGylated gold nanoparticles: Polymer quantification as a function of PEG lengths and nanoparticle dimensions. *RSC Advances* (2013). doi:10.1039/c3ra22739a

5. *Ex Vivo* and *In Vivo* Detection of Estrogen Receptor Alpha (ERα) in Breast Cancer Using Handheld SERS and SESORS Instruments

Contributing authors:

Anastasia Kapara[1,2], Neil C. Shand[3], Duncan Graham[1], Valerie Brunton[2], Karen Faulds[1]

1. Centre for Molecular Nanometrology, Department of Pure and Applied Chemistry, Technology and Innovation Centre, University of Strathclyde, 99 George Street, Glasgow G1 1RD, UK.

2. MRC Institute of Genetics and Molecular Medicine, Edinburgh Cancer Research UK Centre, University of Edinburgh, Western General Hospital, Crewe Road South, Edinburgh, EH4 2XU, UK

3. DSTL, Porton Down, Salisbury, SP4 0JQ, UK.

5.1 Abstract

In the field of optical medical imaging, there is a major need for the detection of molecular biomarkers at high depth through tissue. Surface-enhanced spatially offset Raman spectroscopy (SESORS) is an innovative analytical technique that combines the remarkable enhancement of surface-enhanced Raman spectroscopy (SERS) with the high volume and thickness detection capabilities of spatially offset Raman spectroscopy (SORS).

Herein, we present the use of a handheld SORS instrument with back scattering optics for detection of estrogen receptor alpha (ERα) *ex vivo* in live 3D tumour spheroids through tissue barriers using anti-ERα functionalised gold nanoparticles (ERα-AuNPs). Additionally, we investigate the use of SESORS for *in vivo* detection of breast cancer. The successful imaging of live 3D breast cancer tumour spheroids through 10 mm of porcine tissue and the detection of nanotags' solution through tissue up to 15 mm were achieved using SESORS. The *in vivo* work indicated that the handheld SORS instrument was detecting scattered photons from areas deeper than the breast cancer tumour due to its fixed optical arrangements that were set at 8 mm offset distance. Nevertheless, a higher signal was detected in breast tumours compared to liver *ex vivo* after removal of the organs from the sacrificed animals, suggesting the strong targeting effect of ERα-AuNPs to the tumour site.

Our results highlight the powerful capabilities of SESORS to track and detect SERS nanotags at high tissue thickness *ex vivo*. However, factors such as the depth of the tumour under investigation and the optical arrangements of the SORS spectrometer should be taken into consideration for successful detection *in vivo*. To our knowledge, this is the first report of the assessment of a handheld SORS instrument with back scattering optics for detecting breast cancer both *ex vivo* and *in vivo*. This study highlights the performance and capabilities of small, handheld SORS to detect and track SERS nanotags based on the characteristics of the surface breast cancer *in vivo* and *ex vivo*. This opens up exciting opportunities for using SESORS and SERS as non-destructive and sensitive techniques for improved biomedical imaging in a clinical environment.

Keywords: Surface enhanced spatially offset Raman spectroscopy (SESORS), *ex vivo*, *in vivo*, ERα, tumour spheroids, at depth detection

5.2 Introduction

Breast cancer is the leading cause of oncologic mortality and morbidity among women worldwide.[1,2] Current statistics in the UK suggest than one in eight women will develop breast cancer at some point in their lifetime and more than 71,000 new cases are expected to be diagnosed by 2035.[3] The most prominent limitations of the current screening approaches are the false positive and false negative results and the overdiagnosis that may lead to late and non-efficacious overtreatment. It is estimated that of all screenings, 10-20% are false positive while 15-20% are false negative.[4] Therefore, there is a need for advancements in optical medical imaging for improved analytical tools for more accurate detection of breast cancer.

Surface enhanced spatially offset Raman spectroscopy (SESORS) combines the deep penetration capabilities of SORS with the signal enhancing, sensitivity and specificity benefits of SERS.[5] Although, SESORS requires the introduction of SERS nanotags, the readout can be completely non-invasive and it can be achieved at higher depths in comparison to traditional Raman and SERS techniques.[6,7] Hence, there is the prospect of utilising SESORS for imaging and targeting of small tumours *in vivo* using functionalised nanoparticles.[8,9] Nicolson *et al.* demonstrated for the first time the detection of live breast cancer 3D multicellular tumour spheroids containing surface enhanced resonance Raman scattering (SERRS) active gold nanoparticles through 15 mm of porcine tissue. The group also demonstrated a multiplex system for imaging and distinguishing three singleplex nanotags within breast cancer tumour models through 10 mm of tissue using a handheld SORS instrument.[10] Additional studies have shown that SESORS spectrometers can detect the nanotags at high depths of tissue and bone.[5,6,11] These biomedical applications expand the potential of using SESORS *in vivo*.

Currently, there are no scientific approaches that use SESORS for *in vivo* detection. However, there are *in vivo* experiments that have performed the detection of biomarkers using SERS imaging. One of the first SERS *in vivo* applications was conducted in 2008 where Qian *et al.* functionalised nanotags with single-chain variable fragment (ScFv) antibodies to target EGFR overexpression in different cancers.[8] Another study verified that functionalised nanotags showed greater affinity for the tumour after injection of nanotags in tumour-bearing mice models in comparison to non-functionalised nanotags.[12] Wang *et al*. worked on the functionalisation of nanotags with three different antibodies: anti-HER2, anti-EGFR and an isotype control.[13] The

nanotags were tested *in vivo* into two different tumour types with a varied expression of HER2 and EGFR. After the topical administration of the nanoparticles, the tumours were implanted and were analysed using SERS. The results showed the potential of simultaneous detection of the targeted nanotags for the assessment of the molecular expression of cancer.[13] Nanotags have also been used *in vivo* for the diagnosis of other diseases, such as the indication of atherosclerosis and inflammation.[14] Recently, Noonan *et al*. reported the targeted *in vivo* imaging of different vascular inflammatory biomarkers, using SERS and antibody-functionalised nanoparticles to assess localised vascular inflammation in mouse models, demonstrating the capabilities of SERS as a potential clinical imaging technique.[15]

Here, SESORS was used to detect ERα positive breast tumours *ex vivo* and *in vivo*. Specifically, we report for the first time the use of gold nanoparticles (AuNPs) functionalised with anti-ERα antibody (ERα-AuNPs) for *ex vivo* tracking of live 3D MCF-7 spheroids buried at 10 mm tissue and the detection of breast tumour *in vivo* using a SORS instrument with back scattering optics.

5.3 Experimental

5.3.1 Materials

As previously described in section 2.3.1.

5.3.2 Nanoparticle Synthesis and Functionalisation of ERα-AuNPs

As previously described in section 2.3.2.

5.3.3 Nanotags Characterisation

As previously described in section 2.3.3.

5.3.4 3D Breast Cancer Spheroids Formation and ERα-AuNPs Incubation

MCF-7 cells (ATCC® HTB-22™) were obtained from American Type Culture Collection (ATCC) (Queens Road, Teddington, Middlesex, TW11 0LY, UK). The human breast cancer cells

were cultured in Rosewell Park Memorial Institute medium (RPMI 1640) supplemented with 1% penicillin/streptomycin (10000 units per mL), 1% fungizone, and 10% heat-inactivated fetal bovine serum (FBS). Cells were incubated at 37 °C and 5% CO_2 in a humidified incubator. Cells at a confluence of ca. 90% growing in a T175 flask were trypsinised and re-suspended in medium to give a concentration of ca. 1×10^6 cells per mL. Cells were incubated with ERα-AuNP nanotags (60 pM, 2 h) and they were then were trypsinised and re-suspended in medium to give a concentration of ca. 2.5×10^6 cells/mL. MCF-7 breast cancer spheroids were formed using the hanging drop method, that involved the growing of spheroids from drops of cell suspension (20 µL) onto the lid of a 15 cm petri dish containing 12 mL RPMI medium. The lid was placed on the dish and MCF-7 breast cancer spheroids grew over 9 days at 37 °C and 5% CO_2 in a humidified incubator to a size <1mm. The medium was removed from the drops and replaced after 3 days. MCF-7 cells aggregated in the drops that remained intact by surface tension and therefore grew into breast cancer spheroids. No reduction in growth was observed suggesting that the ERα-AuNP nanotags did not cause any cell toxicity.

5.3.5 Detection of ERα-AuNP Nanotags Through Tissue Barrier Detection

Pork loin tissue was cut into sections of 5 mm thickness each. ERα-AuNP nanotags (60 pM, 400 µL) was placed into a Suprasil quartz microcuvette (1 mm path length). Pork loin tissue was then placed in front of the cuvette and it was brought into contact with the laser using the nose cone of the SORS spectrometer. This ensured there was no air/space between the tissue and instrument. All measurements were carried out using the fixed maximum exposure time (10 sec exposure time in total, 2 sec integration time, 5 accumulations) at an 8 mm offset distance using a handheld SORS instrument with 830 nm laser excitation wavelength (Agilent Resolve instrument).

5.3.6 Detection of Live 3D Breast Cancer Spheroids Through Tissue Barrier

For the 2D SESORS mapping experiments the breast cancer tumour spheroids were placed directly onto a section of tissue and another tissue (5 mm or 10 mm thickness) was placed on top of the tissue containing the spheroids. The two-layer sample was then brought into contact with the laser using the nose cone of the SORS instrument. The SORS spectrometer was positioned above the tissue with the laser pointing down onto the sample. An x-y-positioning stage was used to enable SESORS 2D mapping of the ERα-AuNPs nanotags into the 3D breast cancer tumour spheroids

through 5 mm or 10 mm of tissue. False colour heat maps were produced in Matlab using the intensity of the 1610 cm^{-1} peak (representative peak from BPE Raman reporter) and plotted as a combination surface/contour false colour 2D heat. The stage started from x= 0 and y= 0 point and it was moved in 5 mm steps each time (x= 6 points, y= 4 point) creating a 6 x 4-pixel image out of 24 spectra. The z point remained fixed for the whole mapping (the stage was not moved in the z-direction). All spectra were baselined for the creation of the 2D SERS intensity map.

5.3.7 *In Vivo* Tumour Targeting and Detection

In vivo SESORS and SERS measurements were performed in two female CD-1 nude mice (d.o.b 18/03/19) that were implanted s/c bilaterally with MCF-7 cells (1 x 10^6 cells/mL, 100 µL per implant). The two tumours in each mouse (right and left tumour) were monitored and measured twice weekly. When tumour size reached approximately 5 mm in diameter, ERα-AuNPs nanotags were injected (600 pM, 50 µL) intravenously via the tail in a single injection. 4 h post-injection the mice were anaesthetised and imaged using handheld SORS and handheld SERS instruments. The protocol was Experimental Request Form (ERF) 044-WGH-19, which was reviewed and approved by the vet before the start of the study. The experimental procedures overall and Project Licences were reviewed by the Animal Welfare Ethical Review Board (AWERB).

The *in vivo* SESORS and SERS spectra were measured at the tumour sites and the anatomical location of the liver in live mice using a handheld SORS instrument with 830 nm laser excitation wavelength (Agilent Resolve instrument) and a handheld Raman spectrometer (CBex from Snowy Range Instruments) with 785 nm laser excitation wavelength. The SESORS measurements were obtained using a 2 s integration time, with 5 accumulations at an 8 mm offset. The laser power density was 450 mW which was lower than the maximum permissible expose (MPE) of skin to laser radiation according to British standards.[16] The nose cone was fitted to use the instrument in a contact mode setting. The *in vivo* SERS measurements were obtained using a 2 s integration time, with 5 accumulations. A point and shoot adaptor with a single element lens and a numerical aperture of 0.5 were fitted. This gave an average laser power of 43 mW.

5.3.8 *Ex Vivo* Tumour Targeting and Detection

Mice were euthanized by cervical dislocation. Breast tumours (right and left) and liver were removed and imaged *ex vivo* without any fixation, sectioning or staining. SESORS and SERS spectra were measured using the same instrument settings as the *in vivo* work.

5.3.9 Data Processing

All spectra were baselined before the data analysis. Principal component analysis (PCA) was performed on spectra obtained from the handheld SORS instrument to find any potential difference between the spectrum and the tissue barrier. For PCA the spectra were normalised and processed using Matlab software (Version 2015a, The MathWorks, Natrick, MA, USA). The offset spectra were used for the SESORS data analysis.

5.4 Results and Discussion

5.4.1 Detection of ERα-AuNPs in Solution Through Tissue Barrier

The synthesis and characterisation of ERα-AuNPs have been previously discussed in section 2.4.1. To evaluate the full capabilities of SESORS, ERα-AuNPs (functionalised with an anti-ERα antibody and BPE Raman reporter) were analysed *in vitro* through tissue barriers using a handheld SORS spectrometer with back scattering optics with 830 nm laser excitation wavelength. Specifically, the nanotags' solution was held in a quartz microcuvette and analysed through different thicknesses of porcine tissue barriers. The tissue (5 mm) was mounted on a stage to create the desired thickness and were placed in front of the microcuvette (Figure 1A). The tissue was then brought into contact with the laser from the SORS spectrometer by placing the nose cone against the tissue leaving no air space between the tissue and the instrument (Figure 1A). Previous work from our group has shown that 8 mm offset (maximum capability of SORS instrument) gives the greatest level of detection through barriers[17], hence, 8 mm offset was used for all experiments.

SESORS results showed that it was possible to detect the characteristic peak at 1610 cm^{-1} of BPE Raman reporter (attached on the ERα-AuNPs) through up to 15 mm of tissue (Figure 1B). SERS signal was not detectable after the addition of 20 mm tissue barrier, where the dominant signal

was from the porcine tissue at 1430 cm^{-1} (Figure 1B). Principal component analysis (PCA) was also performed for the identification of variations in spectra. PCA showed clear discrimination between the spectra from the nanotags and tissue barrier at 15 mm (Figure 2A, 2B). The maximum exposure time of the SORS instrument was fixed at 10 sec, therefore a longer exposure time may further improve the signal intensity. Nevertheless, the experiments confirmed the detection of ERα-AuNPs at high depth and demonstrated the potential of SESORS to detect nanotags through tissue thicknesses using a back-scattering configuration. The detection of signal at high depths using SESORS demonstrated the capabilities of a handheld SORS instrument to detect biomolecules *in vitro* and *ex vivo*.

(A) **(B)**

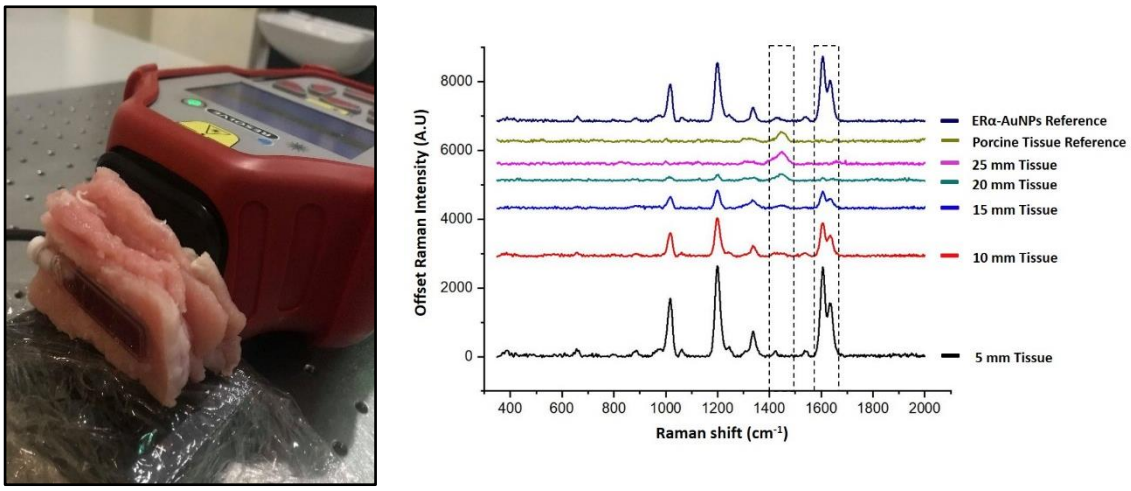

Figure 1: Experimental set up with porcine tissue barrier using handheld SORS instrument. **(A)** The tissues were mounted on a stage and clamped together to create the desired thickness. The thickness of the tissue was increased by 5 mm for each set of spectra acquisition with 25 mm maximum total thickness. Tissues were brought into contact with the laser using the nose cone of the SORS spectrometer which ensured that there was no air/space between the tissue and the instrument. A glass Suprasil quartz micro cuvette (1 mm thickness) containing the ERα-AuNPs nanotags (60 pM, 400 µL) was placed behind the porcine tissue. **(B)** Baselined stacked SESORS spectra of ERα-AuNPs through porcine tissue. Dashed boxes show the characteristic peak of the nanotags at 1610 cm^{-1} and the peak from porcine tissue at 1430 cm^{-1}. As the thickness of the tissue barrier is increased, it is challenging to distinguish the 1610 cm^{-1} at thicknesses beyond 15 mm. The peak at 1430 cm^{-1} starts to be present in the spectra after 20 mm tissue thickness. All measurements were carried out using the fixed maximum exposure time (10 sec exposure time in total, 2 sec integration time, 5 accumulations) at 8 mm offset distance at 830 nm wavelength.

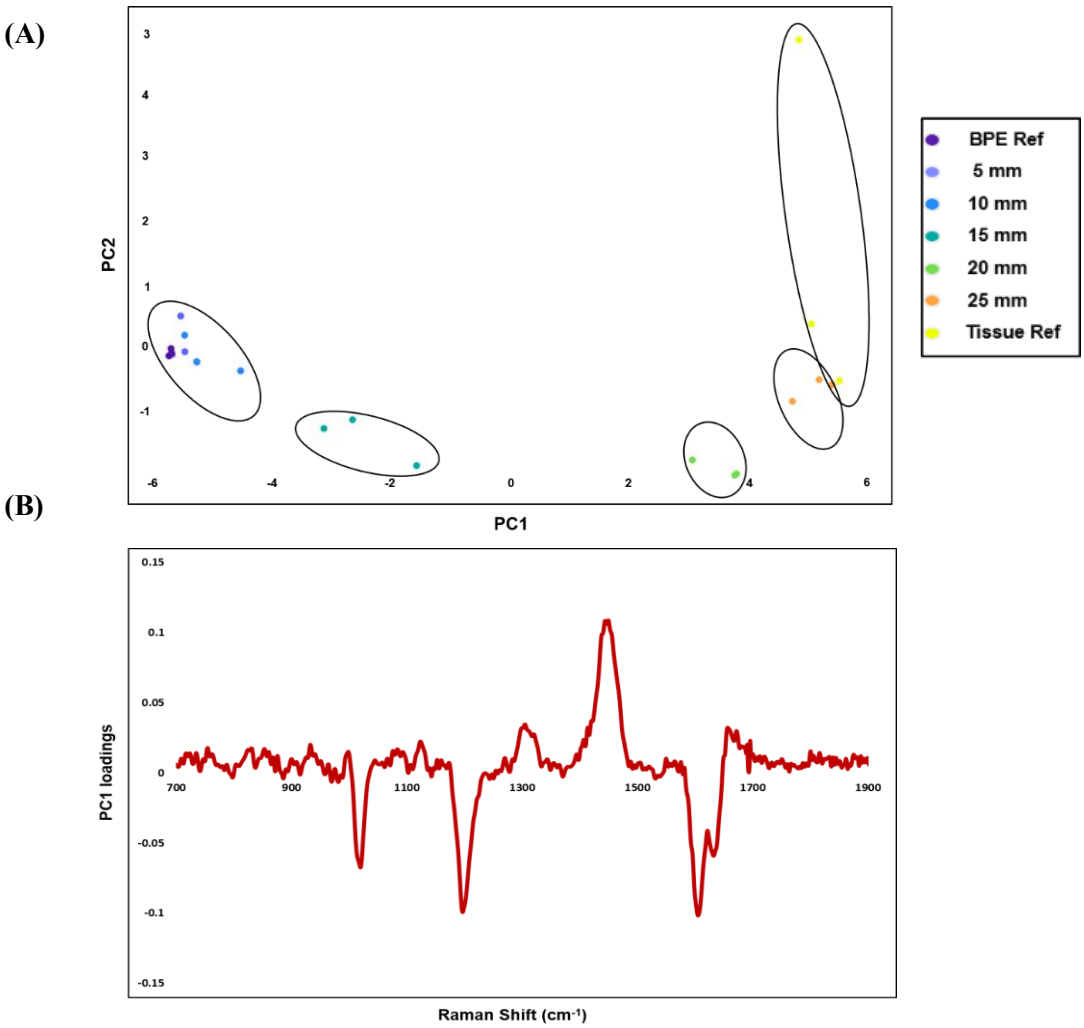

Figure 2: Raman signal was collected from ERα-AuNP nanotags through up to 15 mm of porcine tissue using a handheld SORS spectrometer with back scattering optics at 830 nm laser excitation wavelength **(A)** PCA plots from SERS spectra of different porcine thicknesses (0 mm to 25 mm) with BPE and tissue reference spectrum. PCA was important for the discrimination of the nanotags and the spectra received from the tissue barriers. The results confirmed that ERα-AuNP nanotags were detected through a porcine tissue to depths of up to 15 mm. **(B)** PC1 scores plots discriminating from nanotags through different porcine thicknesses (0 mm to 25 mm) along with BPE and tissue reference spectrum. Distinct separation is observed between the nanotag and tissue spectra.

5.4.2 Detection of ERα-AuNPs in Live 3D Breast Cancer Tumour Spheroids Through Tissue Barrier

This research aimed to establish whether ERα-AuNPs could be detected at high depth within the ERα positive breast cancer tumour spheroids. Therefore, here, live 3D breast cancer tumour spheroids were used as an *ex vivo* model for breast tumour combined with ERα-AuNPs to target and track ERα. Cancer spheroids, in contrast to traditional 2D cell cultures, better resemble the 3D *in vivo* environment making them an excellent model for experimental processes prior to *in vivo* experiments.[18] MCF-7 cells were incubated with ERα-AuNPs (60 pM, 2 h) and the 3D breast cancer tumour spheroids were grown over 9 days at 37 °C and 5% CO_2 in a humidified incubator. The tumour spheroids retained their spherical shape and no reduction in growth was observed during their culture, suggesting that ERα-AuNPs did not cause any cellular toxicity (Figure 3A). Once the spheroids were approximately 1 mm in size, they were placed on a piece of porcine tissue and another 5 mm or 10 mm of tissue was then placed on the top. The two-layer tissue was brought into contact with the laser using the nose cone of the SORS spectrometer (Figure 3B).

(A)

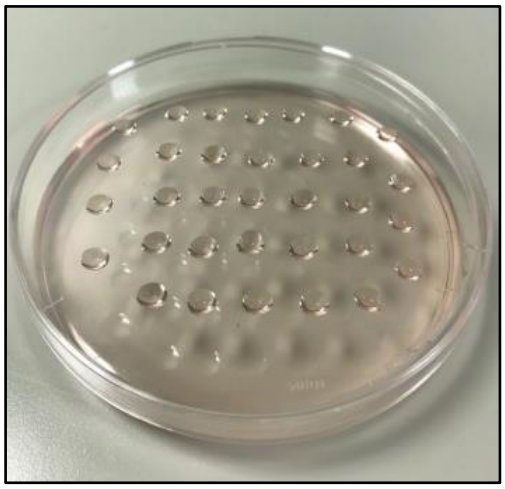

(B)

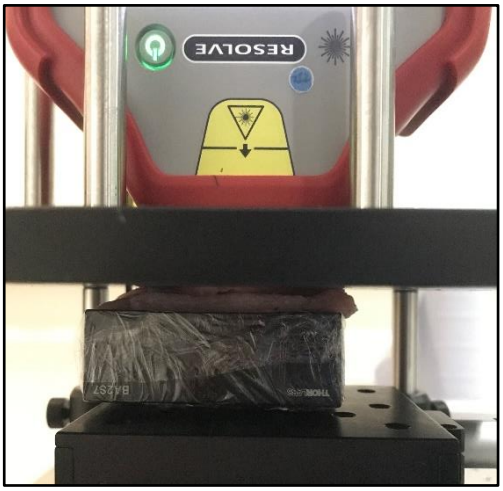

Figure 3: Experimental set up with porcine tissue as a barrier using a handheld SORS instrument with a nose cone. **(A)** Formation of live 3D breast cancer tumour spheroids incubated with ERα-AuNP nanotags. **(B)** Handheld SORS instrument mounted above a flat tissue sample with live 3D breast cancer tumour spheroids containing the ERα-AuNPs nanotags. The tumour spheroids were placed onto 5 mm thickness of porcine tissue. Then, 5 mm or 10 mm thickness tissue was placed on the top of the tissue layer containing the spheroids. The two-layer tissue was brought into contact with the laser using the nose cone of the SORS spectrometer. This ensured there was no air/space between the plastic and the instrument. In comparison to previous work involving the cuvette, the tissue section was laid flat on the stage and the handheld instrument mounted above the sample. This set up is more representative of an *in vivo* approach compared to that using the cuvette. The x-y positioning stage was used to enable mapping of the 3D breast cancer tumour spheroids containing SERS nanotags through tissue. All measurements were carried out using the fixed maximum exposure time (10 sec exposure time in total, 2 sec integration time, 5 accumulations) at an 8 mm offset distance at 830 nm wavelength.

False colour 2D heat intensity maps were then created using the intensity of the BPE peak at 1610 cm^{-1} (attached on ERα-AuNPs) to track the localisation of the 3D breast cancer tumour spheroids within the tissue. The schematic for the creation of the heat maps is shown in SI Figure S1. The 2D heat intensity maps confirmed the detection and localisation of the spheroids through up to 10 mm of porcine tissue. This result confirmed the uptake and accumulation of the nanotags within the tumour. Specifically, the heat intensity maps showed that there was clear discrimination between the areas where the tumour spheroids were present (maximum intensity depicted as the red colour) and where they were not (minimum intensity depicted as the blue colour) (Figure 4A, 4C). Therefore, using the handheld SORS instrument it was possible to sensitively detect and successfully map live 3D breast cancer tumour spheroids at high depths *ex vivo*. This is a significant step towards the detection of nanotags to locate tumours at high depths *in vivo*.

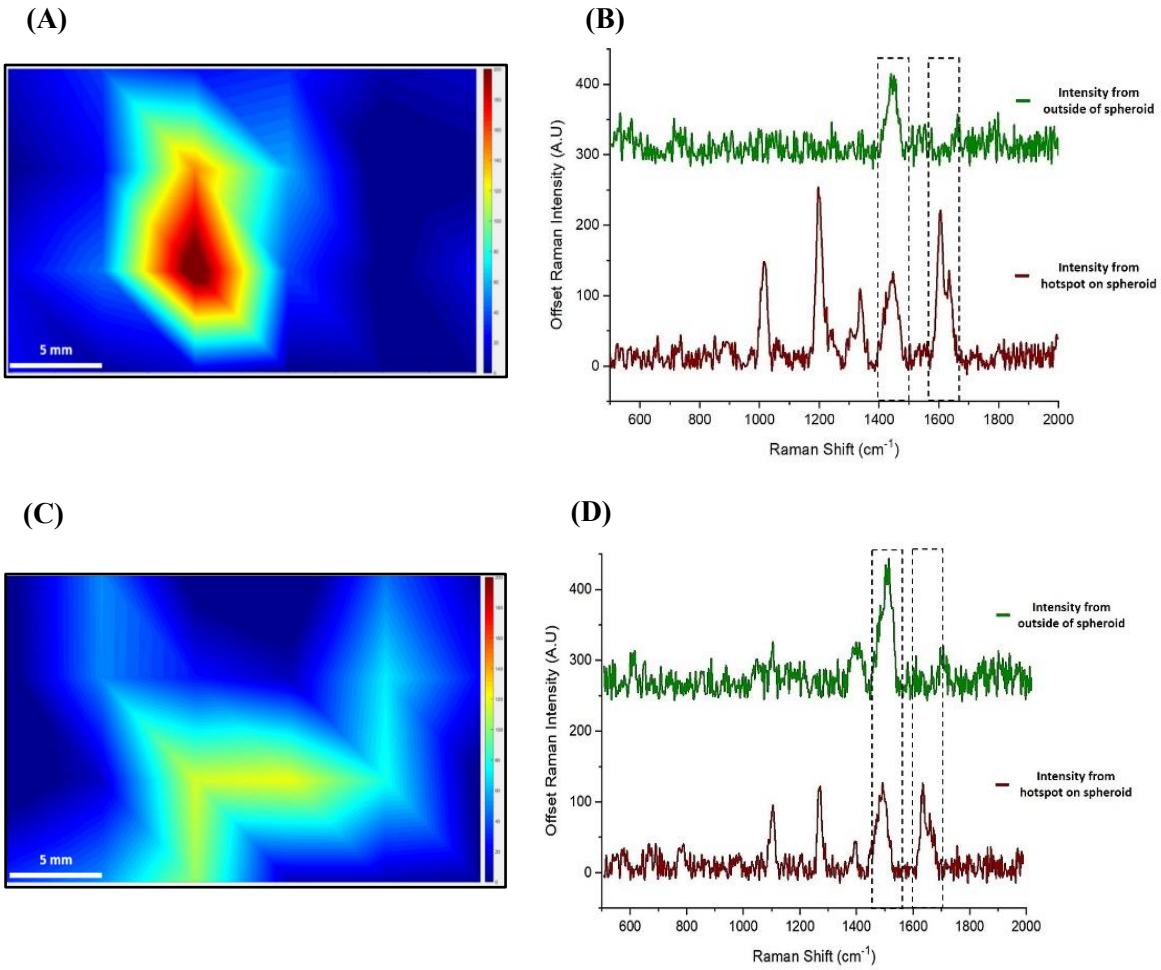

Figure 4: A false colour 2D heat SESORS map of MCF-7 spheroids containing ERα-AuNPs nanotags through **(A)** 5 mm and **(C)** 10 mm of porcine tissue. The map was constructed using the intensity of the nanotag peak at 1610 cm^{-1}. Measurements were carried out using a xy translational stage. The stage started from x= 0 and y= 0 point and it was moved in 5 mm steps size each time (x= 6 points, y= 4 point) creating a 6 x 4 pixels image consisting of 24 spectra. The spectra were baselined prior to processing. A combination surface/contour false colour was used to generate a 2D heat map and show the location of the spheroids through 5 mm and 10 mm of tissue. **(B)** and **(D)** corresponds maximum intensity spectrum from the spheroid (brown) and a spectrum from outside of the spheroid (green) collected at 8 mm offset. Dashed boxes show the characteristic peak of ERα-AuNPs nanotags at 1610 cm^{-1} and the peak from porcine tissue at 1430 cm^{-1}. All measurements were carried out using a 2 s integration time, 5 accumulations and 830 nm excitation wavelength at 450 mW laser power. Clear discrimination is observed between the spectra from the 3D breast cancer spheroids, containing the ERα-AuNPs nanotags, and the tissue where the spheroids were not present. The blue colour corresponds to a minimum intensity where there was no spectral contribution from the ERα-AuNPs nanotags.

5.4.3 *In Vivo* Tumour Targeting Using SESORS and SERS

To further extend the potentials of SESORS and validate the targeting capabilities of ERα-AuNPs, SESORS and SERS were performed *in vivo* to image two live mice with ERα positive breast cancer tumours. The mice were inoculated with ERα overexpressing MCF-7 cells and the tumours allowed to grow to 0.5 cm in diameter which ensured that they would not become too big to avoid the risk of them becoming necrotic. After the tumour growth, ERα-AuNPs (600 pM, 50 μL) were injected through the tail vein of the animals (Figure 5A, 5B). 4 h post nanotag injection, SESORS and SERS spectra were acquired from the anaesthetised mice using a handheld SORS with back scattering optics (830 nm wavelength excitation) and a handheld SERS spectrometer (785 nm wavelength excitation). The measurements were carried out by focusing the laser beam externally through the skin. After the *in vivo* imaging, the animals were sacrificed, and breast tumours and liver were imaged *ex vivo.* For the *ex vivo* imaging, the organs were analysed directly after they were brought into contact with the laser using the nose cone of the SORS instrument or the point shoot adaptor of the SERS spectrometer.

The *in vivo* SESORS imaging did not detect any SESORS signal in breast tumour areas, which was assumed to be due to the fixed optical arrangements of the SORS instrument (Figure 5C). Specifically, SORS spectrometer was fixed at 8 mm offset distance, which probably allowed the detection of scattered photons at deeper areas from where breast tumour was located. This means that the high spatial offset distance led to the domination of the deeper layer photons from the analyte in the acquired spectra.[17] However, SESORS signal was observed in the tail, which was the point of ERα-AuNPs injection, suggesting that some of the nanotags did no travel through the animal's body after 4 h from the injection.

Nevertheless, SESORS signal was detected *ex vivo*, using SORS instrument, in both left and right breast tumours after their removal from the sacrificed animals. Specifically, the signal was detected inside left and right breast tumours, while there was no nanotag accumulation in the liver (Figure 5D). These data confirmed the successful ERα-AuNPs translocation to breast tumour area and suggested the strong targeting capabilities of the nanotags after their systemic delivery *in vivo*

Interestingly, a shift in SESORS signal was observed *ex vivo* as there was an increase at 1000 cm^{-1} peak intensity and a decrease at 1020 cm^{-1} compared to ERα-AuNPs reference spectrum (Figure

5D). This outcome may be related to the systemic injection of ERα-AuNPs that may have led to nanotags' interaction with the mouse's immune system, or the formation of a protein corona, that have changed the arrangement of BPE Raman reporter on ERα-AuNPs surface. However, the main peak at 1610 cm^{-1} of BPE reporter was present in both left and right tumour suggesting the great potentials of using SESORS for detection and phenotypic characterisation of tumours *ex vivo*.

(A)

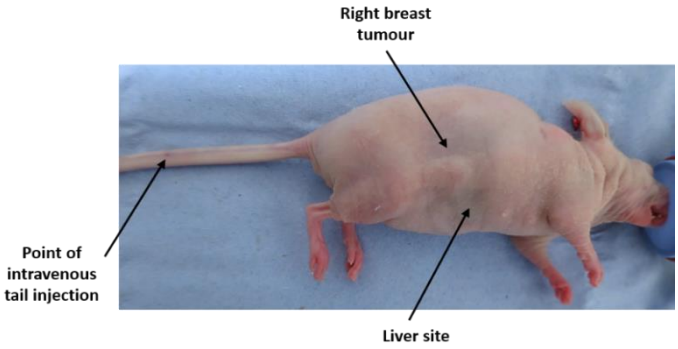

(B)

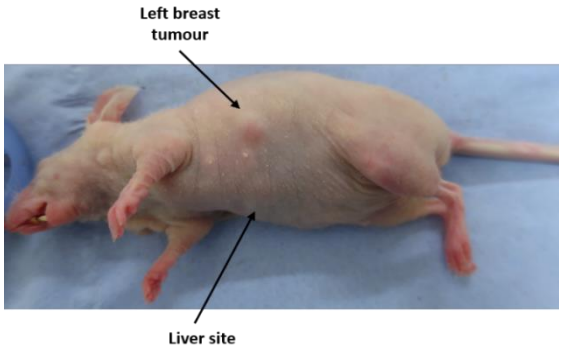

(C)

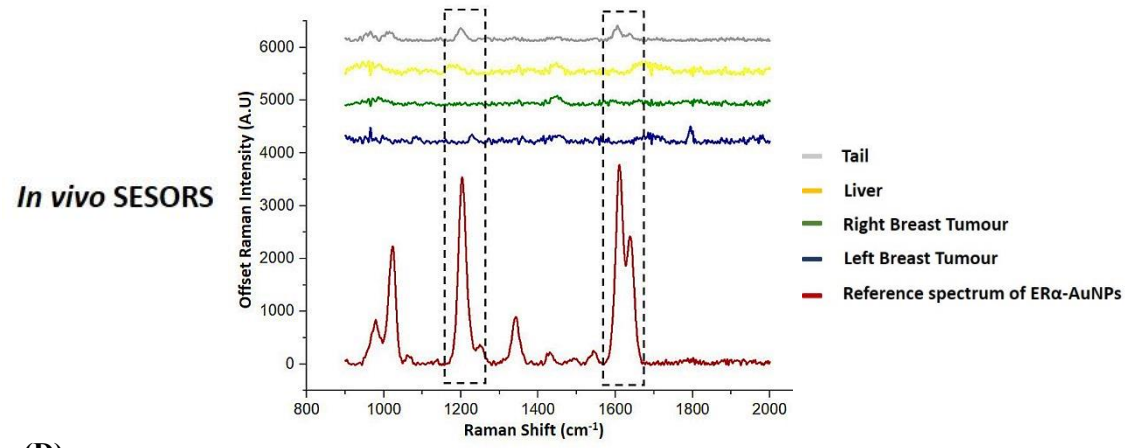

(D)

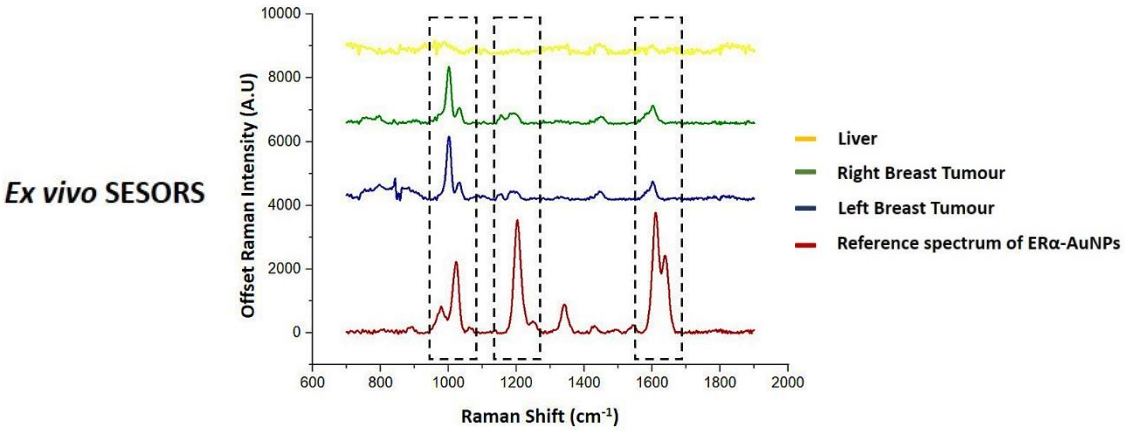

Figure 5*: In vivo* SESORS and SERS imaging. Two female mice that were implanted with ERα positive MCF-7 cells (1 x 10^6 cells/mL, 100 µL per implant). The mice developed a **(A)** right breast tumour and a **(B)** left breast tumour. When tumour size reached approximately 0.5 cm in diameter ERα-AuNPs were injected (600 pM, 50 µL) intravenously via the tail in a single injection. Image **(A)** shows the point of intravenous tail injection and the anatomical region of the liver in the mouse. Baselined stacked SESORS spectra obtained 4 h after nanotag injection **(C)** *in vivo* and **(D)** *ex vivo* in the animal's organs. **(C)** SESORS signal was observed *in vivo* only in the tail (grey) but not in the left breast tumour (blue), right breast tumour (green) or the liver (yellow). **(D)** SESORS signal was observed *ex vivo* in the left breast tumour (blue), right breast tumour (green) but not in the liver (yellow). Dashed boxes show that peaks at 1200 cm^{-1} and 1610 cm^{-1} were present. SESORS measurements *in vivo* and *ex vivo* were carried out using 2 s integration time, 5 accumulations, 830 nm excitation wavelength at 450 mW laser power. The instrument had a fixed 8 mm offset.

To further evaluate the possibility of detecting and imaging breast cancer *in vivo* and *ex vivo* using SERS, the same experiment to SESORS was carried out using a handheld Raman spectrometer (CBex from Snowy Range Instruments) with 785 nm laser excitation wavelength. SERS has the benefits of signal enhancement, sensitivity and specificity, however, it does not hold the SORS penetration capabilities. Previous work from our group showed Raman signals were collected from surface enhanced resonance Raman spectroscopy (SERRS) active nanotags through 10 mm of tissue using the same handheld Raman spectrometer.[19] Here, initial experiments were performed to detect ERα-AuNPs solution, held in a quartz microcuvette, through different thicknesses of porcine tissue *in vitro*. The results showed that SERS signal was detected through up to 10 mm of tissue using the handheld Raman spectrometer while the peak from the porcine tissue was present from the first 5 mm of tissue (SI, Figure S2).

SERS imaging showed that handheld Raman spectrometer detected signal both *in vivo* and *ex vivo*, after the removal of the organs from the sacrificed animals (Figure 6A, 6B). Specifically, high SERS signal was observed in the right and left breast tumours *in vivo* (Figure 6A, 6C). However, a high SERS signal was also detected in the tail of the mouse (Figure 6A, 6C). This result indicated that although the nanotags reached their target, some of them were still accumulated in the tail and did not travel through the animal's body. A higher nanotag incubation time, before SERS imaging, may have led to lower ERα-AuNPs concentration in the tail. Figure 6A shows that a low signal was also measured in the liver of the animals, which was an indication that ERα-AuNPs started clearing from the body 4 h after their injection. SERS imaging at a longer nanotag incubation time may also have shown a decrease in the liver signal due to nanotag excretion from the body. The *ex vivo* imaging confirmed the targeting effect of ERα-AuNPs towards the breast tumour since the highest signal was observed in the left and right breast tumours compared to the liver (Figure 6B, 6D). The clear discrimination of tumour and liver spectra *in vivo* and *ex vivo* is shown in SI, Figure S3 where all spectra have been baselined and normalised.

However, as it can be shown from Figure 4A and 4B a shift of the SERS signal was observed both *in vivo* and *ex vivo* compared to the reference spectrum of BPE Raman reporter (attached on ERα-AuNPs). Specifically, there was an increase in the peak intensity at 1350 cm^{-1} and 1540 cm^{-1}. In contrast, the dominant peak of BPE spectrum, at 1610 cm^{-1}, was not present at all both in the *in vivo* and *ex vivo* imaging. Although it was not clear why the lower intensity peaks were enhanced, it was assumed that this alteration was probably due to the systemic injection of the nanotags.

Specifically, the introduction of the ERα-AuNPs to the animal's body may have led to their interaction with the mouse's immune system, such as macrophages, that may have changed the configuration of BPE Raman reporter around the nanotags' surface. These conformational changes may have led to the generation of bare nanotags in the tumour area that enhanced the signal of other molecules, such as collagen and amino acids. More *in vivo* experiments with different experimental settings using both spectrometers should be performed to investigate this result.

False colour 2D heat SERS intensity maps were also created at 1540 cm^{-1} peak to visualise the tumour *in vivo* using SERS. The map confirmed that it was possible to determine the nanotags' distribution throughout the anatomical location of breast tumour *in vivo*. Specifically, the heat intensity maps showed that there was clear discrimination between the areas where the nanotags were present in the tumour (red colour represents nanotags) and where they were not (blue colour represents background) (Figure 6F). Therefore, SERS mapping indicated that the nanotags were distributed throughout the area of interest in the tumour, while there was a low signal in areas outside of it (Figure 6G). These results showed that SERS is a useful and sensitive technique for *in vivo* detection of surface tumours, such as breast cancer.

(A)

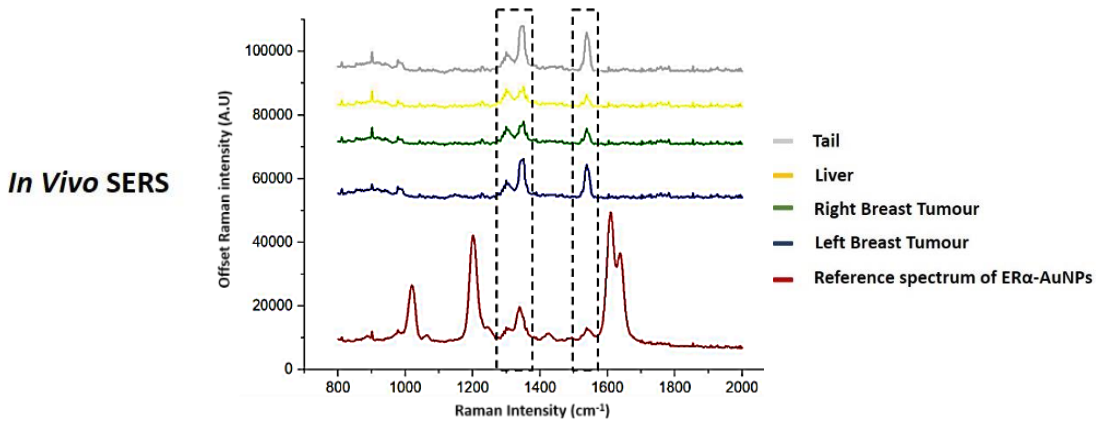

(B)

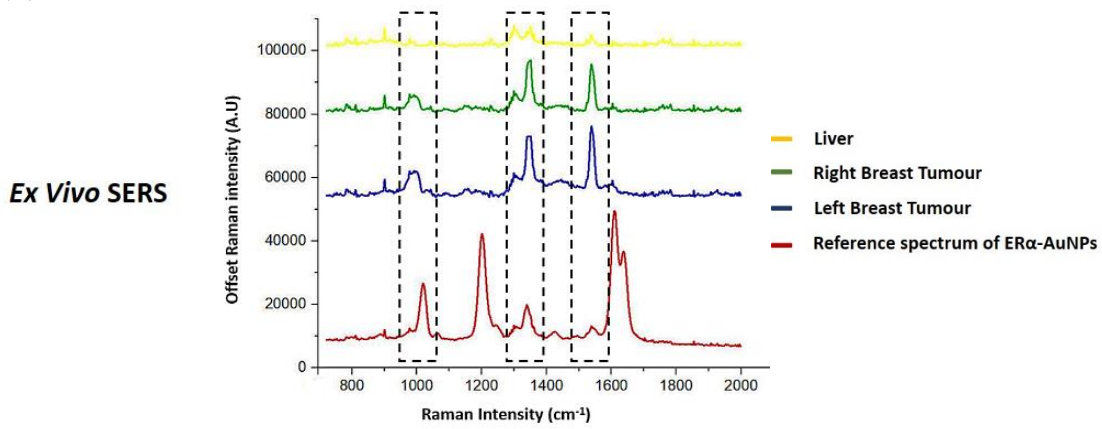
Ex Vivo SERS
Offset Raman intensity (A.U)
Raman Intensity (cm-1)
Liver
Right Breast Tumour
Left Breast Tumour
Reference spectrum of ERα-AuNPs

(C)

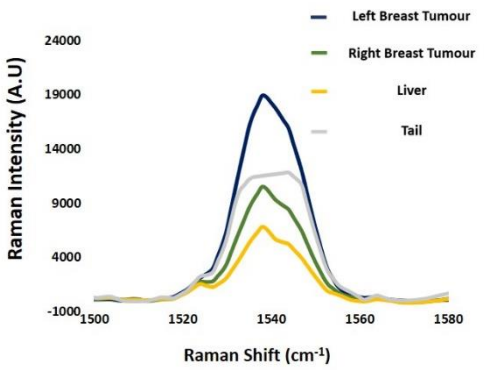
Raman Intensity (A.U)
Raman Shift (cm-1)
Left Breast Tumour
Right Breast Tumour
Liver
Tail

(D)

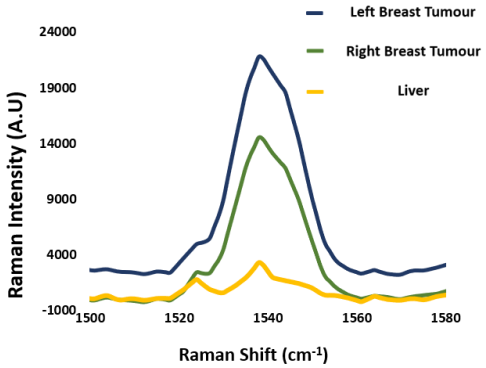
Raman Intensity (A.U)
Raman Shift (cm-1)
Left Breast Tumour
Right Breast Tumour
Liver

(E)

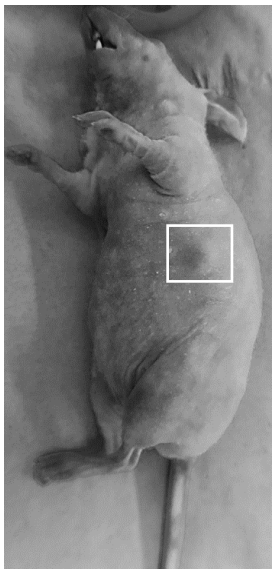

(F)

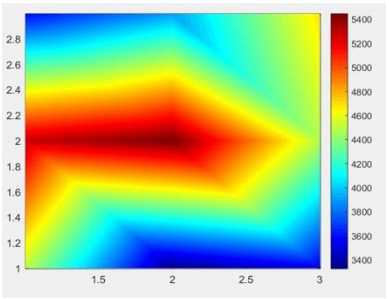

(G)

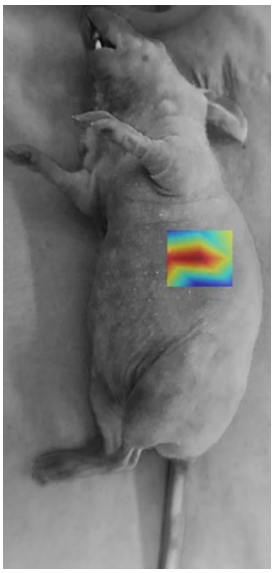

Figure 6: Baselined stacked SERS spectra obtained 4 h after ERα-AuNPs injection **(A)** *in vivo* and **(B)** *ex vivo* after animals were sacrificed **(A)** Highest SERS signal was observed in the left breast tumour (blue) and tail (grey). SERS signal was observed in the liver (yellow) indicating that some of the nanotags started clearing from the body after 4 h incubation. Dashed boxes show that peaks at 1300 cm^{-1}, 1350 cm^{-1} and 1540 cm^{-1} that were present *in vivo*. Another peak at 1020 cm^{-1} that corresponded to BPE Raman reporter spectrum was observed *ex vivo* in the breast tumours, but not in the liver. **(C)** Zoomed SERS spectra at 1540 cm^{-1} *in vivo* showing the spectra from left breast tumour (blue), right breast tumour (green), liver (yellow) and tail (grey). **(D)** Zoomed SERS spectra at 1540 cm^{-1} *ex vivo* showing the spectra from left breast tumour (blue), right breast tumour (green), liver (yellow) and tail (grey). **(E)** Image of the anaesthetised mouse before SERS imaging. The white box represents the area that was mapped **(F)** False colour 2D heat SERS intensity maps of tumours area constructed using the peak intensity at 1540 cm^{-1}. Measurements were carried out starting from x= 0 and y= 0 points and spectrometer were moved in 1 mm steps size each time (x= 3 points, y= 3 points) creating a 3 x 3 pixels image out of 9 spectra. The spectra were baselined before processing. A combination of surface/contour false colour was used to generate a 2D heat map and show the location of the tumour *in vivo*. **(G)** Merged image of anaesthetised mouse and false colour 2D heat SERS intensity map showing clear discrimination between the spectra from tumour containing the ERα-AuNPs and areas outside of tumour where the nanotags were not present. SERS measurements *in vivo* and *ex vivo* were carried out using a handheld Raman spectrometer (CBex from Snowy Range Instruments) with 785 nm laser excitation wavelength 2 s integration time, 5 accumulations at 43 mW laser power. A point and shoot adaptor with a single element lens and a numerical aperture of 0.5 were fitted.

5.5 Conclusion

This work investigated the detection and tracking of ERα *ex vivo* in live 3D breast tumour spheroids incubated with gold nanoparticles functionalised with anti-ERα antibody (ERα-AuNPs) using handheld SORS and *in vivo* using handheld SORS and handheld Raman instruments. The analysis using the handheld SORS spectrometer with 830 nm laser excitation wavelength allowed the successful *ex vivo* detection of spheroids treated with the nanotags through 10 mm of tissue. This outcome established the powerful capabilities of SESORS in detecting molecules at high depths with great specificity and sensitivity.

The *in vivo* experiments indicated that the handheld SORS instrument was detecting scattered photons from greater depths, below the breast tumour, due to its fixed optical arrangements at 8 mm offset distance. However, the nanotags' signal was detected *ex vivo* using the SORS instrument in the tumours removed from sacrificed mice. No signal was generated from the liver *ex vivo* which indicated the targeting effect of the nanotags towards the ERα positive breast cancer tumour. SERS experiments, using a handheld Raman instrument with 785 nm laser excitation wavelength, showed that it was possible to detect the nanotags *in vivo* and *ex vivo* confirming the targeting effect of ERα-AuNPs against breast tumour. However, a shift in SERS signal was observed that was probably related to conformational changes of the nanotags that may have led to enhancement of molecules inside the tumour such as collagen and amino acids. More *in vivo* experiments with different experimental settings using both spectrometers should be performed to investigate this result. 2D SERS intensity map performed *in vivo* around the tumour area confirmed that it was possible to visualise the hotspot of the tumour using SERS. SESORS has great potentials as a new technique to image tumours located at higher depths where other optical techniques have low detection capabilities. Here, we demonstrated the importance of adjusting the optical arrangements of SORS spectrometer based on the tumour depth to utilise the full potentials of the technique for successful *in vivo* detection. The optimisation of these parameters will further increase the performance ability of the handheld SORS spectrometer and open up the opportunities of using SESORS for targeted diagnosis in a clinical environment.

5.6 References

1. Ferlay, J., Soerjomataram, I., Dikshit, R. & All, E. Cancer incidence and mortality worldwide: Sources, methods and major patterns in GLOBOCAN 2012. *Int J Cancer* (2015). doi:10.1002/ijc.29210
2. Torre, L. A., Siegel, R. L., Ward, E. M. & Jemal, A. Global cancer incidence and mortality rates and trends - An update. *Cancer Epidemiology Biomarkers and Prevention* (2016). doi:10.1158/1055-9965.EPI-15-0578
3. UK, C. R. Breast cancer incidence (invasive) statistics: Breast cancer incidence (invasive) statistics. *Online Source* (2016).
4. Seely, J. M. & Alhassan, T. Screening for breast cancer in 2018—what should we be doing today? *Current Oncology* (2018). doi:10.3747/co.25.3770
5. Stone, N. *et al.* Surface enhanced spatially offset Raman spectroscopic (SESORS) imaging - the next dimension. *Chemical Science* (2011). doi:10.1039/c0sc00570c
6. Stone, N., Faulds, K., Graham, D. & Matousek, P. Prospects of deep Raman spectroscopy for noninvasive detection of conjugated surface enhanced resonance Raman scattering nanoparticles buried within 25 mm of mammalian tissue. *Analytical Chemistry* (2010). doi:10.1021/ac100039c

7. Asiala, S. M., Shand, N. C., Faulds, K. & Graham, D. Surface-Enhanced, Spatially Offset Raman Spectroscopy (SESORS) in Tissue Analogues. *ACS Applied Materials and Interfaces* (2017). doi:10.1021/acsami.7b09197
8. Qian, X. *et al.* In vivo tumor targeting and spectroscopic detection with surface-enhanced Raman nanoparticle tags. *Nature Biotechnology* (2008). doi:10.1038/nbt1377
9. Oseledchyk, A., Andreou, C., Wall, M. A. & Kircher, M. F. Folate-Targeted Surface-Enhanced Resonance Raman Scattering Nanoprobe Ratiometry for Detection of Microscopic Ovarian Cancer. *ACS Nano* (2017). doi:10.1021/acsnano.6b06796
10. Nicolson, F. *et al.* Multiplex imaging of live breast cancer tumour models through tissue using handheld surface enhanced spatially offset resonance Raman spectroscopy (SESORRS). *Chemical Communications* (2018). doi:10.1039/c8cc04267e
11. Sharma, B., Ma, K., Glucksberg, M. R. & Van Duyne, R. P. Seeing through bone with surface-enhanced spatially offset Raman spectroscopy. *Journal of the American Chemical Society* (2013). doi:10.1021/ja409378f
12. Keren, S. *et al.* Noninvasive molecular imaging of small living subjects using Raman spectroscopy. *Proceedings of the National Academy of Sciences* (2008). doi:10.1073/pnas.0710575105
13. Wang, Y. 'Winston' *et al.* Rapid ratiometric biomarker detection with topically applied SERS nanoparticles. *TECHNOLOGY* (2014). doi:10.1142/S2339547814500125
14. McQueenie, R. *et al.* Detection of inflammation in vivo by surface-enhanced Raman scattering provides higher sensitivity than conventional fluorescence imaging. *Analytical Chemistry* (2012). doi:10.1021/ac3006445
15. Noonan, J. *et al.* In vivo multiplex molecular imaging of vascular inflammation using surface-enhanced Raman spectroscopy. *Theranostics* (2018). doi:10.7150/thno.28665
16. Document, P. & Tr, P. D. I. E. C. Safety of laser products — Part 14 : A user ' s guide. *Strategy* **3**, (2004).
17. Nicolson, F. *et al.* Through barrier detection of ethanol using handheld Raman spectroscopy—Conventional Raman versus spatially offset Raman spectroscopy (SORS). *Journal of Raman Spectroscopy* (2017). doi:10.1002/jrs.5258
18. Jamieson, L. E., Harrison, D. J. & Campbell, C. J. Chemical analysis of multicellular tumour spheroids. *Analyst* (2015). doi:10.1039/c5an00524h
19. Nicolson, F. *et al.* Surface enhanced resonance Raman spectroscopy (SERRS) for probing through plastic and tissue barriers using a handheld spectrometer. *Analyst* (2018). doi:10.1039/c8an01249k

5.7 Supporting Information

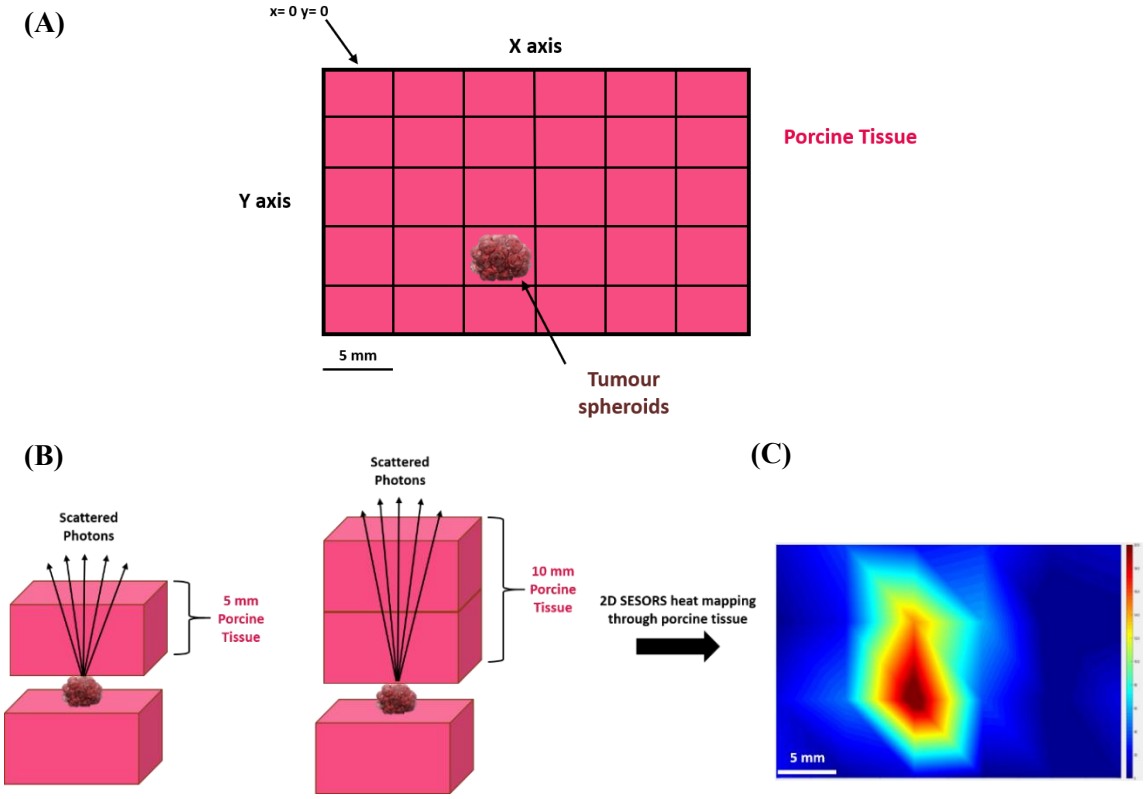

SI Figure S1: Schematic for the top view of the tissue for the 2D heat map creation. **(B)** 3D breast cancer tumour spheroids were placed onto a section of tissue and 5 mm or 10 mm section of porcine tissue was then placed on top of the tissue layer upon which the 3D breast cancer tumour spheroids were positioned. The experimental set-up involved mounting the instrument above the tissue samples. The sample was then brought into contact with the laser via the nose cone. **(C)** Representation of heat SERS intensity observed in the false colour 2D heat map. All spectra were collected at an 8 mm offset. In the region where the spheroids models were present, the highest SERS intensity was observed (red colour). This shows the targeted tracking of 3D breast cancer tumour spheroids through 10 mm of tissue. Before the 2D heat map, the offset spectra were baselined, and 1610 cm^{-1} peak was selected for the creation of the map. The map was constructed using the peak intensity at 1610 cm^{-1}. Measurements were carried out using a xy translational stage which started from x= 0 and y= 0 points and it was moved in 5 mm steps each time (x= 6 points, y= 4 points) creating a 6 x 4-pixel image out of 24 spectra. The z point remained fixed for the whole mapping (the stage was not moved in the z-direction). All measurements were carried out using a 2 s integration time, 5 accumulations, 830 nm laser excitation wavelength.

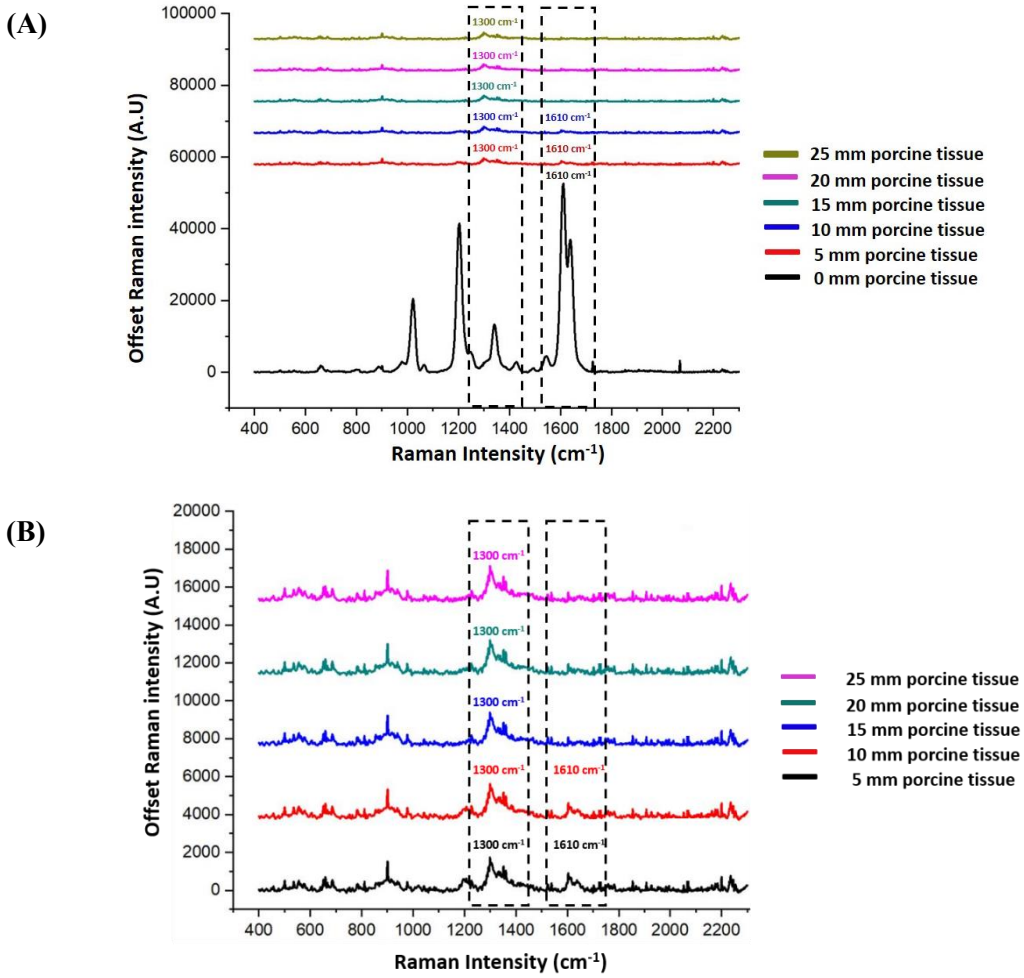

SI Figure S2: SERS signal was collected from ERα-AuNPs solution through up to 10 mm of porcine tissue using a handheld Raman spectrometer (CBex from Snowy Range Instruments) with 785 nm laser excitation wavelength. The tissue (5 mm) was mounted on a stage to create the desired thickness and were placed in front of the Suprasil quartz micro cuvette (1 mm thickness) containing the ERα-AuNPs. The tissue was then brought into contact with the laser from Raman spectrometer by using a point and shoot adaptor with a single element lens and a numerical aperture of 0.5. SERS measurements were obtained using a 2 s integration time, with 5 accumulations. A were fitted. This gave an average laser power of 43 mW **(A)** Baselined stacked SERS spectra of ERα-AuNPs through porcine tissue. Dashed boxes show the characteristic peak of the nanotags at 1610 cm^{-1} and the peak from porcine tissue at 1300 cm^{-1}. As the thickness of the tissue barrier is increased, it is challenging to distinguish the 1610 cm^{-1} at thicknesses beyond 10 mm. The peak from the porcine tissue at 1300 cm^{-1} starts to be present in the spectra after 5 mm tissue thickness. **(B)** Zoomed baselined stacked SERS spectra of ERα-AuNPs through porcine tissue.

(A)

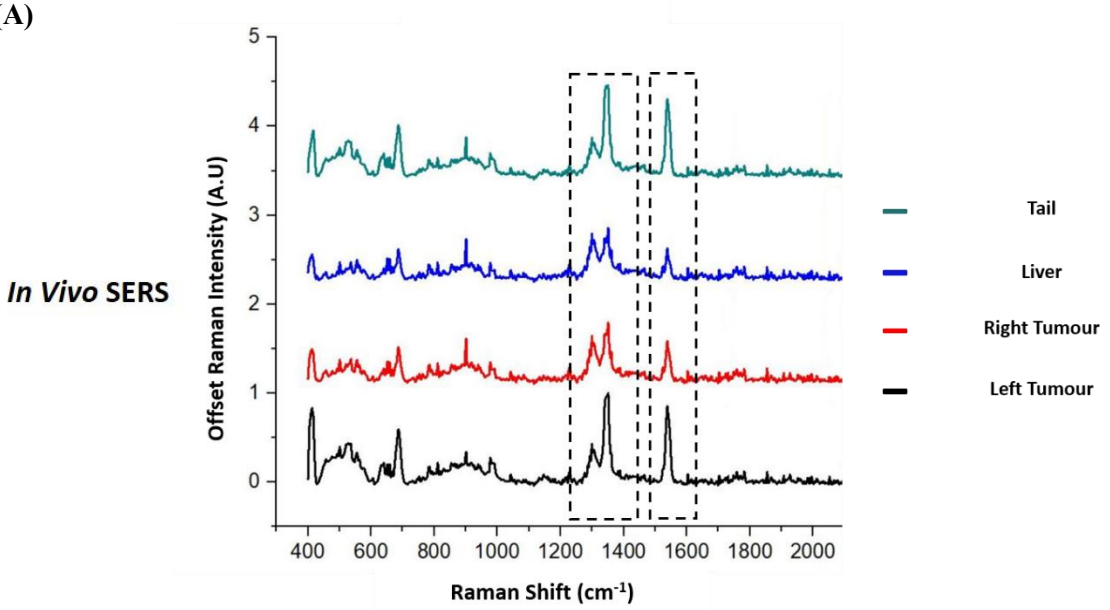
In Vivo SERS
Offset Raman Intensity (A.U)
Raman Shift (cm-1)
Tail
Liver
Right Tumour
Left Tumour

(B)

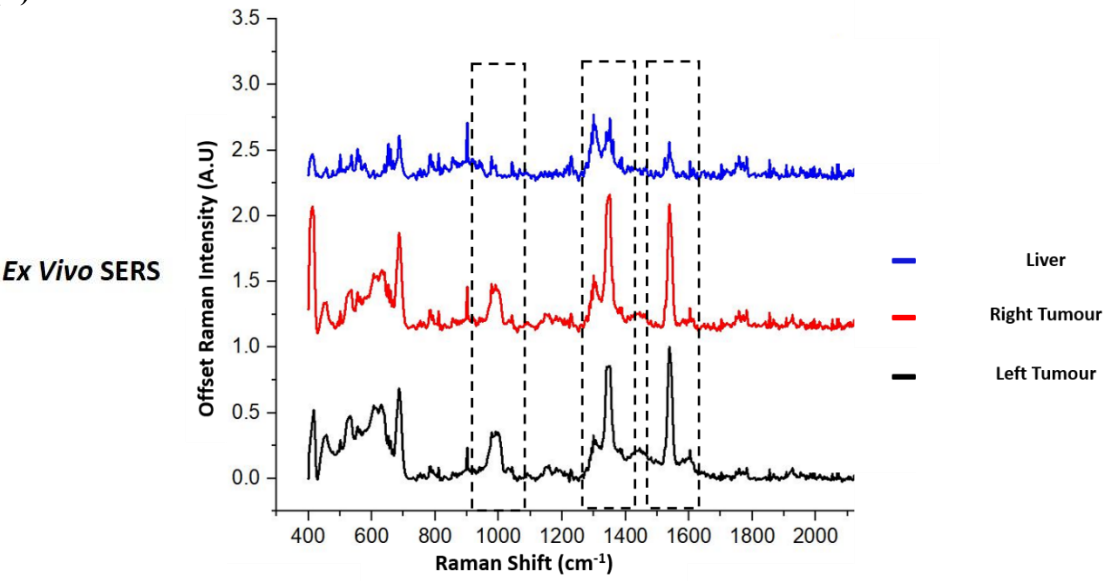
Ex Vivo SERS
Offset Raman Intensity (A.U)
Raman Shift (cm-1)
Liver
Right Tumour
Left Tumour

(C)

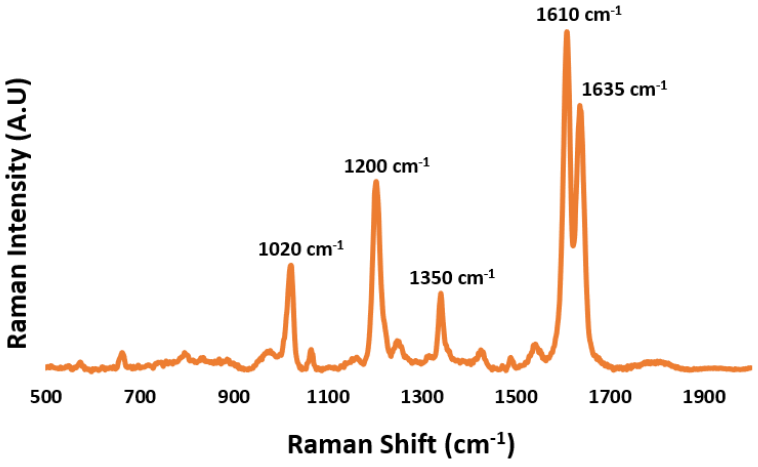
1610 cm-1
1635 cm-1
1200 cm-1
1020 cm-1
1350 cm-1
Raman Intensity (A.U)
Raman Shift (cm-1)

SI Figure S3: Baselined and normalised stacked SERS spectra obtained **(A)** *in vivo* 4 h after nanotag injection and **(B)** *ex vivo* from the removed organs of sacrificed animals. **(A)** Dashed boxes show that peaks at 1300 cm^{-1}, 1350 cm^{-1} and 1540 cm^{-1} that were present *in vivo*. **(B)**Another peak at 1020 cm^{-1} was observed *ex vivo* only in left and right tumour, but not in the liver, that corresponded to the peak from the nanotags reference spectrum. **(C)** Reference spectrum of BPE Raman reporter (attached on ERα-AuNPs) in dH_20. All measurements were carried out using a handheld SERS spectrometer (785 nm wavelength excitation).at 2 s integration time, with 5 accumulations. A point and shoot adaptor with a single element lens and a numerical aperture of 0.5 were fitted. This gave an average laser power of 43 mW.

6. Thesis Conclusions

Breast cancer is fast becoming the leading cause of oncologic morbidity and mortality among women worldwide. Although there are different methods for breast cancer phenotype characterisation, there are still limitations that may lead to false positive and false negative results and consequently to late diagnosis and lower life expectation. Therefore, it is vital to introduce novel optical imaging techniques for overcoming the current analytical challenges.

The aim of this thesis was to use surface enhanced Raman spectroscopy (SERS) as a non-destructive bioanalytical method that offers higher specificity, selectivity and multiplex capacities, in comparison to conventional imaging techniques. Specifically, SERS was combined with anti-estrogen receptor alpha (ERα) antibody functionalised gold nanoparticles (ERα-AuNPs) for targeting, detecting and tracking the intracellular distribution of ERα in breast cancer.

After ERα-AuNPs characterisation, the nanotags cellular uptake, classification of breast cancer, assessment of fulvestrant efficacy, characterisation of 3D breast cancer spheroids, and detection of nanotags at high depths using SESORS were exploited. Various techniques were employed to carry out the aims of the thesis including optical imaging, analytical chemistry and biochemistry.

Initially, the cellular uptake of ERα-AuNPs was investigated under different cellular endocytosis inhibition conditions, using non-destructive 2D and 3D SERS imaging. It was shown that ERα-AuNPs were internalised in MCF-7 cells in a temperature-dependent way, excluding the scenario their passive diffusion to the cells. Additionally, it was found that both dynamin and membrane ERα participated, at least in a part, in ERα-AuNPs uptake in MCF-7 cells since their inhibition resulted in high nanotags' accumulation in the plasma membrane rather than intracellularly. The novelty of this work was also the development of an accurate way for calculating the relative SERS response value in MCF-7 cells to obtain a relative assessment of nanotags uptake using a direct and rapid optical approach averaged across multiple cells. Therefore, this study highlighted the benefits of using non-destructive 3D SERS for investigation of the cellular uptake mechanisms by generating 3D images of the entire cell volume whilst maintaining cell integrity compared to other destructive, time-consuming and expensive techniques, such as TEM. These data can provide important information regarding the optimisation of nanotag design for greater and more efficient cellular uptake that leads to strong targeting effects with lower cellular toxicities.

After the investigation of the uptake mechanisms of ERα-AuNPs in MCF-7 cells, SERS was used to characterise breast cancer cells and inform about fulvestrant efficacy, a commercially available ERα degrader. The results showed that MCF-7 ($ERα^+$) cells had a higher SERS response in comparison to SKBR-3 ($ERα^-$) cells confirming their strong targeting effect towards ERα in breast cancer. SERS also appears to be a more effective method in comparison to immunofluorescence for ERα analysis. Specifically, immunofluorescence ERα staining was also a laborious and time-consuming method that led to high signal background compared to SERS involving cell fixation, permeabilization, blocking and use of two antibodies. SERS also showed excellent correlation with the ERα expression levels obtained by western blot experiments after fulvestrant treatment, since lower SERS response was observed in fulvestrant treated MCF-7 cells. Therefore, it was highlighted that SERS is a great tool for cell characterisation and understanding of drug activity.

To confirm that SERS can also be utilised in a more *in vivo* representative environment, microfluidic devices were used to form live 3D breast cancer spheroids. These 3D tumour models are better mimics of the *in vivo* environment in contrast to conventional 2D monolayered cell cultures. Here, SERS was shown to be a great high-throughput method for the characterisation of the spheroids. Specifically, ERα-AuNPs showed a strong targeting effect in MCF-7 spheroids in contrast to the non-specific HER2-AuNPs. Most importantly, the 3D SERS images showed that the nanotags had great penetration capabilities to travel through the spheroids since SERS signal was detected within the 3D tumour. Additionally, SERS and microfluidics were utilised to assess fulvestrant activity. Although a lower SERS signal was observed in MCF-7 spheroids treated with fulvestrant, the drug concentration was required to be 10 times higher to have an effect on the spheroids compared to the 2D cell culture. These data highlights that 2D and 3D cell cultures may have district biological behaviours, due to their architectural differences, that affect drug penetration and its therapeutic efficacy. Therefore, the importance of including both 2D and 3D models is emphasised here for a better reflection of the *in vivo* environment. These results highlighted that SERS and microfluidics can be successfully applied to identifying and classifying live ERα-positive MCF-7 breast cancer spheroids *ex vivo*.

To further increase the detection capabilities of ERα-AuNPs, SERS was combined with the depth penetration benefits of backscattering SORS (SESORS). ERα-AuNPs were initially tracked through up to 15 mm of porcine tissue and they were then taken up from live 3D MCF-7 breast

cancer spheroid and detected *ex vivo* through 10 mm of tissue using a handheld SORS with a back-scattering configuration. These results confirmed that SESORS was able to detect and identify the localisation of ERα-AuNPs at high tissue thicknesses. The *in vivo* experiments showed that handheld SORS instrument was detecting scattered photons from greater depths, below the breast tumour, due to its optical arrangements that were fixed at 8 mm offset distance. However, the nanotags were detected *ex vivo* using the handheld SORS instrument in breast tumours removed from the sacrificed mice. No signal was generated from the liver *ex vivo* which confirmed the targeting effect of ERα-AuNPs towards the ERα positive breast cancer tumour and their ability to reach their target *in vivo*. Therefore, this research highlighted the importance of adjusting the optical arrangements of SORS spectrometer, based on the tumour depth, to utilise the full potential of the technique for successful *in vivo* detection. The optimisation of these parameters will further increase the performance ability of the handheld SORS spectrometer for a significant step towards potential clinical applications in the field of biomedical imaging and disease detection.

7. Future Work

7.1 Investigation of Cellular Uptake Mechanism of Functionalised Gold Nanoparticles into Breast Cancer Cells Using SERS

To further investigate the cellular uptake of ERα-AuNP nanotags, it will be important to identify if other molecules, such as caveolin, play any role in ERα-AuNPs internalisation. Hence, the use of other targeted endocytosis inhibitors will offer a better understanding of the way that the nanotags are uptaken. Additionally, other breast cancer cells should be examined to identify the effect of the cell line on the nanotags uptake. This will provide information on the effect of cell proliferation on ERα-AuNPs endocytosis.

Another interesting experimental approach would be the endosomal staining of MCF-7 cells with different markers. There are several endosome markers for early endosomes (e.g. Rab5), late endosomes (e.g. Rab7) and recycling endosomes (e.g. Rab11). Therefore, tracking can be performed in the main endocytosis compartments to explain the way that the cargo is transported from one endocytic compartment to another until its elimination from the cells. The fluorescent images from the endosomal staying, and the ones are taken from Raman could be potentially

correlated to co-localise ERα-AuNPs and endosomes. Hence, it will be possible to perform nanotags trafficking and inform about their cell localisation and fate.

Finally, it would be interesting to analyse ERα-AuNPs cellular elimination to investigate whether the nanotags undergo lysosomal exocytosis or if they are recycled back to the plasma membrane. The main challenges for cellular elimination experiments are that it is difficult to quantify the number of excreting nanotags. A combination of different techniques, such as inductively coupled plasma mass spectrometry (ICP-MS) and transmission electron microscopy (TEM), should be performed to study this. All these experimental approaches will be invaluable to understand the physiological functions and mechanisms of the nanotags' cellular endocytosis and exocytosis.

7.2 Characterisation of Estrogen Receptor Alpha (ERα) Positive Breast Cancer Cells and Understanding of Fulvestrant Activity Using SERS

For this experiment, it would be useful to perform ICP-MS to correlate the SERS imaging with the quantification of the total number of nanotags in the cells extracted from ICP-MS. Another option for the nanotags quantification in cells is dark-field microscopy. However, this technique has some limitations such as that it detects scattering light from cellular areas and, therefore, leads to unavoidable fluctuations and measurement errors. Hence, additional optimisations should be also performed for the conduction of dark field experiments.

Future work can involve the performance of TEM in cells treated with the nanotags to allow the optical sectioning throughout various levels of the cell and confirm about nanotags localisation. Additional immunofluorescence experiments that stain ERα could be carried out, after SERS mapping, to investigate ERα-AuNPs localisation compared to ERα. Moreover, additional biomarkers could be targeted using antibody functionalised nanotags, such as HER2 and PR. Identifying and characterising three biomarkers at the same time would prove a strong validation of the multiplex capabilities of SERS, compared to conventional fluorescent imaging.

Furthermore, future experimental approaches could be performed to identify the efficiency of novel anticancer drugs against ERα. For instance, the project could investigate other drug candidates, such as RAD1901 a SERD that is currently into clinical trials (ClinicalTrials.gov #:

NCT02338349). The assessment of RAD1901 efficacy could be compared to fulvestrant using SERS to inform about its clinical niche.

7.3 Detection of Estrogen Receptor Alpha (ERα) and Assessment of Fulvestrant Efficacy in Live MCF-7 Tumour Spheroids Using Microfluidic Devices and SERS

Additional experiments could be carried out to investigate the nanotag targeting effect in co-culture of known and unknown breast cancer cell lines. This will enable us to investigate whether it is possible to characterise different breast cancer phenotypes *ex vivo*. Additional 3D SERS mapping experiments on the spheroids should be carried out using different step sizes, accumulation times and laser powers. This data would provide valuable information on the optimal conditions that should be performed for strong and rapid SERS signals. Moreover, it would be important to further investigate the drug distribution and penetration in the spheroids to understand the drug activity in various drug doses, incubation times and spheroid sizes.

SERS nanotags could also be incubated in spheroids formed from patients' biopsies in the microfluidic devices. This can provide important information regarding the tumour characteristics for potential *ex vivo* clinical breast cancer diagnosis. Future opportunities may involve multiplex detection of different biomarkers in patients' biopsies, and investigation of the efficacy of novel anticancer drugs, by using a combination of nanotechnology and microfluidics.

7.4 *Ex Vivo* and *In Vivo* Detection of Estrogen Receptor Alpha (ERα) in Breast Cancer Using Handheld SERS and SESORS Instruments

Future experimental approaches could be focused on performing multiplex *ex vivo* targeting of biomarkers by using nanotags functionalised with different Raman reporters and antibodies. Specifically, the multiplex detection of both ERα and HER2 with ERα-AuNPs and HER2-AuNPs using SESORS would provide a great tool to identify both biomarkers simultaneously. In the current work, SESORS was used to detect live 3D tumour spheroids with 1 mm size through 10 mm of porcine tissue. Tumour models that are larger in size could probably lead to ERα-AuNPs detection through even higher tissue thicknesses. Previous studies from our group have shown that

resonant chalcogenpyrylium-based SERS nanotags offered highly significant and successful detection of 3D breast tumour models through 15 mm of tissue.[191] Therefore, it would be useful to functionalise the ERα-AuNPs with resonant Raman reporters (SESORRS) to investigate if enhancement of signal will be observed that will lead to signal detection at higher thickness *ex vivo* and *in vivo*. Additionally, a benchtop SORS instrument could also be used to investigate if a higher depth penetration and a better signal to noise SERS spectra would be acquired.

The main challenge of the *in vivo* work was that SESORS instrument was detecting scattered photons deeper that surface breast tumour due to its optical arrangement. Therefore, the main future *in vivo* work would be to carry out the same experiment using a handheld SORS spectrometer with adjustable offset distances to get valuable information of the optimal optical arrangements required to detect the breast tumour *in vivo*. Additionally, it would useful to investigate the detection of other tumours, located deeper in the animal or/and change the animal model used, to see if SORS instrument would be useful for the detection of deeper cancers types. Finally, it would be useful to use other animal models with denser breast tissues that are more clinically relevant to human breast cancer. After the successful *in vivo* targeting of breast cancer using SESORS, a multiplex approach should also be considered to detect different biomarkers simultaneously. These approaches will be vital to explore the full potential of SESORS for *in vivo* breast cancer diagnosis.

8. Introductory References

1. Ferlay, J., Soerjomataram, I., Dikshit, R. & All, E. Cancer incidence and mortality worldwide: Sources, methods and major patterns in GLOBOCAN 2012. *Int J Cancer* (2015). doi:10.1002/ijc.29210
2. Torre, L. A., Siegel, R. L., Ward, E. M. & Jemal, A. Global cancer incidence and mortality rates and trends - An update. *Cancer Epidemiology Biomarkers and Prevention* (2016). doi:10.1158/1055-9965.EPI-15-0578
3. Raza, A. *et al.* Breast Cancer: Major Risk Factors and Recent Developments in Treatment. *Asian Pacific Journal of Cancer Prevention* (2014). doi:10.7314/apjcp.2014.15.8.3353
4. Cancer, I. A. for research of. Estimated age-standardized incidence rates (World) in 2018, leukaemia, both sexes, all ages. *Who* 2018 (2018).
5. UK, C. R. Breast cancer incidence (invasive) statistics: Breast cancer incidence (invasive) statistics. *Online Source* (2016).
6. Becker, S. A historic and scientific review of breast cancer: The next global healthcare challenge. *International Journal of Gynecology and Obstetrics* (2015). doi:10.1016/j.ijgo.2015.03.015
7. Colditz, G. A. & Bohlke, K. Priorities for the primary prevention of breast cancer. *CA: A Cancer Journal for Clinicians* (2014). doi:10.3322/caac.21225
8. Ng, Z., Ong, M., Jegadeesan, T., Deng, S. & Yap, C. Breast Cancer: Exploring the Facts and Holistic Needs during and beyond Treatment. *Healthcare* (2017). doi:10.3390/healthcare5020026
9. O'Sullivan, C. C., Loprinzi, C. L. & Haddad, T. C. Updates in the Evaluation and Management of Breast Cancer. *Mayo Clinic Proceedings* (2018). doi:10.1016/j.mayocp.2018.03.025
10. Ahmad, A. Pathways to Breast Cancer Recurrence. *ISRN Oncology* (2013). doi:10.1155/2013/290568
11. Bissell, M. J. & Hines, W. C. Why don't we get more cancer? A proposed role of the microenvironment in restraining cancer progression. *Nature Medicine* (2011). doi:10.1038/nm.2328
12. Marino, N. *et al.* Breast cancer metastasis: Issues for the personalization of its prevention and treatment. *American Journal of Pathology* **183**, 1084–1095 (2013).

13. Polyak, K. Heterogeneity in breast cancer. *Journal of Clinical Investigation* (2011). doi:10.1172/JCI60534
14. Jin, K. *et al.* Patient-derived human tumour tissue xenografts in immunodeficient mice: A systematic review. *Clinical and Translational Oncology* (2010). doi:10.1007/s12094-010-0540-6
15. Giordano, S. B. & Gradishar, W. Breast cancer: Updates and advances in 2016. *Current Opinion in Obstetrics and Gynecology* (2017). doi:10.1097/GCO.0000000000000343
16. American Cancer Society. Breast Cancer Facts & Figures 2015-2016. *American Cancer Society, Inc* (2016). doi:10.1007/978-1-4614-8063-1
17. Sant, M. *et al.* Breast carcinoma survival in Europe and the United States. *Cancer* (2004). doi:10.1002/cncr.20038
18. Drukteinis, J. S., Mooney, B. P., Flowers, C. I. & Gatenby, R. A. Beyond mammography: New frontiers in breast cancer screening. *American Journal of Medicine* (2013). doi:10.1016/j.amjmed.2012.11.025
19. Bevers, T. B. *et al.* Breast Cancer Screening and Diagnosis. *Journal of the National Comprehensive Cancer Network* (2017). doi:10.6004/jnccn.2009.0070
20. Carney, P. A. *et al.* Individual and combined effects of age, breast density, and hormone replacement therapy use on the accuracy of screening mammography. *Annals of Internal Medicine* (2003). doi:10.7326/0003-4819-138-3-200302040-00008
21. Schwab, F. D., Huang, D. J., Schmid, S. M., Schötzau, A. & Güth, U. Self-detection and clinical breast examination: Comparison of the two 'classical' physical examination methods for the diagnosis of breast cancer. *Breast* (2015). doi:10.1016/j.breast.2014.11.008
22. Brewer, N. T., Salz, T. & Lillie, S. E. Systematic review: the long-term effects of false-positive mammograms. *Annals of internal medicine* (2007).
23. Evans, A. *et al.* Breast ultrasound: recommendations for information to women and referring physicians by the European Society of Breast Imaging. *Insights into Imaging* (2018). doi:10.1007/s13244-018-0636-z
24. Taibi, A. & Vecchio, S. Breast Imaging. in *Comprehensive Biomedical Physics: First Edition* (2014). doi:10.1016/B978-0-444-53632-7.00206-9
25. Garcia, J., Liu, S. Z. & Louie, A. Y. Biological effects of MRI contrast agents: gadolinium retention, potential mechanisms and a role for phosphorus. *Philosophical Transactions of the Royal Society A: Mathematical, Physical and Engineering Sciences*

(2017). doi:10.1098/rsta.2017.0180

26. Raikhlin, A. *et al.* Breast MRI as an adjunct to mammography for breast cancer screening in high-risk patients: Retrospective review. *American Journal of Roentgenology* (2015). doi:10.2214/AJR.13.12264
27. Phi, X. A. *et al.* Magnetic resonance imaging improves breast screening sensitivity in BRCA mutation carriers age ≥50 years: Evidence from an individual patient data meta-analysis. *Journal of Clinical Oncology* (2015). doi:10.1200/JCO.2014.56.6232
28. Nelson, H. D. *et al.* Screening for breast cancer: An update for the U.S. Preventive Services Task Force. *Annals of Internal Medicine* (2009). doi:10.1059/0003-4819-151-10-200911170-00009
29. Oeffinger, K. C. *et al.* Breast cancer screening for women at average risk: 2015 Guideline update from the American cancer society. *JAMA - Journal of the American Medical Association* (2015). doi:10.1001/jama.2015.12783
30. Hubbard, R. A. *et al.* Cumulative probability of false-positive recall or biopsy recommendation after 10 years of screening mammography: A cohort study. *Obstetrical and Gynecological Survey* (2012). doi:10.1097/OGX.0b013e31824b70a2
31. Rosenberg, K. Ten-year risk of false positive screening mammograms and clinical breast examinations. *Journal of nurse-midwifery* **43**, 394–5 (1998).
32. Welch, H. G. & Black, W. C. Overdiagnosis in cancer. *Journal of the National Cancer Institute* (2010). doi:10.1093/jnci/djq099
33. Henry, N. L. & Hayes, D. F. Cancer biomarkers. *Molecular Oncology* (2012). doi:10.1016/j.molonc.2012.01.010
34. Nicolini, A., Ferrari, P. & Duffy, M. J. Prognostic and predictive biomarkers in breast cancer: Past, present and future. *Seminars in Cancer Biology* (2018). doi:10.1016/j.semcancer.2017.08.010
35. Zhang, W., Ji, Y., Wu, X. & Xu, H. Trafficking of gold nanorods in breast cancer cells: Uptake, lysosome maturation, and elimination. *ACS Applied Materials and Interfaces* (2013). doi:10.1021/am4033857
36. Thompson, A. *et al.* Evaluation of the current knowledge limitations in breast cancer research: A gap analysis. *Breast Cancer Research* (2008). doi:10.1186/bcr1983
37. Bass, J. J. *et al.* An overview of technical considerations for Western blotting applications to physiological research. *Scandinavian Journal of Medicine and Science in Sports* (2017). doi:10.1111/sms.12702

38. Smith, C. J. & Osborn, A. M. Advantages and limitations of quantitative PCR (Q-PCR)-based approaches in microbial ecology. *FEMS Microbiology Ecology* (2009). doi:10.1111/j.1574-6941.2008.00629.x

39. Onul, A. *et al.* Application of Immunohistochemical Staining to Detect Antigen Destruction as a Measure of Tissue Damage. *Journal of Histochemistry and Cytochemistry* (2012). doi:10.1369/0022155412452146

40. Yildiz-Aktas, I. Z., Dabbs, D. J. & Bhargava, R. The effect of cold ischemic time on the immunohistochemical evaluation of estrogen receptor, progesterone receptor, and HER2 expression in invasive breast carcinoma. *Modern Pathology* (2012). doi:10.1038/modpathol.2012.59

41. Hicks, D. G. & Schiffhauer, L. Standardized Assessment of the HER2 Status in Breast Cancer by Immunohistochemistry. *Laboratory Medicine* (2011). doi:10.1309/lmgzz58cts0dbgtw

42. Chand, P., Anubha, G., Singla, V. & Rani, N. Evaluation of immunohistochemical profile of breast cancer for prognostics and therapeutic use. *Nigerian Journal of Surgery* (2018). doi:10.4103/njs.njs_2_18

43. Irshad, H., Veillard, A., Roux, L. & Racoceanu, D. Methods for nuclei detection, segmentation, and classification in digital histopathology: A review-current status and future potential. *IEEE Reviews in Biomedical Engineering* (2014). doi:10.1109/RBME.2013.2295804

44. Tosun, A. B. & Gunduz-Demir, C. Graph run-length matrices for histopathological image segmentation. *IEEE Transactions on Medical Imaging* (2011). doi:10.1109/TMI.2010.2094200

45. Dundar, M. M. *et al.* Computerized classification of intraductal breast lesions using histopathological images. *IEEE Transactions on Biomedical Engineering* (2011). doi:10.1109/TBME.2011.2110648

46. Jain, A., Atey, S., Vinayak, S. & Srivastava, V. Cancerous Cell Detection Using Histopathological Image Analysis. *International Journal of Innovative Research in Computer and Communication Engineering* (2015). doi:10.15680/ijircce.2014.0212026

47. Ridolfi, R. L., Jamehdor, M. R. & Arber, J. M. HER-2/neu testing in breast carcinoma: A combined immunohistochemical and fluorescence in situ hybridization approach. *Modern Pathology* (2000). doi:10.1038/modpathol.3880154

48. Duffy, M. J. *et al.* Clinical use of biomarkers in breast cancer: Updated guidelines from

the European Group on Tumor Markers (EGTM). *European Journal of Cancer* (2017). doi:10.1016/j.ejca.2017.01.017

49. Jensen, E. V. *et al.* Estrogen receptors and proliferation markers in primary and recurrent breast cancer. *Proceedings of the National Academy of Sciences* (2001). doi:10.1073/pnas.211556298
50. Louie, M. C. & Sevigny, M. B. Steroid hormone receptors as prognostic markers in breast cancer. *American Journal of Cancer Research* (2017).
51. Muramatsu, M. & Inoue, S. Estrogen receptors: How do they control reproductive and nonreproductive functions? *Biochemical and Biophysical Research Communications* (2000). doi:10.1006/bbrc.2000.2214
52. Lee, H.-R., Kim, T.-H. & Choi, K.-C. Functions and physiological roles of two types of estrogen receptors, ERα and ERβ, identified by estrogen receptor knockout mouse. *Laboratory Animal Research* (2012). doi:10.5625/lar.2012.28.2.71
53. Kovats, S. Estrogen receptors regulate innate immune cells and signaling pathways. *Cellular Immunology* (2015). doi:10.1016/j.cellimm.2015.01.018
54. Khalid, A. B. & Krum, S. A. Estrogen receptors alpha and beta in bone. *Bone* (2016). doi:10.1016/j.bone.2016.03.016
55. Bean, L. A., Ianov, L. & Foster, T. C. Estrogen receptors, the hippocampus, and memory. *Neuroscientist* (2014). doi:10.1177/1073858413519865
56. Kuiper, G. G. J. M. *et al.* Comparison of the ligand binding specificity and transcript tissue distribution of estrogen receptors and α and β. *Endocrinology* (1997). doi:10.1210/endo.138.3.4979
57. Paterni, I., Granchi, C., Katzenellenbogen, J. A. & Minutolo, F. Estrogen receptors alpha (ERα) and beta (ERβ): Subtype-selective ligands and clinical potential. *Steroids* (2014). doi:10.1016/j.steroids.2014.06.012
58. Cheng, G. *et al.* Estrogen Receptors: How Do They Signal and What Are Their Targets. *Physiological Reviews* (2007). doi:10.1152/physrev.00026.2006
59. Borahay, M. A. *et al.* Estrogen Receptors and Signaling in Fibroids: Role in Pathobiology and Therapeutic Implications. *Reproductive Sciences* (2017). doi:10.1177/1933719116678686
60. Stossi, F. *et al.* Transcriptional profiling of estrogen-regulated gene expression via estrogen receptor (ER) α or ERβ in human osteosarcoma cells: Distinct and common target genes for these receptors. *Endocrinology* (2004). doi:10.1210/en.2003-1682

61. Barkhem, T. *et al.* Differential Response of Estrogen Receptor α and Estrogen Receptor β to Partial Estrogen Agonists/Antagonists. *Molecular Pharmacology* (1998). doi:10.1124/mol.54.1.105

62. Parker, M. G. Transcriptional activation by oestrogen receptors. *Biochemical Society Symposia* (1998).

63. Klinge, C. M. Estrogen receptor interaction with estrogen response elements. *Nucleic Acids Research* (2002). doi:10.1093/nar/29.14.2905

64. Kumar, R. *et al.* The dynamic structure of the estrogen receptor. *Journal of Amino Acids* (2011). doi:10.4061/2011/812540

65. Arnal, J. F. *et al.* Lessons from the dissection of the activation functions (AF-1 and AF-2) of the estrogen receptor alpha in vivo. in *Steroids* (2013). doi:10.1016/j.steroids.2012.11.011

66. Platet, N., Cathiard, A. M., Gleizes, M. & Garcia, M. Estrogens and their receptors in breast cancer progression: A dual role in cancer proliferation and invasion. *Critical Reviews in Oncology/Hematology* (2004). doi:10.1016/j.critrevonc.2004.02.001

67. Lin, A. H. Y. *et al.* Differential Ligand Binding Affinities of Human Estrogen Receptor-α Isoforms. *PLoS ONE* (2013). doi:10.1371/journal.pone.0063199

68. Shull, J. D., Dennison, K. L., Chack, A. C. & Trentham-Dietz, A. Rat models of 17β-estradiol-induced mammary cancer reveal novel insights into breast cancer etiology and prevention. *Physiological Genomics* (2018). doi:10.1152/physiolgenomics.00105.2017

69. Wang, Z., Liu, H. & Liu, S. Low-Dose Bisphenol A Exposure: A Seemingly Instigating Carcinogenic Effect on Breast Cancer. *Advanced Science* (2017). doi:10.1002/advs.201600248

70. Marczell, I. *et al.* Membrane-bound estrogen receptor alpha initiated signaling is dynamin dependent in breast cancer cells. *European Journal of Medical Research* (2018). doi:10.1186/s40001-018-0328-7

71. Acconcia, F. *et al.* Survival versus apoptotic 17beta-estradiol effect: role of ER alpha and ER beta activated non-genomic signaling. *Journal of Cellular Physiology* (2005). doi:10.1002/jcp.20219

72. Schiff, R., Massarweh, S., Shou, J. & Osborne, C. K. Breast cancer endocrine resistance: How growth factor signaling and estrogen receptor coregulators modulate response. in *Clinical Cancer Research* (2003).

73. McKenna, N. J. & O'Malley, B. W. Combinatorial control of gene expression by nuclear

receptors and coregulators. *Cell* (2002). doi:10.1016/S0092-8674(02)00641-4

74. Pedram, A., Razandi, M., Lewis, M., Hammes, S. & Levin, E. R. Membrane-localized estrogen receptor α is required for normal organ development and function. *Developmental Cell* (2014). doi:10.1016/j.devcel.2014.04.016
75. Pietras, R. J. & Szego, C. M. Specific binding sites for oestrogen at the outer surfaces of isolated endometrial cells [28]. *Nature* (1977). doi:10.1038/265069a0
76. Soltysik, K. & Czekaj, P. Membrane estrogen receptors - is it an alternative way of estrogen action? *Journal of physiology and pharmacology : an official journal of the Polish Physiological Society* (2013).
77. Pedram, A., Razandi, M., Deschenes, R. J. & Levin, E. R. DHHC-7 and -21 are palmitoylacyltransferases for sex steroid receptors. *Molecular Biology of the Cell* (2012). doi:10.1091/mbc.E11-07-0638
78. MIZUKAMI, Y. In Vivo Functions of GPR30/GPER-1, a Membrane Receptor for Estrogen: From Discovery to Functions In Vivo. *Endocrine journal* (2010). doi:10.1507/endocrj.K09E-332
79. Levin, E. R. Plasma membrane estrogen receptors. *Trends in Endocrinology and Metabolism* (2009). doi:10.1016/j.tem.2009.06.009
80. Gu, Q. & Moss, R. L. 17 beta-Estradiol potentiates kainate-induced currents via activation of the cAMP cascade. *The Journal of neuroscience : the official journal of the Society for Neuroscience* (1996). doi:10.1103/PhysRevB.47.95
81. Acconcia, F. & Marino, M. The effects of 17β-estradiol in cancer are mediated by estrogen receptor signaling at the plasma membrane. *Frontiers in Physiology* (2011). doi:10.3389/fphys.2011.00030
82. Levin, E. R. Rapid signaling by steroid receptors. *AJP: Regulatory, Integrative and Comparative Physiology* (2008). doi:10.1152/ajpregu.90605.2008
83. Bondar, G., Kuo, J., Hamid, N. & Micevych, P. Estradiol-Induced Estrogen Receptor-Trafficking. *Journal of Neuroscience* (2009). doi:10.1523/JNEUROSCI.2107-09.2009
84. Cabioglu, N. *et al.* Expression of growth factor and chemokine receptors: New insights in the biology of inflammatory breast cancer. *Annals of Oncology* (2007). doi:10.1093/annonc/mdm060
85. James, J. J. *et al.* Bone metastases from breast carcinoma: Histopathological-radiological correlations and prognostic features. *British Journal of Cancer* (2003). doi:10.1038/sj.bjc.6601198

86. Kingsley, L. A., Fournier, P. G. J., Chirgwin, J. M. & Guise, T. A. Molecular Biology of Bone Metastasis. *Molecular Cancer Therapeutics* (2007). doi:10.1158/1535-7163.MCT-07-0234

87. Olivotto, I. A. *et al.* Population-based validation of the prognostic model ADJUVANT! for early breast cancer. *Journal of Clinical Oncology* (2005). doi:10.1200/JCO.2005.06.178

88. Ishikawa, T. *et al.* The role of HER-2 in Breast Cancer. *Journal of surgery and science* **2**, 4–9 (2014).

89. Fukushige, S. *et al.* Localization of a novel v-erbB-related gene, c-erbB-2, on human chromosome 17 and its amplification in a gastric cancer cell line. *Molecular and Cellular Biology* (1986). doi:10.1128/MCB.6.3.955

90. van der Geer, P. Receptor Protein-Tyrosine Kinases and Their Signal Transduction Pathways. *Annual Review of Cell and Developmental Biology* (2002). doi:10.1146/annurev.cellbio.10.1.251

91. Iqbal, N. & Iqbal, N. Human Epidermal Growth Factor Receptor 2 (HER2) in Cancers: Overexpression and Therapeutic Implications. *Molecular Biology International* (2014). doi:10.1155/2014/852748

92. Bailey, T. A. *et al.* Mechanisms of Trastuzumab resistance in ErbB2-driven breast cancer and newer opportunities to overcome therapy resistance. *Journal of carcinogenesis* (2011). doi:10.4103/1477-3163.90442; 10.4103/1477-3163.90442

93. Feng, Y. *et al.* Breast cancer development and progression: Risk factors, cancer stem cells, signaling pathways, genomics, and molecular pathogenesis. *Genes and Diseases* (2018). doi:10.1016/j.gendis.2018.05.001

94. Hynes, N. E. & Lane, H. A. ERBB receptors and cancer: The complexity of targeted inhibitors. *Nature Reviews Cancer* (2005). doi:10.1038/nrc1609

95. Arpino, G., Milano, M. & De Placido, S. Features of aggressive breast cancer. *Breast* (2015). doi:10.1016/j.breast.2015.06.001

96. Rubin, I. & Yarden, Y. The basic biology of HER2. *Annals of Oncology* (2001). doi:10.1093/annonc/12.suppl_1.S3

97. Slamon, D. J. *et al.* Human breast cancer: Correlation of relapse and survival with amplification of the HER-2/neu oncogene. *Science* (1987). doi:10.1126/science.3798106

98. Lim, B. E. & Lin, N. U. Updates on the Management of Breast Cancer Brain Metastases. *Oncology* (2014). doi:10.1109/BADGERS.2015.16

99. Gabos, Z. *et al.* Prognostic significance of human epidermal growth factor receptor positivity for the development of brain metastasis after newly diagnosed breast cancer. *Journal of Clinical Oncology* (2006). doi:10.1200/JCO.2006.07.0250

100. Sauter, G., Lee, J., Bartlett, J. M. S., Slamon, D. J. & Press, M. F. Guidelines for human epidermal growth factor receptor 2 testing: Biologic and methodologic considerations. *Journal of Clinical Oncology* (2009). doi:10.1200/JCO.2007.14.8197

101. Burstein, H. J. The Distinctive Nature of HER2-Positive Breast Cancers. *New England Journal of Medicine* (2005). doi:10.1056/nejmp058197

102. Surgical guidelines for the management of breast cancer. *European Journal of Surgical Oncology* (2009). doi:10.1016/j.ejso.2008.11.001

103. Bellavance, E. C. & Kesmodel, S. B. Decision-Making in the Surgical Treatment of Breast Cancer: Factors Influencing Women's Choices for Mastectomy and Breast Conserving Surgery. *Frontiers in Oncology* (2016). doi:10.3389/fonc.2016.00074

104. Núñez, C. *et al.* An overview of the effective combination therapies for the treatment of breast cancer. *Biomaterials* (2016). doi:10.1016/j.biomaterials.2016.04.027

105. Fluegen, G. *et al.* Phenotypic heterogeneity of disseminated tumour cells is preset by primary tumour hypoxic microenvironments. *Nature Cell Biology* (2017). doi:10.1038/ncb3465

106. Richman, J. & Dowsett, M. Beyond 5 years: enduring risk of recurrence in oestrogen receptor-positive breast cancer. *Nature Reviews Clinical Oncology* (2018). doi:10.1038/s41571-018-0145-5

107. Carroll, J. S. EJE PRIZE 2016: Mechanisms of oestrogen receptor (ER) gene regulation in breast cancer. *European Journal of Endocrinology* (2016). doi:10.1530/eje-16-0124

108. National Comprehensive Cancer Network. NCCN Clinical Practice Guidelines in Oncology: Breast Cancer. *National Comprehensive Cancer Network* (2017). doi:10.1016/j.amepre.2011.02.015

109. Bonotto, M. *et al.* Chemotherapy versus endocrine therapy as first-line treatment in patients with luminal-like HER2-negative metastatic breast cancer: A propensity score analysis. *Breast* (2017). doi:10.1016/j.breast.2016.10.021

110. Hiscox, S., Davies, E. L. & Barrett-Lee, P. Aromatase inhibitors in breast cancer. *Maturitas* (2009). doi:10.1016/j.maturitas.2009.05.008

111. Patel, H. K. & Bihani, T. Selective estrogen receptor modulators (SERMs) and selective estrogen receptor degraders (SERDs) in cancer treatment. *Pharmacology and*

Therapeutics (2018). doi:10.1016/j.pharmthera.2017.12.012

112. Nounou, M. I. *et al.* Breast Cancer: Conventional Diagnosis and Treatment Modalities and Recent Patents and Technologies. *Breast Cancer: Basic and Clinical Research* (2015). doi:10.4137/bcbcr.s29420
113. Rochira, V. *et al. Estrogens and male reproduction*. *Endotext* (2000).
114. Shiau, A. K. *et al.* The structural basis of estrogen receptor/coactivator recognition and the antagonism of this interaction by tamoxifen. *Cell* (1998). doi:10.1016/S0092-8674(00)81717-1
115. Tsai-Turton, M. Tamoxifen. in *Encyclopedia of Toxicology: Third Edition* (2014). doi:10.1016/B978-0-12-386454-3.00066-X
116. Scholar, E. Raloxifene. in *xPharm: The Comprehensive Pharmacology Reference* (2011). doi:10.1016/B978-008055232-3.62511-5
117. Vogel, C. L., Johnston, M. A., Capers, C. & Braccia, D. Toremifene for breast cancer: A review of 20 years of data. *Clinical Breast Cancer* (2014). doi:10.1016/j.clbc.2013.10.014
118. Jordan, V. C. Tamoxifen: A most unlikely pioneering medicine. *Nature Reviews Drug Discovery* (2003). doi:10.1038/nrd1031
119. McDonnell, D. P., Wardell, S. E. & Norris, J. D. Oral Selective Estrogen Receptor Downregulators (SERDs), a Breakthrough Endocrine Therapy for Breast Cancer. *Journal of Medicinal Chemistry* (2015). doi:10.1021/acs.jmedchem.5b00760
120. Osborne, C. K., Wakeling, A. & Nicholson, R. I. Fulvestrant: An oestrogen receptor antagonist with a novel mechanism of action. *British Journal of Cancer* (2004). doi:10.1038/sj.bjc.6601629
121. van Kruchten, M. *et al.* Measuring residual estrogen receptor availability during fulvestrant therapy in patients with metastatic breast cancer. *Cancer Discovery* (2015). doi:10.1158/2159-8290.CD-14-0697
122. Howell, A. Fulvestrant ('Faslodex'): Current and future role in breast cancer management. *Critical Reviews in Oncology/Hematology* (2006). doi:10.1016/j.critrevonc.2005.08.001
123. Russell, C. A. Combination anastrozole and fulvestrant in metastatic breast cancer. *Breast Diseases* (2013). doi:10.1016/j.breastdis.2013.07.033
124. Giordano, S. H. *et al.* Systemic therapy for patients with advanced human epidermal growth factor receptor 2-positive breast cancer: American Society of Clinical Oncology

clinical practice guideline. *Journal of Clinical Oncology* (2014). doi:10.1200/JCO.2013.54.0948

125. Nuti, M. *et al.* Immune effects of Trastuzumab. *Journal of Cancer* (2011). doi:10.7150/jca.2.317
126. Baselga, J. *et al.* Phase II study of efficacy, safety, and pharmacokinetics of trastuzumab monotherapy administered on a 3-weekly schedule. *Journal of Clinical Oncology* (2005). doi:10.1200/JCO.2005.01.014
127. Madarnas, Y. *et al.* Adjuvant/neoadjuvant trastuzumab therapy in women with HER-2/neu-overexpressing breast cancer: A systematic review. *Cancer Treatment Reviews* (2008). doi:10.1016/j.ctrv.2008.03.013
128. Romond, E. H. *et al.* Trastuzumab plus adjuvant chemotherapy for operable HER2-positive breast cancer. *New England journal of medicine* (2005). doi:10.1056/NEJMoa052122
129. Vogel, C. L. *et al.* Efficacy and safety of trastuzumab as a single agent in first-line treatment of HER2-overexpressing metastatic breast cancer. *Journal of Clinical Oncology* (2002). doi:10.1200/JCO.20.3.719
130. Gu, G., Dustin, D. & Fuqua, S. A. Targeted therapy for breast cancer and molecular mechanisms of resistance to treatment. *Current Opinion in Pharmacology* (2016). doi:10.1016/j.coph.2016.11.005
131. Verma, S. *et al.* Trastuzumab emtansine for HER2-positive advanced breast cancer. *The New England journal of medicine* (2012). doi:10.1056/NEJMoa1209124
132. Swain, S. M. *et al.* Pertuzumab, Trastuzumab, and Docetaxel in HER2-Positive Metastatic Breast Cancer. *New England Journal of Medicine* (2015). doi:10.1056/NEJMoa1413513
133. Niikura, N. *et al.* Changes in tumor expression of HER2 and hormone receptors status after neoadjuvant chemotherapy in 21 755 patients from the Japanese breast cancer registry. *Annals of Oncology* (2016). doi:10.1093/annonc/mdv611
134. Agus, D. B. *et al.* Targeting ligand-activated ErbB2 signaling inhibits breast and prostate tumor growth. *Cancer Cell* (2002). doi:10.1016/S1535-6108(02)00097-1
135. Gradishar, W. J. Optimizing treatment of HER2-positive breast cancer. in *JNCCN Journal of the National Comprehensive Cancer Network* (2015). doi:10.6004/jnccn.2015.0193
136. Cameron, D. *et al.* A phase III randomized comparison of lapatinib plus capecitabine

versus capecitabine alone in women with advanced breast cancer that has progressed on trastuzumab: Updated efficacy and biomarker analyses. *Breast Cancer Research and Treatment* (2008). doi:10.1007/s10549-007-9885-0

137. Rosi, N. L. & Mirkin, C. A. Nanostructures in Biodiagnostics. *Chemical Reviews* (2005). doi:10.1021/cr030067f
138. Jain, P. K. Gold Nanoparticles for Physics, Chemistry, and Biology. Edited by Catherine Louis and Olivier Pluchery. *Angewandte Chemie International Edition* (2014). doi:10.1002/anie.201309807
139. Yeh, Y. C., Creran, B. & Rotello, V. M. Gold nanoparticles: Preparation, properties, and applications in bionanotechnology. *Nanoscale* (2012). doi:10.1039/c1nr11188d
140. Nehl, C. L., Liao, H. & Hafner, J. H. Optical properties of star-shaped gold nanoparticles. *Nano Letters* (2006). doi:10.1021/nl052409y
141. Chen, H., Shao, L., Li, Q. & Wang, J. Gold nanorods and their plasmonic properties. *Chemical Society Reviews* (2013). doi:10.1039/c2cs35367a
142. Schwartzberg, A. M., Olson, T. Y., Talley, C. E. & Zhang, J. Z. Synthesis, characterization, and tunable optical properties of hollow gold nanospheres. *Journal of Physical Chemistry B* (2006). doi:10.1021/jp062136a
143. Mulfinger, L. *et al.* Synthesis and Study of Silver Nanoparticles. *Journal of Chemical Education* (2007). doi:10.1021/ed084p322
144. Dhas, N. A., Raj, C. P. & Gedanken, A. Synthesis, Characterization, and Properties of Metallic Copper Nanoparticles. *Chemistry of Materials* (1998). doi:10.1021/cm9708269
145. Willets, K. A. & Van Duyne, R. P. Localized Surface Plasmon Resonance Spectroscopy and Sensing. *Annual Review of Physical Chemistry* (2006). doi:10.1146/annurev.physchem.58.032806.104607
146. Daniel, M.-C. & Astruc, D. Gold Nanoparticles: Assembly, Supramolecular Chemistry, Quantum-Size-Related Properties, and Applications toward Biology, Catalysis, and Nanotechnology. *Chemical Reviews* (2004). doi:10.1021/cr030698+
147. Liz-Marzán, L. M. Tailoring surface plasmons through the morphology and assembly of metal nanoparticles. *Langmuir* (2006). doi:10.1021/la0513353
148. Hu, M. *et al.* Gold nanostructures: Engineering their plasmonic properties for biomedical applications. *Chemical Society Reviews* (2006). doi:10.1039/b517615h
149. Strutt, J. W. & Strutt, J. W. On the Light from the Sky, its Polarization and Colour. in *Scientific Papers* (2011). doi:10.1017/cbo9780511703966.009

150. Smith, E. & Dent, G. *Modern Raman Spectroscopy - A Practical Approach*. *Modern Raman Spectroscopy - A Practical Approach* (2005). doi:10.1002/0470011831

151. Raman, C. V. & Krishnan, K. S. A new type of secondary radiation [11]. *Nature* (1928). doi:10.1038/121501c0

152. Gardner, B., Matousek, P. & Stone, N. Temperature Spatially Offset Raman Spectroscopy (T-SORS): Subsurface Chemically Specific Measurement of Temperature in Turbid Media Using Anti-Stokes Spatially Offset Raman Spectroscopy. *Analytical Chemistry* (2016). doi:10.1021/acs.analchem.5b03360

153. Kimbrell, J. B. *et al.* Analysis of mixtures of C 60 and C 70 by Raman spectrometry . *Nanoscience Methods* **3**, 40–46 (2014).

154. Ember, K. J. I. *et al.* Raman spectroscopy and regenerative medicine: a review. *npj Regenerative Medicine* (2017). doi:10.1038/s41536-017-0014-3

155. Fleischmann, M., Hendra, P. J. & McQuillan, A. J. Raman spectra of pyridine adsorbed at a silver electrode. *Chemical Physics Letters* (1974). doi:10.1016/0009-2614(74)85388-1

156. Jeanmaire, D. L. & Van Duyne, R. P. Surface raman spectroelectrochemistry. Part I. Heterocyclic, aromatic, and aliphatic amines adsorbed on the anodized silver electrode. *Journal of Electroanalytical Chemistry* (1977). doi:10.1016/S0022-0728(77)80224-6

157. Liao, P. F. *et al.* Surface-enhanced raman scattering from microlithographic silver particle surfaces. *Chemical Physics Letters* (1981). doi:10.1016/0009-2614(81)85172-X

158. Faulds, K., Hernandez-Santana, A. & Smith, W. E. The inorganic chemistry of surface enhanced Raman scattering (SERS). in (2010). doi:10.1039/9781849730853-00001

159. Vandenabeele, P. Enhancement of the Raman Signal. in *Practical Raman Spectroscopy - An Introduction* (2013). doi:10.1002/9781119961284.ch3

160. Wang, Y., Yan, B. & Chen, L. SERS Tags: Novel optical nanoprobes for bioanalysis. *Chemical Reviews* (2013). doi:10.1021/cr300120g

161. Rycenga, M. *et al.* Controlling the Synthesis and Assembly of Silver Nanostructures for Plasmonic Applications. *Chemical Reviews* (2011). doi:10.1021/cr100275d

162. McNay, G., Eustace, D., Smith, W. E., Faulds, K. & Graham, D. Surface-enhanced Raman scattering (SERS) and surface-enhanced resonance raman scattering (SERRS): A review of applications. *Applied Spectroscopy* (2011). doi:10.1366/11-06365

163. Asiala, S. M. & Schultz, Z. D. Characterization of hotspots in a highly enhancing SERS substrate. *Analyst* (2011). doi:10.1039/c1an15432j

164. Laing, S., Gracie, K. & Faulds, K. Multiplex in vitro detection using SERS. *Chemical Society Reviews* (2016). doi:10.1039/c5cs00644a

165. Dougan, J. A. & Faulds, K. Surface enhanced Raman scattering for multiplexed detection. *Analyst* (2012). doi:10.1039/c2an15979a

166. Stacy, A. A. & Van Duyne, R. P. Surface enhanced raman and resonance raman spectroscopy in a non-aqueous electrochemical environment: Tris(2,2′-bipyridine)ruthenium(II) adsorbed on silver from acetonitrile. *Chemical Physics Letters* (1983). doi:10.1016/0009-2614(83)87057-2

167. Harmsen, S. *et al.* Rational design of a chalcogenopyrylium-based surface-enhanced resonance Raman scattering nanoprobe with attomolar sensitivity. *Nature Communications* (2015). doi:10.1038/ncomms7570

168. Qian, X. *et al.* In vivo tumor targeting and spectroscopic detection with surface-enhanced Raman nanoparticle tags. *Nature Biotechnology* (2008). doi:10.1038/nbt1377

169. Graham, D. *et al.* Selective Detection of Deoxyribonucleic Acid at Ultralow Concentrations by SERRS. *Analytical Chemistry* (1997). doi:10.1021/ac970657b

170. Schlücker, S. Surface-enhanced raman spectroscopy: Concepts and chemical applications. *Angewandte Chemie - International Edition* (2014). doi:10.1002/anie.201205748

171. Faulds, K., McKenzie, F., Smith, W. E. & Graham, D. Quantitative simultaneous multianalyte detection of DNA by dual-wavelength surface-enhanced resonance raman scattering. *Angewandte Chemie - International Edition* (2007). doi:10.1002/anie.200604265

172. Gracie, K. *et al.* Simultaneous detection and quantification of three bacterial meningitis pathogens by SERS. *Chemical Science* (2014). doi:10.1039/c3sc52875h

173. Stoeva, S. I., Lee, J. S., Thaxton, C. S. & Mirkin, C. A. Multiplexed DNA detection with biobarcoded nanoparticle probes. *Angewandte Chemie - International Edition* (2006). doi:10.1002/anie.200600124

174. Faulds, K., Jarvis, R., Smith, W. E., Graham, D. & Goodacre, R. Multiplexed detection of six labelled oligonucleotides using surface enhanced resonance Raman scattering (SERRS). *Analyst* (2008). doi:10.1002/asna.2113130204

175. Henry, A. I., Sharma, B., Cardinal, M. F., Kurouski, D. & Van Duyne, R. P. Surface-enhanced Raman spectroscopy biosensing: In vivo diagnostics and multimodal imaging. *Analytical Chemistry* (2016). doi:10.1021/acs.analchem.6b01597

176. Bedics, M. A. *et al.* Extreme red shifted SERS nanotags. *Chemical Science* (2015). doi:10.1039/c4sc03917c

177. Kearns, H. *et al.* Sensitive SERS nanotags for use with 1550 nm (retina-safe) laser excitation. *Analyst* (2016). doi:10.1039/c5an02662h

178. Matousek, P. Spatially offset Raman spectroscopy for non-invasive analysis of turbid samples. *TrAC - Trends in Analytical Chemistry* (2018). doi:10.1016/j.trac.2018.04.002

179. Matousek, P. & Stone, N. Development of deep subsurface Raman spectroscopy for medical diagnosis and disease monitoring. *Chemical Society Reviews* (2016). doi:10.1039/c5cs00466g

180. Sowoidnich, K. *et al.* Spatially offset Raman spectroscopy for photon migration studies in bones with different mineralization levels. *Analyst* (2017). doi:10.1039/c7an00408g

181. Matousek, P. *et al.* Subsurface probing in diffusely scattering media using spatially offset Raman spectroscopys. *Applied Spectroscopy* (2005). doi:10.1366/0003702053641450

182. Feng, G., Ochoa, M., Maher, J. R., Awad, H. A. & Berger, A. J. Sensitivity of spatially offset Raman spectroscopy (SORS) to subcortical bone tissue. *Journal of Biophotonics* (2017). doi:10.1002/jbio.201600317

183. Stone, N., Baker, R., Rogers, K., Parker, A. W. & Matousek, P. Subsurface probing of calcifications with spatially offset Raman spectroscopy (SORS): Future possibilities for the diagnosis of breast cancer. *Analyst* (2007). doi:10.1039/b705029a

184. Keller, M. D. *et al.* Development of a spatially offset Raman spectroscopy probe for breast tumor surgical margin evaluation. *Journal of Biomedical Optics* (2011). doi:10.1117/1.3600708

185. Buckley, K. *et al.* Towards the in vivo prediction of fragility fractures with Raman spectroscopy. *Journal of Raman Spectroscopy* (2015). doi:10.1002/jrs.4706

186. Mawdsley, G. E., Tyson, A. H., Peressotti, C. L., Jong, R. A. & Yaffe, M. J. Accurate estimation of compressed breast thickness in mammography. *Medical Physics* (2009). doi:10.1118/1.3065068

187. Stone, N. & Matousek, P. Advanced transmission Raman spectroscopy: A promising tool for breast disease diagnosis. *Cancer Research* (2008). doi:10.1158/0008-5472.CAN-07-6557

188. Stone, N. *et al.* Surface enhanced spatially offset Raman spectroscopic (SESORS) imaging - the next dimension. *Chemical Science* (2011). doi:10.1039/c0sc00570c

189. Stone, N., Faulds, K., Graham, D. & Matousek, P. Prospects of deep Raman spectroscopy

for noninvasive detection of conjugated surface enhanced resonance Raman scattering nanoparticles buried within 25 mm of mammalian tissue. *Analytical Chemistry* (2010). doi:10.1021/ac100039c

190. Oseledchyk, A., Andreou, C., Wall, M. A. & Kircher, M. F. Folate-Targeted Surface-Enhanced Resonance Raman Scattering Nanoprobe Ratiometry for Detection of Microscopic Ovarian Cancer. *ACS Nano* (2017). doi:10.1021/acsnano.6b06796
191. Nicolson, F. *et al.* Multiplex imaging of live breast cancer tumour models through tissue using handheld surface enhanced spatially offset resonance Raman spectroscopy (SESORRS). *Chemical Communications* (2018). doi:10.1039/c8cc04267e
192. Yuen, J. M., Shah, N. C., Walsh, J. T., Glucksberg, M. R. & Van Duyne, R. P. Transcutaneous glucose sensing by surface-enhanced spatially offset Raman spectroscopy in a rat model. *Analytical Chemistry* (2010). doi:10.1021/ac101951j
193. Sharma, B., Ma, K., Glucksberg, M. R. & Van Duyne, R. P. Seeing through bone with surface-enhanced spatially offset Raman spectroscopy. *Journal of the American Chemical Society* (2013). doi:10.1021/ja409378f
194. Moody, A. S., Baghernejad, P. C., Webb, K. R. & Sharma, B. Surface Enhanced Spatially Offset Raman Spectroscopy Detection of Neurochemicals Through the Skull. *Analytical Chemistry* (2017). doi:10.1021/acs.analchem.7b00985
195. Li, M. *et al.* Shape-dependent surface-enhanced Raman scattering in gold-Raman-probe-silica sandwiched nanoparticles for biocompatible applications. *Nanotechnology* (2012). doi:10.1088/0957-4484/23/11/115501
196. Gracie, K. *et al.* Preferential Attachment of Specific Fluorescent Dyes and Dye Labeled DNA Sequences in a Surface Enhanced Raman Scattering Multiplex. *Analytical Chemistry* (2016). doi:10.1021/acs.analchem.5b02776
197. Harper, M. M., McKeating, K. S. & Faulds, K. Recent developments and future directions in SERS for bioanalysis. *Physical Chemistry Chemical Physics* (2013). doi:10.1039/c2cp43859c
198. Bartczak, D. & Kanaras, A. G. Preparation of peptide-functionalized gold nanoparticles using one pot EDC/Sulfo-NHS coupling. *Langmuir* (2011). doi:10.1021/la2022177
199. Trachsel, E. & Neri, D. Antibodies for angiogenesis inhibition, vascular targeting and endothelial cell transcytosis. *Advanced Drug Delivery Reviews* (2006). doi:10.1016/j.addr.2005.11.002
200. Walkey, C. D. *et al.* Protein corona fingerprinting predicts the cellular interaction of gold

and silver nanoparticles. *ACS Nano* (2014). doi:10.1021/nn406018q

201. Otsuka, H., Nagasaki, Y. & Kataoka, K. PEGylated nanoparticles for biological and pharmaceutical applications. *Advanced Drug Delivery Reviews* (2012). doi:10.1016/j.addr.2012.09.022
202. Kim, H. R. *et al.* Analysis of plasma protein adsorption onto PEGylated nanoparticles by complementary methods: 2-DE, CE and Protein Lab-on-chip® system. *Electrophoresis* (2007). doi:10.1002/elps.200600694
203. Canton, I. & Battaglia, G. Endocytosis at the nanoscale. *Chemical Society Reviews* (2012). doi:10.1039/c2cs15309b
204. Kou, L., Sun, J., Zhai, Y. & He, Z. The endocytosis and intracellular fate of nanomedicines: Implication for rational design. *Asian Journal of Pharmaceutical Sciences* (2013). doi:10.1016/j.ajps.2013.07.001
205. Aderem, A. & Underhill, D. M. MECHANISMS OF PHAGOCYTOSIS IN MACROPHAGES. *Annual Review of Immunology* (1999). doi:10.1146/annurev.immunol.17.1.593
206. Mercer, J. & Helenius, A. Virus entry by macropinocytosis. *Nature Cell Biology* (2009). doi:10.1038/ncb0509-510
207. Mayor, S. & Pagano, R. E. Pathways of clathrin-independent endocytosis. *Nature Reviews Molecular Cell Biology* (2007). doi:10.1038/nrm2216
208. Ng, C. T. *et al.* Clathrin-mediated endocytosis of gold nanoparticles in vitro. *Anatomical Record* (2015). doi:10.1002/ar.23051
209. Rappoport, J. Z. Focusing on clathrin-mediated endocytosis. *Biochemical Journal* (2008). doi:10.1042/BJ20080474
210. Deng, H., Dutta, P. & Liu, J. Stochastic simulations of nanoparticle internalization through transferrin receptor dependent clathrin-mediated endocytosis. *Biochimica et Biophysica Acta - General Subjects* (2018). doi:10.1016/j.bbagen.2018.06.018
211. Medina-Kauwe, L. K. 'Alternative' endocytic mechanisms exploited by pathogens: New avenues for therapeutic delivery? *Advanced Drug Delivery Reviews* (2007). doi:10.1016/j.addr.2007.06.009
212. Pelkmans, L., Kartenbeck, J. & Helenius, A. Caveolar endocytosis of simian virus 40 reveals a new two-step vesicular-transport pathway to the ER. *Nature Cell Biology* (2001). doi:10.1038/35074539
213. Guo, C.-J. *et al.* Infectious Spleen and Kidney Necrosis Virus (a Fish Iridovirus) Enters

Mandarin Fish Fry Cells via Caveola-Dependent Endocytosis. *Journal of Virology* (2012). doi:10.1128/JVI.06947-11

214. Dutta, D. & Donaldson, J. G. Search for inhibitors of endocytosis Intended specificity and unintended consequences. *Cellular Logistics* (2012). doi:http://dx.doi.org/10.4161/cl.23967
215. Ivanov, A. I. Pharmacological inhibition of endocytic pathways: Is it specific enough to be useful? *Methods in Molecular Biology* (2008). doi:10.1007/978-1-59745-178-9_2
216. Preta, G., Cronin, J. G. & Sheldon, I. M. Dynasore - Not just a dynamin inhibitor. *Cell Communication and Signaling* (2015). doi:10.1186/s12964-015-0102-1
217. Sigismund, S. *et al.* Endocytosis and Signaling: Cell Logistics Shape the Eukaryotic Cell Plan. *Physiological Reviews* (2012). doi:10.1152/physrev.00005.2011
218. Totta, P., Busonero, C., Leone, S., Marino, M. & Acconcia, F. Dynamin II is required for 17β-estradiol signaling and autophagy-based ERα degradation. *Scientific Reports* (2016). doi:10.1038/srep23727
219. Macia, E. *et al.* Dynasore, a Cell-Permeable Inhibitor of Dynamin. *Developmental Cell* (2006). doi:10.1016/j.devcel.2006.04.002
220. Xiang, S. *et al.* Uptake mechanisms of non-viral gene delivery. *Journal of Controlled Release* (2012). doi:10.1016/j.jconrel.2011.09.093
221. Zhang, S., Li, J., Lykotrafitis, G., Bao, G. & Suresh, S. Size-dependent endocytosis of nanoparticles. *Advanced Materials* (2009). doi:10.1002/adma.200801393
222. Benmerah, A. & Lamaze, C. Clathrin-coated pits: Vive la différence? *Traffic* (2007). doi:10.1111/j.1600-0854.2007.00585.x
223. Behzadi, S. *et al.* Cellular uptake of nanoparticles: Journey inside the cell. *Chemical Society Reviews* (2017). doi:10.1039/c6cs00636a
224. Foroozandeh, P. & Aziz, A. A. Insight into Cellular Uptake and Intracellular Trafficking of Nanoparticles. *Nanoscale Research Letters* (2018). doi:10.1186/s11671-018-2728-6
225. Vandamme, T. F. & Brobeck, L. Poly(amidoamine) dendrimers as ophthalmic vehicles for ocular delivery of pilocarpine nitrate and tropicamide. *Journal of Controlled Release* (2005). doi:10.1016/j.jconrel.2004.09.015
226. Rauch, J., Kolch, W., Laurent, S. & Mahmoudi, M. Big signals from small particles: Regulation of cell signaling pathways by nanoparticles. *Chemical Reviews* (2013). doi:10.1021/cr3002627
227. Chithrani, B. D. & Chan, W. C. W. Elucidating the mechanism of cellular uptake and

removal of protein-coated gold nanoparticles of different sizes and shapes. *Nano Letters* (2007). doi:10.1021/nl070363y

228. Fujimoto, T., Kogo, H., Nomura, R. & Une, T. Isoforms of caveolin-1 and caveolar structure. *J Cell Science* (2000). doi:10.1242/jcs.070102
229. Marano, F., Hussain, S., Rodrigues-Lima, F., Baeza-Squiban, A. & Boland, S. Nanoparticles: Molecular targets and cell signalling. *Archives of Toxicology* (2011). doi:10.1007/s00204-010-0546-4
230. Papp, T. *et al.* Human health implications of nanomaterial exposure. *Nanotoxicology* (2008). doi:10.1080/17435390701847935
231. Aillon, K. L., Xie, Y., El-Gendy, N., Berkland, C. J. & Forrest, M. L. Effects of nanomaterial physicochemical properties on in vivo toxicity. *Advanced Drug Delivery Reviews* (2009). doi:10.1016/j.addr.2009.03.010
232. Zhou, X. *et al.* A quantitative study of the intracellular concentration of graphene/noble metal nanoparticle composites and their cytotoxicity. *Nanoscale* (2014). doi:10.1039/c4nr01763c
233. Yu, D., Zhang, Y., Zhou, X., Mao, Z. & Gao, C. Influence of surface coating of PLGA particles on the internalization and functions of human endothelial cells. *Biomacromolecules* (2012). doi:10.1021/bm3010484
234. Kim, J. A., Aberg, C., Salvati, A. & Dawson, K. A. Role of cell cycle on the cellular uptake and dilution of nanoparticles in a cell population. *Nature Nanotechnology* (2012). doi:10.1038/nnano.2011.191
235. Deng, J. & Gao, C. Recent advances in interactions of designed nanoparticles and cells with respect to cellular uptake, intracellular fate, degradation and cytotoxicity. *Nanotechnology* (2016). doi:10.1088/0957-4484/27/41/412002
236. Jia, Y. P., Ma, B. Y., Wei, X. W. & Qian, Z. Y. The in vitro and in vivo toxicity of gold nanoparticles. *Chinese Chemical Letters* (2017). doi:10.1016/j.cclet.2017.01.021
237. Kennedy, D. C. *et al.* Carbohydrate functionalization of silver nanoparticles modulates cytotoxicity and cellular uptake. *Journal of Nanobiotechnology* (2014). doi:10.1186/s12951-014-0059-z
238. Anselmo, A. C. & Mitragotri, S. Nanoparticles in the clinic. *Bioengineering & Translational Medicine* (2016). doi:10.1002/btm2.10003
239. Ahn, J. M., Eom, H. J., Yang, X., Meyer, J. N. & Choi, J. Comparative toxicity of silver nanoparticles on oxidative stress and DNA damage in the nematode, Caenorhabditis

elegans. *Chemosphere* (2014). doi:10.1016/j.chemosphere.2014.01.078

240. Wang, F. *et al.* The biomolecular corona is retained during nanoparticle uptake and protects the cells from the damage induced by cationic nanoparticles until degraded in the lysosomes. *Nanomedicine: Nanotechnology, Biology, and Medicine* (2013). doi:10.1016/j.nano.2013.04.010
241. Xie, J., Xu, C., Kohler, N., Hou, Y. & Sun, S. Controlled PEGylation of monodisperse Fe3O4 nanoparticles for reduced non-specific uptake by macrophage cells. *Advanced Materials* (2007). doi:10.1002/adma.200701975
242. Connor, E. E., Mwamuka, J., Gole, A., Murphy, C. J. & Wyatt, M. D. Gold Nanoparticles Are Taken Up by Human Cells but Do Not Cause Acute Cytotoxicity. *Small* (2005). doi:10.1002/smll.200400093
243. Qu, Y. & Lü, X. Aqueous synthesis of gold nanoparticles and their cytotoxicity in human dermal fibroblasts-fetal. *Biomedical Materials* (2009). doi:10.1088/1748-6041/4/2/025007
244. Brandenberger, C. *et al.* Effects and uptake of gold nanoparticles deposited at the air-liquid interface of a human epithelial airway model. *Toxicology and Applied Pharmacology* (2010). doi:10.1016/j.taap.2009.09.014
245. Laurent, S. & Mahmoudi, M. Superparamagnetic iron oxide nanoparticles: Promises for diagnosis and treatment of cancer. *International Journal of Molecular Epidemiology and Genetics* (2011). doi:10.1021/cn100100e
246. Biju, V. Chemical modifications and bioconjugate reactions of nanomaterials for sensing, imaging, drug delivery and therapy. *Chemical Society Reviews* (2014). doi:10.1039/c3cs60273g
247. McAughtrie, S., Faulds, K. & Graham, D. Surface enhanced Raman spectroscopy (SERS): Potential applications for disease detection and treatment. *Journal of Photochemistry and Photobiology C: Photochemistry Reviews* (2014). doi:10.1016/j.jphotochemrev.2014.09.002
248. Schlücker, S. SERS microscopy: Nanoparticle probes and biomedical applications. *ChemPhysChem* (2009). doi:10.1002/cphc.200900119
249. Karabeber, H. *et al.* Guiding brain tumor resection using surface-enhanced Raman scattering nanoparticles and a hand-held Raman scanner. *ACS Nano* (2014). doi:10.1021/nn503948b
250. Lee, S. *et al.* Biological imaging of HEK293 cells expressing PLCγ1 using surface-

enhanced raman microscopy. *Analytical Chemistry* (2007). doi:10.1021/ac061246a

251. Lee, S. *et al.* Surface-enhanced Raman scattering imaging of HER2 cancer markers overexpressed in single MCF7 cells using antibody conjugated hollow gold nanospheres. *Biosensors and Bioelectronics* (2009). doi:10.1016/j.bios.2008.10.018
252. Lee, S. *et al.* Rapid and sensitive phenotypic marker detection on breast cancer cells using surface-enhanced Raman scattering (SERS) imaging. *Biosensors and Bioelectronics* (2014). doi:10.1016/j.bios.2013.07.063
253. Camus, V. L., Stewart, G., Nailon, W. H., McLaren, D. B. & Campbell, C. J. Measuring the effects of fractionated radiation therapy in a 3D prostate cancer model system using SERS nanosensors. *Analyst* (2016). doi:10.1039/c6an01032f
254. Jamieson, L. E. *et al.* Targeted SERS nanosensors measure physicochemical gradients and free energy changes in live 3D tumor spheroids. *Nanoscale* (2016). doi:10.1039/c6nr06031e
255. Shafer-Peltier, K. E., Haynes, C. L., Glucksberg, M. R. & Van Duyne, R. P. Toward a glucose biosensor based on surface-enhanced Raman scattering. *Journal of the American Chemical Society* (2003). doi:10.1021/ja028255v
256. Isola, N. R., Stokes, D. L. & Vo-Dinh, T. Surface-Enhanced Raman Gene Probe for HIV Detection. *Analytical Chemistry* (1998). doi:10.1021/ac970901z
257. Graham, D., Mallinder, B. J. & Smith, W. E. Surface-enhanced resonance Raman scattering as a novel method of DNA discrimination. *Angewandte Chemie - International Edition* (2000). doi:10.1002/(SICI)1521-3773(20000317)39:6<1061::AID-ANIE1061>3.0.CO;2-9
258. Rohr, T. E., Cotton, T., Fan, N. & Tarcha, P. J. Immunoassay employing surface-enhanced Raman spectroscopy. *Analytical Biochemistry* (1989). doi:10.1016/0003-2697(89)90613-1
259. Wang, G., Park, H. Y., Lipert, R. J. & Porter, M. D. Mixed monolayers on gold nanoparticle labels for multiplexed surface-enhanced Raman scattering based immunoassays. *Analytical Chemistry* (2009). doi:10.1021/ac901711f
260. Dou, X., Takama, T., Yamaguchi, Y., Yamamoto, H. & Ozaki, Y. Enzyme Immunoassay Utilizing Surface-Enhanced Raman Scattering of the Enzyme Reaction Product. *Analytical Chemistry* (1997). doi:10.1021/ac960995x
261. Schlücker, S. *et al.* Immuno-Raman microspectroscopy: In situ detection of antigens in tissue specimens by surface-enhanced Raman scattering. *Journal of Raman Spectroscopy*

(2006). doi:10.1002/jrs.1534

262. Sinha, L. *et al.* Quantification of the binding potential of cell-surface receptors in fresh excised specimens via dual-probe modeling of SERS nanoparticles. *Scientific Reports* (2015). doi:10.1038/srep08582
263. Lutz, B. R. *et al.* Spectral analysis of multiplex Raman probe signatures. *ACS Nano* (2008). doi:10.1021/nn800243g
264. Keren, S. *et al.* Noninvasive molecular imaging of small living subjects using Raman spectroscopy. *Proceedings of the National Academy of Sciences* (2008). doi:10.1073/pnas.0710575105
265. Wang, Y. 'Winston' *et al.* Rapid ratiometric biomarker detection with topically applied SERS nanoparticles. *TECHNOLOGY* (2014). doi:10.1142/S2339547814500125
266. McQueenie, R. *et al.* Detection of inflammation in vivo by surface-enhanced Raman scattering provides higher sensitivity than conventional fluorescence imaging. *Analytical Chemistry* (2012). doi:10.1021/ac3006445
267. Noonan, J. *et al.* In vivo multiplex molecular imaging of vascular inflammation using surface-enhanced Raman spectroscopy. *Theranostics* (2018). doi:10.7150/thno.28665
268. Moisoiu, V. *et al.* Breast Cancer Diagnosis by Surface-Enhanced Raman Scattering (SERS) of Urine. *Applied Sciences* (2019). doi:10.3390/app9040806
269. Cervo, S. *et al.* SERS analysis of serum for detection of early and locally advanced breast cancer. *Analytical and Bioanalytical Chemistry* (2015). doi:10.1007/s00216-015-8923-8
270. Wabuyele, M. B., Yan, F. & Vo-Dinh, T. Plasmonics nanoprobes: Detection of single-nucleotide polymorphisms in the breast cancer BRCA1 gene. *Analytical and Bioanalytical Chemistry* (2010). doi:10.1007/s00216-010-3992-1
271. Davis, R. *et al.* A Raman Imaging Approach Using CD47 Antibody-Labeled SERS Nanoparticles for Identifying Breast Cancer and Its Potential to Guide Surgical Resection. *Nanomaterials* (2018). doi:10.3390/nano8110953
272. Wang, Y. *et al.* Quantitative molecular phenotyping with topically applied SERS nanoparticles for intraoperative guidance of breast cancer lumpectomy. *Scientific Reports* (2016). doi:10.1038/srep21242
273. Dinish, U. S., Balasundaram, G., Chang, Y. T. & Olivo, M. Actively targeted in vivo multiplex detection of intrinsic cancer biomarkers using biocompatible SERS nanotags. *Scientific Reports* (2014). doi:10.1038/srep04075
274. Xiao, L., Harihar, S., Welch, D. R. & Zhou, A. Imaging of epidermal growth factor

receptor on single breast cancer cells using surface-enhanced Raman spectroscopy. *Analytica Chimica Acta* (2014). doi:10.1016/j.aca.2014.06.036

275. Feng, J. *et al.* Bioconjugation of Gold Nanobipyramids for SERS Detection and Targeted Photothermal Therapy in Breast Cancer. *ACS Biomaterials Science and Engineering* (2017). doi:10.1021/acsbiomaterials.7b00021

276. Hudis, C. A. Trastuzumab--mechanism of action and use in clinical practice. *The New England journal of medicine* (2007). doi:10.1056/NEJMra043186

9. Appendix

9.1 Instrumentation

9.2.1 Extinction Spectroscopy

All extinction spectroscopy was carried out on an Agilent Carry 60 UV-visible spectrophotometer in combination with Cary Win UV software. The instrument was left to warm up and equilibrate for at least 10 min. The range of wavelengths scanned was 300-800 nm. A dH_2O blank was used before the sample analysis to perform the baseline correction.

9.2.2 Dynamic Light Scattering and Zeta Potential

A Malvern Zetasizer Nano ZS was used to carry out all size measurements along with Zetasizer µV and APS version 6.20 software. Approximately 1 ml of sample was run in a disposable plastic cuvette with a standard Malvern Dip cell.

9.2.3 Scanning Electron Microscopy Imaging

All the SEM experiments were carried out on a Sirion 200 Schottky Field Emission Electron Microscope operating at an accelerating voltage of 30 kV and a magnification of 500 nm. Silicon wafers were cleaned before use with dH_20 and EtOH and were dried under nitrogen flow. The wafers were placed in an oxygen plasma cleaner for 60 s before the treatment with 50 µL

poly(diallyldimethylammonium) chloride (30 µL PDDA in 1 mL 1 mM NaCl for 30 min. Then, the wafers were washed with dH_20 and were dried under nitrogen flow. 10 µL of the nanoparticles was placed onto the silica wafer and left to be dried overnight before the analysis.

9.3 Experimental

9.3.1 Protein Estimation- Bicinchoninic Acid Assay (BCA Assay)

Protein content was estimated per sample with a BCA assay. A calibration curve prepared by adding to a 96 well plate in duplicate 0.25, 0.5, 1, 1.5, 2, 3, 4 mg/mL protein from a stock BSA solution. Each of these was made to a total volume of 10 µL, similarly, the test samples were added as 1 µL to 9 µL dH2O. The BCA reagent was made freshly each time and added at the last moment as a 1:50 dilution of Solution B: Solution A (#1859078 and #23228, Pierce). The BCA reagent (100 µL) was added to each well containing 1 µL of the appropriate protein standard and incubated for 1 h at 37 °C in a dark chamber before reading on the TECAN Spark 20M plate reader with Spark Control V2.1 software for protein determination with BCA assay. The results were plotted on Microsoft Excel 2013 to achieve a linear response of 0.997 R^2 value. The absorbance of the test samples was plotted against this and a concentration gained from the equation of the line.

The amount of antibody absorbed onto AuNPs presented as the concentration and calculated as the difference in the antibody added and antibody remaining in the supernatant after the functionalisation. The average number of antibody molecules adsorbed onto each AuNPs was calculated by dividing the concentration of adsorbed antibody (converted to 133.75 nM using antibody MW of 160,000 g/ml) by the concentration of AuNPs (initial concentration was 0.028 nM and AuNPs were centrifuged and concentrated to 2.8 nM). The absorbance from the antibody sample was corrected by subtracting the absorbance from the PEGylated control.

9.3.2 Agarose Gel Electrophoresis

1 % agarose gel was prepared by dissolving 100 mg of agarose in 100 mL 1x TBE buffer by applying heat and then leaving the gel to cool and set. The gel was added to the electrophoresis tank and it got completely covered with 1 x TBE buffer. The PEG5000-AuNPs and Ab-PEG5000-AuNPs were centrifuged at 6000 rpm for 20 min. The supernatant was removed, and the pellet

was re-suspended with 10 µL dH2O. The sample was mixed with 1 µL 6 x loading bugger and was loaded into a well of the agarose gel. A voltage of 160 V was applied to the gel for 40 min.

9.3.3 Lateral Flow Assay

Secondary IgG antibody (0.5 µg/mL) was spotted onto the nitrocellulose strip and left to dry. 10 µL of the PEG5000-AuNPs and Ab-PEG5000-AuNPs was added to the conjugate pad and the strip was placed in 100 µL HEPES buffer (1M, pH 7.0) which initiated the flow. A non-specific secondary IgG antibody was used as a control.

9.4 Publications and Presentations

Oral Presentations

1 “Image and Characterisation of Cancer Cells Using SERS and Responsive Enhanced Reporters in Breast Cancer”, International Conference on Enhanced Spectroscopies, Ontario, Canada, June 2019 (Award for Best Oral Presentation)

2 ”Image and Characterisation of Cancer Cells Using SERS and Responsive Enhanced Reporters in Breast”, Analytical Research Forum, London, UK, June 2019 (Award for Best Oral Presentation)

3 “Image and Characterisation of Cancer Cells Using SERS and Responsive Enhanced Reporters in Breast”, Federation of Analytical Chemistry & Spectroscopy Societies, Atlanta, USA, October 2018

4 “Image and Characterisation of Cancer Cells Using SERS and Responsive Enhanced Reporters in Breast”, Spring SciX, Glasgow, UK, April 2018

5 “Characterisation of Breast Cancer Using Optical Medical Imaging”, Medical Imaging Conference, London, UK, September 2017

6 “Characterisation of Breast Cancer Using Optical Medical Imaging”, BioPhotonics Approaches: From Molecules to Living Systems, Dundee, UK, September 2016

Poster Presentations

1. “Image and Characterisation of Cancer Cells Using SERS and Responsive Enhanced Reporters in Breast Cancer”, Bioorthogonal and Bioresponsive RSC symposium, Edinburgh, UK, June 2017 (Selected for Flash Presentation)

2 “Image and Characterisation of Cancer Cells Using SERS and Responsive Enhanced Reporters in Breast Cancer”, Medical Imaging Conference, London, UK, September 2017

3 “Image and Characterisation of Cancer Cells Using SERS and Responsive Enhanced Reporters in Breast Cancer”, TransMed Conference, Edinburgh, UK, June 2016

Intention to Submit Publications

1.“Investigation of Cellular Uptake Mechanisms of Functionalised Gold Nanoparticles into Breast Cancer Cells Using SERS”
A. Kapara, V. Brunton, D. Graham and K. Faulds

2 “Characterisation of ERα Positive Breast Cancer Cells and Understanding of Fulvestrant Activity Using SERS”
A. Kapara, V. Brunton, D. Graham and K. Faulds

3 “Detection of Estrogen Receptor Alpha and Assessment of Fulvestrant Activity in Live MCF-7 Tumour Spheroids Using Microfluidic Devices and SERS”
A. Kapara, K. A. F. Paterson, V. Brunton, D. Graham, M. Zagnoni and K. Faulds